Thermodynamic signatures of topological spin-texture transitions in magnetic field gradients

Dissertation

zur Erlangung des akademischen Grades

Dr. rer. nat.

eingereicht an der

Mathematisch-Naturwissenschaftlich-Technischen Fakultät

der Universität Augsburg

von

Stefan Gorol

Augsburg, November 2022

Universität
Augsburg
University

Erstgutachter:	Prof. Dr. Thilo Kopp
Zweitgutachter:	Prof. Dr. Liviu Chioncel
Tag der mündlichen Prüfung:	22.02.2023

Vorwort

Zunächst bedanke ich mich herzlichst bei Prof. Thilo Kopp, der mir diese Promotionsarbeit ermöglicht hat und mich als mein Doktorvater hervorragend unterstützt hat. Ich habe in der ganzen Zeit bei ihm die ausgesprochen gute Arbeitsatmosphäre und den wissenschaftlichen Freiraum für Ideen in der Forschung sehr geschätzt. Ich bedanke mich für den fachlichen Austausch und dafür, dass Prof. Kopp für sämtliche Anliegen immer ein offenes Ohr hatte. Mein herzlicher Dank gilt ebenfalls Prof. Arno Kampf und Dr. Daniel Braak für die ausgesprochen guten und kritischen Gespräche über die Ergebnisse unserer Forschung zusammen mit Prof. Kopp und mir.

Mein aufrichtiger Dank gilt auch Dr. Florian Loder, auf dessen Arbeit zusammen mit Prof. Thilo Kopp, Prof. Arno Kampf und Dr. Daniel Braak die Ergebnisse dieser Promotionsarbeit aufbauen. Sie hatten sich mit Spintexturen in topologischen Supraleitern beschäftigt. Dr. Loder hat sich Zeit für den fachlichen Austausch der Ergebnisse genommen, obwohl er bereits nicht mehr am Lehrstuhl tätig war. Ich bedanke mich dafür sehr herzlich. Schließlich bedanke ich mich bei Elias Lettl für die detaillierten Diskussionen über verschiedene fachliche Fragestellungen, die während der Arbeit an dieser Promotion entstanden sind.

Die Ergebnisse dieser Dissertation wurden im Rahmen meiner Forschungstätigkeit am Lehrstuhl für Experimentalphysik VI der Universität Augsburg erarbeitet. Dabei wurde ein erheblicher Teil durch die Deutsche Forschungsgesellschaft (DFG) im Rahmen des TRR 80 finanziert. An dieser Stelle bedanke ich mich für diese Unterstützung. Abschließend spreche ich meinen Dank dem gesamten Lehrstuhl für Experimentalphysik VI für die angenehme Zeit während dieser Arbeit aus.

Thermodynamic signatures of topological spin-texture transitions in magnetic field gradients

Stefan Gorol

Abstract

Topological phases are commonly characterized by a non-trivial Chern number which is related in many cases to non-trivial topological spin-textures. There are measurable quantities, such as the transverse Hall conductivity, being proportional to the Chern number. The transverse Hall conductivity is a transport quantity depending on edge state physics. In contrast to these transport quantities, thermodynamic response signatures unequivocally indicating topological spin-texture transitions are investigated in this thesis. These signatures are bulk properties, analyzed in two dimensional electronic systems where the information about non-trivial topological phase transitions are manifest in the second order response of the spin polarization to external in-plane magnetic field gradients. This response is shown to directly provide topological information. In addition, the change in the spin magnetization due to the magnetic field gradients shows a clear increase in its amplitude towards the phase boundary with a sign change across the phase transition. The results demonstrate that the magnetization response can in principle be in measurable ranges and therefore appropriate to gain qualitative information about changes in topological invariants across the phase transitions.

Contents

I. Motivation

Topology is a vast branch in mathematics. Probably the most popular example of geometrical topology is the topological equivalence of the bagel and the coffee cup since the coffee cup can be continuously deformed into a bagel and vice versa. This example was used as an illustration of topology in 2016 by Haldane [1] in his physics Nobel price lecture. The concept of topology allows to define topological invariants which describe the equivalence of spaces in terms of integers. The reason for the Nobel price in 2016 was the perception of the importance of topology in physics when in 1982 Thouless and collaborators proved the transverse conductivity of the quantum Hall effect to be proportional to a topological invariant [2], the Chern number. This transverse Hall conductivity had been measured by von Klitzing two years before in 1980 [3] for which he received the Nobel price in 1985 for the discovery of the quantization of the Hall effect in a two-dimensional electron gas at low temperatures [4]. There, the transverse Hall conductivity σ_{xy} shows to have pronounced plateaus. The very interesting point in the transverse Hall conductivity and in topological invariants is the identification of exact integer values obtained from experiments. The plateaus in the quantum Hall effect are precisely given at $\sigma_{xy} = N_{\mathrm{C}}\mathrm{e}^2/\mathrm{h}$ [5] where N_{C} is an integer while e and h denote the elementary charge and the Planck constant, respectively. The importance of topology reaches far beyond the quantum Hall effect and the relevance of research in that field is still high. A variety of materials have been identified hosting non-trivial topological states [6] among which the topological superconductors [7], topological insulators and Chern insulators [8], and Weyl and Dirac semimetals [9] have to be mentioned.

In any case, in the context of fermionic systems, the topological invariants are defined by the bulk states. However, there is a correspondence between the occurrence of gapless edge states and bulk topological states referred to as bulk boundary correspondence [8]. This link between the bulk topology and the edge states opens up the possibility to analyze topological properties from edge state measurements. In fact, quantum Hall conductivity rely on the existence of edge states in topological insulators [10, 11].

The field of potential application and research for topology is wide and includes for example spintronics, where topological spin textures such as skyrmions are of much interest [12–14]. The skyrmion is defined in terms of the full cover of a compact manifold under the map defined by the spin expectation above some compact parameter space (e. g. the real or momentum space). Although the concept of skyrmion numbers is different to the concept of the Chern number, in a variety of systems [15, 16], both concepts can be applied yielding the exact same information about their topologies.

The analysis of topological spin textures raises the question, whether topological phases or transitions between them can be identified in the magnetization, a thermodynamic quantity. This question has been taken up within the framework of this thesis. Thermodynamics have been discussed in the context of topological phase transitions in the literature. However, signatures not restricted to non-trivial spin-texture transitions have not been identified yet. One example of a thermodynamic signature which has been addressed to topological phase transitions is the Lifshitz transition [17, 18] which is solely driven by structural Fermi surface transitions, a prerequisite of topological phase transitions, and thus not sufficient to identify topological phase transitions.

This leads to the question if it is even possible to identify bulk thermodynamic signatures confined to non-trivial topological phase transitions. Such an identification is very important because the transport quantities such as the transverse conductivity — which can be directly related to non-trivial topological phases — are caused by edge state physics. However, topology is defined within the bulk. Moreover, the occurrence of edge states are also not restricted to topologically non-trivial bulk states. This issue is also addressed within the analysis of this thesis.

The spin-polarization response to an in-plane electric field can produce a collective spin magnetization [19] in the out-of-plane direction. Instead of in-plane electric fields (corresponding to in-plane gradients of the electric potential), in-plane gradients of the magnetic field are used within the context of this thesis in order to obtain bulk quantities bearing directly topological information. The presented results on thermodynamic response quantities clearly suggests that the second order out-of-plane magnetization response to an applied magnetic field gradient linear in both in-plane directions shows thermodynamic signatures connected to non-trivial spin-texture transitions. In this way, the response analysis may be pivotal for the detection of non-trivial spin-texture transitions.

II. Introduction

In the first section, a brief introduction into the field of topology including mathematical basics and historical background of topology is presented. The main results of this thesis are examined for two different, well known fermionic systems which are introduced in the second and third section of this introductory chapter.

II.1. Basics of topology

Topology is a vast branch in mathematics with many application in physics. An example is the quantum Hall effect which is related to the Chern number, a topological property observable in Chern insulators [20]. In the following, basic concepts of topology that are related to the main part of this work are introduced.

Historical background and Basic concepts

The concept of topology goes back to Leonhard Euler [21]. In 1750, he found that any convex polyhedron fulfills the condition [22]

$$K - E + F = \chi_{\text{polyhedron}} = 2, \tag{II.1.1}$$

where E, K and F denote the number of edges, vertices and faces, respecively, e. g. a tetrahedron has four faces $F = 4$, six edges $E = 6$ and four vertices $K = 4$ resulting in $\chi_{\text{tetrahedron}} = 4 - 6 + 2 = 2$. Since any convex polyhedron yields the same result, $\chi = \chi_{\text{polyhedron}}$ is said to be a topological invariant. Later, Simon Lhuilier generalized the formula to include non-convex polyhedra including g holes to [23]

$$K - E + F = \chi_{\text{polyhedron}} - 2g. \tag{II.1.2}$$

Since a sphere can be thought of a polyhedron with the number of vertices going to infinity, the sphere has the same Euler characteristic $\chi_{\text{sphere}} = 2$ as the polyhedron. Actually, a polyhedron is homeomorphic to a sphere (See Definition 1.0 below for homeomorphism). The sphere and the polyhedron are therefore topologically identical. The first formal proof was obtained by Legendre [24, 25] using radial projections from a polyhedron onto a surrounding sphere.

Therefore, any purely convex three dimensional object, such as the sphere, the polyhedron or an ellipsoid for example, have the same Euler characteristic. So one can think of the Euler characteristic as an invariant under smooth deformation as long the resulting object has no extra holes in it. This scheme is illustrated in Figure II.1. The sphere in Subfigure II.1 a) can be deformed into the cube in II.1 b) without a change in its topology. The torus depicted in II.1 c) cannot be

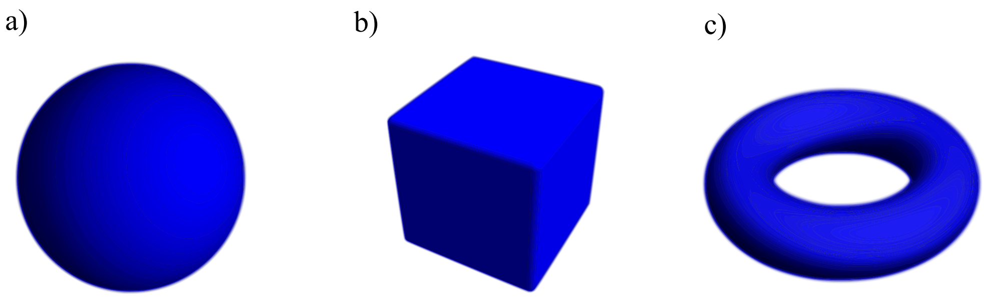

Figure II.1.: The sphere given in a) can be continuously deformed for example into the cube given in b). For both, the sphere and the cube, the Euler characteristic is equal $\chi_{\text{Cube}} = \chi_{\text{Sphere}} = 2$. The torus given in c) cannot be deformed continuously into a sphere. The torus has thus a different Euler characteristic which is given by $\chi_{\text{c}} = 0$.

deformed into the sphere without allowing for discontinuities and has another Euler characteristic. This concept can be generalized to higher dimensions which was done by Poincare [26].

Independent on the Euler characteristic, Carl Friedrich Gauß analyzed the curvature on surfaces in three dimensional space [27]. He found that the product of the principal curvatures referred to as "Gaussian curvature" which is defined as the product of the largest and the smallest curvature on each point of the surface is a property that is only dependent on the inner geometry of the surface which means that it can be described using only the so called first fundamental form of surfaces. The first fundamental form is given by the inner product of two tangent vectors defined on the surface in three dimensional space. With the first fundamental form, the length of lines on curved surfaces or the area on a curved surface can be determined [28].

Interestingly, the total Gaussian curvature, which is the integral of the Gaussian curvature over the entire surface, is related to the Euler characteristic which is a global topological property whereas the curvature at a single point on the surface is a local geometric property. This relation between the Gaussian curvature and the Euler characteristic was published by Bonnet [29], which is why this is referred to as the Gauß-Bonnet theorem.

The concept of topology establishes meanwhile a huge branch in mathematics. Some of the mathematical definitions are important in the context below and are therefore presented here. These definitions are well known and can be found in common literature on topology.

Definition II.1.1: Topological space

A topological space is called a pair $(\mathbb{X}, \tau)$ where $\mathbb{X}$ is a set, τ a collection of subsets of $\mathbb{X}$ satisfying the following properties

1. $\emptyset$ and $\mathbb{X} \in \tau$
2. $U, V \in \tau$ implies $U \cap V \in \tau$ any intersecting set of two subsets in τ are included in τ.
3. $U, V \in \tau$ implies $U \cup V \in \tau$ any union of subsets in τ is a member of τ.

The collection τ is called a topology on $\mathbb{X}$ and the ordered pair $(\mathbb{X}, \tau)$ is called a topological space. The elements of τ are said to be open sets.

The simplest example of a topological space would be $(\mathbb{X}, \{\emptyset, \mathbb{X}\})$, where τ consist only of the set itself and the empty set — the trivial topology. There are of course many other possibilities to define in this manner an example of a topological space.

In physics, one usually deals with metric spaces (Euclidean) and every metric d on a set $\mathbb{X}$ induces a topology τ on $\mathbb{X}$. Therefore, one can define the open set $B(x, \epsilon) = \{y \in \mathbb{X} : d(x, y) < \epsilon\}$. The collection of sets $\tau_d = \{B(x, \epsilon) : x \in \mathbb{X}, \epsilon > 0\}$ is then a topology on $\mathbb{X}$. Therefore a metric space fulfills the definitions of a topological space and is thus a special type of topological space. In physics, we thus naturally deal with topological spaces most of the time. Examples for topological spaces are the 2-sphere (S^2) which is given by $\mathrm{S}^2 := \{x \in \mathbb{R}^3 : ||x|| = 1\}$, the 1-sphere ($\mathrm{S}^1$) defined through $\mathrm{S}^1 := \{x \in \mathbb{R}^2 : ||x|| = 1\}$ or the torus $\mathrm{T} := \mathrm{S}^1 \times \mathrm{S}^1$.

In order to discuss topological invariants, the concept of homeomorphism is important. A topological invariant is defined as a property preserved under homeomorphisms.

Definition II.1.2: Homeomorphism

Let $(\mathbb{X}, \tau_{\mathbb{X}})$ and $(\mathbb{Y}, \tau_{\mathbb{Y}})$ be two topological spaces, then a function $f : \mathbb{X} \to \mathbb{Y}$ is a homeomorphism if it has the following properties

1. f is a bijection
2. f is continuous
3. the inverse function f^{-1} is continuous

A homeomorphism is called a bicontinuous function and is said to be an equivalence relation between topological spaces.

Another fundamental concept of topology is the invariance under smooth deformations called a homotopy invariance.

Definition II.1.3: Homotopy

Let $(\mathbb{X}, \tau_x)$, $(\mathbb{Y}, \tau_y)$ be topological spaces, and $f, g : \mathbb{X} \to \mathbb{Y}$ two continuous maps. A homotopy from f to g is a continuous function $F : \mathbb{X} \times [0,1] \to \mathbb{Y}$ satisfying $F(x, 0) = f(x)$ and $F(x, 1) = g(x)$, for all $x \in \mathbb{X}$. If such a homotopy exists, then f is homotopic to g.

Simply speaking, a homotopy is a continuous deformation of two continuous functions. If a function can be smoothly deformed into the other function, then both functions are homotopic to each other.

Theorem II.1.1: Homotopy equivalence

Let $f : \mathbb{X} \to \mathbb{Y}$ be a continuous map. Then f is said to be homotopy equivalence if there exists a continuous map $g : \mathbb{Y} \to \mathbb{X}$ such that $f \circ g$ is homotopic to $\mathrm{id}_{\mathbb{Y}}$ and $g \circ f$ is homotopic to $\mathrm{id}_{\mathbb{X}}$. The map g in the above definition is said to be a homotopy inverse to f.

That means that two topological spaces are homotopy equivalent if they can be continuously deformed into each other. So the polyhedron is homotopy equivalent to the sphere. The homotopy groups therefore yield information about basic shapes, these are the point, the sphere, the torus and so on. The above mentioned Euler characteristic is thus a homotopy invariant.

Being a topological invariant and homotopy invariant are two different concepts, however, the Euler characteristic is both, invariant under homeomorphisms [30] and invariant under homotopies. There are examples of topological invariants which are homotopy invariant but not invariant under homeomorphisms. An example for such an invariant is the degree of a continuous map.

Definition II.1.4: Degree of a continuous map

The degree of a continuous mapping between two compact oriented manifolds of the same dimension is a number that represents the number of times that the domain manifold wraps around the range manifold under the mapping. The degree is always an integer, but may be positive or negative depending on the orientations.

As an example, the continuous map from the torus T^2 to the unit sphere S^2 $f{:}\mathrm{T}^2 \to \mathrm{S}^2$ is a homotopy invariant since it is a continuous map between two compact oriented manifolds of the same dimension and its degree is therefore an integer and any smooth deformation of this mapping yields still the same integer. However, the T^2 is not homeomorphic to the S^2 so there is not a one to one correspondence between the T^2 and the S^2. The formulation of such a degree of a continuous map was first introduced by Brouwer [31, 32]. The important invariants under consideration in this thesis are the degrees of a continuous map and the Chern number which are both homotopy invariants. However, in the following, the term “topological invariant” is used also in the context of homotopy invariants such as the Chern number or the degree of a continuous map while strictly speaking, topological invariants are defined such that they are invariant under homeomorphism.

Parallel transport

As mentioned above, the Euler characteristic can be determined by the integration of the Gaussian curvature of a closed manifold. In order to determine the "curvature" of a surface, the concept of parallel transport is useful to establish the connection to topological quantum systems.

The concept of parallel transport works as follows. Imagine a curved surface embedded in a three dimensional Euclidean space. Choose one tangent vector of the tangent vector space at a certain point on the curved surface and a direction of the displacement of the tangent vector and then move this vector along a path on the surface such that the angle between the chosen tangent vector and the direction of the displacement along the chosen path is kept constant. This method allows one to compare two different tangent vectors on different positions on a curved surface. Therefore one transports one of the tangent vectors parallel in this way to the position of the other vector. The angle of the two vectors can now be compared as both vectors are defined on the same position of the surface. The result of this procedure is dependent on the chosen path. One could now choose a tangent vector on a curved surface and transport the vector parallel along a straight line (a geodesic) to another point on the surface (e. g. from point A to point B in Figure II.2), then to a third position on the surface (point C) and finally return to the starting point. After the closed loop, dependent on the chosen path, the initial direction and the final direction of the tangent vector at the same point on the surface are different. This difference depends on the curvature of the surface. The angle between the initial and the final tangent vector is called anholonomy angle α and is given by

$$\alpha = \int_A K \mathrm{d}S \tag{II.1.3}$$

where A is the area enclosed by the path where K denotes the Gaussian curvature [33]. Therefore if one takes the limit of infinitesimal small areas enclosed by the chosen path, the anholonomy angle α is given by the Gaussian curvature multiplied by the enclosed area. Thus, within the concept of parallel transport, the Gaussian curvature can be obtained. Instead of moving a single tangent vector along geodesics of a surface, one could move an entire orthonormal frame consisting of a unit normal vector $\hat{\boldsymbol{n}}$ perpendicular to the surface and two orthogonal unit tangent vectors $\hat{\boldsymbol{t}}_1$ and $\hat{\boldsymbol{t}}_2$ within the surface plane along the geodesics. The advantage of the moving frame is that simple mathematical conditions can be formulated ensuring that the frame is moved parallel along the geodesics. Here the presentation follows closely the one given by Berry [34, 35]. Being transported parallel means that the orthonormal frame should not twist around $\hat{\boldsymbol{n}}$ when moving across the surface. That means that the angular velocity $\boldsymbol{\omega} = \hat{\boldsymbol{t}}_1 \times \mathrm{d}\hat{t}_1$ of the frame needs to be orthogonal to the unit

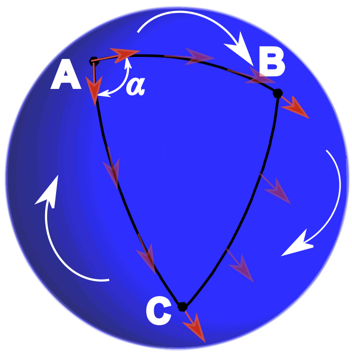

Figure II.2.: The concept of parallel transport along a triangle on the surface of a sphere is shown. The description is given in the main text.

normal vector which translates into the condition

$$\left(\hat{\boldsymbol{t}}_1 \times \mathrm{d}\hat{\boldsymbol{t}}_1\right) \cdot \hat{\boldsymbol{n}} \stackrel{!}{=} 0 \tag{II.1.4}$$

$$\Leftrightarrow \left(\hat{t}_1 \hat{t}_1\right)\left(\mathrm{d}\hat{\boldsymbol{t}}_1 \hat{\boldsymbol{t}}_2\right) - \left(\hat{t}_1 \hat{t}_2\right)\left(\mathrm{d}\hat{\boldsymbol{t}}_1 \hat{\boldsymbol{t}}_1\right) \stackrel{!}{=} 0 \tag{II.1.5}$$

$$\Rightarrow \mathrm{d}\hat{\boldsymbol{t}}_1 \hat{\boldsymbol{t}}_2 \stackrel{!}{=} 0 \tag{II.1.6}$$

Defining

$$\psi = \frac{1}{\sqrt{2}}\left(\hat{t}_1 + \mathrm{i}\hat{t}_2\right) \tag{II.1.7}$$

The conditions for the transport being parallel in (II.1.5) and (II.1.6) then translate into

$$\psi^* \cdot \mathrm{d}\psi \stackrel{!}{=} 0 \tag{II.1.8}$$

The moved frame can be compared to a fixed frame $(\hat{\boldsymbol{n}}, \hat{\boldsymbol{u}}_1, \hat{\boldsymbol{u}}_2)$ at some position $\boldsymbol{x} = (x_1, x_2)$ on the surface while the frames can differ by a twist angle $\alpha(\boldsymbol{x})$ around the unit normal $\hat{\boldsymbol{n}}$. The moved and the fixed frame are thus related such that

$$\psi'(x) = \mathrm{e}^{\mathrm{i}\alpha(\boldsymbol{x})}\psi(\boldsymbol{x}) \tag{II.1.9}$$

with

$$\psi'(x) = \frac{1}{\sqrt{2}}\left(\hat{\boldsymbol{u}}_1 + \mathrm{i}\hat{\boldsymbol{u}}_2\right). \tag{II.1.10}$$

From the parallel transport condition (II.1.8) it follows that

$$\mathrm{d}\alpha(\boldsymbol{x}) = -\mathrm{i}\psi'(\boldsymbol{x})\mathrm{d}\psi'(\boldsymbol{x}). \tag{II.1.11}$$

The full anholonomy angle α after moving one complete loop on the surface is thus

$$\alpha(C) = -\mathrm{i}\oint_C \mathrm{d}\boldsymbol{x}\,\psi'(\boldsymbol{x})\nabla_{\boldsymbol{x}}\psi(\boldsymbol{x}). \tag{II.1.12}$$

By use of Stokes theorem, the line integral can be rewritten as a surface integral yielding

$$\alpha(C) = -\mathrm{i}\int_{A(C)} \mathrm{d}x_1 \mathrm{d}x_2 \nabla_{\boldsymbol{x}} \times \left(\psi'(\boldsymbol{x})\nabla_{\boldsymbol{x}}\psi'(\boldsymbol{x})\right) \tag{II.1.13}$$

Comparing (II.1.13) and (II.1.3), the Gaussian curvature on a surface of three dimensional objects can be written as

$$K(\boldsymbol{x}) = -\mathrm{i}\nabla_{\boldsymbol{x}} \times \left(\psi'(\boldsymbol{x})\nabla_{\boldsymbol{x}}\psi'(\boldsymbol{x})\right). \tag{II.1.14}$$

This expression for the curvature is similarly given in the context of topological fermionic systems and this link is discussed in the following.

Berry Phase and skyrmion number

Above, the Gauß-Bonnet theorem was addressed which relates the Gaussian curvature which is a local geometrical property to the global topology of three dimensional manifolds. In quantum mechanics, systems are described by Hamiltonians that vary smoothly in parameter space. A Hamiltonian is not a geometrical object. However, topological invariants can be defined for Hamiltonians and these invariants can be found to be related to physically measurable quantities. Following the presentation of Berry [36], a Hamiltonian $H(\boldsymbol{x}(t))$ where $\boldsymbol{x}(t) = (x_1(t), x_2(t), \dots)$ are parameterized by the time t is considered. The eigenstates of the Hamiltonian at the initial time $t = 0$ are given by the solutions of the eigenequation

$$H(\boldsymbol{x}(0))|n(0)\rangle = E_n|n(0)\rangle.$$

The system $H(\boldsymbol{x}(t))$ evolves in time through its parameters. It is assumed that $H(\boldsymbol{x}(t))$ evolves adiabatically in time which means that the Hamiltonian changes slowly in time such that the state $|\psi(\boldsymbol{x}(t))\rangle$ is always an eigenstate of $H(\boldsymbol{x}(t))$. Consequently due to the adiabatic theorem, one can write

$$H(\boldsymbol{x}(t))|\psi(\boldsymbol{x}(t))\rangle = E(\boldsymbol{x}(t))|\psi(\boldsymbol{x}(t))\rangle. \tag{II.1.15}$$

The states stay in an eigenstate due to the adiabatic theorem but their phase can still change.

The ansatz

$$\Rightarrow |\psi(\boldsymbol{x}(t))\rangle \rightarrow \mathrm{e}^{-\mathrm{i}\phi(t)}|n(\boldsymbol{x}(t))\rangle$$

can be used in the Schrödinger equation which now reads

$$\mathrm{i}\hbar\frac{\mathrm{d}}{\mathrm{d}t}|\psi(t)\rangle = H(\boldsymbol{x}(t))|\psi(t)\rangle. \tag{II.1.16}$$

$$\Leftrightarrow \hbar|\psi(\boldsymbol{x}(t))\rangle\frac{\mathrm{d}}{\mathrm{d}t}\phi(t) + \mathrm{i}\hbar\frac{\mathrm{d}}{\mathrm{d}t}|\psi(\boldsymbol{x}(t))\rangle = E|\psi(\boldsymbol{x}(t))\rangle$$

Solving for the phase $\phi(t)$ by integration in time eventually yields

$$\phi(\tau) = \int_0^\tau \mathrm{d}t' \, \frac{E(t')}{\hbar} - \mathrm{i}\int_0^\tau \mathrm{d}t\langle\psi(\boldsymbol{x}(t))|\frac{\mathrm{d}}{\mathrm{d}t}|\psi(\boldsymbol{x}(t))\rangle \tag{II.1.17}$$

$$\Leftrightarrow \phi(\tau) = \underbrace{\int_{\boldsymbol{x}(0)}^{\boldsymbol{x}(\tau)} \mathrm{d}\boldsymbol{x}' \, \frac{E(\boldsymbol{x}')}{\hbar}}_{\text{dynamical phase}} \underbrace{- \mathrm{i}\int_{\boldsymbol{x}(0)}^{\boldsymbol{x}(\tau)} \mathrm{d}\boldsymbol{x}\langle\psi(\boldsymbol{x}(t))|\nabla_{\boldsymbol{x}}|\psi(\boldsymbol{x}(t))\rangle}_{\text{geometrical phase}}. \tag{II.1.18}$$

The first term on the left is identified with the dynamical phase. The reason for the second term being called geometrical phase is explained subsequently. One could ask how the phase changed when the system evolves from $t = 0$ after a period $t = \tau$ such that $\boldsymbol{x}(0) = \boldsymbol{x}(\tau)$ which means that the system returns to its initial parameters after the adiabatic evolution in time. To do so, the phase is calculated after integrating over a closed loop. The eigenstates only depend on time through their parameters. One can therefore write

$$\phi(C) = \underbrace{-\mathrm{i}\oint_C \mathrm{d}\boldsymbol{x}\langle\psi(\boldsymbol{x})|\nabla_{\boldsymbol{x}}|\psi(\boldsymbol{x})\rangle}_{:=\gamma(C)}.$$

The phase $\phi(C)$ is called Berry phase and $\gamma(C)$ is called Berry connection. Of course, the geometrical phase needs to be real which is clearly fulfilled because of $\langle\psi(\boldsymbol{x})|\psi(\boldsymbol{x})\rangle = 1$ which means that

$$\mathrm{i}\left(\nabla_{\boldsymbol{x}}\langle\psi(\boldsymbol{x})|\right)|\psi(\boldsymbol{x})\rangle = -\mathrm{i}\langle\psi(\boldsymbol{x})|\left(\nabla|\psi(\boldsymbol{x})\rangle\right) \Rightarrow \langle\psi(\boldsymbol{x})|\nabla_{\boldsymbol{x}}|\psi(\boldsymbol{x})\rangle \in \mathbb{R}. \tag{II.1.19}$$

Applying Stokes theorem, the relation

$$\phi(C) = \int_A \mathrm{d}x_1 \mathrm{d}x_2\, \Omega_{\mathrm{B}}(\boldsymbol{x}) \tag{II.1.20}$$

holds where the Berry curvature is identified as

$$\Omega_{\mathrm{B}}(\boldsymbol{x}) = -\mathrm{i}\nabla \times \langle\psi(\boldsymbol{x})|\nabla_{\boldsymbol{x}}|\psi(\boldsymbol{x})\rangle; \qquad \text{Berry curvature.}$$

The Berry curvature is here defined for a single state $\psi(\boldsymbol{x})$. The definition can be extended to band Hamiltonians yielding

$$\Omega_{\mathrm{B},\nu}(\boldsymbol{x}) = -\mathrm{i}\nabla \times \langle\psi(\boldsymbol{x},\nu)|\nabla_{\boldsymbol{x},\nu}|\psi(\boldsymbol{x},\nu)\rangle; \qquad \text{Berry curvature for a band } \nu. \tag{II.1.21}$$

The total Berry curvature is then given by the $\Omega_{\mathrm{B},\nu}$ summed over all occupied bands. By using an alternative representation of the derivative of an eigenstate given in Equation (A.1.6) the total Berry curvature can be brought to the more convenient formula [20]

$$\Omega_{\mathrm{B}}(\boldsymbol{k}) = \sum_{\nu}^{\mathrm{occ}} \sum_{\mu\neq\nu} \frac{\langle\nu,\boldsymbol{k}|\partial_{k_{\mathrm{x}}} H(\boldsymbol{k})|\mu,\boldsymbol{k}\rangle\langle\mu,\boldsymbol{k}|\partial_{k_{\mathrm{y}}} H(\boldsymbol{k})|\nu,\boldsymbol{k}\rangle - \mathrm{h.c.}}{(\nu(\boldsymbol{k}) - \mu(\boldsymbol{k}))^2}. \tag{II.1.22}$$

By comparison of (II.1.13) and (II.1.20) the reason for the terminology geometrical phase becomes evident. In the context of quantum states the angle difference after one complete loop is given by

$$\phi(C) = 2\pi N_{\mathrm{c}}; \quad N_{\mathrm{C}} \in \mathbb{Z} \tag{II.1.23}$$

while N_{C} is called the Chern number. The Chern number is integer valued, and defined for each band of translation invariant band Hamiltonians. The total Chern number is given by the sum over all Chern number of each filled band.

There are other possibilities to define a topological invariant in a quantum mechanical system. One of these is through the use of the degree of a continuous map. The degree of a continuous map between two compact orientable manifolds of the same dimension is a topological invariant (to be more precise an invariant among homotopies) as mentioned above. The degree from the S^1 to the S^1 is called the winding number and the map from a two-dimensional manifold to the S^2 is called skyrmion number. In this work, systems with non-zero skyrmion numbers N_{S} are analyzed. In general, the degree of a map $\hat{\boldsymbol{d}}$ from some domain manifold M to the S^2 is given by the analytic formula

$$\deg(\hat{\boldsymbol{d}}) = N_{\mathrm{S}} = \frac{1}{\mathcal{S}(\mathrm{S}^2)} \int_M \mathrm{d}x\mathrm{d}y\, \Omega_{\mathrm{S}}; \quad \Omega_{\mathrm{S}} \equiv \hat{\boldsymbol{d}} \cdot \left(\partial_x \hat{\boldsymbol{d}} \times \partial_y \hat{\boldsymbol{d}}\right); \quad \mathcal{S}(\mathrm{S}^2) = 4\pi \tag{II.1.24}$$

where $S(\mathrm{S}^2)$ denotes the surface area of the S^2. Equation (II.1.24) has a simple intuitive interpretation. The integrand consists of a cross product term and a scalar product. The dot product yields the infinitesimal surface element $\mathrm{d}\boldsymbol{S}$ of the S^2 embedded in the three dimensional Euclidean space. The direction of the surface element $\mathrm{d}\boldsymbol{S}$ is either parallel or antiparallel to $\hat{\boldsymbol{d}}$ by construction because $\boldsymbol{d}$ is a map onto the unit sphere and the surface elements of the unit sphere are parallel or antiparallel to its position vector. The integrand is thus the flux of $\hat{\boldsymbol{d}}$ through the surface element $\mathrm{d}\boldsymbol{S}$ of the unit sphere which is however equal to the surface element itself multiplied by either 1 or -1 depending on whether $\left(\partial_x \hat{\boldsymbol{d}} \times \partial_y \hat{\boldsymbol{d}}\right)$ is parallel or antiparallel to $\hat{\boldsymbol{d}}$. It is clear that the integral can only yield an integer of entire coverings of the unit sphere because the map between the two compact manifolds is continuous. Any hole in the map from the domain to the range manifold would imply a discontinuity in the map since any small neighborhood in the range manifold needs to be a small neighborhood in the domain manifold. Therefore (II.1.24) can only yield integer values. Interestingly, for the special case of a simple 2x2 hermitian matrix $\mathcal{M}$ given by

$$\mathcal{M} = \boldsymbol{d}\boldsymbol{\sigma}, \qquad \text{(II.1.25)}$$

the Berry curvature $\Omega_{\mathrm{B}} = \Omega_{\mathrm{S}}$ which was shown in Ref [37]. This relation does not hold in general as discussed for the topological s-wave superconductor in Section III.2.

II.2. Topological s-wave superconductor

This thesis focuses on two common topological systems discussed extensively in the literature. This thesis deals with the analysis of these systems with respect to their ground-state spin textures and the textures in finite size systems or at finite temperatures. The discussion extends to the analysis of thermodynamic signatures at topological phase transitions. The model of the topological s-wave superconductors is explained below. This model has been investigated in terms of its topological properties in References [38–40]. The Hamiltonian for such a superconducting system reads

$$\mathcal{H}_{\mathrm{SC}} = \mathcal{H}_{\mathrm{TB}} + \mathcal{H}_{\mathrm{SOC}} + \mathcal{H}_{\mathrm{Z}} + \mathcal{H}_{\mathrm{I}} \tag{II.2.1}$$

with $\mathcal{H}_{\mathrm{TB}}$, $\mathcal{H}_{\mathrm{SOC}}$, $\mathcal{H}_{\mathrm{Z}}$ and $\mathcal{H}_{\mathrm{I}}$ denoting the tight binding-, the spin-orbit coupling- the Zeeman-splitting and the electron-electron interaction Hamiltonian, respectively.

The tight-binding Hamiltonian is supposed to contain only nearest neighbor hopping terms describing the kinetic energy of the electrons. In canonical quantization the energy is given by

$$\mathcal{H}_{\mathrm{TB}} = \sum_i \sum_j \sum_{s=\uparrow,\downarrow} \left(-t\hat{c}^{\dagger}_{i,j,s}\hat{c}_{i+1,j,s} - t\hat{c}^{\dagger}_{i,j,s}\hat{c}_{i,j+1,s} \right) + \text{h.c.} \tag{II.2.2}$$

with $\hat{c}^{\dagger}_{i,u,s}$ and $\hat{c}_{j,v,s}$ denoting the annihilation and creation operators for Fermions at the position $\boldsymbol{r}_{i,u}$ and $\boldsymbol{r}_{j,v}$ and spin s in canonical quantization, respectively. They obey the anticommutator relations

$$[\hat{c}_{i,u,s}, \hat{c}_{j,v,s'}]_+ = 0; \quad [\hat{c}^{\dagger}_{i,u,s}, \hat{c}_{j,v,s'}]_+ = \delta_{i,j}\delta_{u,v}\delta_{s,s'} \tag{II.2.3}$$

with $[A, B]_+ = AB + BA$. The incorporation of the the coupling of an magnetic field to the orbital energy of the electrons, the hopping energy t is supplemented by the Peierls phase

$$t \to t_{|\boldsymbol{r}_{i,u}-\boldsymbol{r}_{j,v}|}\mathrm{e}^{\mathrm{i}\frac{e}{\hbar c}\int_{\boldsymbol{r}_{i,u}}^{\boldsymbol{r}_{j,v}} \mathrm{d}\boldsymbol{r}\boldsymbol{A}(\boldsymbol{r})} \tag{II.2.4}$$

while the integration $\int_{\boldsymbol{r}_{j,v}}^{\boldsymbol{r}_{i,u}} \mathrm{d}\boldsymbol{r}$ is applied along the direct connection between the points $\boldsymbol{r}_{i,u}$ and $\boldsymbol{r}_{j,v}$ and $\boldsymbol{A}(\boldsymbol{r})$ denotes the vector potential defined by $\boldsymbol{B}(\boldsymbol{r}) = \nabla \times \boldsymbol{A}(\boldsymbol{r})$. Due to this definition, the vector potential is not uniquely defined since a given $\boldsymbol{A}(\boldsymbol{r})$ can be replaced by $\boldsymbol{A}(\boldsymbol{r}) + \nabla\boldsymbol{\phi}(\boldsymbol{r})$ with $\phi(\boldsymbol{r})$ being an arbitrary analytic scalar-field. The resulting tight-binding term is then given by

$$\mathcal{H}_{\mathrm{TB}} = -\sum_{\langle i,j\rangle} \langle u, v\rangle \sum_s t \left[\mathrm{e}^{\mathrm{i}\frac{e}{\hbar c}\int_{r_{i,u}}^{r_{j,v}} A(\boldsymbol{r})\mathrm{d}\boldsymbol{r}}\hat{c}^{\dagger}_{i,u,s}\hat{c}_{j,v,s} + \text{h. c.} \right]. \tag{II.2.5}$$

In this thesis, the effects of magnetic fields on the spin magnetization is analyzed leaving aside the effects of the Peierls coupling. This is reasonable for almost in-plane magnetic field setups in the two-dimensional topological s-wave superconductor [41]. Some effects of the incorporation of the Peierls phase is mentioned but a comprehensive analysis taking into account this orbital magnetic field coupling is beyond the scope of this thesis and leaves open questions which are discussed further in the outlook of this thesis.

Applying the definition of the Fourier transform

$$\hat{\boldsymbol{c}}^{\dagger}_{\boldsymbol{k}} = \frac{1}{\sqrt{N}} \sum_{\boldsymbol{R}} \mathrm{e}^{\mathrm{i}\boldsymbol{k}\boldsymbol{R}}\hat{\boldsymbol{c}}^{\dagger}_{\boldsymbol{R}} \tag{II.2.6}$$

to the kinetic energy part of the Hamiltonian yields

$$\mathcal{H}_{\mathrm{TB}} = -2t \sum_{k_{\mathrm{x}}} \sum_{k_{\mathrm{y}}} \sum_{s} \epsilon(\boldsymbol{k}) \hat{c}^{\dagger}_{k_{\mathrm{x}},k_{\mathrm{y}},s} \hat{c}_{k_{\mathrm{x}},k_{\mathrm{y}},s}; \quad \epsilon(\boldsymbol{k}) = \cos(k_{\mathrm{x}} a) + \cos(k_{\mathrm{y}} a) \tag{II.2.7}$$

consisting of the standard cosine bands valid for a basis with one orbital per lattice site with a denoting the lattice constant. The second ingredient of the topological s-wave superconductor in the Hamiltonian given in (II.2.1) is the Rashba spin-orbit coupling.

The origin of Rashba spin-orbit coupling results from broken inversion symmetry at interfaces where the gradient of the crystal potential causes the emergence of an electric field $\boldsymbol{E}$. The electron moving in the electric field is affected by an effective magnetic field contribution given through

$$\boldsymbol{B} = -\gamma \frac{\boldsymbol{v}}{v} \times \boldsymbol{E} \tag{II.2.8}$$

with $\gamma = 1/\sqrt{1-(v/\mathrm{c})^2} \approx 1 + (v/\mathrm{c})^2/2$ being the Lorentz factor where c is the speed of light and v denotes the speed of the electron in the frame of the crystal lattice. The electron spin interacts with this magnetic field through Zeeman splitting resulting in [42]

$$\mathcal{H}_{\mathrm{SOC}} = \alpha_{\mathrm{R}} \sum_{i} \sum_{j} \sum_{s,s'=\uparrow,\downarrow} \left(\mathrm{i}\hat{c}^{\dagger}_{i,j,s} \hat{c}_{i+1,j,s'} - \mathrm{i}\hat{c}^{\dagger}_{i,j,s} \hat{c}_{i,j+1,s'} \right) + \mathrm{h.\,c.} \tag{II.2.9}$$

on a square lattice in the tight binding description with $\alpha_{\mathrm{R}}/a = \hbar \mu_{\mathrm{B}} E / 2 m_{\mathrm{e}} \mathrm{c}$ being the Rashba spin-orbit coupling parameter, where e denote the elementary charge, $\hbar$ the usual reduced Planck constant, and m_{e} is the electron mass. The spin-orbit interaction is a relativistic effect which results in small energy shifts which are about $\alpha_{\mathrm{R}} \approx 10^{-7}$ eV. However, experiments [43, 44] have shown that the spin-orbit can be much greater which is the case e. g. at lanthanum aluminate-strontium titanate interfaces (LAO/STO). The reason for the much larger spin-orbit interaction is that the atomic spin-orbit interaction in multi-band systems can lead to an effective Rashba-like spin-orbit interaction. The strength of the large spin-orbit coupling terms in crystals can be estimated by [45]

$$\alpha_{\mathrm{R}} \approx \frac{\gamma \xi}{\Delta_{\mathrm{I}}} \tag{II.2.10}$$

with Δ_{I} being a band gap between in-plane and out of plane bands resulting from an inversion symmetry breaking potential at interfaces, γ is the hopping energy between xy and yz orbitals, ξ is the strength of atomic spin-orbit coupling. The resultant Rashba spin-orbit coupling in LAO/STO heterostructures yields energy shifts of about $\alpha_{\mathrm{R}} \approx 10^{-2}$ eV. Assuming the square lattice with nearest neighbor hopping and performing the Fourier transformation leads to

$$\mathcal{H}_{\mathrm{SOC}} = \alpha_{\mathrm{R}} \sum_{\boldsymbol{k}} \sum_{s} \sum_{s'} \hat{c}^{\dagger}_{\boldsymbol{k},s} \begin{pmatrix} 0 & \epsilon_{\mathrm{R}}(\boldsymbol{k}) \\ \epsilon^{*}_{\mathrm{R}}(\boldsymbol{k}) & 0 \end{pmatrix}_{s,s'} \hat{c}_{\boldsymbol{k},s'}; \quad \epsilon_{\mathrm{R}}(\boldsymbol{k}) = \sin(k_{\mathrm{y}} a) - \mathrm{i} \sin(k_{\mathrm{x}} a). \tag{II.2.11}$$

The interaction between the magnetic moments of the electron spins and a magnetic field is taken into account by the so-called Zeeman splitting. Its energy scale is determined by the Bohr magneton μ_{B}. The Zeeman splitting term is described by

$$\mathcal{H}_{\mathrm{Z}} = \mu_{\mathrm{B}} \sum_{i,j} \sum_{s=\uparrow,\downarrow} \hat{c}^{\dagger}_{i,j,s} \boldsymbol{B} \boldsymbol{\sigma}_{s,s} \hat{c}_{i,j,s} \tag{II.2.12}$$

which is diagonal in position space. The Zeeman splitting simply transforms in momentum space to

$$\mathcal{H}_\mathrm{Z} = \mu_\mathrm{B} \sum_{\boldsymbol{k}} \sum_{s} \sum_{s'} \hat{c}^{\dagger}_{\boldsymbol{k},s} \left(\boldsymbol{B}\boldsymbol{\sigma}\right)_{s,s'} \hat{c}_{\boldsymbol{k},s'}. \tag{II.2.13}$$

The last ingredient of the Hamiltonian given in (II.2.1) is the effective s-wave electron-electron interaction with the attractive on-site pairing potential $V_{s,s'}\delta(\boldsymbol{r}_{i,u} - \boldsymbol{r}_{j,v})$ such that

$$\mathcal{H}_\mathrm{I} = \sum_{i,j,u,v} \sum_{s,s'} V_{s,s'}\delta(\boldsymbol{r}_{i,u} - \boldsymbol{r}_{j,v})\hat{c}^{\dagger}_{i,u,s}\hat{c}_{i,u,s}\hat{c}^{\dagger}_{j,v,s'}\hat{c}_{j,v,s'}. \tag{II.2.14}$$

This Hamiltonian is a two particle Hamiltonian. Exact results for such two particle problems are in general cumbersome. Below, a common approximation is used to deal with this interaction term on mean field level. Transforming into Fourier space, the interaction Hamiltonian $\mathcal{H}_\mathrm{I}$ becomes (see Appendix A.3 or for example Reference [46])

$$H_\mathrm{I} = \frac{V}{N} \sum_{s} \sum_{s'} \sum_{\boldsymbol{k}} \sum_{\boldsymbol{k}'} \sum_{\boldsymbol{q}} (\mathrm{i}\sigma_\mathrm{y})_{s,s'} c^{\dagger}_{\boldsymbol{k},s} c^{\dagger}_{\boldsymbol{k}',s'} c_{\boldsymbol{k}'-\boldsymbol{q},s'} c_{\boldsymbol{k}+\boldsymbol{q},s} \tag{II.2.15}$$

where the momenta $\boldsymbol{q}$ are referred to as finite center of mass momenta [47]. The Hamiltonian allows for many finite momentum pairing vectors $\boldsymbol{q}$. In the case, where an out of plane magnetic field $\boldsymbol{h} = (0, 0, h_\mathrm{z})^\mathrm{T}$ is applied, only one finite momentum pairing vector with $\boldsymbol{q} = 0$ is realized [48]. However, out of plane magnetic field setups allow for solutions with $\boldsymbol{q} \neq 0$. There are different possibilities for the finite $\boldsymbol{q}$-solutions. One possibility is, that there is only one momentum $\boldsymbol{q}$ which is referred to as the Fulde-Ferrell pairing [49]. In the case where two finite momenta are allowed with $\boldsymbol{q}$ and $-\boldsymbol{q}$ is referred to as the Larkin-Ovchinnikov pairing [50]. In Ref [41, 48] finite momentum pairing states with two different momenta $\boldsymbol{q}_1$ and $\boldsymbol{q}_2$ have been found. Their results show that the solution $\boldsymbol{q} = 0$ is even stable for slightly in-plane tilted magnetic field setups as sketched in Figure II.2. When the magnetic field tilt and the strength of the magnetic field exceeds a certain value a region with two different $\boldsymbol{q}_1$ and $\boldsymbol{q}_2$ occurs.

In Appendix A.3, the well known thermodynamic potential of the topological s-wave superconductor is explicitly calculated and it can also be found for example in References [51–54]. The thermodynamics are determined by the thermodynamic potentials. The grand canonical potential Ω can, in general, be expressed in the form (see Appendix A.3 for a more detailed discussion)

$$\Omega \approx -\frac{1}{\beta} \ln\left(\exp\left(-S_\mathrm{eff}\right)\right) \tag{II.2.16}$$

with the effective action S_eff. For the topological superconductor S_eff given by

$$S_\mathrm{eff} = N\beta\frac{\mu}{2} - \frac{1}{\hbar}\int_0^{\hbar\beta} \mathrm{d}\tau \left(-\frac{1}{2}\mathrm{Tr}\,(\ln)\left[\mathcal{G}^{-1}(\tau)\right]_{\Delta(\boldsymbol{q})=\Delta(\boldsymbol{q})} + \sum_{\boldsymbol{q}} \frac{|\Delta(\boldsymbol{q})|^2}{V} \right). \tag{II.2.17}$$

The value of $\Delta(\boldsymbol{q})$ is determined by the extremal condition used in the saddle-point approximation

$$\left.\frac{\partial S_\mathrm{eff}(\Delta(\boldsymbol{q}))}{\partial\Delta(\boldsymbol{q})}\right|_{\Delta=\Delta_\mathrm{OP}} = 0 \tag{II.2.18}$$

$$\Leftrightarrow \hbar\beta\Delta(\boldsymbol{q})\frac{N}{\mathcal{V}} = \frac{1}{2+Q}\sum_{\boldsymbol{k}}\sum_{\omega_n} \mathcal{G}\partial_{\Delta_q}\mathcal{G}^{-1}, \tag{II.2.19}$$

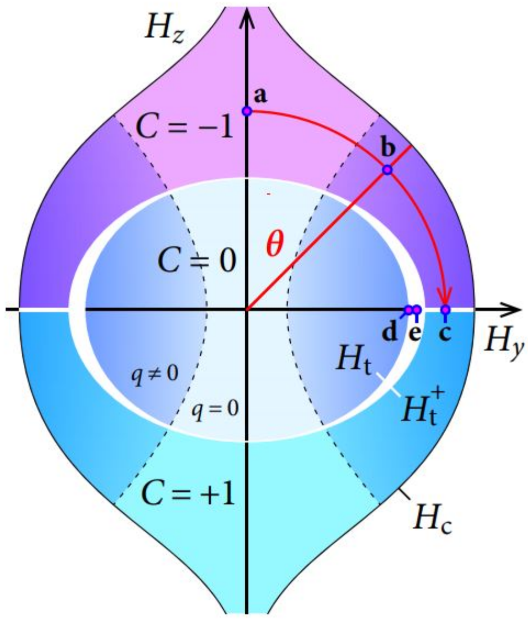

Figure II.3.: Qualitative results obtained for tilted magnetic field setups in the topological s-wave superconductor indicating that finite momentum pairing is absent for perpendicular magnetic field setups and small tilt angles. For almost in-plane setups, finite momentum pairing needs to be considered. The figure is taken from Reference [41].

which is common approximation on mean field level. Equation (II.2.19) is referred to as gap equation, since the solutions of this equation determines the superconducting order parameter Δ_{OP} which accounts for the energy gap between particle and hole space in the conventional superconductor — at which the Rashba spin-orbit coupling is not present. The action S_{eff} has to be minimized at all different $\Delta_{\mathrm{OP}}(\boldsymbol{q})$. the inverse Green's function $\mathcal{G}^{-1}$ is given by

$$\mathcal{G}^{-1}_{\tau,\boldsymbol{k},\boldsymbol{q}} = \partial_\tau + H(\boldsymbol{k},\boldsymbol{q}) = \frac{\partial}{\partial\tau} + \begin{pmatrix} E(\boldsymbol{k}) & \underline{\Delta}(\boldsymbol{q}_1) & \underline{\Delta}(\boldsymbol{q}_2) & \cdots \\ \underline{\Delta}(\boldsymbol{q}_1) & -\frac{1}{Q}E^{\mathrm{T}}(-\boldsymbol{k}+\boldsymbol{q}_1) & 0 & \cdots \\ \underline{\Delta}(\boldsymbol{q}_2) & 0 & -\frac{1}{Q}E^{\mathrm{T}}(-\boldsymbol{k}+\boldsymbol{q}_2) & \cdots \\ \vdots & \ddots & \ddots & \ddots \end{pmatrix} \tag{II.2.20}$$

with

$$E(\boldsymbol{k}) = \begin{pmatrix} \zeta^+_{\boldsymbol{k}} & \xi_{\boldsymbol{k}} \\ \xi^*_{\boldsymbol{k}} & \zeta^-_{\boldsymbol{k}} \end{pmatrix}, \quad \underline{\Delta}(\boldsymbol{q}) = \begin{pmatrix} 0 & \Delta_{\mathrm{OP}}(\boldsymbol{q}) \\ -\Delta_{\mathrm{OP}}(\boldsymbol{q}) & 0 \end{pmatrix} \tag{II.2.21}$$

where Q is the total number of different $\boldsymbol{q}$-vectors and τ is the Matsubara time [55]. Supplemental details on the Matsubara time formalism is given in Appendix A.7. Here, the quantities

$$\zeta^\pm_{\boldsymbol{k}} = \epsilon^{\mathrm{TB}}_{\boldsymbol{k}} \pm \mu_{\mathrm{B}} B, \quad \xi_{\boldsymbol{k}} = \epsilon_{\mathrm{R}}(\boldsymbol{k}) + h_{\mathrm{x}} - \mathrm{i}h_{\mathrm{y}} \tag{II.2.22}$$

are introduced. However, there is a constraint on this equation namely the conservation of particle number. The particle number is obtained by Equation (A.7.50) which yields

$$N = -\frac{\partial \Omega}{\partial \mu} = \frac{N}{2} + \frac{1}{2} \sum_{\boldsymbol{k}} \sum_{\omega_n} \mathcal{G} \partial_\mu \mathcal{G}^{-1}. \tag{II.2.23}$$

The summation over the Matsubara frequencies in the gap Equation (II.2.19) and the particle-number Equation (II.2.23) can be performed using the calculation described in Section (A.7) with the eigenvalues of $\boldsymbol{H}(\boldsymbol{k}, \boldsymbol{q})$ denoted by λ_i where i counts the number of bands. In the following the eigenvalues are supposed to be ordered such that $\lambda_i \leq \lambda_{i+1}$.

II.3. Qi-Wu-Zhang model

A standard model for topological Chern insulators is a model considered by Qi, Wu and Zhang (QWZ-model) which was introduced in Reference [15]. Here a short review of this model is given.

The QWZ-model is a two-band model. It is a basic and simple model which however contains the important features of a Chern insulator. The model is defined on a square lattice with nearest neighbor hoppings resulting in two bands, a particle-like and a hole-like bad, and Rashba spin-orbit coupling. The particle and the hole band carry different spin, ↑-spin and ↓-spin or pseudo-spin [56–58]. A pseudo-spin is some degree of freedom that transforms analogous to a spin and is thus represented by σ-matrices. The Hamiltonian of that model reads

$$H = \sum_i \sum_j \left[\left(\hat{\boldsymbol{c}}^\dagger_{\boldsymbol{r}_{i,m}} \left(t\sigma_\mathrm{z} + \frac{\alpha_\mathrm{R}}{2} \mathrm{i}\sigma_\mathrm{x} \right) \hat{\boldsymbol{c}}_{\boldsymbol{r}_{i+1,j}} + \hat{\boldsymbol{c}}^\dagger_{\boldsymbol{r}_{i,j}} \left(t\sigma_\mathrm{z} + \frac{\alpha_\mathrm{R}}{2} \mathrm{i}\sigma_\mathrm{y} \right) \hat{\boldsymbol{c}}_{\boldsymbol{r}_{i,j+1}} + \mathrm{h.\,c.} \right) + \boldsymbol{h\sigma} \hat{\boldsymbol{c}}^\dagger_{\boldsymbol{r}_{i,j}} \hat{\boldsymbol{c}}_{\boldsymbol{r}_{i,j}} \right] \tag{II.3.1}$$

with t being the hopping energy, α_R the Rashba coupling and $\boldsymbol{h\sigma}$ the Zeeman splitting energy. Transforming the system into Fourier space, the Hamiltonian becomes diagonal in momentum space and its matrix elements are given by

$$\mathcal{H}(\boldsymbol{k}) = \boldsymbol{d}(\boldsymbol{k}) \cdot \boldsymbol{\sigma} \tag{II.3.2}$$

in two dimensions with $\boldsymbol{k} = (k_\mathrm{x}, k_\mathrm{y})$. The Hamiltonian is translation invariant and thus diagonal in the crystal momentum $\boldsymbol{k}$. The momentum dependent vector

$$\boldsymbol{d}(\boldsymbol{k}) = (\alpha_\mathrm{R} \sin(k_\mathrm{y}) + h_\mathrm{x}, \alpha_\mathrm{R} \sin(k_\mathrm{x}) + h_\mathrm{y}, h_\mathrm{z} - 2t(\cos(k_\mathrm{x}) + \cos(k_\mathrm{y})))^\mathrm{T} \tag{II.3.3}$$

is called Bloch vector [20]. The above introduced vector notation $\boldsymbol{\sigma} = (\sigma_x, \sigma_y, \sigma_z)$ where $\sigma_{\mathrm{x,y,z}}$ are the Pauli matrices is used. The parameter h_z shifts the particle and hole bands in energy according to their spin.

The eigenvalues of (II.3.2) are identified as

$$\lambda_{\substack{1\\(2)}} = {\scriptstyle(\pm)} |\boldsymbol{d}(\boldsymbol{k})| \tag{II.3.4}$$

and the eigenvectors are [37]

$$u_\pm(\boldsymbol{k}) = \frac{1}{\sqrt{2|\boldsymbol{d}(\boldsymbol{k})|(|\boldsymbol{d}(\boldsymbol{k})| \pm d_\mathrm{z}(\boldsymbol{k}))}} \left(d_\mathrm{z}(\boldsymbol{k}) \pm |\boldsymbol{d}(\boldsymbol{k})|, d_\mathrm{x}(\boldsymbol{k}) + \mathrm{i} d_\mathrm{y}(\boldsymbol{k}) \right)^\mathrm{T}. \tag{II.3.5}$$

Within this model, two spin (pseudo-spin) bands exist with $\lambda_2 \geq \mu$, and $\lambda_1 \leq \mu$ where the equality is only fulfilled when a number of momenta $\boldsymbol{k}_\mathrm{t}$ for which $|\boldsymbol{d}(\boldsymbol{k}_\mathrm{t})| = 0$ holds exist. Hence, the Hamiltonian is gapped except for certain parameters $\boldsymbol{h}_\mathrm{t}$ at which the Hamiltonian has isolated band crossing points in the Brillouin zone denoted by $\boldsymbol{k}_\mathrm{t}$ for which one has $\lambda_1(\boldsymbol{k}_\mathrm{t}) = \lambda_2(\boldsymbol{k}_\mathrm{t})$. For $h_\mathrm{x} = h_\mathrm{y} = 0$, three distinct transitions fields $\boldsymbol{h}_{\mathrm{t},i} = (0, 0, h_{\mathrm{t},i})$ with $i \in \{1, 2, 3\}$ are given by

$$\begin{aligned} h_{\mathrm{t},1} &= -4t && \text{with } \boldsymbol{k}_{\mathrm{t},1} = (\pi, \pi) \\ h_{\mathrm{t},2} &= 0 && \text{with } \boldsymbol{k}_{\mathrm{t},2} = (0, \pi) \text{ and } \boldsymbol{k}_{\mathrm{t},4} = (\pi, 0) \\ h_{\mathrm{t},3} &= 4t && \text{with } \boldsymbol{k}_{\mathrm{t},3} = (0, 0) \end{aligned} \tag{II.3.6}$$

exist. Hence, there are four points where the band gap can close at the transition fields $\boldsymbol{h}_{\mathrm{t},i}$. According to (III.4.9), these are located at $\boldsymbol{k}_\mathrm{t} \in \{(0,0), (-\pi, 0), (0, \pi), (\pi, \pi)\}$ for $h_\mathrm{x} = h_\mathrm{y} = 0$. If the applied magnetic field is not exactly perpendicular to the plane, the transition fields $\boldsymbol{h}_{\mathrm{t},i}$ and the momenta $\boldsymbol{k}_\mathrm{t}$ In the following it is assumed that h_x and h_y are small compared to α_R which is realized for small tilt angles of the magnetic field. Assuming, as an example, a band dispersion at which the bands are close to a band crossing at the momentum $\boldsymbol{k}_{\mathrm{t},3}$ for $\boldsymbol{h}_\mathrm{z} \approx h_{\mathrm{t},3}$. The expansion around the momentum $\boldsymbol{k}_{\mathrm{t},3}$ up to second order yields consequently $d_\mathrm{z}(\boldsymbol{k}) \approx -|\boldsymbol{h}_{\mathrm{t},3}(h_{\mathrm{x,y}} = 0)| + tk_\mathrm{x}^2 + tk_\mathrm{y}^2$ and $d_{\mathrm{x,y}}(\boldsymbol{k}) \approx \alpha_\mathrm{R} k_{\mathrm{x,y}}$. It is straightforward to show that

$$\boldsymbol{h}_{\mathrm{t},3}(h_\mathrm{x}, h_\mathrm{y}) = \boldsymbol{h}_{\mathrm{t},3}(h_{\mathrm{x,y}} = 0) - \left(t\frac{h_\mathrm{x}^2 + h_\mathrm{y}^2}{\alpha_\mathrm{R}^2}, h_\mathrm{x}, h_\mathrm{y} \right) \tag{II.3.7}$$

$$\boldsymbol{k}_{\mathrm{t},3}(h_\mathrm{x}, h_\mathrm{y}) = \left(-\frac{h_\mathrm{x}}{\alpha_\mathrm{R}}, -\frac{h_\mathrm{y}}{\alpha_\mathrm{R}} \right). \tag{II.3.8}$$

Thus, the z-component of the magnetic field at the transition is suppressed due to the in-plane field components and the momenta $\boldsymbol{k}_\mathrm{t}$ of the band gap closing points at are shifted by $h_{\mathrm{x},y}/\alpha_\mathrm{R}$.

In order to analyze the thermodynamics of the QWZ-model, its necessary to calculate its thermodynamic potential. Using (A.7.37) given in the appendix, the grand canonical potential is given by

$$\Omega = -\frac{1}{\beta} \sum_{\omega_n} \ln\left(\left(\det\left[\hbar \mathcal{G}^{-1}(\omega_n) \right] \right) \right) \tag{II.3.9}$$

$$= -\frac{1}{\beta} \sum_{\omega_n} \sum_{\boldsymbol{k}} \ln\left[\left(\lambda_1(\boldsymbol{k}) - \mathrm{i}\hbar\omega_n \right) \left(-\lambda_1(\boldsymbol{k}) - \mathrm{i}\hbar\omega_n \right) \right] \tag{II.3.10}$$

with $\mathcal{G}^{-1}(\omega_n)$ denoting the inverse Matsubara Green's function. The sum over the Matsubara frequencies ω can be performed analogous to Appendix A.7 yielding the grand canonical potential for the QWZ model

$$\Omega = -\frac{1}{\beta} \sum_{\boldsymbol{k}} \ln\left(2\cosh\left(\frac{\beta\lambda_1(\boldsymbol{k})}{2} \right) \right). \tag{II.3.11}$$

This grand canonical potential is the basis for the calculations of the thermodynamics in the QWZ model.

III. Topological spin-textures and topological invariants

Topological quantization expressed by concomitant topological invariants has become relevant not only for the description of topological defects in condensed matter physics [60] but also in solid state physics [8, 20, 61, 62] where topological insulators [63], Chern insulators [64] and topological superconductors [20, 48] have been studied intensively over the last few decades. In general, topological phases are manifest in their ground state wave functions. Their topological phase can be described by the Chern number which was discussed in the previous Section II.1. The Chern number may be measured by the quantum Hall conductivity [20] and thermal Hall conductivity [65, 66]. These measurements rely on the existence of topological edge states. The existence of such boundary states is assumed by the bulk boundary correspondence.

Definition III.0.1: Bulk boundary correspondence

The bulk boundary correspondence [2, 67] is considered as a one-to-one relation between gapless chiral (or helical) edge states for infinite systems with open boundary conditions and topologically non-trivial bulk states.

These topological edge currents lead to the above mentioned transverse transport quantities proportional to the the Chern number. These quantities associated with the Chern number depend on the nature of the edge currents.

Definition III.0.2: Chiral (helical) edge states [8]

Edge states being chiral (helical) means that the edge modes are counter propagating at the opposite ends of a finite size system. The $\uparrow$- and $\downarrow$-spin states propagate into the same (opposite) direction at each edge.

In the case of chiral edge currents, for example, one speaks of the quantum Hall effect [3, 5] whereas the quantum spin Hall effects is associated with the helical edge currents [68].

On the other hand different topological bulk states can be characterized by topological ground state spin- or pseudo-spin-like textures in real or reciprocal space [15, 38, 69, 70]. In real space, spin-textures have been found that are topologically non-trivial; called skyrmions [71], yielding non-zero skyrmion numbers. There are different kinds of real space skyrmions (antiskyrmions), these are the Néel- or Bloch-type skyrmions (antiskyrmions). In both types, the spin winds around the radius vector emanating from the origin. In the Bloch-type skyrmion, the in-plane component of the spin points perpendicular to the origin. The spin points towards the center or away from

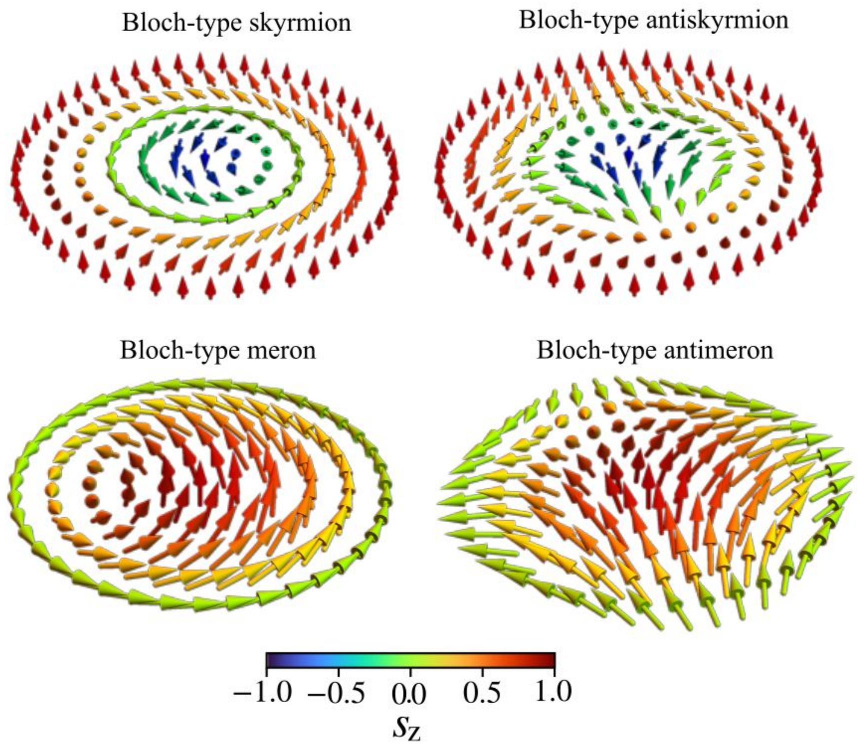

Figure III.1.: Bloch-type meron and skyrmion spin-textures. The presentation is similar to that in Reference [59].

it in the Néel type skyrmion. Although both kinds of skyrmions are in their spatial structure different, they are topologically identical. In addition to the skyrmion spin-textures, meron [72, 73] spin-textures have been identified and investigated. There, the spin is completely in-plane far away from the center (at infinity) as shown in Figure III.1. Besides the real space skyrmions there can be skyrmion textures in momentum space which are analyzed within this thesis and will be discussed below in detail because of a direct association with the Berry curvature or likewise the Chern number in the analyzed systems, the QWZ model and the topological s-wave superconductor. The following section addresses their non-trivial topological spin-textures.

III.1. Spin-textures of the QWZ model and the topological s-wave superconductor

The QWZ model has three different topological phases expressed by Chern numbers. The phase diagram of the QWZ model in terms of its Chern numbers is depicted in the following figure.

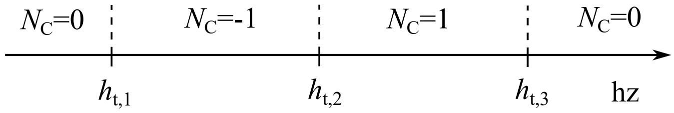

Figure III.2.: Phase diagram of the QWZ model.

This phase diagram is valid for the situation at which the magnetic field $\boldsymbol{h}$ is exactly perpendicular to the plane. In the case $h_x, h_y \neq 0$, the phase boundaries are shifted as described in the previous section. Topological phase transitions can only take place when the band gap closes. Therefore, the condition for a topological phase transition is $|\boldsymbol{d}(\boldsymbol{k}_t)| = 0$.

The Berry curvature for the three different topological phases is shown in Figure III.3.

Subfigure III.3 a) depicts the the topologically trivial situation at which the total Berry Curvature vanishes. The non-trivial Berry curvatures are given in Figure III.3 b) and III.3 c) for the phases $N_C = -1$ and $N_C = 1$, respectively.

Besides the Chern numbers, the topology of this system can be described by the skyrmion numbers N_S, defined in (II.1.24). Here the spin is defined

$$\boldsymbol{s}(\boldsymbol{k}, T) = -\sum_{\nu=\pm} \langle \nu, \boldsymbol{k} | \boldsymbol{\sigma} | \nu, \boldsymbol{k} \rangle \tanh\left(\frac{\lambda_\nu(\boldsymbol{k})}{2T}\right). \tag{III.1.1}$$

The ground state spin-texture is analyzed at first setting $T = 0$. The parameters used for the displayed ground-state textures correspond to those used for the calculation of the respective curvatures given above each texture in Figure,III.3. The textures at non-zero temperature are discussed further below in Section III.3.

The in-plane spin components of the spin display vortex and antivortex textures around the $\boldsymbol{k}_t$ while the in-plane spin components vanish at the different momenta $\boldsymbol{k}_t$. The z-components of the pseudo-spin is however either positive or negative which results in a z-component of the normalized spin vector

$$\boldsymbol{S}(\boldsymbol{k}_t) = (S_x(\boldsymbol{k}_t), S_y(\boldsymbol{k}_t), S_z(\boldsymbol{k}_t)) = \boldsymbol{s}(\boldsymbol{k}_t)/|\boldsymbol{s}(\boldsymbol{k}_t)| \tag{III.1.2}$$

with values $S_z(\boldsymbol{k}_t) = \pm 1$. There are vortices around the Γ-point $(0, 0)$ and the M-point (π, π) where antivortices are located around the X- and Y-point $(\pi, 0)$ and $(0, \pi)$. The skyrmion numbers corresponding to the different topological spin textures are given in the figure caption.

Actually, the skyrmion number can be deduced easily by examining the spin texture around the different $\boldsymbol{k}_t$. A vortex-texture of the in-plane components counts ± 1 if the z-component is positive of negative, respectively. For the antivortices the opposite is true. There are as many vortices as antivortices such that all vorticities sum up to zero. The simple scheme to read off the skyrmion number is proven below.

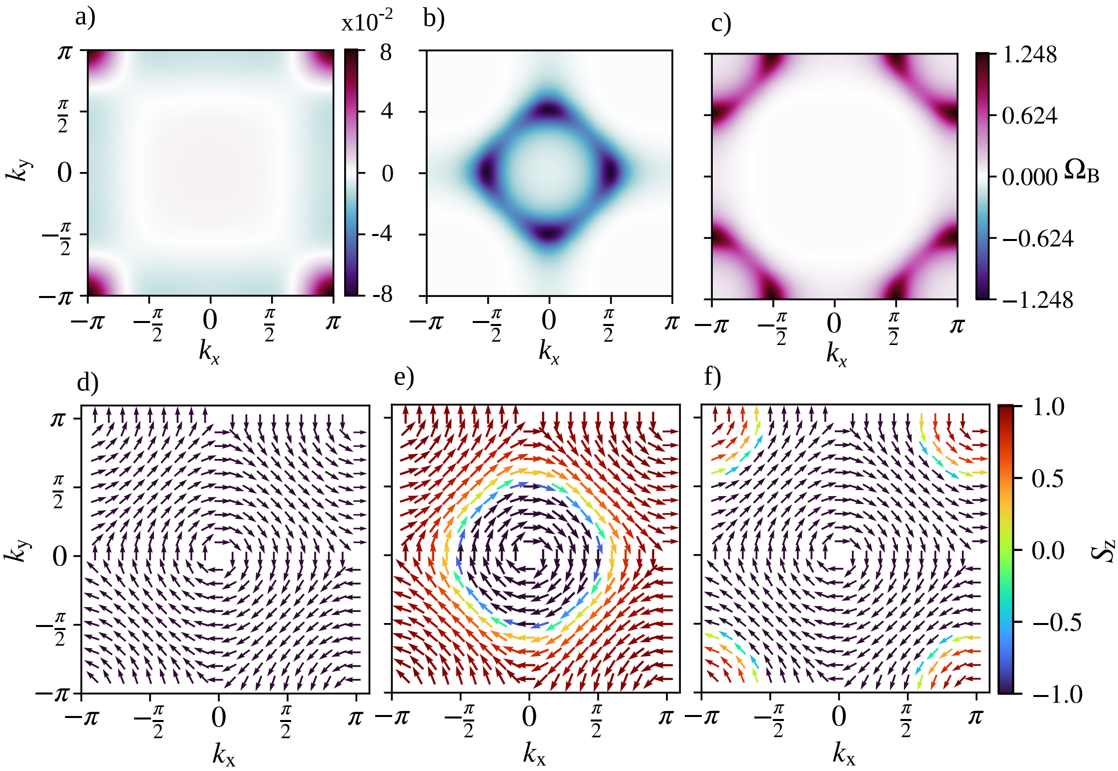

Figure III.3.: Berry Curvatures for a) $N_C = 0$, b) $N_C = -1$ and c) $N_C = 1$. The corresponding spin-textures are given below the Berry curvatures with d) $N_S = 0$ and e) $N_S = -1$, f) $N_S = 1$. The arrows represent the projection of the in-plane components of the spin-vectors normalized to unity.

The skyrmion number is realized by the degree of the map from the torus T (the Brillouin zone) onto the S^2 (the unit sphere) as discussed above. The right hand side of Equation (II.1.24) is completely unchanged if the single vortex center points $\boldsymbol{k}_t$ are excluded from the integral. This step is important because a connection between the skyrmion number and the vorticities in the textures desired but the vorticities are not defined at the exact momenta $\boldsymbol{k}_t$. One can therefore express the skyrmion number as

$$N_S = \frac{1}{S(S^2)} \int_{\backslash\{\boldsymbol{k}_t\}} d^2k\, \boldsymbol{S} \cdot \left(\partial_{k_x} \boldsymbol{S} \times \partial_{k_y} \boldsymbol{S} \right) \tag{III.1.3}$$

However, it is known that the skyrmion number is invariant under homotopies. It is therefore allowed to smoothly deform the spin space which is not necessary but which is useful for the following considerations.

The function

$$\mathbf{\Phi} : \mathrm{S}^2\backslash\{(0,0,1),(0,0,-1)\} \to \mathrm{S}^1 \times (-1,1) \text{ with } \mathbf{\Phi}(x,y,z) := \left(\frac{x}{\sqrt{x^2+y^2}}, \frac{y}{\sqrt{x^2+y^2}}, z\right) \tag{III.1.4}$$

can be defined which defines a map from the S^2 — where the north-pole and the south pole are excluded — onto the cylinder surface $S^1 \times (-1,1)$ such that this map is a bijection. On the other hand, the smooth function

$$\boldsymbol{\phi}_\mathrm{S} : \mathrm{S}^1 \times (-1,1) \to \mathrm{S}^2\backslash\{(0,0,1),(0,0,-1)\} \text{ with } \boldsymbol{\phi}_\mathrm{S}(x,y,z) := \left(\sqrt{1-z^2}x, \sqrt{1-z^2}y, z\right) \tag{III.1.5}$$

defines a map from the open cylinder surface $\mathrm{S}^1 \times (-1,1)$ onto the $\mathrm{S}^2\backslash\{(0,0,1),(0,0,-1)\}$ and $\boldsymbol{\phi}_\mathrm{S}$ is a bijection. Taking the composition of both $\mathbf{\Phi}$ and $\boldsymbol{\phi}_\mathrm{S}$ yields

$$\mathbf{\Phi}\circ\boldsymbol{\phi}_\mathrm{S} = \mathrm{id}_{\mathrm{S}^1\times(-1,1)} \tag{III.1.6}$$

so $\mathbf{\Phi}$ is the inverse of $\boldsymbol{\phi}_\mathrm{S}$ which is why $S^1 \times (-1,1)$ is homotopy equivalent to the unit sphere with the north and south-pole excluded.

Now, apart from normalizing the vector $\boldsymbol{s}$, a new vector $\boldsymbol{S}_\mathrm{SC}$ is defined by

$$\boldsymbol{S}_\mathrm{SC} := \Phi(\boldsymbol{S}(\boldsymbol{k})) \tag{III.1.7}$$

that maps the normalized spin vector $\boldsymbol{S}(\boldsymbol{k})$ onto the open cylinder surface $\mathrm{S}^2 \times (-1,1)$ such that the finite number of points from the domain manifold, the vortex cores, are mapped onto the top and the bottom of the cylinder $\mathrm{S}^1 \times \{1\}$ and $\mathrm{S}^2 \times \{-1\}$, respectively. The exact top and bottom of this cylinder are however undefined and a finite number of points given by $\{\boldsymbol{k}_\mathrm{t}\}$ have to be removed from the domain. A similar map was suggested and discussed in Reference [37] in the context of the topological s-wave superconductor. The difference between the map defined in the reference and the map introduced here, is that Φ of (III.1.4) is defined as the map from $\mathrm{S}^2\backslash\{(0,0,-1),(0,0,1)\}$ to $\mathrm{S}^1 \times (-1,1)$ while the map that is suggested in the reference is a map from a surface given by the spin expectation values $\boldsymbol{s}$ to the $\mathrm{S}^1\times(-1,1)$ given by $S_\mathrm{L}(\boldsymbol{k}) = \mathbf{\Phi}(s(\boldsymbol{k}))$.

The above constructed map from the Brillouin zone to the cylinder is thus homotopy equivalent to the map of the Brillouin zone to $\mathrm{S}^2\backslash\{(0,0,-1),(0,0,1)\}$ as the range manifold can be smoothly mapped onto the $\mathrm{S}^2\backslash\{(0,0,-1),(0,0,1)\}$, which does not hold for $\boldsymbol{S}_\mathrm{L}$ in general. Thus it is possible to describe the skyrmion number by

$$N_\mathrm{S} = \frac{1}{\mathcal{S}(S^1 \times [-1,1])} \int_{\backslash\{\boldsymbol{k}_\mathrm{t}\}} \mathrm{d}^2k \boldsymbol{S}_\mathrm{SC}(\boldsymbol{k}) \cdot \left(\partial_{k_\mathrm{x}} \boldsymbol{S}_\mathrm{SC}(\boldsymbol{k}) \times \partial_{k_\mathrm{y}} \boldsymbol{S}_\mathrm{SC}(\boldsymbol{k})\right), \tag{III.1.8}$$

where $\backslash\{\boldsymbol{k}_\mathrm{t}\}$ denotes the exclusion of the set of points $\{\boldsymbol{k}_\mathrm{t}\}$ from the Brillouin zone. The right hand side of (III.1.8) differs from the "Loder" number which is defined as

$$\Sigma_\mathrm{L} = \frac{1}{2\pi} \int_{\backslash\{\boldsymbol{k}_\mathrm{t}\}} \mathrm{d}^2k\, \Omega_\mathrm{L}(\boldsymbol{k}); \quad \Omega_\mathrm{L}(\boldsymbol{k}) = \boldsymbol{S}_\mathrm{L}(\boldsymbol{k}) \cdot \left(\partial_{k_\mathrm{x}} \boldsymbol{S}_\mathrm{L}(\boldsymbol{k}) \times \partial_{k_\mathrm{y}} \boldsymbol{S}_\mathrm{L}(\boldsymbol{k})\right) \tag{III.1.9}$$

with $\Omega_\mathrm{L}(\boldsymbol{k})$ defining the "Loder curvature" by the replacement of $\boldsymbol{S}_\mathrm{SC}$ with with $\boldsymbol{S}_\mathrm{L}$. Equation (III.1.8) can be integrated by parts yielding [74]

$$\begin{aligned} N_\mathrm{S} &= \sum_i S_{\mathrm{SC}_\mathrm{z}}(\boldsymbol{k}_{\mathrm{t},i}) \\ &\times \frac{1}{2} \lim_{\epsilon\to 0} \oint_{C(\boldsymbol{k}_{\mathrm{t},i},\epsilon)} \frac{\mathrm{d}\boldsymbol{k}}{2\pi} \Big(S_{\mathrm{SC}_\mathrm{x}}(\boldsymbol{k}) \nabla_{\boldsymbol{k}} S_{\mathrm{SC}_\mathrm{y}}(\boldsymbol{k}) - S_{\mathrm{SC}_\mathrm{y}}(\boldsymbol{k}) \nabla_{\boldsymbol{k}} S_{\mathrm{SC}_\mathrm{x}}(\boldsymbol{k}) \Big) \\ &= \frac{1}{2} \sum_i S_{\mathrm{SC}_\mathrm{z}}(\boldsymbol{k}_{\mathrm{t},i}) \mathcal{V}(\boldsymbol{k}_{\mathrm{t},i}) = \frac{1}{2} \sum_i S_\mathrm{z}(\boldsymbol{k}_{\mathrm{t},i}) \mathcal{V}(\boldsymbol{k}_{\mathrm{t},i}). \end{aligned} \tag{III.1.10}$$

The index i runs over all vortex-center points where $s_\mathrm{x}(\boldsymbol{k}_{\mathrm{t},i}) = s_\mathrm{y}(\boldsymbol{k}_{\mathrm{t},i}) = 0$, and the quantity $\mathcal{V}(\boldsymbol{k})$ denotes the vorticity of the in-plane spin around the vector $\boldsymbol{k}$ as defined in (III.1.10). Here, $\boldsymbol{k}_\mathrm{t}$ is used as an expression for $\lim_{\epsilon\to 0}(\boldsymbol{k}_\mathrm{t} + \epsilon\boldsymbol{u})$ where $\boldsymbol{u}$ is an arbitrary vector in the Brillouin zone. In addition $C(\boldsymbol{k}_\mathrm{t}, \epsilon)$ denotes an infinitesimal circle around $\boldsymbol{k}_\mathrm{t}$ with a radius ϵ. Equation (III.1.10) shows that the topological invariant is in fact given by just the vorticity $\mathcal{V}$ and the spin expectation value of the z-component at the four points $\boldsymbol{k}_\mathrm{t}$ in the Brillouin zone. If all pseudo-spins are pointing into the same direction at each $\boldsymbol{k}_\mathrm{t}$ the spin-texture is trivial since $\sum_i \mathcal{V}(\boldsymbol{k}_{\mathrm{t},i}) = 0$. At a topological phase transitions, the z-components of the spin hast to change at some of the $\boldsymbol{k}_\mathrm{t}$. The vorticity $\mathcal{V}$ can also be defined in the lattice model which is then still confined to integers. So the right hand side of (III.1.10) can be determined for lattice models still yielding integers.

It is important to note that the $\mathrm{S}^1\times[-1,1]$ is not homotopy equivalent to the S^2 but it is homotopy equivalent to the $\mathrm{S}^2\backslash\{(0,0,-1),(0,0,1)\}$. Strictly speaking, the Brouwer degree is only defined for compact manifolds which the $\mathrm{S}^2\backslash\{(0,0,-1),(0,0,1)\}$ does not fulfill. However, the non-singular cover of the $\mathrm{S}^2\backslash\{(0,0,-1),(0,0,1)\}$ can, in the situation above, easily be compactified to the cover of the full S^2 which does fulfill the requirement. It is therefore the special situation of the cover of the $\mathrm{S}^1 \times [-1,1]$ or likewise the $\mathrm{S}^2\backslash\{(0,0,-1),(0,0,1)\}$ which allows one to define the skyrmion number in terms of the cover of a non-compact manifold the $S^1 \times [-1,1]$. The compactification is possible because the cover of the cylinder is smooth except for the vortex cores and the number of these is finite.

The possibility to rewrite the skyrmion number in terms of (III.1.8) leads to Equation (III.1.10) which enables new perspectives on the interpretation of spin-textures in terms of the topological character as discussed in Section III.3.

Topological s-wave superconductor

The topological s-wave superconductor, the model of which is introduced in Section II.2, has been analyzed many times. The reason is, that this system is realizable and can in principle show non-trivial topological phases. These non-trivial phases can be characterized by non-zero Chern numbers where these depend on two parameters, the band-filling and the magnetic field.

The calculation of the full topological phase diagram in terms of the Chern numbers as a function of the band filling and the magnetic field in z-direction is given in Figure III.6. The phase diagram is obtained by self-consistent calculations taking into account the gap Equation (II.2.19) and the particle number Equation (II.2.23). The diagram shows that the topological s-wave

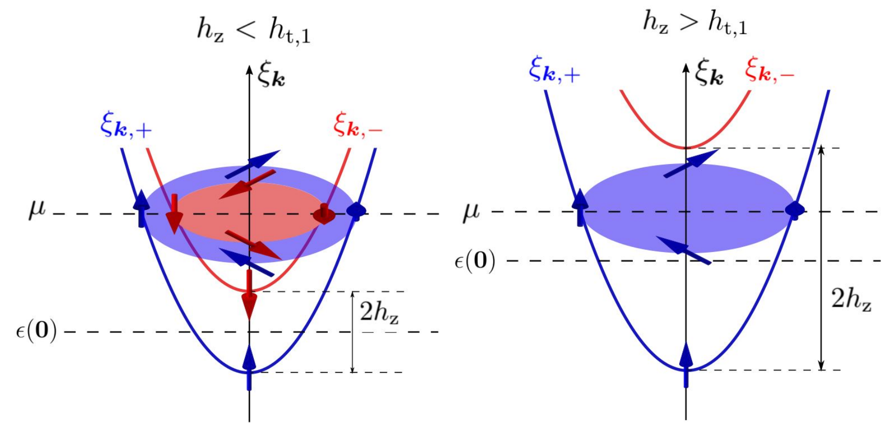

Figure III.4.: Dispersion of the normal conducting bands $\xi_{\boldsymbol{k}}^{+}$ and $\xi_{\boldsymbol{k}}^{-}$ for the cases $h_z < h_{t,1}$ (left figure), $h_z > h_{t,1}$ (right figure). The arrows indicate the spin direction related to each band. The situation around $h_{t,2}$ is similar. The figure is taken from Reference [74].

superconductor has three possible different topological phases. Two different topological phases ($N_C = -2$ and $N_C = -1$) can be found in the region between quarter filling and half filling corresponding to $n = 1/2$ and $n = 1$, respectively. Due to the inclusion of Rashba spin-orbit coupling and the neglection of the coupling of the magnetic field to the momentum by the Peierls phase, the system does not show any superconducting to normal conducting phase transition due to the finite Zeeman field in perpendicular direction which is also addressed in References [41, 53, 75]. Thus, the order parameter $\Delta(h_z)$ is always finite at any h_z, however it is exponentially decreasing [41] with increasing h_z and exponentially small at large magnetic fields. In order to enter any non-trivial topological phase it is necessary to apply magnetic field energies larger than Δ_{OP} but the upper critical magnetic field energy set by h_{c2}^2 is usually smaller than Δ_{OP}. So the experimental realizability of topologically non-trivial phases in the topological s-wave superconductor is in question and is at least arduous. There are suggestions to tilt the magnetic field almost in-plane in order circumvent this issue as the in-plane magnetic fields increase the value of $|\boldsymbol{h}_c|$ [76] but preserves the non-trivial topology [41]. In this regard, the topological phase transition may be observed in spin-orbit coupled s-wave superconductors with sufficiently strong Zeeman splitting [38, 74].

The topological phase-transition fields are defined by two magnetic fields $h_{t,1}(n)$ and $h_{t,2}(n)$ at which the band gap closes, given by [77, 78]

$$h_{t,1}(h_{x,y} = 0) = \sqrt{\left(\Delta_{OP}\right)^2 + (\epsilon(\mathbf{0}) - \mu(n))^2}, \tag{III.1.11}$$

$$h_{t,2}(h_{x,y} = 0) = \sqrt{\left(\Delta_{OP}\right)^2 + \mu^2(n)}. \tag{III.1.12}$$

For low band fillings $n \ll 1$ one has $\mu(n) \approx \epsilon(\mathbf{0})$ and hence $h_{t,1} < h_{t,2}$. However, around half filling $n \approx 1$ one finds $\mu(n) \approx 0$ and thus $h_{t,1} > h_{t,2}$. In between these cases the crossing point of both transition-field curves is found at around quarter filling $n \approx 1/2$ which corresponds to $\mu = -2t$. At this point all topological phases merge as shown in Figure III.6 a).

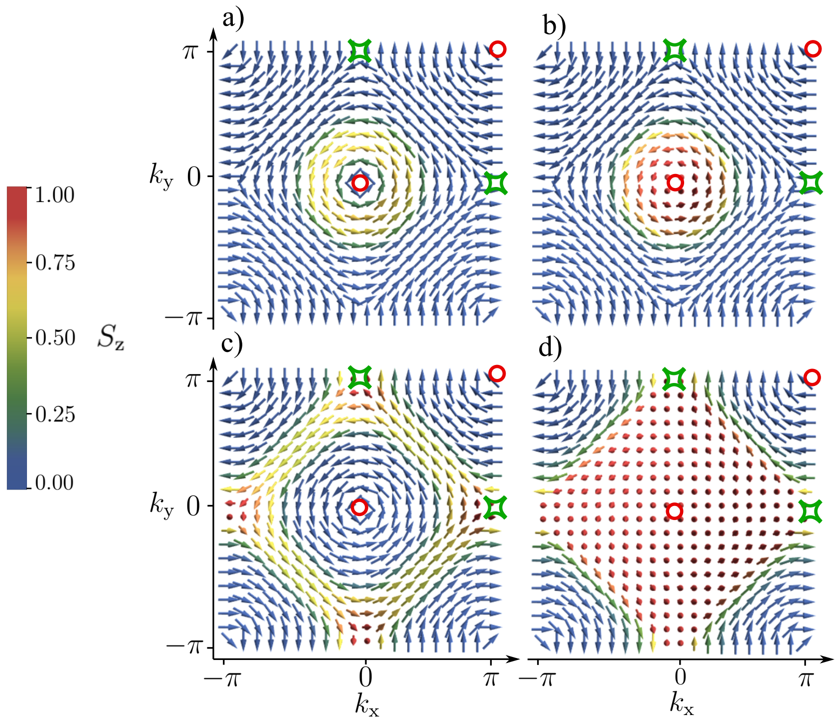

Figure III.5.: The zero temperature spin-textures are depicted for (a) the topologically trivial phase with $N_S = N_C = 0$, $n = 0.19$, $(h_z - h_{t,1})/h_{t,1} = -0.5$, (b) for the topologically non-trivial phases with $N_S = 1/2$, $N_C = -1$, $n = 0.12$, (c) $(h_z - h_{t,1})/h_{t,1} = 0.18$, $N_S = -1$, $N_C = 2$, $n = 0.9$, $(h_z - h_{t,2})/h_{t,2} = 0.3$, and (d) $N_S = -1/2$, $N_C = 1$, $n = 0.54$, $(h_z - h_{t,1})/h_{t,1} = 0.05$. The arrows indicate the direction of the normalized spin vectors. The color codes the z-component of the normalized spin, where red corresponds to $S_z = 1$ whereas blue corresponds to $S_z = 0$. The positions of the $\boldsymbol{k}_t$, which are defined in the main text, are marked with red and green symbols for vortices and antivortices, respectively. The figures are taken from Reference [74].

The gap closes whenever one band of the normal conducting state is depleted — related to $h_{t,1}$ and $h_{t,2}$ of Equations (III.1.11) and (III.1.12) in the $\Delta_{OP} \to 0$ limit — as illustrated in Figure III.4. There, $\xi_{\boldsymbol{k}}^+$ and $\xi_{\boldsymbol{k}}^-$ are the helical spin-split eigenbands of the normal conducting Hamiltonian. The transition fields depend on α_R through $\mu(n)$ obtained by solving the particle-number equation.

As mentioned above, in the region between quarter filling and half filling corresponding to $n = 1/2$ and $n = 1$, respectively, two non-trivial topological phases with $N_C = 2$ and $N_C = 1$ are possible. However, the latter requires large magnetic fields with $h_z \geq \epsilon(\mathbf{0})/2 = h_0$ where h_0 is the minimal magnetic field for which $h_z > h_{t,1}, h_{t,2}$ is fulfilled. In the low filling regime, the minimum transition field $\min(h_{t,1}(n)) = \Delta_{OP}$ is obtained for a filling n^* for which $\mu(n^*) = \epsilon(\mathbf{0})$; n^* depends on the Rashba spin-orbit coupling as shown in Figure III.6 b). Here, it should be noted that $\epsilon(\mathbf{0})$ is not the lowest band energy on account of the finite Rashba spin-orbit coupling. The topological phase diagram of the topological s-wave superconductor is given in Figure III.6.

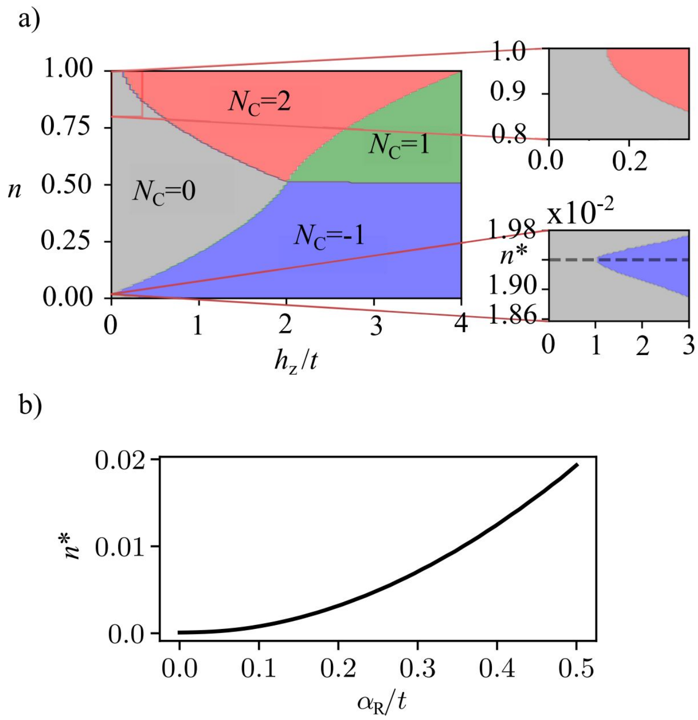

Figure III.6.: a) Phase diagram of topological ground states specified by the Chern numbers N_C for $\alpha_\mathrm{R}/t = 0.5$ and $V/t = 0.75$. b) Filling n^* as a function of α_R/t, defined as the band filling at which $h_{\mathrm{t},1} = \Delta_\mathrm{OP}$ (see text). The figures are taken from Reference [74].

If the magnetic field is rotated into an in-plane orientation, the topological transition fields $h_{\mathrm{t},1}$ and $h_{\mathrm{t},2}$ are decreased. For h_x, $h_\mathrm{y} \ll \alpha_\mathrm{R}$

$$h_{\mathrm{t},1,2}(h_{\mathrm{x,y}} \neq 0) \approx h_{\mathrm{t},1,2}(h_{\mathrm{x,y}} = 0) - t\frac{h_\mathrm{x}^2 + h_\mathrm{y}^2}{\alpha_\mathrm{R}^2} \tag{III.1.13}$$

is obtained analogous to the QWZ-model. The required field rotation into an in-plane orientation which may be required in order to realize this model experimentally leads to pairing with finite center-of-mass momentum [79–83], however, this does not destroy the inherent topological character of the considered phases [69] and, consequently, thermodynamic signatures which are addressed in Section IV.3 are not affected qualitatively. Therefore, without loss of generality, the analysis of thermodynamic quantities in the following sections concentrate on the situation without finite momentum pairing.

As in the QWZ-model, the topological s-wave superconductor also amounts to topologically distinct spin-textures in reciprocal space related to the different Chern numbers [69]. In contrast to the QWZ model, four different topologically non-trivial phases can be identified. The spin-expectation value is determined by

$$\langle \boldsymbol{s}(\boldsymbol{k})\rangle = \frac{1}{2}\sum_{\nu=1,2} \tanh\left(\frac{\beta\lambda_\nu(\boldsymbol{k},\mu)}{2}\right)\langle \nu,\boldsymbol{k}|\left(c^\dagger_{\boldsymbol{k},\uparrow}c^\dagger_{\boldsymbol{k},\downarrow}\right)\boldsymbol{\sigma}\left(c_{\boldsymbol{k},\uparrow}c_{\boldsymbol{k},\downarrow}\right)^{\mathrm{T}}|\nu,\boldsymbol{k}\rangle. \tag{III.1.14}$$

At $h_{\mathrm{x,y}} = 0$ and $T = 0$, the spin-texture for the topologically trivial phase for low band filling is depicted in Figure III.5 a. There are vortex patterns at the momenta $(0,0)$ and (π,π) and antivortices at $(0,\pi)$ and $(\pi,0)$. For $h_{\mathrm{x,y}} \neq 0$, the $\boldsymbol{k}_{\mathrm{t}}$ are shifted like in the QWZ model. In contrast to the QWZ-model, at some of the centers of a vortex or antivortex the spin normalization must be defined by the limit $\boldsymbol{k} \to \boldsymbol{k}_{\mathrm{t}}$ since all three spin components can vanish simultaneously. For $N_{\mathrm{C}} = 0$, the spin-texture is non-normalizable at all four $\boldsymbol{k}_{\mathrm{t}}$ because all spin-components vanish as shown in Figure III.5 a). The normalized spin-textures for the phases with $N_{\mathrm{C}} = -1, 2, 1$ are shown in Figures III.5 b - d. In each of the these phases, the spin points in positive z-direction, $\boldsymbol{S} = (0,0,1)^T$, at one or more of the $\boldsymbol{k}_{\mathrm{t}}$ and its normalization is hence possible there as depicted in Figure III.5.

As the normalized spin $\boldsymbol{S}(\boldsymbol{k})$ can be viewed as a map from the torus (the 2d Brillouin zone) to the upper hemisphere of the sphere S^2, the number of the $\boldsymbol{k}_{\mathrm{t}}$ mapped onto the "north pole" are less than or equal to four, whereas the remaining points are mapped to the equator, where the map becomes undefined. The manifold of the spin expectation values can be compactified to the unit sphere such that the equator is mapped to the south pole [69] of the sphere proving the spin-texture's topological non-trivial nature because the continuous map between the compact manifolds is a topological invariant and application of Equation (III.1.10) is possible. In Figure III.5, the color of the arrows indicates on which latitude of the sphere the normalized spin expectation value is positioned after compactification. Dark red corresponds to the covering of the north pole while dark blue implies the mapping onto the equator. Similar to the QWZ-model the mapping is defined by Equation (III.1.4). The number of north pole coverings is one, zero, two, and three for the phases $N_{\mathrm{C}} = -1, 0, 1, 2$, respectively.

III.2. Relation of the Loder curvature and the Berry curvature in the topological s-wave superconductor

According to Reference [69], the skyrmion number and the Chern number are closely related such that the $N_{\mathrm{S}} = -0.5N_{\mathrm{C}}$. Moreover, according to the reference, the Berry curvature is pointwise identical to Ω_{S} defined in (II.1.24). However, this identity does not hold in the topological s-wave superconductor which is discussed in the following. Here, finite momentum pairing in the Fulde-Ferrell regime with a single momentum $\boldsymbol{q}$ is considered. However, states with more than one single $\boldsymbol{q}$-vector may be favored in energy [48]. The Hamiltonian of the topological s-wave superconductor with Rashba spin-orbit coupling and Zeeman splitting in the Fulde-Ferrell situation is given by

$$H(\boldsymbol{k}) = \begin{pmatrix} \epsilon(\boldsymbol{k}) + h_{\mathrm{z}} & \xi(\boldsymbol{k}) & 0 & \Delta_{\mathrm{OP}} \\ \xi^*(\boldsymbol{k}) & \epsilon(\boldsymbol{k}) - h_{\mathrm{z}} & -\Delta_{\mathrm{OP}} & 0 \\ 0 & -\Delta_{\mathrm{OP}} & -\epsilon(-\boldsymbol{k}+\boldsymbol{q}) - h_{\mathrm{z}} & -\xi^*(-\boldsymbol{k}+\boldsymbol{q}) \\ \Delta_{\mathrm{OP}} & 0 & -\xi(-\boldsymbol{k}+\boldsymbol{q}) & -\epsilon(-\boldsymbol{k}+\boldsymbol{q}) + h_{\mathrm{z}} \end{pmatrix} \tag{III.2.1}$$

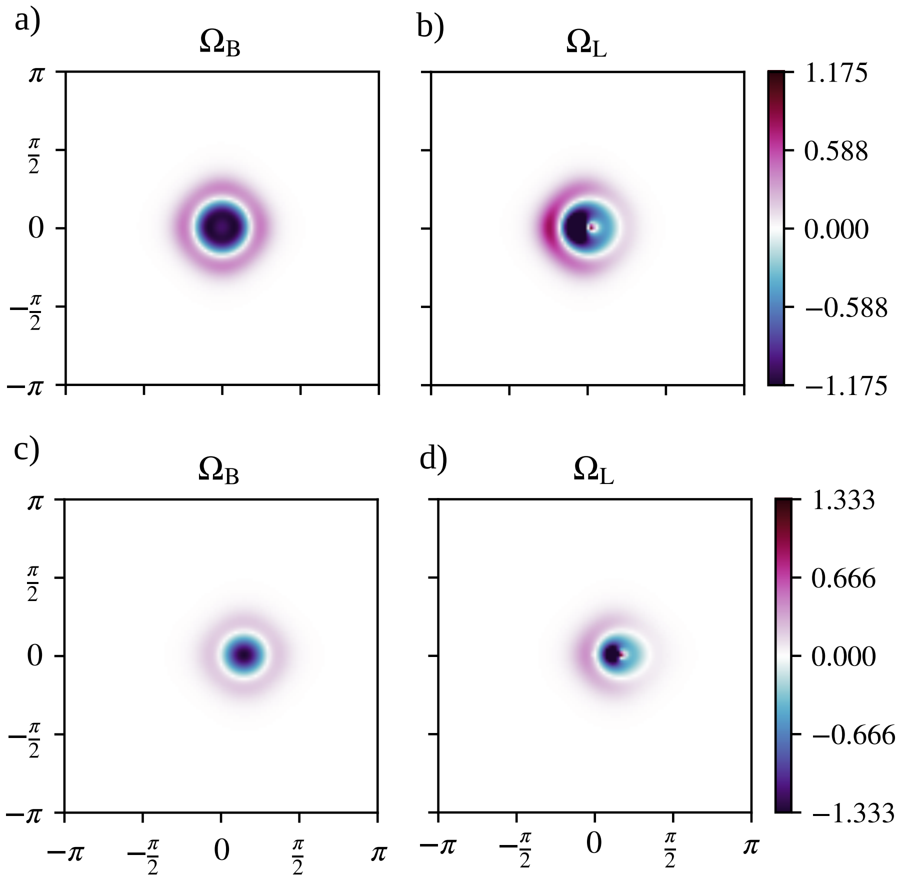

Figure III.7.: a) Ω_B and b) Ω_L obtained for $h_y = 0.2t$, $h_x = 0$, $q_x = 0$, $q_y = 0$; c): Ω_B and d) Ω_L at $h_y = 0$, $h_x = 0$, $q_x = \pi/10$, $q_y = 0$. Other parameters are $\alpha_R = 0.4t$, $\Delta_{OP} = 0.5t$ and $h_z = h_{t,1}/2$.

in the basis $|\psi\rangle = (\hat{c}_{\boldsymbol{k},\uparrow}, \hat{c}_{\boldsymbol{k},\downarrow}, \hat{c}^\dagger_{-\boldsymbol{k}+\boldsymbol{q},\uparrow}, \hat{c}^\dagger_{-\boldsymbol{k}+\boldsymbol{q},\downarrow})$ with $\xi(\boldsymbol{k}) = \epsilon_R(\boldsymbol{k}) + h_x - \mathrm{i}h_y$.

Numerically, it was suggested in Reference [69] that the Loder curvature defined in (III.1.9) may be related to the Berry curvature by

$$\Omega_B(\boldsymbol{k}) = -\frac{1}{2}\left(\Omega_L(\boldsymbol{k}) + \Omega_L(-\boldsymbol{k}+\boldsymbol{q})\right) \quad \boldsymbol{k} \notin \{(0,0), (\pi,0), (0,\pi), (\pi,\pi)\}\,. \tag{III.2.2}$$

This suggestion was not investigated further in the reference and has not been analyzed so far. The numerical analysis shows that this identity is not fulfilled as discussed below.

Apparently, the Loder curvature is very tedious to analyze analytically since terms get lengthy because of the square root terms in the denominator in the spin-normalization. Setting $\boldsymbol{q} \neq 0$ but keeping $h_x, h_y = 0$ shifts the Berry curvature in momentum space by the vector $\boldsymbol{q}$ but it remains symmetric as shown in Figure III.7 c) On the other hand, for $h_x \neq 0$ or $h_y \neq 0$ while keeping $\boldsymbol{q} = 0$ the Berry curvature does not shift and the Berry curvature is symmetric depicted in Figure III.7 a). In comparison, the Loder curvature is shown for both cases in Figure III.7 d) and b), respectively. In contrast to the Berry curvature the Loder curvature is not symmetric in both

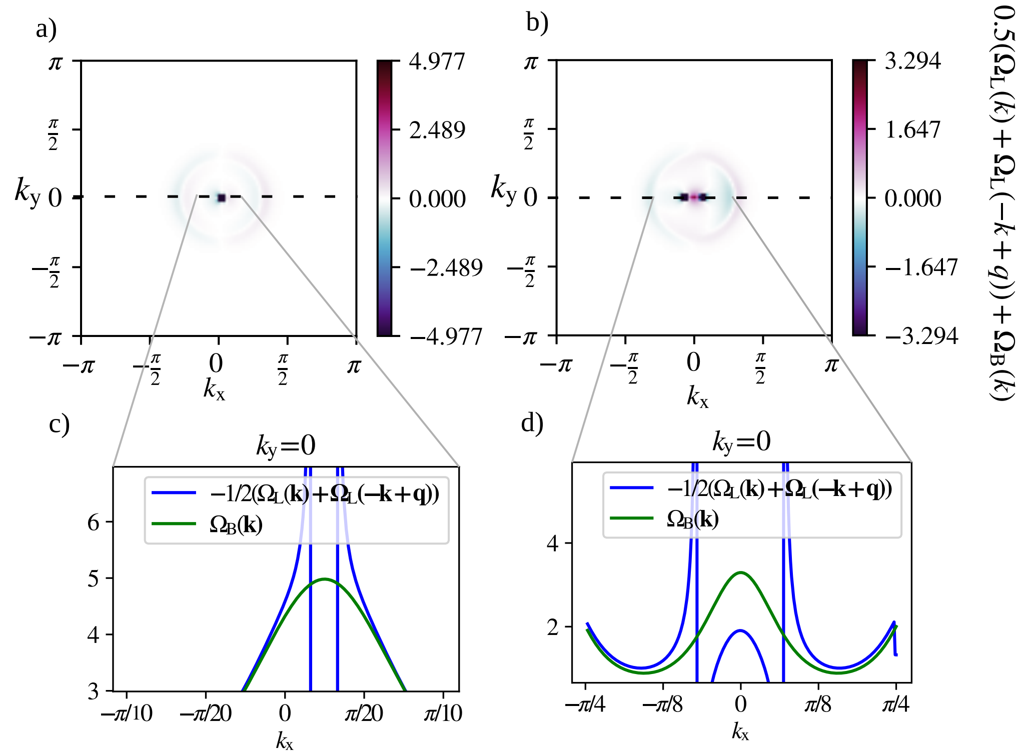

Figure III.8.: Comparison of $1/2 \cdot \left(\Omega_L(\boldsymbol{k}) + \Omega_L(-\boldsymbol{k}+\boldsymbol{q})\right)$ with the Berry curvature. The parameters used in a) and c) correspond to the parameters chosen in Figure III.7 a) and b). The parameters used in b) and d) correspond to the parameters chosen in Figure III.7 c) and d).

cases. In order to symmetrize the Loder curvature one has to take $1/2 \cdot \left(\Omega_L(\boldsymbol{k}) + \Omega_L(-\boldsymbol{k}+\boldsymbol{q})\right)$ which is suggested in Ref [69].

The equality in (III.2.2) is tedious to analyze analytically since the terms become cumbersome. Restricting the evaluation to $k_y = 0$ and allowing only for $h_y \neq 0$ and $q_x \neq 0$ while $q_y = 0$ simplifies the expression for Ω_L significantly. Then $S_{Lx} = 0$ and $|S_{Ly}| = |s_y/(s_x^2 + s_y^2)| = 1$ such that one finds

$$\Omega_L(k_y = 0, k_x) = \frac{\operatorname{sign}(s_y)}{|s_y|} \left(\sum_{\nu}^{\text{occ}} 4\mathrm{Re} \left(\sum_{\mu \neq \nu} \langle \nu, \boldsymbol{k} | \sigma_z \otimes \tau_{11} | \mu, \boldsymbol{k} \rangle \frac{\langle \mu, \boldsymbol{k} | \partial_{k_x} H | \nu, \boldsymbol{k} \rangle}{E_{\nu,\boldsymbol{k}} - E_{\mu,\boldsymbol{k}}} \right) \right.$$
$$\left. \times \left(\sum_{\alpha}^{\text{occ}} \mathrm{Re} \left(\sum_{\beta \neq \alpha} \langle \alpha R, \boldsymbol{k} | \sigma_x \otimes \tau_{11} | \beta, \boldsymbol{k} \rangle \frac{\langle \beta, \boldsymbol{k} | \partial_{k_y} H | \alpha, \boldsymbol{k} \rangle}{E_{\alpha,\boldsymbol{k}} - E_{\beta,\boldsymbol{k}}} \right) \right) \right). \tag{III.2.3}$$

The expression for $\Omega_L(k_y = 0, k_x)$ depends only on the eigenvectors and the derivative of the Hamiltonian. This expression is thus numerically simple and comparable to the Berry curvature given in (II.1.22). The numerical analysis confirms the correctness of Equation (III.2.2) for

$h_x, h_y = 0$ and $\boldsymbol{q} = 0$. For $h_x, h_y \neq 0$ or $\boldsymbol{q} \neq 0$ this equality is numerically not fulfilled but differences are small except for a small region around the vortex center point. The numerical comparison of $\Omega_L(k_y = 0, k_x)$ calculated with (III.2.3) and $\Omega_B(k_y = 0, k_x)$ is given in Figure III.8. Due to the finite momentum pairing vector $\boldsymbol{q}$, the vortex center is shifted in momentum space.

For $\boldsymbol{q} \neq 0$ and $h_x = h_y = 0$, the result of the comparison within the full Brillouin zone where Ω_L is calculated through (III.1.9) is given in Figure III.8 a). A small but non-zero difference is recognizable around the Γ-point where a large difference is given in the vicinity to that point. This difference is confirmed by the evaluation of Equation (III.2.3) along the dashed line indicated in the inset. There, the vortex center is given at $\boldsymbol{q}$ where a singularity in $\Omega_L(\boldsymbol{q})$ is found in the numerical results. Therefore $\Omega_L(-\boldsymbol{k})$ has a singularity at $-\boldsymbol{q}$ and another singularity arising from $\Omega_L(-\boldsymbol{k} + \boldsymbol{q})$ is given at $\boldsymbol{k} = 2\boldsymbol{q}$. The criticalities are caused by the vanishing of $|s_y|$ at the vortex center points.

The pronounced differences in the obtained results are not numerical artifacts as one may think due to the vortex texture and the undefinedness of the texture at the vortex center point. This is shown by the evaluation of Equation (III.2.3) where the difference is a smooth function of k_x.

The analogous situation is obtained by taking $\boldsymbol{q} = 0$, $h_x = 0$ but $h_y = 0.2t$. The results are depicted in Figure III.8 b). The identity (III.2.2) is thus only fulfilled in the situation with total out-of plane magnetic field which however does support finite center of mass momentum pairing [41, 48].

III.3. Finite size and temperature

The spin-textures shown above are the ground state spin-textures for systems with periodic boundary conditions. Here, the effects of finite temperature and finite size on the spin-textures are analyzed. First, the changes in the spin-texture due to finite temperatures are investigated. At finite temperature, the vortex and antivortex texture is maintained. Moreover, the z components of the normalized spin expectation vector is stable against finite temperatures at the different $\boldsymbol{k}_t$. Therefore, according to Equation (III.1.10), the topological spin-texture is — in terms of the skyrmion number — invariant under any finite temperatures in the QWZ-model. As discussed in Chapter IV qualitative differences in the change of the magnetization with respect to a temperature increase can be identified across a topological phase transition. The difference in the s_z values defined in (III.1.14) due to the change in temperature are displayed in Figure III.9 above and below a topological transition field h_t. The change in the magnetization is largest in the vicinity of the gap closing momentum $\boldsymbol{k}_t$, which is in the case depicted in the figure given at $\boldsymbol{k}_t = (0, 0)$. The derivative of the magnetization with respect to the temperature shows a sign change of the spin polarization across the topological phase transition at small temperatures. At high temperatures, two regions with a different sign in $\partial_T m(\boldsymbol{k})$ are found for $h_z < h_{t,z,3}$. The change in the magnetization in z-direction is thus different for the distinct topological phases. The net magnetization of the entire system is used to identify topological phase transitions in the spin magnetization which is discussed in more detail in Section IV.2.

The QWZ-model is translation invariant and thus diagonal in reciprocal space. At finite size with open boundary conditions, the translation invariance is of course no longer fulfilled which results in off-diagonal matrix elements in momentum space. It is thus more convenient to stay in

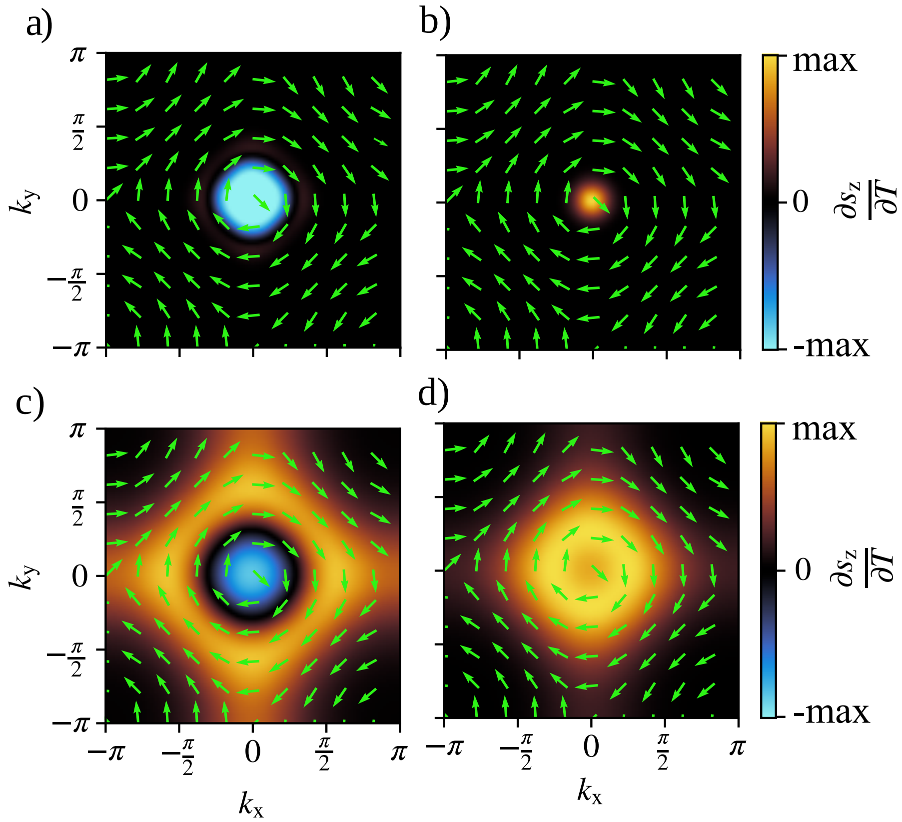

Figure III.9.: Change of the momentum-resolved spin polarization in the QWZ model with respect to the temperature T. The results are displayed in a) and b) for $T = 0.1t$ and in c) and d) for $T = 0.5t$. The topological non-trivial phase is shown in a) and c) with $h_z = h_{t,3} - h_{t,3}/5$. The trivial phase is given in b) and d) for $h_z = h_{t,3} + h_{t,3}/5$. The green arrows indicate the direction of the in-plane components of the spin expectation values.

real space calculations for finite size systems by directly implementing the Hamiltonian given in Equation (II.3.1). Compared with the translation invariant system the full real-space Hamiltonian needs to be implemented, therefore the calculation time is highly increased for open boundary calculations and thus smaller systems have to be implemented. Here, the real space Hamiltonian is implemented with the possibility of choosing the boundary conditions in the different directions being either open or periodic.

For periodic boundary conditions, the real space representation yields a vanishing in-plane polarization at each point in real space and the z-component is finite but constant in the Brillouin-zone. These result are expected since the system needs to be translation invariant and thus needs to be homogeneous. As the total magnetization in the in-plane components need to vanish, all in-plane spin components need to be zero at any lattice point.

Switching to open boundary conditions, the obtained results in momentum space and in real space are summarized in Figures III.10. Although the system is not translation invariant with

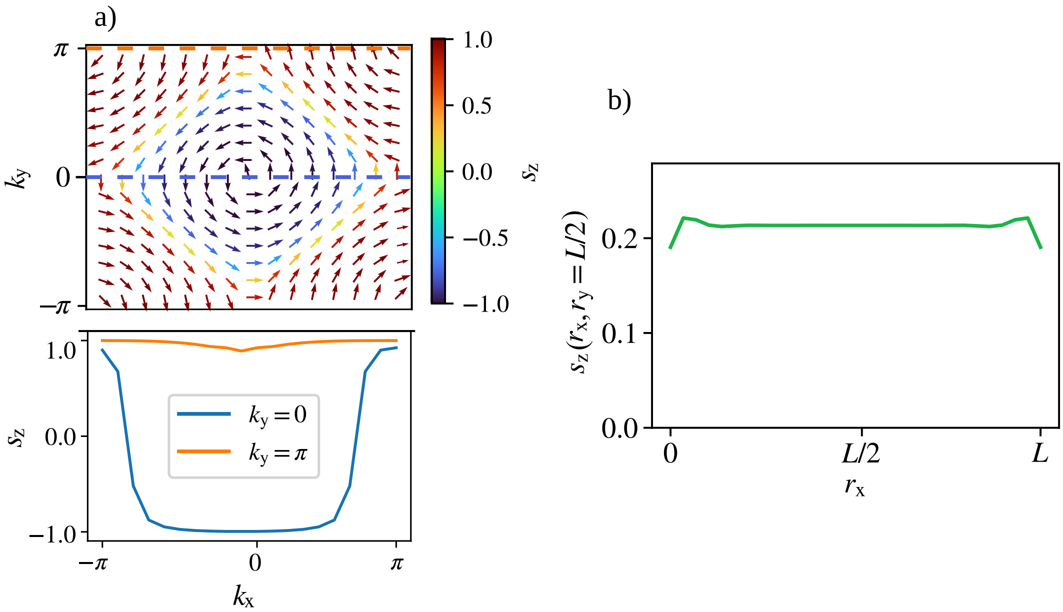

Figure III.10.: Spin-textures of the QWZ model with open boundary conditions represented in reciprocal space in a) and in real space in b). The parameters $h_z = 0.5t$, $\alpha_R = 0.5t, h_x = h_y = 0t$ are used corresponding to the topological phase with $N_C = -1$. The spin-texture in a) has an 1D inset below.

open boundary conditions and hence not diagonal in momentum space, the expectation value of the spin for a certain momentum can still be taken by Fourier transforming the Hamiltonian into momentum space and calculating its eigenvectors. The expectation value of a spin state in momentum space is then defined by

$$\boldsymbol{s}(\boldsymbol{k}, T = 0) = \left(\psi_{k_1,\uparrow}, \psi_{k_2,\uparrow}, \ldots, \psi_{k_1,\downarrow}, \psi_{k_2,\downarrow}, \ldots, \psi_{k_{N-1},\downarrow}, \psi_{k_N,\downarrow}\right)^* \mathbb{1}_{\boldsymbol{k}} \otimes \boldsymbol{\sigma} \begin{pmatrix} \psi_{k_1,\uparrow} \\ \psi_{k_2,\uparrow} \\ \vdots \\ \psi_{k_1,\downarrow} \\ \psi_{k_2,\downarrow} \\ \vdots \\ \psi_{k_{N-1},\downarrow} \\ \psi_{k_N,\downarrow} \end{pmatrix}. \quad \text{(III.3.1)}$$

At any finite size, the skyrmion number, being an exact topological invariant, cannot be determined through Equation (II.1.24) since this equation requires infinite systems in order to obtain the continuum description. However, Equation (III.1.10) can be generalized for finite size lattice models at which the vorticity is still confined to integers. Thus, the vortex- and antivortex-like patterns can still be identified in finite size systems which can then be related to the topological invariants of the corresponding continuum spin-texture. For distinguishability, the term topological character of the spin-texture is used in the finite lattice model instead of skyrmion number which denotes the topological invariant which is defined through the continuum model.

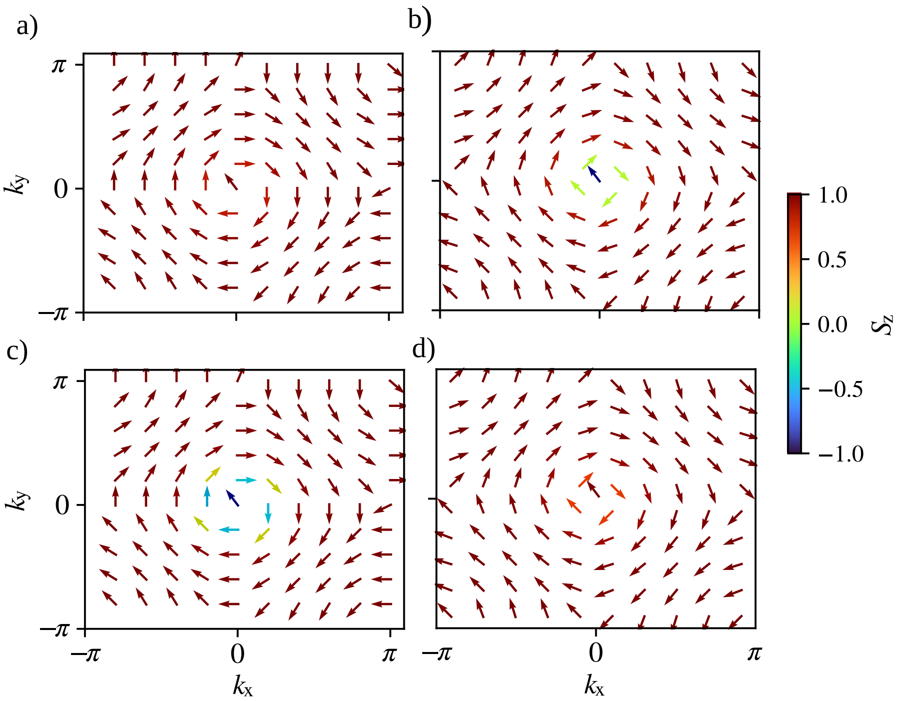

Figure III.11.: Spin-textures of the QWZ-model at different homogeneous magnetic fields in z-direction and system sizes. The used parameters are a) $N = N_x = N_y = 10$ and $h_z = h_{t,z,3} - 0.2t$; b) $N = 20$ and $h_z = h_{t,z,3} - 0.2t$; c) $N = 10$ and $h_z = h_{t,z,3} - 0.9t$; d) $N = 20$ and $h_z = h_{t,z,3} - 0.1t$.

The results show that the vortex and antivortex texture in momentum space is maintained but the z-component of the spin is modified which is clearly visible in the real space solution. Instead of a homogeneous polarization in r_x, the polarization is dependent on r_x showing the largest magnitudes of the polarization at the edges as indicated in Figure III.10 b).

Depending on the size of the system and the chosen parameter sets in the Hamiltonian the topological character of the spin-texture can differ from the topological invariant of the related texture with the periodic boundary conditions. For example in Figure III.11 a) the z-component of the spin points towards the north-pole at all the $\boldsymbol{k}_t$ for $h_z = h_{t,z,3} - 0.2$t and its spin-texture has therefore a trivial topological character. For periodic boundary conditions in the continuum limit, however, a non-trivial phase with $N_C = 1$ is established for that parameter set. However, the difference between the topological character of the finite size system and the topological spin-texture in the periodic system are dependent on the parameter set of the Hamiltonian and the system size. One can identify that the $s_z(\boldsymbol{k}_t)$ values differ from -1 and 1 due to the finite size effects as shown in Figure III.10 a). This difference is enhanced by shrinking the system size. It turns out that the transitions fields $h_{ts}(N_x, N_y)$ are functions of the system size. For magnetic fields $|h_z - h_t| < |h_{ts}(N_x, N_y) - h_t|$, the spin-texture changes its topological character. Therefore, a topological character transition can be driven by the system size as demonstrated in Figure III.11. The spin character is trivial in Subfigure III.11 a) for which a system size of $N = 10$ and a value of

$h_z = h_{t,z,3} - 0.2t$ are chosen. The value for h_z corresponds to a topological non-trivial spin-texture for periodic boundary conditions. Keeping h_z at the same value but choosing $N = 20$ leads to a non-trivial character of the spin-texture as depicted in Subfigure III.11 b). The increase of the system size does therefore lead to a change in the topological spin-texture character. On the other hand a topologically non-trivial spin-texture character is obtained for $N = 10$ but $h_z = h_{t,z,3} - 0.9t$ depicted in c). Finally, a trivial spin-texture is obtained for $N = 20$ and $h_z = h_{t,z,3} - 0.1t$ shown in subfigure d). The change of the topological character is not necessarily a change into a trivial character. Transitions between non-trivial topological spin-texture characters are possible since the sign of the $s_z(\boldsymbol{k}_t)$ can change at single momenta $\boldsymbol{k}_t$. These observations allow to introduce the concept of system size driven topological character transitions.

A major difference between the results for open boundary and periodic boundary results is that in case of open boundaries, the systems can possess gapless edge states and for periodic boundary conditions it cannot which is referred to as bulk-boundary correspondence [8]. In order to analyze the edge states, different boundary conditions are enforced in the x and y direction. At first, the cylinder geometry is used. There, in the x-direction, the boundary conditions are open, whereas in the y-direction periodic boundary conditions are chosen.

In fact, edge states for the open boundary conditions are only present for parameter sets for which the corresponding system with periodic boundary conditions is topologically non-trivial. This is fulfilled for all $h_z \in \left\{h_{t,1}(h_{x,y} = 0), h_{t,3}(h_{x,y} = 0)\right\}$. The edge modes are indicated with the colored lines in the dispersion shown in Figure III.12 b). They fill the gap between the bulk (black colored) states. The color provides information about the real space distribution of the states. The used color map is generated by the function

$$\mathcal{E}_{1(2)}(s, k_y) = \frac{1}{L} \sum_{r_x} \left(r_x - \frac{L}{2} \right) |\langle s, \hat{r}_x, \hat{k}_y \rangle_{1(2)}|^2 \tag{III.3.2}$$

where $\langle \dots \rangle_{1(2)}$ denotes the expectation value taken for a single edge mode where the index corresponds to the lower (1) and the higher (2) band and $s \in \{\uparrow, \downarrow\}$.

The indicated colors orange to yellow corresponds to a state distributed dominantly around $r_x = L$ and dark to light blue correspond to a state distributed around $r_x = 0$. Likewise black corresponds to a state that is distributed across the full system length which thus corresponds to a bulk state distribution. At any topological trivial phase, no edge states can be found whereas in the topological bulk phase, edge modes are clearly identified. The edge states show a linear dispersion the $k_{y,t}$ as shown in Figure III.12. The have its probability at the edges of the system as the results in Figure III.12 illustrate. The band gap is vanishing for towards infinite systems. However, at any finite size, there is a small but finite overlap of the edge states from both ends of the system. As a result, the edge states display a small but finite gap [84]. Besides the probabilities for an edge state to be localized at a certain position, the probability for the pseudo-$\uparrow$-spin and $\downarrow$-spin have been distinguished as well. The edge states with $\uparrow$-spin and group velocity $v_G := \partial_{k_y} \lambda > 0$ are found at the edge $r_x = 0$ while the states with $\uparrow$-spin with $v_G < 0$ are located at the opposite edge. The situation for the $\downarrow$-spin expectation values are equivalent. This means that all the edge states carry electrons with both $\uparrow$-spin and $\downarrow$-spin in the positive y-direction at $r_x = 0$ and in negative y-direction at $r_x = L$ resulting in an edge current. The edge modes are thus chiral. These results are well known from the quantum Hall effect [85].

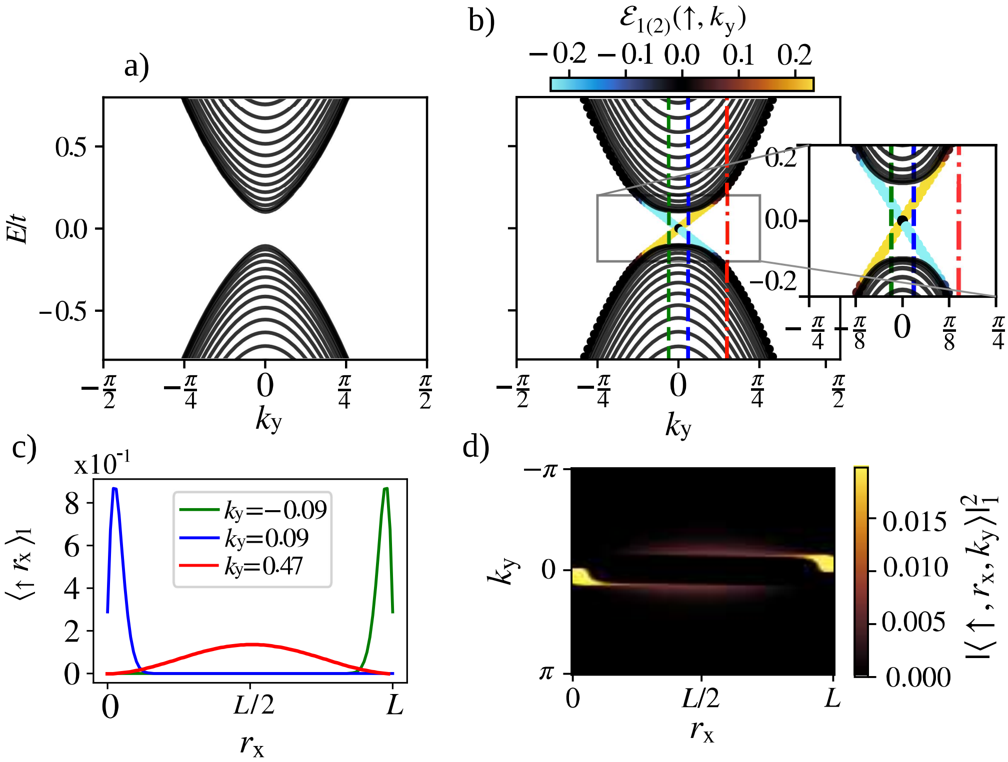

Figure III.12.: Dispersions and edge states in the QWZ-model; a) Dispersion in the topological trivial phase which has no edge states. b) Dispersion in the non-trivial phase where edge modes are identified displayed in colors. c) Edge modes and bulk states distributed in position space. The colors correspond to the states marked in Subfigure b). d) Distribution of the edge modes in the $r_x - k_y$-space for the lower band. Further details are given in the main text.

In the next step, the edge states with energy closest to the chemical potential μ are analyzed for open boundary conditions in both, x- and y-direction. In the density of states (DOS) or likewise the local density of states (LDOS), one can recognize the edge states as those which fill the band gap as depicted in Figure III.14 a) and b). The LDOS is shown at the edge $r_x = 0$ as a function of r_y and the energy E. The color indicates the intensity of the LDOS and the band gap is marked by the dashed lines. In the trivial phase, no edge state can be identified. The LDOS and DOS is plotted for $h_z = h_{t,z,3} + 0.5t$ in Figure III.14 a) which corresponds to the trivial bulk phase and for $h_z = -0.5t$ in Figure III.14 b) corresponding to the non-trivial bulk phase. The DOS clearly indicates the bulk gap where the DOS is zero in a) and small but almost constant in b). The edge modes are distributed along the entire edge for $h_z = h_{t,z,3} - 0.5t$ while its highest probability is found at the corners.

These findings are confirmed by the results displayed in Figure III.13 where the distribution of the spin-resolved expectation values of the position operator are given in position space. The results clearly show that the edge states are localized at the corners for $h_z = 0.5t$ (Figure III.13a)

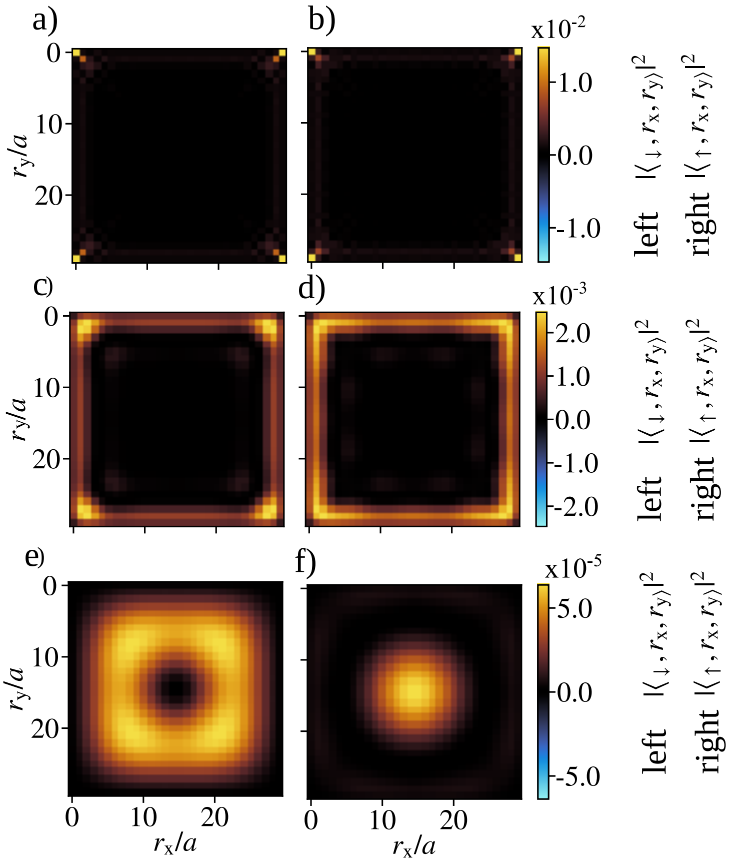

Figure III.13.: Distribution of the edge modes in the QWZ model in real space. At $h_z = 0.5t$, which is presented in a) and b), the edge modes are localized at the corners. At $h_z = h_{t,z,3} - 0.5t$ given in c) and d), the edge modes are found along the entire edge but with highest probability at the corners. Particular bulk states are depicted in e) and f).

and III.13 b)) and spread across the edge for $h_z = h_{t,z,3} - 0.5t$ (Figure III.13 c) and III.13 d) with highest probability at the corners. The distributions are different for ↑-spin and ↓-spin as one would expect because there is an imbalance between ↑-spin and ↓-spin resulting in a net-polarization. Moreover, the ↓-states are more localized at the corners than the ↑-states at $h_z = h_{t,z,3} - 0.5t$. The bulk states are plotted in Figure III.13 e) and III.13 f) showing no ↓-spin at the center of the system or the edge but the probability is highest in a region in between the center and the edges. The bulk states, on the other hand, have a non-zero ↑-spin expectation value at the center of the system. Thus, the results confirm the existence of edge states when the corresponding bulk is topologically non-trivial.

Topological s-wave superconductor

The situation regarding the finite temperature and the finite size results is in the topological s-wave superconductor different than in the QWZ model as discussed in the following. A major reason

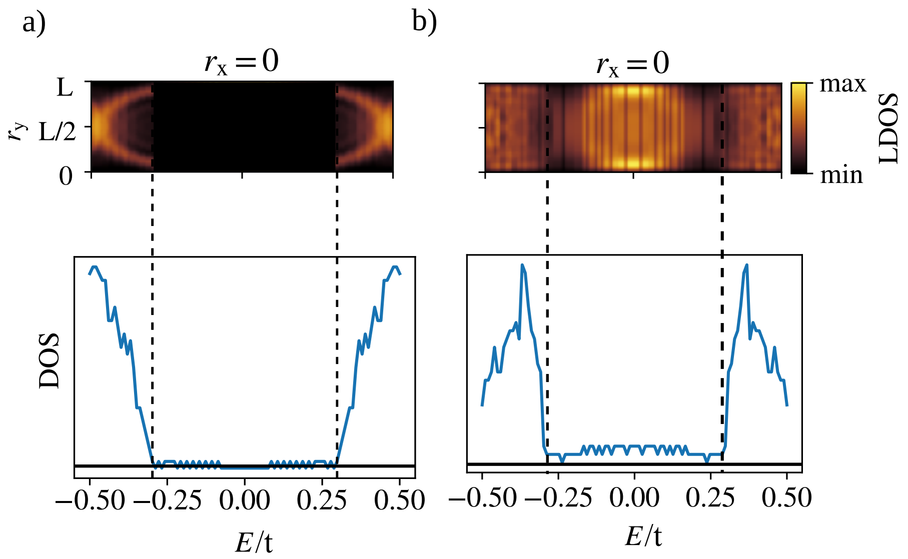

Figure III.14.: Local density of states (LDOS) at $r_x = 0$ as a function of r_y and E (figures above) and the density of states (DOS) (figures below) for the QZW model in a) the trivial phase at $h_z = h_{t,3} + 0.5t$ and in b) the non-trivial phase at $h_z = h_{t,3} - 0.5t$.

for the differences is that the topological s-wave superconductor exhibits a meron-like spin-texture in momentum space whereas the spin-texture is skyrmion-like in the QWZ-model. This has consequences on the stability of the topological character of the spin-textures.

Important for understanding the meron spin-textures is the existence of distinct points at which all three spin-components vanish simultaneously. At those points, the spin-normalization is not defined. However, the topological state can be described by the skyrmion number which can be determined by Equation (III.1.10). At any finite temperature T, the $s_z(\boldsymbol{k})$ are non-zero everywhere in the Brillouin zone because any small excitation induces a non-zero polarization. The north pole is then covered four times since the in-plane spin components $s_x(\boldsymbol{k}_t) = s_y(\boldsymbol{k}_t) = 0$ by symmetry. Hence, the number of $\boldsymbol{k}_t$ mapped onto the equator is zero and the compactified map does not yield a full covering of the S^2. Because the map is still smooth, the associated skyrmion number vanishes for any $T > 0$. Yet, the change in the spin polarization around the gap closing points is in the topological s-wave superconductor quite similar to the QWZ-model. In Figure III.15 $\partial_T M_z(\boldsymbol{k})$ is plotted in the Brillouin zone. Similarly as in the QWZ-model, $\partial_T M_z(\boldsymbol{k})$ changes sign across the topological phase transition which has consequences for the total change of the magnetization in the vicinity of the topological phase transition which is analyzed further in Section IV.2.

Also, the Hamiltonian for the topological s-wave superconductor is analyzed for open boundary conditions. The results in the QWZ model in the case of open boundary conditions show that the systems can possess edge states just when the bulk is topologically non-trivial. This situation is different in the topological superconductor. Different boundary conditions are enforced in the x and y direction in order to analyze the edge states. First, open boundary conditions in x-direction and periodic boundary conditions in y-direction are used.

The edge states are clearly identified for the system with non-trivial topology shown in Fig-

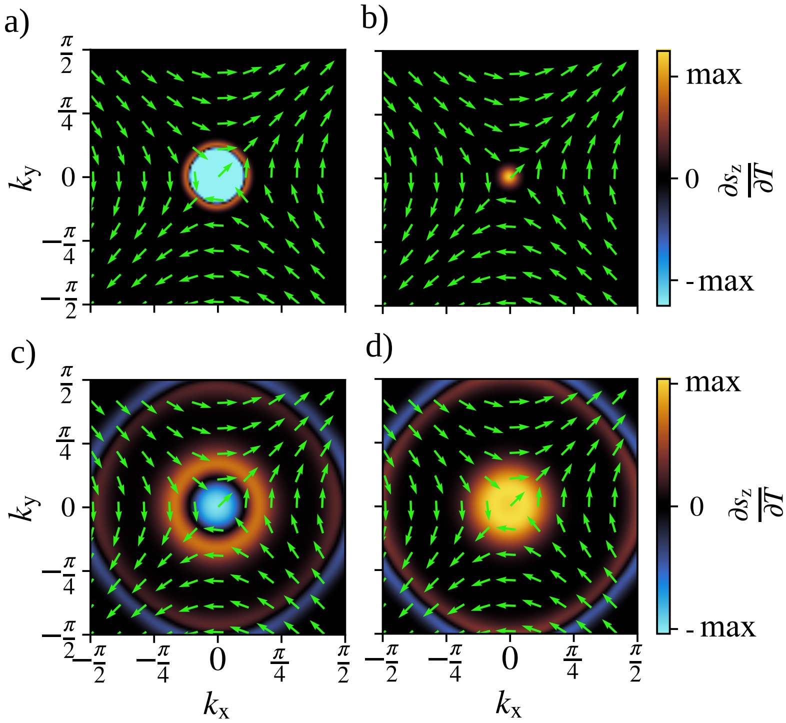

Figure III.15.: Change of the spin polarization in the topological s-wave superconductor model with respect to the temperature T. The results are displayed in a) and b) for $T = 0.01t$ and in c) and d) for $T = 0.1t$. The topological trivial phase is given in a) and c) with $h_z = h_{t,1} - h_{t,1}/5$. The non-trivial phase is shown in b) and d) with $h_z = h_{t,1} + h_{t,1}/5$. The green arrows indicate the direction of the in-plane components of the spin expectation values. Further parameters are $\mu = -3t$, $\Delta_{OP} = 0.5t$ and $\alpha_R = 0.5t$.

ure III.16 a) and b). The edge states are indicated colored as for the QWZ model described above. There, the used color map is generated by the function given in Equation (III.3.2). Setting $h_z = h_{t,1}$, there are two edge states for each momentum $\boldsymbol{k} \in \left[-\pi/2, \pi/2\right]$ where the states with $v_G > 0$ are found at the edge $r_x = L$ while the edge states with $v_G < 0$ are located at $r_x = 0$ as shown in Figure III.16 a), b). The states with $v_{Gy} > 0$ or $v_{Gy} < 0$ carry both , ↑-spin and ↓-spin, however, the ↓-spin is much more localized at the edge as shown by the color map in Figure III.16 a) and b), for ↓- and ↑-spin, respectively.

Another major difference between the QWZ model and the topological s-wave superconductor is that the latter exhibits edge states even for parameter sets which do not support non-trivial topology in the periodic setup. These edge states are depicted in Figure III.16 c) and d). They carry also a non-vanishing charge current since the states with a positive group velocity in y direction are found at $r_x = L$ and the states with a negative group velocity are found at $r_x = 0$. The topological s-wave superconductor exhibits thus chiral edge states when the bulk is topological trivial. In addition the edge states have a rather ↑-spin character than ↓-spin character which is

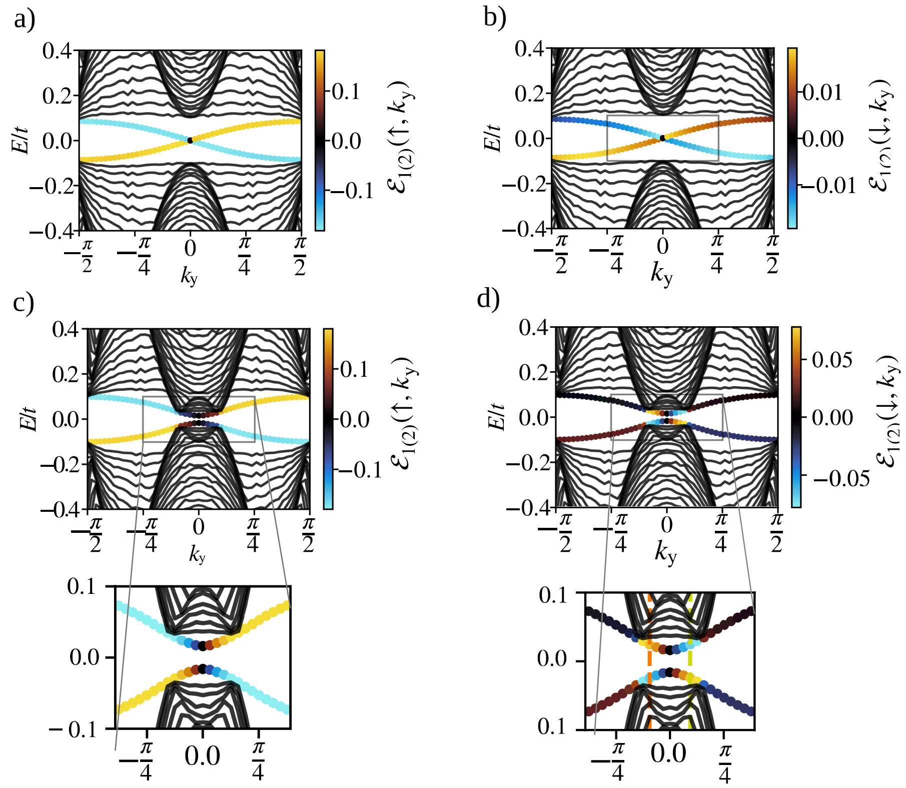

Figure III.16.: Superconducting model with open boundary conditions. a) and b): Edge states spin-resolved in the topological bulk phase with $N_C = -1$. ↓-states are given in a) and ↑-states are depicted in b). The ↓-states are closer confined to the edge than the ↑-states as indicated by the colors. c), d): Edge states spin-resolved in the trivial bulk phase characterized by $N_C = -1$. ↓-states are given in c) and ↑-states are depicted in d). The ↓-states are closer confined to the edge than the ↑-states. The parameters $\alpha_R = 0.5t$, $\mu = -3.0t$ and $h_z = h_{t,1} + 0.1t$ (in a) and b)) and $h_z = h_{t,1} - 0.1t$ (in c) and d)) are used.

the result of the strong Zeeman field which breaks time reversal symmetry and suppresses the ↓-spin chanel. However, these edge states are gapped as indicated in the figures.

In the next step, the edge states are analyzed for open boundary conditions in both, x- and y-direction. The results are presented in Figures III.17 a) and b) for a parameter set, where the corresponding bulk solution is trivial and in Figures III.17 c) and d) for a non-trivial bulk solution. It can be recognized that the edge states that fill the band gap identified in the DOS are present in both parameter sets (where the bulk is trivial and where the bulk is topological).

The existence of the edge states in the trivial bulk phase and the differences in the distribution of the ↑-spin expectations and ↓-spin expectations are confirmed by the results of the distribution of the edge states for the ↑- and ↓-spin polarization of the edge modes for open boundary conditions in both, x and y direction. The distribution of the edge states for the parameter set corresponding to a trivial bulk phase are depicted in Figure III.17 a) and b). While the ↓-spin expectation value is

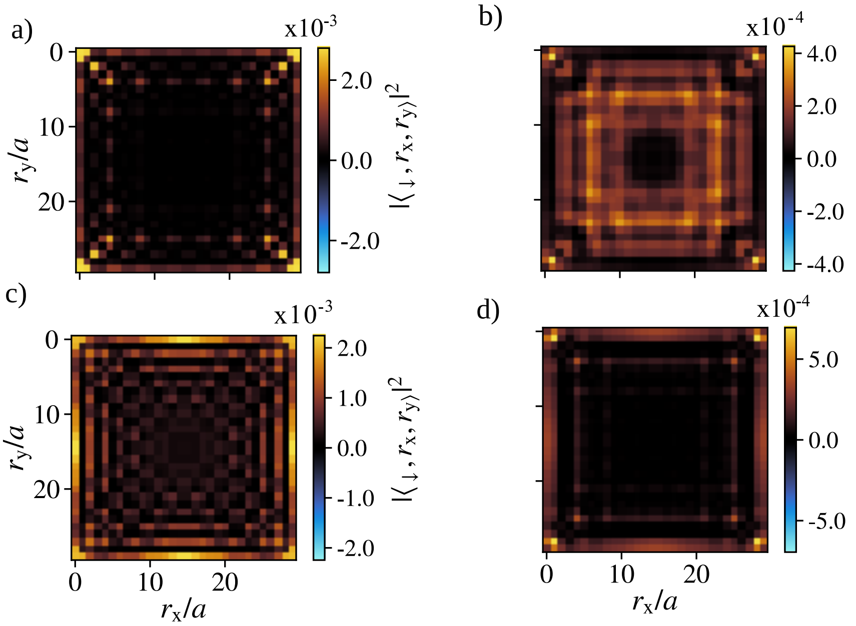

Figure III.17.: Real space distribution of the edge states in the topological s-wave superconductor. Further descriptions are given in the main text. Subfigures a) and b) correspond to the trivial phase and c), d) correspond to the topological non-trivial state.

distributed along the edge and most conspicuous at the corners, the ↑-spin is rather spread allover the system.

The parameter set corresponding to a topological bulk phase is depicted in Figure III.17 c) and d), where the edge states are mainly distributed across the edge for both ↑- and ↓-spin. However, the expectation value for the ↓-spin reaches further into the bulk whereas the ↑-spin expectation value is distributed closer along the edge. A square like-pattern in the distribution of the edge modes can be identified. This pattern can also be recognized in the real space spin-textures given in Figure III.18.

The spin-textures for open boundary conditions are given in Figure III.18 showing that the vortex and antivortex texture in momentum space is maintained such as for the QWZ-model. In contrast to the topological two-band model, the topological character of the spin-texture corresponds to a trivial skyrmion number for every finite system due to the fragility of the meron like spin-texture. At any finite size system, the s_z expectation value is different to zero at the vortex cores such that the component $S_z(\boldsymbol{k}_t)$ of the normalized spin points onto the north pole at every $\boldsymbol{k}_t$. This is in clear contrast to the dependence of the topological character of the spin-texture as a function of the systems size in the QWZ-model where the non-trivial character can be stable against the effects of the finite size for sufficiently large systems.

The corresponding spin-textures in real space are given in Figure III.18 c) and d). The real space spin-texture has a non-zero spin-expectation value in the in-plane spin components while the overall in-plane spin-expectation value sums up to zero. So for the topological s-wave superconductor, the real space spin-texture is complicated, however at the edge of the system, the

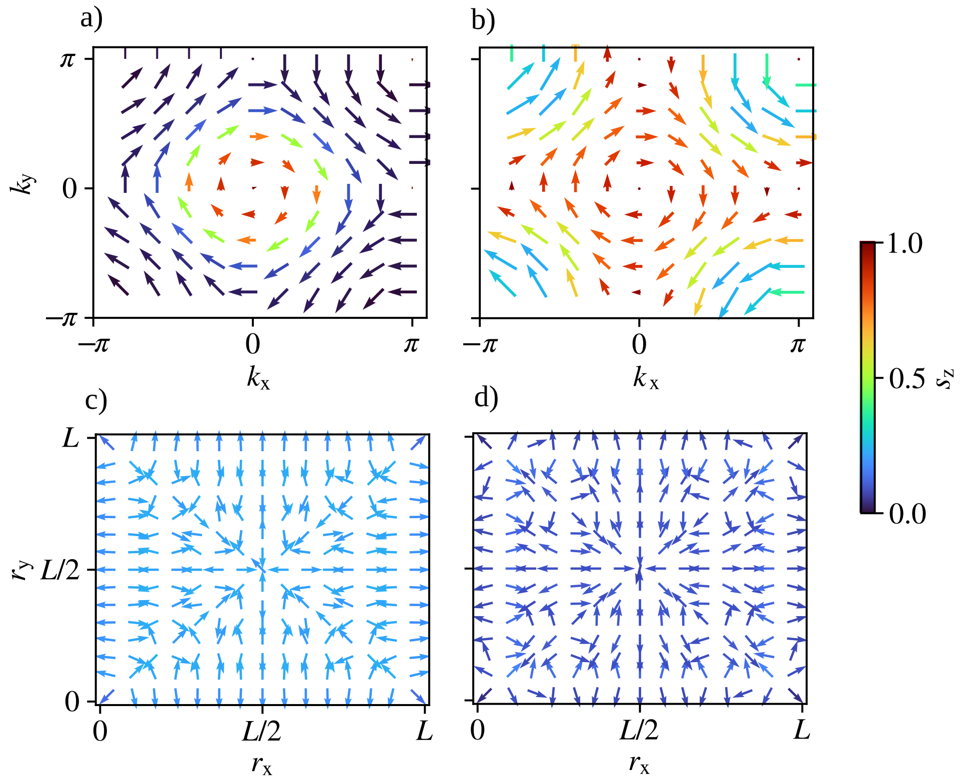

Figure III.18.: Spin textures obtained from the real space calculations in the topological s-wave superconductor with periodic boundary conditions in a) and c) and for open boundary conditions in b) and d). The shown arrows represent the full normalized spin-vectors in a) and b). The arrows in c) and d) represent the in-plane components of the spin-vectors normalized to unit length. The used parameters are $\alpha_R = 0.5t$, $\Delta_{OP} = 0.5t$, $\mu = -3t$ and $h_z = h_{t,1} + h_{t,1}/2$.

in-plane spin components point towards the edge of the system both in the trivial and topological phase while the spins are more disordered in the trivial phase at the boundary. In the bulk, the in-plane spin direction changes drastically its direction while the spin direction is ordered along linear patterns inside the system. This pattern is similarly obtained for the edge state wave function distribution inside the system given in Figure III.17. Yet, the real space spin-texture is not useful to interpret the non-triviality of the spin-states.

The edge states for the half-open boundary conditions are gapped in the trivial phase, whereas the edge states cross (albeit there is a finite gap due to finite size effects) for the non-trivial setup. For open boundary conditions the gap — as a function of the system size in the topological and the trivial bulk phase — are shown in Figure III.19 b). The corresponding gap for the QWZ-model with open boundary conditions is given in Figure III.19 a). For the topological parameter set, the finite size gap vanishes for increasing system sizes whereas for the trivial phase the finite size gap converges towards a constant value as the system size is enlarged. While the gap is decreasing monotonously as a function of the system size in the QWZ model the gap is

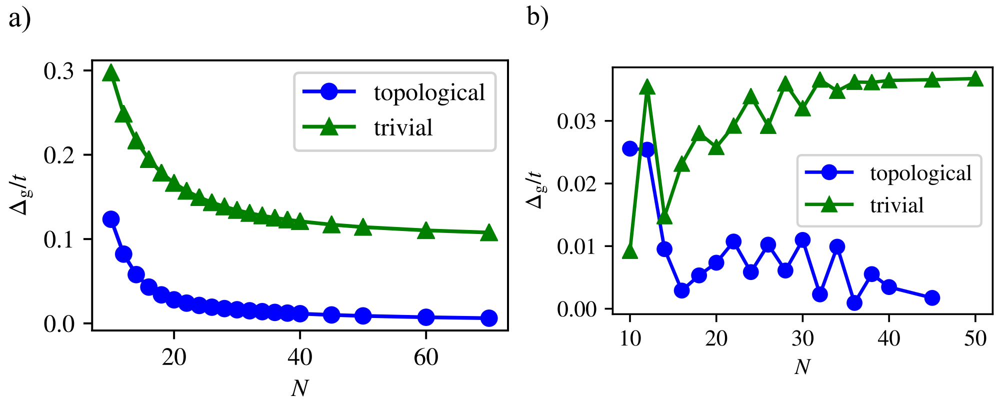

Figure III.19.: Gap as a function of the system size given by $N = N_x = N_y$ for fully open boundary conditions in the QWZ model in a) and in the topological s-wave superconductor in b). The finite size gap vanishes as the system size increases in the non-trivial phases while the gap is finite for the non-trivial phases.

an oscillatory increasing or decreasing function of the system size for the topological s-wave superconductor in the trivial and topological phase, respectively. These results confirm the bulk boundary correspondence. They show however, that chiral edge states exist even in the trivial bulk phase carrying a non-vanishing edge current.

III.4. Extension to higher winding numbers

Tracing the in-plane component of the spin expectation value along a path around the $\boldsymbol{k}_t$, the spin winds around only once in the model used above. In principal, any spin winding $w \in \mathbb{Z}$ is possible. To allow for trivial windings $w = 0$ or higher $|w| > 1$ with linear band crossings at the topological transition, the Hamiltonian used in (II.3.2) is modified. This modified QWZ-model is introduced because the analysis in section IV.3, where thermodynamic signatures of topological phase transitions are analyzed numerically, deals with the uniqueness of thermodynamic signatures for topologically non-trivial phase transitions. It is there of considerable interest whether the analyzed signatures are indeed only non-zero for non-trivial spin-texture transitions. For this purpose, these signatures need to be tested on distinct spin-textures.

In the following, a $\boldsymbol{d}(\boldsymbol{k})$-vector allowing for more general windings is defined for the QWZ-model. In order to obtain the topological band crossings around the momenta $\boldsymbol{k}_t$, points in the Brillouin-zone at which $d_x \propto k_y$ and $d_y \propto k_x$ are constructed. In polar coordinates one has

$$k_x(r, w, \varphi) = r\cos(f(w, \varphi)) \tag{III.4.1}$$

$$k_y(r, w, \varphi) = r\sin(f(w, \varphi)) \tag{III.4.2}$$

$$\varphi(k_x, k_y) = \operatorname{atan2}\left(\frac{k_y}{k_x}\right) \tag{III.4.3}$$

$$r(k_x, k_y) = \sqrt{k_x^2 + k_y^2} \tag{III.4.4}$$

where atan2 is the signed arctangent. In contrast to the regular atan which is defined in the interval $[-\pi/2, \pi/2]$, the atan2 returns the angle in $[-\pi, \pi]$. The $\boldsymbol{d}$-vector in (II.3.3) is replaced by $(\tilde{d}_{\mathrm{x}}, \lambda\tilde{d}_{\mathrm{y}}, \tilde{d}_{\mathrm{z}})$ with

$$\tilde{d}_{\mathrm{x}} = \alpha_{\mathrm{R}} \cdot r(k_{\mathrm{x}}, k_{\mathrm{y}}) \sin\left(f(w, \varphi(k_{\mathrm{x}}, k_{\mathrm{y}}))\right) \tag{III.4.5}$$

$$\tilde{d}_{\mathrm{y}} = \alpha_{\mathrm{R}} \cdot r(k_{\mathrm{x}}, k_{\mathrm{y}}) \cos\left(f(w, \varphi(k_{\mathrm{x}}, k_{\mathrm{y}}))\right) \tag{III.4.6}$$

$$\tilde{d}_{\mathrm{z}} = h_{\mathrm{z}} - t(\cos(k_{\mathrm{x}}) + \cos(k_{\mathrm{y}})) \tag{III.4.7}$$

introducing the additional parameter $\lambda \in \{-1, 1\}$ which is related to the vorticity $\mathcal{V}$ defined in (III.1.10). The function $f(w, \varphi)$ is constructed such that it is a smooth function fulfilling the condition

$$f(w, 2\pi) = 2w\pi + f(0, 0) \tag{III.4.8}$$

with $w \in \mathbb{N}$ allowing for spin-textures whose in-plane spin projection is not constant along a closed loop around the momenta $\boldsymbol{k}_{\mathrm{t}}$ but with a vanishing total winding. Examples for such functions $f(w, \varphi)$ are $f(1, \varphi) = \sin(\varphi)$ or $f(2, \varphi) = \cos(2\varphi)$. This function generates a class of Hamiltonians which allow for different spin-textures which are either topologically trivial or topologically non-trivial with higher winding numbers. This modified QWZ-model has the following topological phases:

$$N_{\mathrm{C}} = \begin{cases} 0 & \text{for } h_{\mathrm{z}} < h_{\mathrm{t},1} \text{ or } h_{\mathrm{z}} > h_{\mathrm{t},3} \\ -w\lambda & \text{for } h_{\mathrm{z}} > h_{\mathrm{t},1} \text{ and } h_{\mathrm{z}} < h_{\mathrm{t},2} \\ w\lambda & \text{for } h_{\mathrm{z}} > h_{\mathrm{t},2} \text{ and } h_{\mathrm{z}} < h_{\mathrm{t},3} \end{cases} . \tag{III.4.9}$$

The phase boundaries $h_{\mathrm{t}} \in \left\{h^{\mathrm{QWZ}}_{\mathrm{t,z,1}}, h^{\mathrm{QWZ}}_{\mathrm{t,z,2}}, h^{\mathrm{QWZ}}_{\mathrm{t,z,3}}\right\}$ are thus not affected by the modification but the Chern number is determined by the product of the parameters w and λ. Examples for obtained spin-textures using different $f(w, \varphi)$ and λ are depicted in Figure III.20 a) to d). In subfigure a) the spin-texture is non-trivial with $w\lambda = 1$ and corresponds therefore to the regular QWZ-model. The subfigures b) and c) show topological spin-textures with $w\lambda = 2, 3$, respectively. The last subfigure is realized by a spin-texture which is partially like a vortex and partially like an antivortex such that its overall vorticity is $\mathcal{V} = 0$. The positions and numbers of vortex (antivortex) center points is equal to the positions and numbers of the standard QWZ model. The skyrmion number does therefore only depend on the vorticity at each momenta $\boldsymbol{k}_{\mathrm{t}}$. By the evaluation of Equation (III.1.10) the skyrmion numbers can be read off from the spin-textures easily.

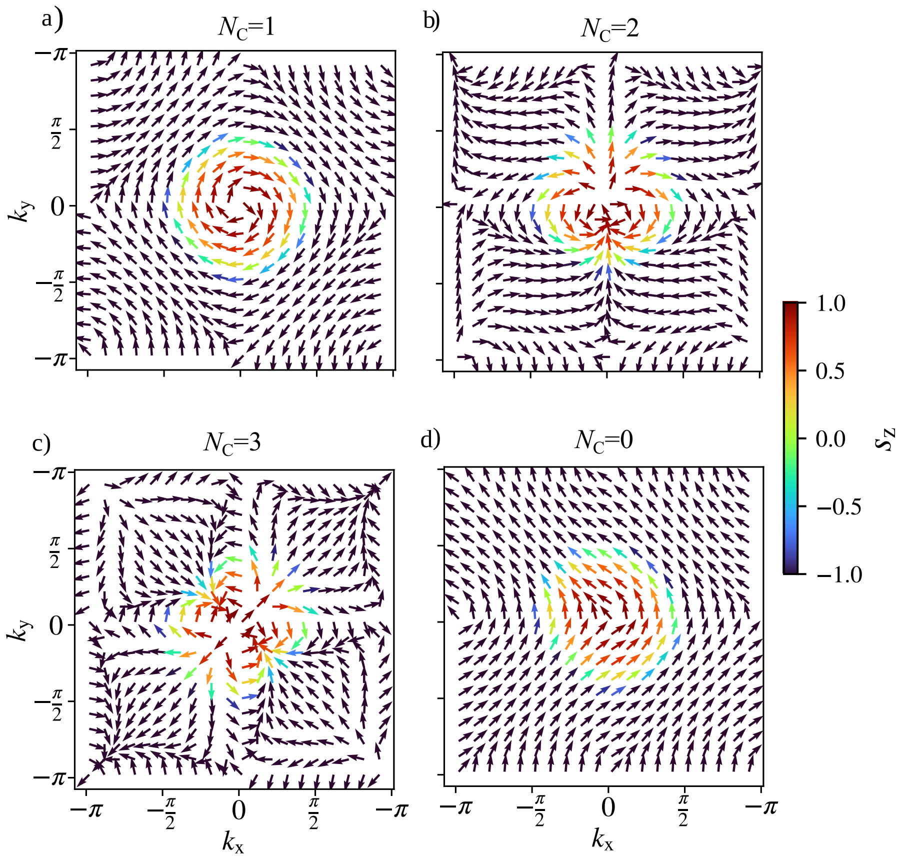

Figure III.20.: Spin-textures for a) $w = 1$, $f(1, \varphi) = \varphi$, b) $w = 2$, $f(2, \varphi) = \varphi$, c) $w = 3$, $f(3, \varphi) = \varphi$, d) $w = 1$, $f(0, \varphi) = \sin(\varphi)$. Other parameters used are $\lambda = 1$, $h_z = 0.5t$, $\alpha_R = 0.5t$. The arrows show the normalized in-plane pseudo-spin components while the color yields the values of the z-components of the normalized spin. The corresponding values for N_C are given in the figure.

III.5. Spin textures in other topological superconductors

Combinations of singlet and triplet pairings are possible in two-dimensional superconducting systems [86, 87]. Moreover, the realization of topological p-wave superconductors have been proposed due to proximity effects of s-wave pairing on the surface of topological insulators [88] or due to the placement of magnetic moments on regular s-wave superconductors [89]. The topological p-wave superconductor is therefore a promising candidate for the realization of non-trivial topology in superconductors and is claimed to be realized in Strontium Ruthenate (Sr_2RuO_4) for example [90]. The admixture of singlet and $p_x + \mathrm{i}p_y$ triplet pairing — the $p_x + \mathrm{i}p_y$ is itself topologically non-trivial in terms of Berry phase analysis — affects the topological spin-texture or the non-trivial Berry phase. In the following, the spin-textures for an s-wave superconductor with the admixture of $p_x + ip_y$ pairing is discussed.

Only on-site interactions do not support triplet pairing [91] and thus the consideration of extended s-wave pairing [92] is required. The following Hamiltonian incorporates all of the above addressed superconducting pairings. It is given in matrix form by

$$\mathcal{H}^{\mathrm{SCs}} = \begin{pmatrix} \epsilon(\boldsymbol{k}) + h_{\mathrm{z}} & \alpha_{\mathrm{R}}(\boldsymbol{k}) & \Delta_1^{\mathrm{t}}(\boldsymbol{k}) & \Delta^{\mathrm{s}}(\boldsymbol{k}) \\ \alpha_{\mathrm{R}}{}^*(\boldsymbol{k}) & \epsilon(\boldsymbol{k}) - h_{\mathrm{z}} & -\Delta^{\mathrm{s}}(\boldsymbol{k}) & -\Delta^{\mathrm{t}*}(\boldsymbol{k}) \\ \Delta^{\mathrm{t}*} & -\Delta^{\mathrm{s}*}(\boldsymbol{k}) & -\epsilon(\boldsymbol{k}) - h_{\mathrm{z}} & \alpha_{\mathrm{R}}{}^*(\boldsymbol{k}) \\ \Delta^{\mathrm{s}*}(\boldsymbol{k}) & -\Delta^{\mathrm{t}}(\boldsymbol{k}) & \alpha_{\mathrm{R}}(\boldsymbol{k}) & -\epsilon(\boldsymbol{k}) + h_{\mathrm{z}} \end{pmatrix} \tag{III.5.1}$$

with

$$\Delta^{\mathrm{s}} = \left(\Delta_1^{\mathrm{s}} + \Delta_2^{\mathrm{s}}(\cos(k_{\mathrm{x}}) + \cos(k_{\mathrm{y}}))\right) \tag{III.5.2}$$

$$\Delta^{\mathrm{t}} = \Delta_1^{\mathrm{t}}(\sin(k_{\mathrm{y}}) + \mathrm{i}\sin(k_{\mathrm{x}})). \tag{III.5.3}$$

Choosing $\Delta_1^{\mathrm{s}} \neq 0$ and $\Delta_2^{\mathrm{s}}, \Delta_1^{\mathrm{t}} = 0$ yields the topological s-wave superconductor described above. For all pairings the spin expectation value is calculated using Equation (III.1.14) while self-consistency is dispensed. At first, the extended s-wave superconductor is analyzed. Correspondingly, the s-wave pairing amplitudes are set to $\Delta_1^{\mathrm{s}}, \Delta_2^{\mathrm{s}} \neq 0$ while the triplet pairing is zero. The obtained phase diagram includes the same Berry phases as the topological s-wave superconductor discussed above. The phase diagram is given in Figure III.21.

The phase boundaries are shifted for extended topological s-wave superconductivity and, as shown in Figure III.21, the topology of the spin-texture is retained when compared to exclusive on-site pairing. Thus, the discussed analysis described above and in the following also applies for the extended topological s-wave superconductor and it is therefore sufficient to analyze the simplified situation of pure on-site singlet pairing.

For the inclusion of $p_{\mathrm{x}} + \mathrm{i}p_{\mathrm{y}}$ triplet pairing $\Delta_2^{\mathrm{s}}, \Delta_1^{\mathrm{s}}, \Delta_1^{\mathrm{r}} \neq 0$ is set. The inclusion of the triplet pairing requires the consideration of a model allowing for finite range pairing interactions. The situation at which the triplet pairing is small compared to the s-wave pairing is considered. As shown in Figure III.22, the topological s-wave superconductor with the admixture of $p_{\mathrm{x}} + \mathrm{i}p_{\mathrm{y}}$ triplet pairing has a similar topological phase diagram with the distinct phases characterized by $N_{\mathrm{C}} \in \{-2, -1, 0, 1\}$. The different spin-textures related to the different Chern numbers are displayed in the figure. One can see that the spin-textures are very different in this case.

In the trivial and in the non-trivial phase with $N_{\mathrm{C}} = 1$, vortices are located at the Γ-point, the X and the Y point while antivortices are found at the M-point and in between the Γ-point and the X-point. There are thus three vortices and three antivortices found. Applying Equation (III.1.10) shows that the phase with $N_{\mathrm{C}} = 1$ corresponds to the phase with $N_{\mathrm{S}} = -1$. In the non-trivial phase with $N_{\mathrm{C}} = -1$, there are vortices at the Γ-point and in between the Y and M - point while antivortices are identified at the X-, Y, and M-point. Thus there are also a total number of three vortices and three antivortices identified. The spin-texture corresponds to a skyrmion number $N_{\mathrm{S}} = 1$. Finally, the spin-texture corresponding to the phase with $N_{\mathrm{C}} = -2$ exhibits vortices in between the Y and M-point and in between the Γ- and Y-point and antivortices at the Γ-, X-, Y- and M-point. Therefore there are four vortices and four antivortices identified. The application of Equation (III.1.10) yields $N_{\mathrm{S}} = 2$. There are additional vortex-antivortex pairs found and the total number of vortices and antivortices is dependent on distinct topological phases. Moreover, at the topological transitions lines, the type of vorticity can change form a vortex to an antivortex at the Γ, X-, Y- or M-point. During such a vorticity change, vortex-antivortex pairs unite or new

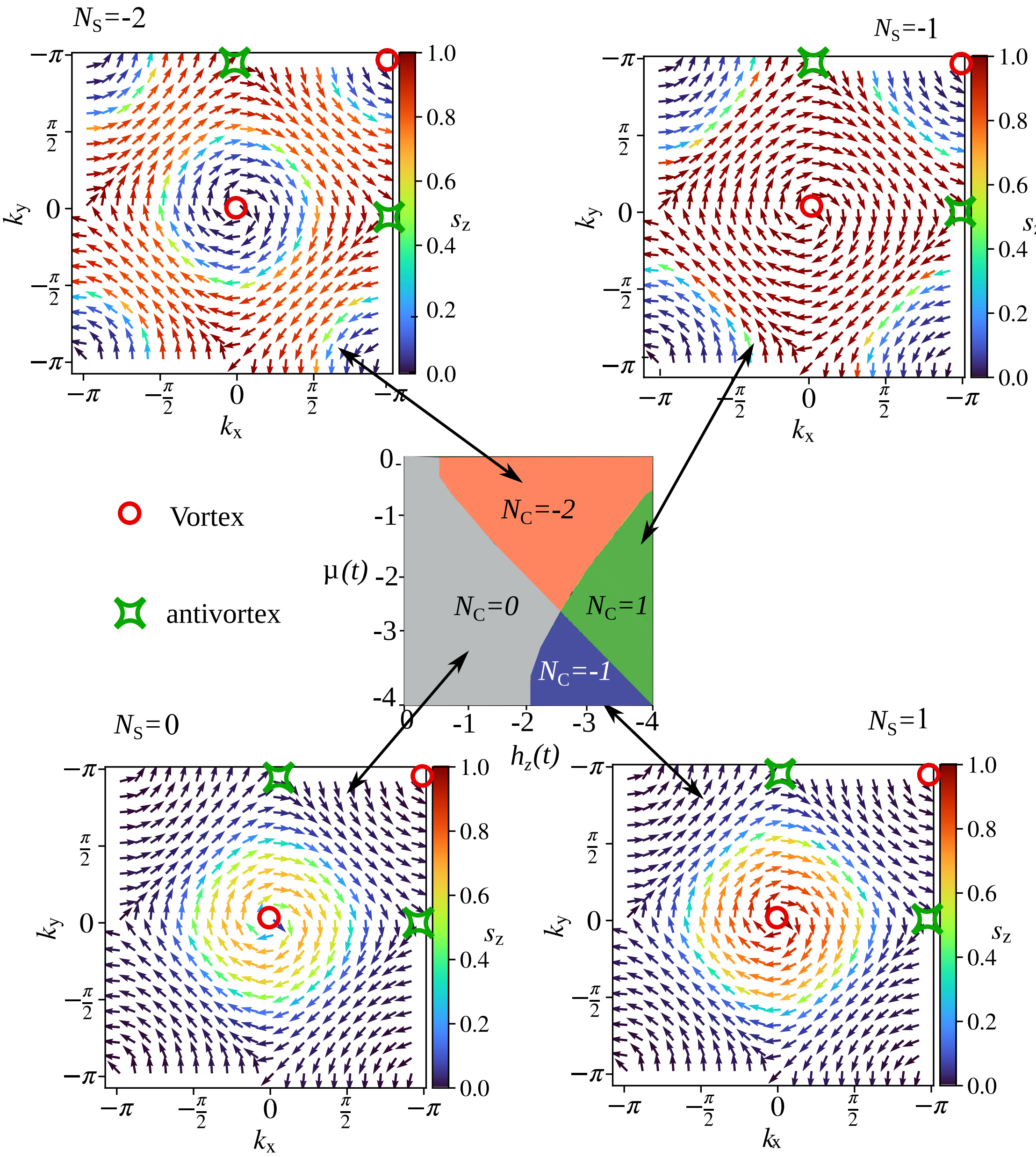

Figure III.21.: Topological phase diagram and the corresponding spin-textures for the topological extended s-wave superconductor. The parameters $\alpha_R = 0.5t$, $\Delta_1^s = 0.5t$, $\Delta_2^s = 0.1t$ and $\Delta_1^t = 0$ are used.

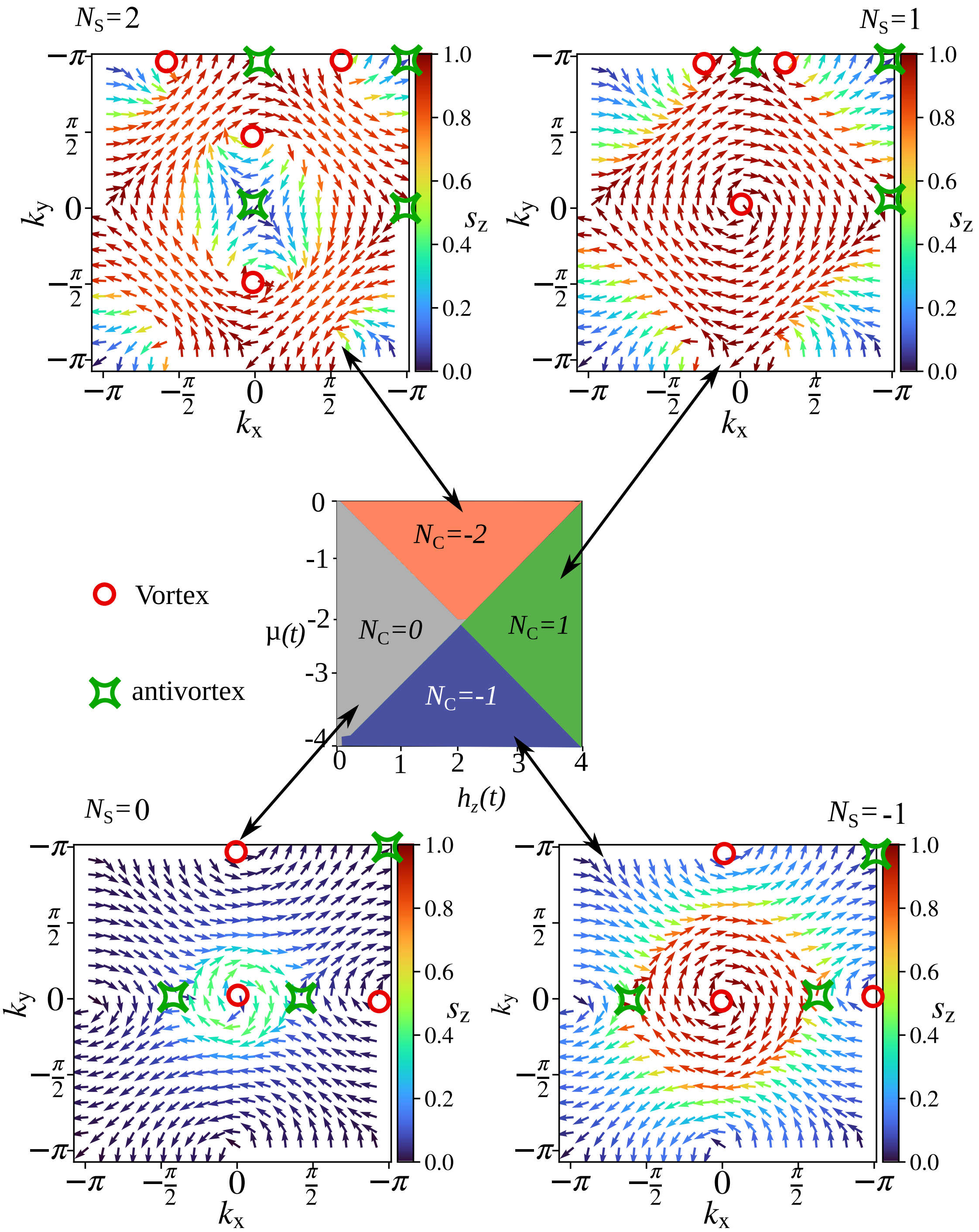

Figure III.22.: Topological phase diagram and the corresponding spin-textures for the topological s- plus p-wave superconductor. The parameters $\alpha_R = 0.5t$, $\Delta_1^s = 0.4t$, $\Delta_2^s = 0.08t$ and $\Delta_1^t = 0.1t$ are used.

vortex-antivortex pairs form. However, the skyrmion number is still related to the Chern number in the topological s- plus p-wave superconductor. The triplet pairing amplitude has been chosen smaller than the s-wave pairing amplitude in these results. The situation might be different in the case of a dominant triplet pairing. In this case Equation (III.1.10) may not apply and the topology may not be describable by a topological spin-texture. This situation has not been analyzed yet and further investigations are required here.

IV. Thermodynamic signatures at topological phase transitions

IV.1. Thermodynamic signatures of topological phase transitions in homogeneous magnetic fields

Thermodynamic signatures of topological phase transitions have been investigated many times [93–96] and, by the use of Hill thermodynamics, contributions of topological edge states in finite-size systems are taken into account in the thermodynamic observables [93, 94], resulting in a linear contribution to the heat capacity. In 1960 I. M. Lifshitz described "anomalies of thermodynamic quantities" [17] when electron bands are depleted or new bands enter the Fermi level such that the Fermi surface topology is changed. The terminology 'Fermi-surface topology' is to be clearly distinguished from topology used in the context of Berry phase and skyrmion numbers. The sudden qualitative change in the Fermi surface are accompanied by the occurrence of critical points $\boldsymbol{k}_{\mathrm{L}}$ at which $\nabla_{\boldsymbol{k}}\epsilon_n(\boldsymbol{k}) = 0$ in the Brillouin zone. These have consequences for example on thermodynamic quantities. Then, the change in the density of states — as a function of some parameter which drives this so-called Lifshitz transition — translates into a kink in first derivative of the thermodynamic potential with respect to the parameter driving the Fermi surface transition. The Lifshitz transition is only a ground state phenomenon, however finite temperature signatures survive which can be related to the zero temperature transition. At finite temperature, the kink is broadened but may still be visible as a peak in the third derivative of the thermodynamic potential [95, 97–99]. It has been observed experimentally and related to topological phase transitions several times [93–96]. However, the observation of a Lifshitz is not sufficient to conclude topological phase transitions in general. So, a topological phase transition needs to be accompanied by a Lifshitz transition but the reverse does not apply. A topological phase transition is automatically accompanied by a Fermi surface change. Such a Fermi surface change does however not need to be non-trivial in terms of Berry phase or spin textures in general.

Topological fermionic systems are usually described by non-trivial spin textures or Chern numbers. Using the concept of Uhlmann numbers which defines geometric phases on mixed states at finite temperature [100] different topological phases have been investigated [58, 101, 102]. The Uhlmann numbers can be viewed as the finite temperature extension of the Chern numbers. However, the Uhlmann numbers are not topological invariants as they are not always integer valued [103]. They have a physical meaning as they are related to the dynamical susceptibility and conductivity [103].

Within this thesis, thermodynamic quantities close to topological phase transitions are investigated. While the Lifshitz transition is related to the Fermi surface structure of the corresponding normal conducting phase, here the thermodynamic signatures tied to spin-texture changes across topological phase transitions are analyzed. These are visible in the change of the magnetization as a response to a change of the temperature as discussed in section IV.2 or as a response to in-plane magnetic field gradients discussed in section IV.3.

From the thermodynamic potential given in (II.2.16) and (II.3.11) for the superconductor and the QWZ model, respectively, three important thermodynamic quantities, analyzed within this thesis are obtained; these are

$$S = -\left.\frac{\partial\Omega}{\partial T}\right|_{\mathcal{V},\mu,H} \tag{IV.1.1}$$

$$N = -\left.\frac{\partial\Omega}{\partial \mu}\right|_{\mathcal{V},H,T} \tag{IV.1.2}$$

$$M = -\frac{1}{\mathcal{V}}\left.\frac{\partial\Omega}{\partial H}\right|_{\mathcal{V},\mu,T} \tag{IV.1.3}$$

with S, N, $\mathcal{V}$ and M denoting the entropy, particle number, volume and magnetization, respectively.

IV.2. Spin polarization in homogeneous Zeeman fields

As discussed in Section III.1, the topological spin-textures are qualitatively different for the QWZ model with skyrmion-type spin-textures and the topological s-wave superconductor where the spin-textures are meron-like. Here, both systems are analyzed for their thermodynamic signatures in the vicinity of a topological phase transition related to the non-trivial topological spin-textures in homogeneous static Zeeman splitting fields. The QWZ-model may have a topological pseudo-spin texture and thus the Zeeman splitting field is replaced by a pseudo Zeeman splitting field. In the case of the topological s-wave superconductor, the Zeeman splitting field is realized by a real magnetic field.

QWZ-model

The thermodynamic properties of a system can be described by the thermodynamic potentials which are given by Equation (II.3.11) and (A.3.8) for the QWZ and the superconducting models, respectively. As shown in Equation (III.1.10), the skyrmion number depends on the vorticity $\mathcal{V}(\boldsymbol{k}_\mathrm{t})$ and the spin expectation values $S_\mathrm{z}(\boldsymbol{k}_\mathrm{t})$ at the four different vortex centers $\boldsymbol{k}_\mathrm{t}$. Due to Zeeman splitting, the $S_\mathrm{z}(\boldsymbol{k}_\mathrm{t})$ expectation values change at a topological phase transition while the vortex and antivortex spin-textures remain. The values of $s_\mathrm{z}(\boldsymbol{k}_\mathrm{t})$ at isolated points of the Brillouin zone are not accessible by measurements of thermodynamic quantities. However, the modification of the spin-structure in a sizable region around the momenta $\boldsymbol{k}_\mathrm{t}$ can affect thermodynamic properties and can therefore give rise to signatures of the topological phase transitions. The spin magnetization, which is a direct thermodynamic property of the spin-texture does always take into account the entire spin-texture and not just sizable regions around the momenta $\boldsymbol{k}_\mathrm{t}$ at which the essential topological phase transition take place. Instead, the analysis of the change in the magnetization due to thermal excitations yields signatures which are confined to a sizable region around the band gap minimum. Across the topological phase transitions, the band gap closes and reopens at some of the momenta $\boldsymbol{k}_\mathrm{t}$. Because excitations are particularly pronounced around the band gap minima,

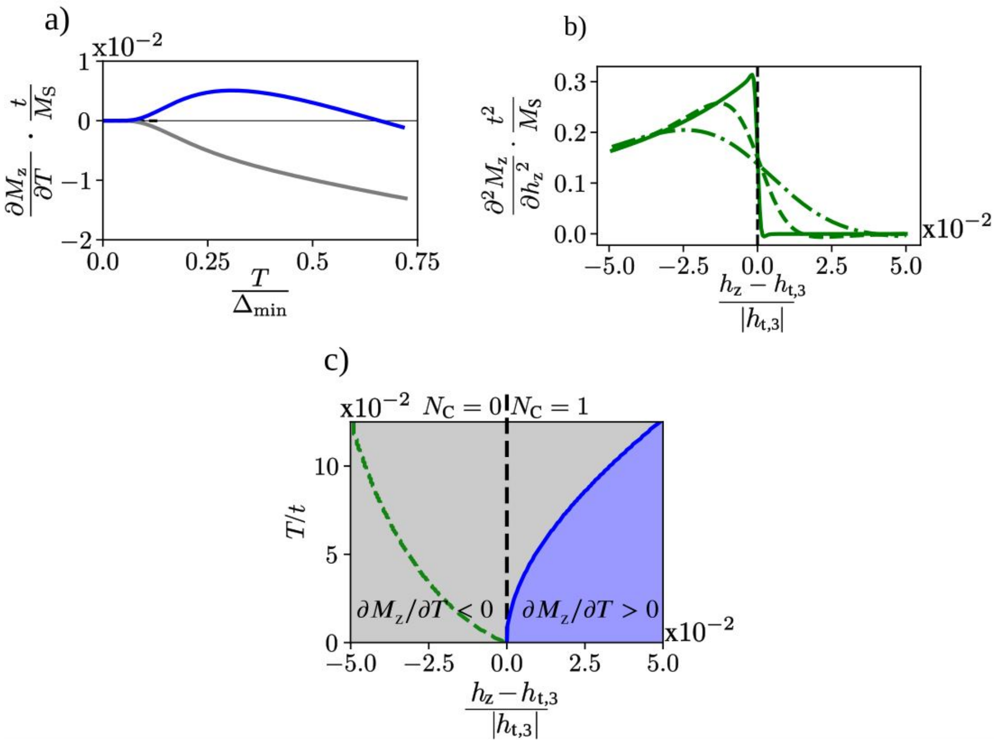

Figure IV.1.: Thermal excitations of the magnetization. a) solid line: $\partial_T M_z$ in blue corresponding to $(h_z - h_{t,3})/h_{t,3} = -4.5 \cdot 10^{-2}$ in the topological phase and in gray corresponding to $(h_z - h_{t,3})/h_t = 4.5 \cdot 10^{-2}$ in the trivial phase. M_S is the saturation magnetization in z-direction. b) $\partial^2 M_z/\partial h_z$ at $T = 0.1 \cdot 10^{-2}t$, $T = 1.3 \cdot 10^{-2}t$ and $T = 3.3 \cdot 10^{-2}t$ for the solid, dashed and dash-dotted lines, respectively. For $T \to 0$ the maxima in $\partial^2 M_z/\partial h_z$ diverge, indicating the Lifshitz transition. c) blue/(gray) filled: $\partial_T M_z >$ 0. In addition $\alpha_R = 1.0t$ is used.

changes in the magnetization due to thermal excitations are thus adequate as a thermodynamic quantity analyzed across topological phase transitions.

Taking the derivative of the magnetization

$$M = -\frac{1}{\mathcal{V}} \left.\frac{\partial \Omega}{\partial H}\right|_{V,\mu,T} \tag{IV.2.1}$$

with respect to the temperature $\partial M/\partial T$ and using the symmetry $\lambda_+(\boldsymbol{k}) = -\lambda_-(\boldsymbol{k})$ yields

$$\begin{aligned}\nabla_{\boldsymbol{h}} \frac{\partial \Omega}{\partial T} = \nabla_{\boldsymbol{h}} S &= \sum_{\boldsymbol{k}} \frac{\boldsymbol{d}(\boldsymbol{k})}{T^2 \cosh^2(\lambda_+(\boldsymbol{k})/2T)} \\ &= \langle \boldsymbol{d} \rangle_{T,\mathrm{E}} \sum_{\boldsymbol{k}} \frac{\cosh^2(\lambda_+(\boldsymbol{k})/2T)}{T^2}\end{aligned} \tag{IV.2.2}$$

where Ω is the grand canonical potential, S is the entropy and $\mathcal{V}$ denotes the volume. The Bloch vector $\boldsymbol{d}(\boldsymbol{k})$ is defined in (II.3.3). The Maxwell relation is used to relate the derivative of the magnetization with respect to T to the derivative of the entropy with respect to the magnetic field. Here, it is defined

$$\langle \boldsymbol{h} \rangle_T = \frac{\sum_{\boldsymbol{k}} \boldsymbol{d}(\boldsymbol{k}) \cosh^{-2}(\lambda_+(\boldsymbol{k})/2T)}{\sum_{\boldsymbol{k}} \cosh^{-2}(\lambda_+(\boldsymbol{k})/2T)} \tag{IV.2.3}$$

which is the mean thermal polarization excitation. The function $\cosh^{-2}(\lambda_+(\boldsymbol{k})/(2T))/T^2$ in (IV.2.2) has a peak around $\boldsymbol{k}_{\rm min}$ and one can define a cut-off $\boldsymbol{k}_{\rm c}$ in the Brillouin zone by

$$\delta\lambda_1(\boldsymbol{k}_{\rm c}) = 2T \operatorname{arccosh}\left(\sqrt{2}\cosh\left(\frac{\lambda_{\rm min}}{2T}\right)\right) - \lambda_{\rm min}, \tag{IV.2.4}$$

where $\lambda_+(\boldsymbol{k}) = \lambda_{\rm min} + \delta\lambda_+(\boldsymbol{k})$ is used while the notation $\lambda_{\rm min} = \lambda_+(\boldsymbol{k}_{\rm min})$ is introduced. One has $\delta\lambda_+(\boldsymbol{k}_{\rm c}) \to 0$ for $T \to 0$. It can thus be concluded that a finite temperature range exists for which the Bloch vector $\boldsymbol{d}(\boldsymbol{k})$ does not change significantly within the summation in (IV.2.2) which is given by the numerator in (IV.2.2).

Rewriting hence the summation in (IV.2.2) as an integral while approximating $\cosh^{-2}(\lambda_+(\boldsymbol{k})/(2T))$ by a constant up to the cutoff and taking $\boldsymbol{d}(\boldsymbol{k}) \approx \boldsymbol{d}(\boldsymbol{k}_{\rm min})$ yield

$$\langle h \rangle_T = c(T, \lambda_{\rm min})\boldsymbol{d}(\boldsymbol{k}_{\rm min}) \tag{IV.2.5}$$

with $c(T, \lambda_{\rm min})$ being a constant for fixed temperature T and $\lambda_{\rm min}$. Within this approximation $\langle h \rangle_T$ does only depend on T through $c(T, \lambda_{\rm min})$. The obtained vector in (IV.2.5) is therefore, at a given temperature and band gap minimum, proportional to the $\boldsymbol{d}$-vector at $\boldsymbol{k}_{\rm min}$. For higher temperatures or for band structures without distinct gap minima, Equation (IV.2.2) yields the average thermal polarization excitation of the spins $\boldsymbol{s}$ taking into account a broad region of k-values as depicted in Figure III.9. As the spin-texture changes across a topological phase transition, a region around the gap closing point in momentum space exists which induced a sign reversal of $\partial_T M_{\rm z}$ shown in Figure IV.1 c). The change in the magnetization with respect to the temperature as a function of T is shown in Figure IV.1 a). In the topological phase $\partial_T M_{\rm z} > 0$ up to a certain temperature T^*. Thus, as expected, $\partial_T M_{\rm z}$ changes its sign across the topological phase transition in the low temperature regime. According to Equation (IV.2.2), this sign change in the derivative of the magnetization as a function of the temperature is equivalent to a maximum of the entropy as a function of the magnetic field. At $T = 0$, $s_{\rm z}(\boldsymbol{0}) = 0$ for magnetic fields $h_{\rm z} < h_{\rm t,3}$ because the spin expectation values of the chiral spin split bands compensate each other. However, $s_{\rm z}$ turns into a maximum if $h_{\rm z}$ is tuned through the topological phase transition (the image in the spin map of the momentum $\boldsymbol{k} = \boldsymbol{0}$ switches from the south to the north pole). Finite temperature excitations have a quantitatively different effect on the $s_{\rm z}(\boldsymbol{k} = 0)$-values in the trivial and the topological phase where $s_{\rm z}(\boldsymbol{k} = 0, T)$ is increasing and decreasing with temperature, respectively. This qualitative difference extends to a finite region around the Γ-point such that the change from the minimum in $s_{\rm z}$ to the maximum is visible as a sign change in $\partial_T M_{\rm z}$.

On the other hand, a topological phase transition is accompanied by a Lifshitz transition [18]. At finite temperatures, the Lifshitz transition is visible as a peak in the third derivative of the thermodynamic potential [97] as shown in Figure IV.1 b). Consequently, the Lifshitz transition may be indicated as a peak in the second derivative of the magnetization with respect $h_{\rm z}$ in the vicinity of $h_{\rm t}$ [104]. Therefore, around a topological phase transition the Lifshitz transition in combination with the sign change in $\partial_T M_z$ should be present in the low temperature regime around the topological phase transitions. The combination of the change in sign($\partial_T M_z$) (Figure IV.1) and the signatures of the Lifshitz transition is shown in Figure IV.1 c).

The Lifshitz peak and the sign change in $\partial_T M_z$ are found on different sites of the topological phase transition. This observation may be used to enclose the topological ground state phase transition in between the green dashed and solid blue line in Figure IV.1 c). Both, the Lifshitz transition or the change in sign($\partial_T M_{x,y,z}$) are not enough to conclude a topological phase transition. The Lifshitz transition is not uniquely restricted to non-trivial topological phase transitions [105, 106] and the change in the derivative of the magnetization may be observable even without a gap closing.

As mentioned above, the temperature derivative of the magnetization is, by the Maxwell relation, the same as the derivative of the entropy with respect to the magnetic field. The sign change in $\partial_T M_{\mathrm{x,y,z}}$ is therefore related to a relative maximum in the entropy as a function of the magnetic field. A similar analysis can be carried out for the topological superconductor where additionally the self-consistent calculation of the superconducting order parameter needs to be taken into account.

Topological s-wave superconductor

At first, the thermodynamics of the conventional superconductor is revisited on the level of mean field approximation before the thermodynamics of the topological s-wave superconductor is discussed. The conventional s-wave superconductor has an energy gap, which does not depend on the applied magnetic field until the superconductivity breaks down. The gap is therefore constant as a function of the magnetic field (this is the result in mean field approximation when the coupling of the magnetic field to the electrons momentum is neglected) up to a critical magnetic field at which superconductivity breaks down [107]. At $T = 0$, the magnetization is always vanishing in the superconducting phase because ↑-spin and ↓-spin are paired (known as Cooper pairs) resulting in the vanishing magnetization. With increasing temperature, the magnetization is increasing monotonously until the paramagnetic magnetization of the normal metal is reached at the superconducting transition temperature T_c and the order parameter Δ_{OP} is monotonously decreasing as the temperature increases until Δ_{OP} vanishes at T_c.

Due to Rashba spin-orbit coupling in the topological s-wave superconductor, the magnetization does not vanish in the ground state when a finite Zeeman splitting is applied resulting in a non-zero ground-state spin-texture. Far below the topological transition Zeeman splitting $h_z \ll h_t$, the magnetization is still increasing monotonously as a function of the temperature. Likewise, according to a Maxwell-relation, the entropy is a monotonous function of the magnetic field.

The energy gap in the topological s-wave superconductor Δ_{min} depends on $\boldsymbol{k}$ due to the Rashba spin-orbit coupling but Δ_{min} is not equal to Δ_{OP}. This is discussed in more detail in Reference [48]. As in the QWZ model, at low temperatures $T \ll \Delta_{\mathrm{min}}$, thermal excitations of the spin polarization are restricted to a small neighborhood of the energy gap minima. Thus, information about variations in the $s_z(\boldsymbol{k})$-values in the vicinity of the gap closing points can be obtained similarly. Taking the partial derivative of the magnetization in z-direction with respect to temperature, and

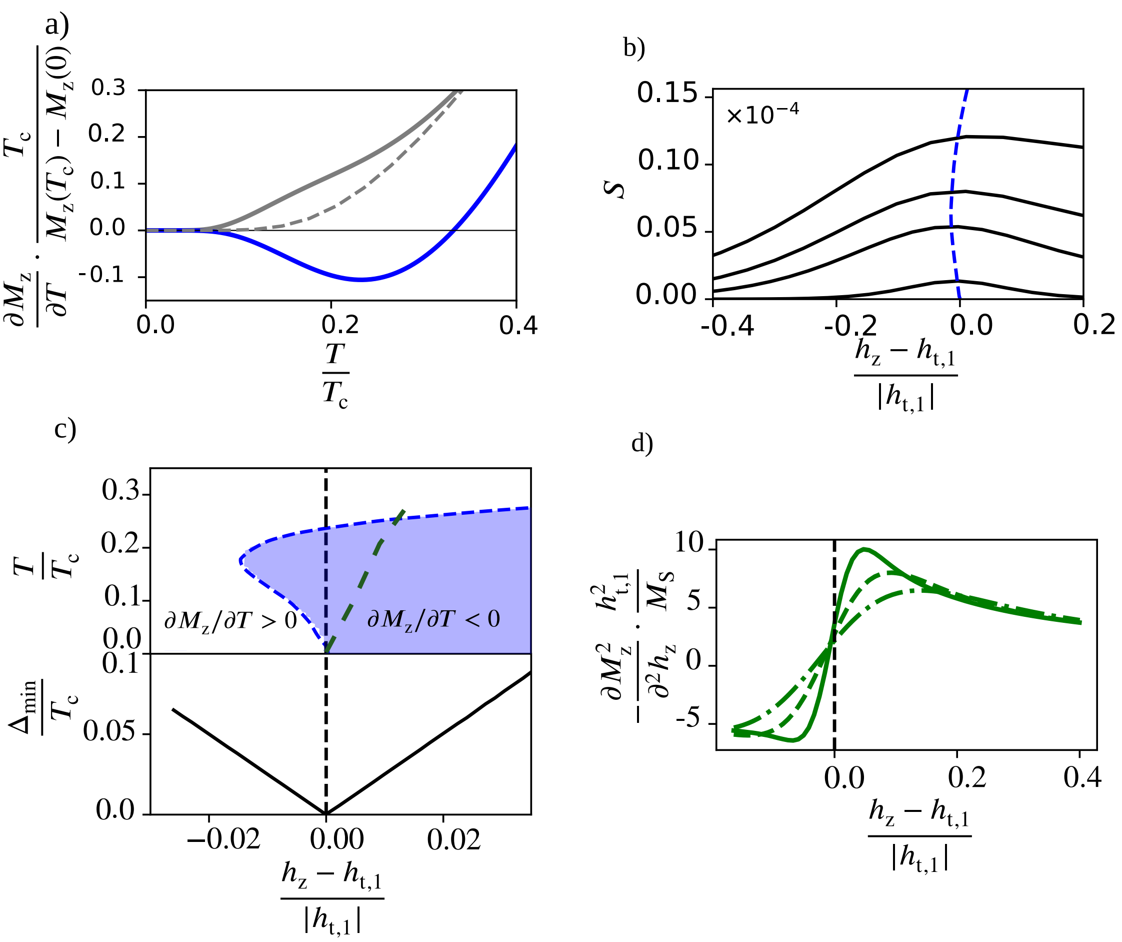

Figure IV.2.: Thermodynamic signatures of topological spin-texture changes in the ground state close to the transition field $h_{t,1}$ obtained from self-consistent calculations. (a) $\partial_T M_z \cdot T_c/(M_z(T_c) - M_z(0))$ while $(M_z(T_c) - M_z(0))$ is positive. The magnetic field values are $(h_z - h_{t,1})/h_{t,1} = 0.19$, $\Delta_{OP}(T = 0) = 0.05t$ (blue curve) and $(h_z - h_{t,1})/h_{t,1} = -0.19$, $\Delta_{OP}(T = 0) = 0.06t$ (gray curve). The dashed gray curve corresponds to a conventional s-wave superconductor without for $\Delta_{OP} = 0.05t$ and $h_z = 0.6\Delta_{OP}$. (b) Entropy S as functions of $(h_z - h_{t,1})/h_{t,1}$ for different temperatures $T/T_c = 0.11, 0.21, 0.23, 0.27$ from bottom to top. The blue dashed line connects the local maxima of $S(h_z, T)$. c) $\partial M_z/\partial T < 0$ (blue area); $\partial M_z/\partial T > 0$ (white area) and minimum gap Δ_{min} as a function of $(h_z - h_{t,1})/h_{t,1}$ (solid black). d) Lifshitz peak in $\partial^2 M_z/\partial h_z^2$ for different temperatures $T/T_c = 0.11, 0.21, 0.23$. Further, $V/t = 1.5$ corresponding to a $T_c \approx 3 \cdot 10^{-2} t$, $n = 0.028$ and $\alpha_R/t = 0.5$ was used.

neglecting contributions further away from the Fermi-level yields

$$-\frac{\partial}{\partial T}\left(\frac{\partial \Omega}{\partial h_{\mathrm{z}}}\bigg|_{T,\mu}\right)\Bigg|_{h_{\mathrm{z}},n} = \frac{\partial M_{\mathrm{z}}}{\partial T}\bigg|_{n,h_{\mathrm{z}}} = \frac{\partial S}{\partial h_{\mathrm{z}}}\bigg|_{n,T} = \frac{1}{N}\int \mathrm{d}^2 k\, \frac{\partial \lambda_3(\boldsymbol{k},\mu)}{\partial h_{\mathrm{z}}} \frac{\lambda_3(\boldsymbol{k},\mu)}{T^2}\, \mathrm{sech}^2\left(\frac{\lambda_3(\boldsymbol{k},\mu)}{2T}\right). \tag{IV.2.6}$$

which is the analogue to the result of the QWZ model given in (IV.2.2). In (IV.2.6), the symmetry $\lambda_2(\boldsymbol{k},\mu) = -\lambda_3(\boldsymbol{k},\mu)$ is used. $T \ll \Delta_{\mathrm{min}}$ is reflected in a peak in $T^{-2}\mathrm{sech}^2(\lambda_3(\boldsymbol{k},\mu)/2T)$ at the gap minimum $\boldsymbol{k}_{\mathrm{min}}$ where $\lambda_3(\boldsymbol{k},\mu)$ is minimal.

Figure IV.2 a) shows $\partial_T M_{\mathrm{z}}$ for $h_{\mathrm{x}} = h_{\mathrm{y}} = 0$ and h_{z} above and below $h_{t,1}$ (see blue and gray line, respectively). In contrast to the conventional s-wave superconductor, $\partial_T M_{\mathrm{z}}$ is non-monotonous and even negative as a function of T for $h_{\mathrm{z}} > h_{\mathrm{t},1}$ and $T \ll T_{\mathrm{c}}$. The temperature scale for non-vanishing $\partial_T M_{\mathrm{z}}$ is set by the band gap minimum which is proportional to $h_{\mathrm{z}} - h_{\mathrm{t},1}$ as shown in Figure IV.2 a). The dependence of $\partial_T M_{\mathrm{z}}$ on T for a superconductor without spin-orbit coupling is given by the dashed gray curve.

At finite temperatures in the regime $T \ll T_{\mathrm{c}}$, the sign change of $\partial_T M_{\mathrm{z}}$ does not occur exactly at the transition field $h_{\mathrm{t},1}$ but in a magnetic field range where the two normal conducting bands are still filled in the vicinity of the Γ-point similar to the situation in the QWZ-model above. The points at which $\partial_T M_{\mathrm{z}} = 0$ (as a function of h_{z} and T) are given by the blue dashed line in Figure IV.2 c). They correspond to the positions of the relative maxima in the entropy in the region with $T \ll \Delta_{\mathrm{min}}$ around $h_{\mathrm{t},1}$ as shown by the blue dashed line in Figure IV.2 b).

In the topological superconductor and the QWZ model signatures of the topological phase transition at finite temperature related to the profound change in the spin-texture exist in particular thermodynamic quantities.

The topological superconductor or the QWZ-model show a characteristic vortex structure of the in-plane spin components at the momenta $\boldsymbol{k}_{\mathrm{t}}$. The out-of-plane spin component at distinct vortex centers flips from zero to one at a critical Zeeman splitting for $T = 0$ and attains a maximum in the topologically non-trivial phase even for $T > 0$. This sudden change manifests itself in a maximum of the entropy as function of magnetic field at constant temperature. Equivalently, it corresponds to a sign change of the derivative of the magnetization with respect to temperature. Other two-dimensional topological systems with non-trivial spin-textures such as the s+p-wave superconductor are candidates for similar investigations close to topological phase transitions.

At this point, in distinction to the discussed thermodynamic quantities, it is pointed out that in topological Chern systems the thermal Hall conductance is a finite temperature transport property which is directly related to the Chern number. However, as for the Hall conductivity, the thermal Hall conductivity is crucially related to the existence of edge modes [108] and does not stem from the bulk which is the case for the thermodynamic signatures discussed above.

IV.3. Magnetic field gradients in the Bloch state basis

A topological spin-texture change leads to the above described thermodynamic signatures. However, like the signatures of a Lifshitz transition, these do not allow in general to infer a topological phase transition. The reason is, that the above quantities only take into account one direction of the spin at a time. Therefore, the information about vorticity and the additional spin expectation

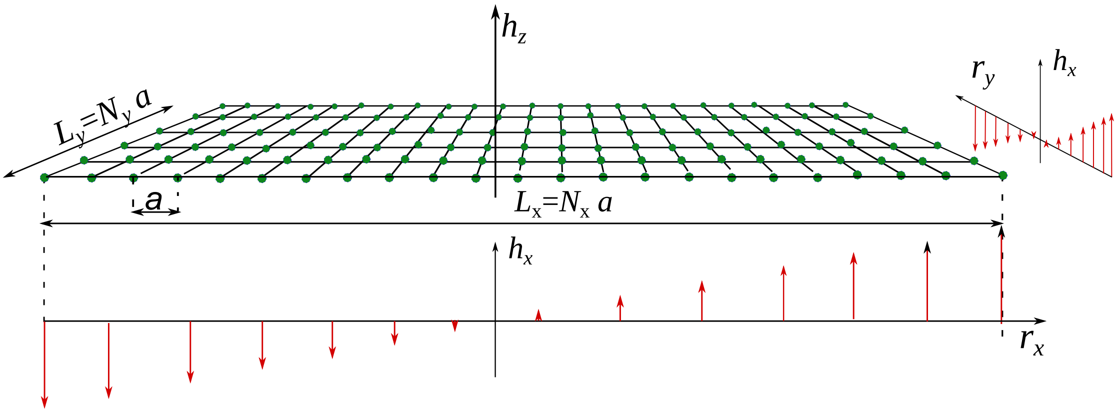

Figure IV.3.: Illustration of the analyzed model setup. The two-dimensional square lattice is exposed to a homogeneous magnetic field in z-direction and to a magnetic field gradient in x- or y-direction. The linear magnetic field gradient is applied such that the net magnetic field is zero.

in z-direction cannot be obtained simultaneously which is however crucial for the topological phases.

It is highly desirable to identify thermodynamic signatures of a topological phase transition, which are bulk properties and which are uniquely related to non-trivial spin-texture transitions. The following sections discuss the possibility for such a thermodynamic quantity.

Linear response theory has shown that the spin-polarization response to an electric field can produce a collective spin magnetization [19, 109, 110] in systems among which possess non-trivial topological spin textures. These magnetization effects are however also not confined to non-trivial spin textures or transitions between them. It seems natural to assume that an in-plane magnetic field gradient does likewise produce a net spin polarization in the out-of-plane component in a two-dimensional system with non-trivial spin-texture topology. However, in-plane magnetic field gradients can provide information about spin polarization in the plane. This leads to the idea, that information about spin vorticity and spin polarizations in z-direction can be accessed by the spin-polarization response to magnetic field gradients in the in-plane components which provide all information about the topological nature of spin textures. The presented work on thermodynamic response quantities clearly suggests that the second order out-of-plane magnetization response to an applied magnetic field gradient linear in both in-plane directions shows thermodynamic signatures connected to non-trivial spin-texture transitions. In this way, the response analysis may be useful for the detection of non-trivial spin-texture transitions.

The discussed setup is sketched in Figure IV.3. The important terms in the spin polarization under consideration are generated by mutually perpendicular magnetic field gradients.

Electrons in a periodic potential (in an infinite lattice) are described by Bloch states. First, an expression for a magnetic field gradient in the Bloch states basis is derived. Without the use of a specific representation basis, the Bloch state can be defined as [111]

$$|\psi_{n,\boldsymbol{k}}\rangle = \mathrm{e}^{\mathrm{i}\boldsymbol{k}\hat{\boldsymbol{r}}}|u_{n,\boldsymbol{k}}\rangle \mathrm{e}^{i\phi_n(\boldsymbol{k})} \tag{IV.3.1}$$

which reads in the position representation

$$\psi_{n,\boldsymbol{k}}(\boldsymbol{r}) = \langle \boldsymbol{r}|\psi_{n,\boldsymbol{k}}\rangle = \mathrm{e}^{\mathrm{i}\boldsymbol{k}\boldsymbol{r}} u_{nk}(\boldsymbol{r}) \tag{IV.3.2}$$

where $\mathrm{e}^{\mathrm{i}\boldsymbol{k}\boldsymbol{r}}$ is a plane wave-part and $u_{nk}(\boldsymbol{r})$ is a lattice-periodic function

$$u_{nk}(\boldsymbol{r}+\boldsymbol{R}) = u_{nk}(\boldsymbol{r}). \tag{IV.3.3}$$

The Bloch-state on the other hand fulfills twisted periodic boundary conditions with respect to a unit cell [112]

$$\psi_{n,\boldsymbol{k}}(\boldsymbol{r}+\boldsymbol{R}) = \mathrm{e}^{\mathrm{i}\boldsymbol{k}\boldsymbol{R}}\psi_{nk}(\boldsymbol{r}). \tag{IV.3.4}$$

However, $\psi_{n,\boldsymbol{k}}(\boldsymbol{r})$ is periodic in the Brillouin zone

$$\psi_{n,\boldsymbol{k}+\boldsymbol{G}}(\boldsymbol{r}) = \psi_{n,\boldsymbol{k}}(\boldsymbol{r}) \tag{IV.3.5}$$

while $\boldsymbol{G}$ denotes a lattice vector in reciprocal space.

Bloch states have been discussed in electric potential gradients many times [19, 111–113]. Here, the coupling of the magnetic field to the spin degree of freedom is added. Specifically, the Bloch states are studied in potentials like

$$\hat{V}_{\mathrm{x}} = \frac{1}{2}\left(\hat{\sigma}_{\mathrm{x}}\hat{r}_{\mathrm{x}} + \hat{r}_{\mathrm{x}}\hat{\sigma}_{\mathrm{x}}\right). \tag{IV.3.6}$$

The position operator can be expressed in the Bloch state basis which was discussed by Blount [111] in much detail. The Bloch states are denoted with $|\psi_{n,\boldsymbol{k}}\rangle$ where n is a band index. Blount showed that the position operator in the Bloch state basis is given by

$$\langle\psi_{n',\boldsymbol{k}'}|\hat{\boldsymbol{r}}|\psi_{n,\boldsymbol{k}}\rangle = -\mathrm{i}\nabla_{\boldsymbol{k}}\delta_{\boldsymbol{k},\boldsymbol{k}'}\delta_{n,n'} + \delta_{\boldsymbol{k},\boldsymbol{k}'}\langle u_{n',\boldsymbol{k}}|\mathrm{i}\nabla_{\boldsymbol{k}}|u_{n,\boldsymbol{k}}\rangle. \tag{IV.3.7}$$

Here, it is important to note that $\nabla_{\boldsymbol{k}}$ acts on the $\delta_{\boldsymbol{k},\boldsymbol{k}'}$-distribution only in the first term in (IV.3.7) but not in the second. One has to notice that the first term in (IV.3.7) grows with the position $\boldsymbol{r}$ [113] and is therefore unbounded. The second term is well behaved since this term is lattice periodic.

In order to analyze the effect of the magnetic field gradients in the Bloch state representation, it is necessary to find the representation of the product of the spin-operator $\hat{\boldsymbol{\sigma}}$ and the position operator $\hat{\boldsymbol{r}}$. It is shown in Appendix A.4 that the matrix elements of the operator $\hat{\boldsymbol{\sigma}}\hat{\boldsymbol{r}}$ are given by

$$\langle\psi_{n',\boldsymbol{k}'}|\hat{\boldsymbol{\sigma}}\hat{\boldsymbol{r}}|\psi_{n,\boldsymbol{k}}\rangle = \sum_{n''}\langle u_{n',\boldsymbol{k}'}|\hat{\boldsymbol{\sigma}}|u_{n'',\boldsymbol{k}'}\rangle\left(-\mathrm{i}\nabla_{\boldsymbol{k}}\delta_{\boldsymbol{k},\boldsymbol{k}'}\delta_{n'',n} + \delta_{\boldsymbol{k}',\boldsymbol{k}}\langle u_{n'',\boldsymbol{k}'}|\mathrm{i}\nabla_{\boldsymbol{k}}|u_{n,\boldsymbol{k}}\rangle\right) \tag{IV.3.8}$$

in the Bloch basis where the second term is diagonal in $\boldsymbol{k}$. Hence, quantities like

$$\begin{aligned}\sum_{n}\sum_{n'}\sum_{\boldsymbol{k}}\sum_{\boldsymbol{k}'}&\langle\psi_{n',\boldsymbol{k}'}|\hat{\boldsymbol{\sigma}}\hat{\boldsymbol{r}}|\psi_{n,\boldsymbol{k}}\rangle f_n(\boldsymbol{k})\\ &= \sum_{n}\sum_{n'}\frac{V}{4\pi^2}\int \mathrm{d}^2k\langle u_{n',\boldsymbol{k}}|\hat{\boldsymbol{\sigma}}|u_{n,\boldsymbol{k}}\rangle\langle u_{n,\boldsymbol{k}}|\mathrm{i}\left(\nabla_{\boldsymbol{k}}|u_{n,\boldsymbol{k}}\rangle\right) f_n(\boldsymbol{k}).\end{aligned} \tag{IV.3.9}$$

can be evaluated showing that the contribution from the first term in (A.4.40) which are related to momentum space surface contributions vanish as long as $f_n(\boldsymbol{k})$ is a periodic function which has no discontinuities. Even if one allows for isolated point-like discontinuities in $f_n(\boldsymbol{k})$, they would not affect the result as long as $f_n(\boldsymbol{k})$ is not divergent at those points. The matrix elements of the product of the spin and the position operator are thus determined by

$$\sum_{\boldsymbol{k}} \sum_{\boldsymbol{k}'} \langle \psi_{n',\boldsymbol{k}'} | \hat{\boldsymbol{\sigma}} \hat{\boldsymbol{r}} | \psi_{n,\boldsymbol{k}} \rangle f_n(\boldsymbol{k}) \approx \frac{\mathcal{V}}{4\pi^2} \int \mathrm{d}^2 k \sum_{n''} \langle u_{n',\boldsymbol{k}} | \hat{\boldsymbol{\sigma}} | u_{n'',\boldsymbol{k}} \rangle \langle u_{n'',\boldsymbol{k}} | \mathrm{i} \left(\nabla_{\boldsymbol{k}} | u_{n,\boldsymbol{k}} \rangle \right) f_n(\boldsymbol{k}). \tag{IV.3.10}$$

IV.4. Perturbation theory up to second order in magnetic field gradients

In the following, the representation of the position operator in the Bloch basis is discussed for tight binding Hamiltonians. The Bravais-lattice vectors, specifying the unit cell, are denoted as $\boldsymbol{\eta}$. Within a unit cell, localized atomic states located at position $\boldsymbol{R} + \boldsymbol{\eta}$ are defined where $\boldsymbol{\eta}$ accounts for the position of other atoms in the same unit cell. The different atoms are indexed by μ and different orbitals (e.g. s, p or d) by α and spin with σ. The localized atomic wave functions are denoted in position space $\varphi_{\mu,\alpha,\sigma}(\boldsymbol{r} - \boldsymbol{R} - \boldsymbol{\eta}_\mu)$ with $\boldsymbol{r}$ being the position vector. These definitions are based on the presentation in Reference [112]. Summarizing the orbital and spin by one single index j, the atomic wave function is written as $\varphi_{\mu,\alpha,\sigma}(\boldsymbol{r} - \boldsymbol{R} - \boldsymbol{\eta}_\mu) =: \phi_{\boldsymbol{R},j,\mu}(\boldsymbol{r})$. The atomic wave functions are orthonormalized

$$\langle \phi_{\boldsymbol{R},i,\mu} | \phi_{\boldsymbol{R}',j,\nu} \rangle = \delta_{i,j} \delta_{\mu,\nu} \delta_{\boldsymbol{R},\boldsymbol{R}'}. \tag{IV.4.1}$$

Additionally, it is assumed that the position matrix is diagonal in the $|\phi_{\boldsymbol{R},j,\mu}\rangle$-space

$$\langle \phi_{\boldsymbol{R},i,\mu} | \hat{\boldsymbol{r}} | \phi_{\boldsymbol{R}',j,\nu} \rangle = \left(\boldsymbol{R} + \boldsymbol{\tau}_\mu \right) \delta_{i,j} \delta_{\mu,\nu} \delta_{\boldsymbol{R},\boldsymbol{R}'} \tag{IV.4.2}$$

Here it is noted that this assumption is not always fulfilled, the position operator is not diagonal in the atomic wave function representation in sp-orbitals [114] for example. In such case, $|\phi_{\boldsymbol{R},j,\mu}\rangle$ denote some other wave functions where the position operator is diagonal. However, in tight binding descriptions, a systems that couple to external magnetic fields or systems containing spin-orbit coupling, the position operator has to be diagonal in the position space basis which is discussed in [115] corroborating the use of (IV.4.2). A tight binding Hamiltonian with matrix elements defined as

$$H_{i,j,\nu,\mu}(\tilde{\boldsymbol{R}}) := \langle \phi_{\boldsymbol{R}',i,\mu} | H | \phi_{\boldsymbol{R}'+\tilde{\boldsymbol{R}},j,\mu} \rangle \tag{IV.4.3}$$

is introduced. In second quantization, the corresponding Hamiltonian reads

$$H = \sum_i \sum_j \sum_{\boldsymbol{R}'} \sum_{\tilde{\boldsymbol{R}}} \sum_\mu \sum_\nu \hat{c}^\dagger_{\boldsymbol{R}',i,\nu} H_{i,j,\nu,\mu}(\boldsymbol{R}', \tilde{\boldsymbol{R}}) \hat{c}_{\boldsymbol{R}'+\tilde{\boldsymbol{R}},j,\mu} \tag{IV.4.4}$$

while $\hat{c}_{\boldsymbol{R}',j,\nu}$ and $\hat{c}^\dagger_{\boldsymbol{R}',j,\nu}$ are the annihilation and creation operators of a state $|\phi_{\boldsymbol{R}',j,\nu}\rangle$, respectively. Since the matrix defined by the matrix elements given in (IV.4.3) is not diagonal in the atomic orbital space with respect to $\boldsymbol{R} + \boldsymbol{\eta}_\mu$, the Fourier transformed basis functions are given by [112]

$$|\chi_{\boldsymbol{k},i,\mu}\rangle = \frac{1}{\sqrt{N}} \sum_{\boldsymbol{R}} \mathrm{e}^{\mathrm{i}\boldsymbol{k}(\boldsymbol{R}+\boldsymbol{\eta}_\mu)} |\phi_{\boldsymbol{R},i,\mu}\rangle \tag{IV.4.5}$$

which is the common procedure in a tight-binding problem in order to block-diagonalize $\boldsymbol{H}$. Subsequently, only systems with one single atom per unit cell are considered. The vectors $\boldsymbol{\eta}$ will therefore not be considered further. However, it is important to mention that the inclusion of additional atoms per unit cell would not affect the results described below. The matrix elements of the Hamiltonian $\boldsymbol{H}$ in the $|\chi_{\boldsymbol{k},i,\mu}\rangle$-basis are defined as

$$\mathcal{H}_{i,j,\mu,\nu}(\boldsymbol{k}) := \langle \chi_{\boldsymbol{k},i,\mu} | \boldsymbol{H} | \chi_{\boldsymbol{k},j,\nu}\rangle. \tag{IV.4.6}$$

So in a regular tight-binding problem, the Hamiltonian $\boldsymbol{H}$ is usually expressed in terms of the Fourier-transformed basis functions $|\chi_{\boldsymbol{k},i,\mu}\rangle$. The expansion of the Bloch states in terms of these Fourier-transformed atomic basis functions reads

$$|\psi_{n,\boldsymbol{k}}\rangle = \sum_{\mu} \sum_{j} C_{n,\boldsymbol{k},j,\mu} |\chi_{\boldsymbol{k},j,\mu}\rangle. \tag{IV.4.7}$$

The eigenvalue equation then becomes in terms of the Fourier transformed atomic basis functions after the projection onto a state $\langle \chi_{\boldsymbol{k},i,\nu}|$

$$\sum_{j} \sum_{\mu} \mathcal{H}_{i,j,\nu,\mu}(k) C_{n,\boldsymbol{k},j,\mu} = E_{n,\boldsymbol{k}} C_{n,\boldsymbol{k},i,\nu}. \tag{IV.4.8}$$

Thus, the $C_{n,\boldsymbol{k},i,\mu}$ are the elements of the eigenvector of the eigenequation in the $|\chi_{\boldsymbol{k},i,\nu}\rangle$-basis (IV.4.8). In the next step, the matrix-elements of the position operator in the Bloch-state basis are expressed in terms of the Fourier-transformed basis states (IV.4.5). In Appendix A.5, it is shown that the second term of the position operator given in (IV.3.7) can be expressed in terms of the expansion coefficients of the Bloch states

$$\langle \psi_{n',\boldsymbol{k}} | \mathrm{e}^{\mathrm{i}\boldsymbol{k}\hat{\boldsymbol{r}}} \mathrm{i}\nabla_{\boldsymbol{k}} \mathrm{e}^{-\mathrm{i}\boldsymbol{k}\hat{\boldsymbol{r}}} | \psi_{n,\boldsymbol{k}}\rangle = \langle u_{n',\boldsymbol{k}} | \mathrm{i}\nabla_{\boldsymbol{k}} | u_{n,\boldsymbol{k}}\rangle = \boldsymbol{C}^{\dagger}_{n',\boldsymbol{k}} \mathrm{i}\nabla_{\boldsymbol{k}} \boldsymbol{C}_{n,\boldsymbol{k}}. \tag{IV.4.9}$$

In the discrete tight-binding formalism, the $|u_{n,\boldsymbol{k}}\rangle$ are replaced by the vector $\boldsymbol{C}_{n,\boldsymbol{k}}$ where the elements of the vector are given by $C_{n,\boldsymbol{k},i,\mu}$.

In the following, the subscript V attached to the eigenstates such as $|n\rangle_V$ means that the eigenstate is perturbed by the operator $\hat{V}$. Let the operator $\hat{V}$ (here, the operator is expressed through its matrix elements in the $|\chi_{\boldsymbol{k},i,\mu}\rangle$-basis) be composed of two parts

$$V^{\mathrm{TB}}_{ij,\mu\nu}(\boldsymbol{k}) = V^{\mathrm{TB}}_{1,ij,\mu\nu}(\boldsymbol{k}) + V^{\mathrm{TB}}_{2,ij,\mu\nu}(\boldsymbol{k}) \tag{IV.4.10}$$

$$= \sum_{i} \sum_{j} \sum_{\mu} \sum_{\nu} \langle \chi_{\boldsymbol{k},i,\mu} | (-G_{\mathrm{y}}) \left(\hat{\sigma}_{\mathrm{x}}\hat{r}_{\mathrm{y}} + \hat{r}_{\mathrm{y}}\hat{\sigma}_{\mathrm{x}}\right) + G_{\mathrm{x}} \left(\hat{\sigma}_{\mathrm{y}}\hat{r}_{\mathrm{x}} + \hat{r}_{\mathrm{x}}\hat{\sigma}_{\mathrm{y}}\right) | \chi_{\boldsymbol{k}j,\nu}\rangle. \tag{IV.4.11}$$

This operator corresponds to in-plane magnetic field gradients linear in r_{x} and r_{y}, respectively while G_{x} and G_{y} determine the strength of magnetic field gradient. In the following, the notation

$$|n\rangle := \boldsymbol{C}_{n,\boldsymbol{k}}; \quad \langle n| := \boldsymbol{C}^{\dagger}_{n,\boldsymbol{k}}; \quad E_n := E_{n,\boldsymbol{k}} \tag{IV.4.12}$$

is used where the index $\boldsymbol{k}$ in this abbreviated notation is dropped. One can thus write

$$
{}_{V_1+V_2}\widetilde{\langle n|}O^{\mathrm{TB}}\widetilde{|n\rangle}_{V_1+V_2} - \langle n|O^{\mathrm{TB}}|n\rangle = {}_{V_1}\widetilde{\langle n|}O^{\mathrm{TB}}\widetilde{|n\rangle}_{V_1} + {}_{V_2}\widetilde{\langle n|}O^{\mathrm{TB}}\widetilde{|n\rangle}_{V_2} + {}_{V_1+V_2}\widetilde{\langle n|}O^{\mathrm{TB}}\widetilde{|n\rangle}^{\times}_{V_1+V_2}, \tag{IV.4.13}
$$

where O^{TB} is defined in the $|\chi\rangle$-basis similar as in (A.5.4). The change of the observable due to the external perturbations $\hat{V}_1$ and $\hat{V}_2$ into contributions, which stem separately from perturbations $\hat{V}_1$ and $\hat{V}_2$ and a contribution which contains both $\hat{V}_1$ and $\hat{V}_2$ simultaneously. Here, ${}_{V_1}\widetilde{\langle n|}O^{\mathrm{TB}}\widetilde{|n\rangle}_{V_1}$ denotes the contributions containing exclusively V_1 and likewise denotes ${}_{V_1}\widetilde{\langle n|}O^{\mathrm{TB}}\widetilde{|n\rangle}_{V_1}$ the contributions containing V_2 only. The last terms in (IV.4.13) are the cross terms (denoted with the superscript "×") which consists of both V_1 and V_2. For example, the state $|n^{(1)}\rangle_{V_\mathrm{x}}$ is given by (A.6.18) and $|n^{(2)}\rangle_{V_\mathrm{x}}$ is explicitly given though (A.6.19).

The first (and second) term in (IV.4.13) are given by

$$
\begin{aligned}
{}_{V_1(V_2)}\widetilde{\langle n|}O^{\mathrm{TB}}\widetilde{|n\rangle}_{V_1(V_2)} &= 2\mathrm{Re}\left(\langle n|O^{\mathrm{TB}}|n^{(1)}\rangle_{V_1(V_2)}\right) \\
&\quad + {}_{V_1(V_2)}\langle n^{(1)}|O^{\mathrm{TB}}|n^{(1)}\rangle_{V_1(V_2)} + 2\mathrm{Re}\left({}_{V_1(V_2)}\langle n|O^{\mathrm{TB}}|n^{(2)}\rangle_{V_1(V_2)}\right).
\end{aligned} \tag{IV.4.14}
$$

The first term on the right contains the linear perturbations and the other terms consist of the second order corrections. The cross terms contain only second order perturbation terms given by

$$
{}_{V_1+V_2}\widetilde{\langle n|}O^{\mathrm{TB}}\widetilde{|n\rangle}^{\times}_{V_1+V_2} = {}_{V_1+V_2}\langle n^{(1)}|O^{\mathrm{TB}}|n^{(1)}\rangle^{\times}_{V_1+V_2} + 2\mathrm{Re}\left({}_{V_1+V_2}\langle n|O^{\mathrm{TB}}|n^{(2)}\rangle^{\times}_{V_1+V_2}\right) \tag{IV.4.15}
$$

and these terms are the most important in the following analysis. One can obtain similar expressions for the terms given in (IV.4.14), however these terms contain also the linear perturbations. The linear terms are obtained such that

$$
\langle n|O^{\mathrm{TB}}|n^{(1)}\rangle_{V_1(V_2)} = \sum_u \sum_{m\neq n} \langle n|O^{\mathrm{TB}}|m\rangle \frac{\langle m|\hat{V}_1(\hat{V}_2)|n\rangle}{E_n - E_m} \tag{IV.4.16}
$$

Using the definition of $\hat{V}_1$ and $\hat{V}_2$ defined in (IV.4.11), the first order response terms explicitly read

$$
\begin{aligned}
&\langle n|O^{\mathrm{TB}}|n^{(1)}\rangle_{V_1(V_2)} \\
&= \sum_u \sum_{m\neq n} \langle n|O^{\mathrm{TB}}|m\rangle \left(\frac{\langle m|\underset{(-)}{+}\sigma^{\mathrm{TB}}_{\mathrm{y(x)}}|u\rangle\langle u|\mathrm{i}\partial_{k_\mathrm{x}(k_\mathrm{y})}|n\rangle}{E_n - E_m} + \frac{\langle m|\mathrm{i}\partial_{k_\mathrm{x}(k_\mathrm{y})}|u\rangle\langle u|\underset{(-)}{+}\sigma^{\mathrm{TB}}_{\mathrm{y(x)}}|n\rangle}{E_n - E_m} \right) \\
&= \sum_{u\neq n} \sum_{m\neq n} \langle n|O^{\mathrm{TB}}|m\rangle \left(\frac{\langle m|\underset{(-)}{+}\sigma^{\mathrm{TB}}_{y(x)}|u\rangle\langle u|\mathrm{i}\partial_{k_\mathrm{x}(k_\mathrm{y})}\mathcal{H}|n\rangle}{(E_n - E_m)(E_n - E_u)} + \frac{\langle m|\mathrm{i}\partial_{k_\mathrm{x}(k_\mathrm{y})}\mathcal{H}|u\rangle\langle u|\underset{(-)}{+}\sigma^{\mathrm{TB}}_{y(x)}|n\rangle}{(E_n - E_m)(E_u - E_m)} \right).
\end{aligned} \tag{IV.4.17}
$$

where the derivative of an eigenvector (see Equation A.1.6) is used, while $\mathcal{H}$ is introduced as the matrix whose elements are defined in (A.5.1).

The first quadratic expansion terms are given by

$$
{}_{V_1(V_2)}\langle n^{(1)}|O^{\mathrm{TB}}|n^{(1)}\rangle^{\times}_{V_1(V_2)} = \sum_{m\neq n} \sum_{l\neq n} \frac{\langle n|\hat{V}_1(\hat{V}_2)|m\rangle\langle m|O^{\mathrm{TB}}|l\rangle\langle l|\hat{V}_1(\hat{V}_2)|n\rangle}{(E_n - E_m)(E_n - E_l)} \tag{IV.4.18}
$$

and the other second order terms read

$$ {}_{V_1(V_2)}\langle n|O^{\mathrm{TB}}|n^{(2)}\rangle^{\times}_{V_1(V_2)} = \sum_{m\neq n}\sum_{l\neq n}\frac{\langle n|O^{\mathrm{TB}}|m\rangle\langle m|\hat{V}_1(\hat{V}_2)|l\rangle\langle l|\hat{V}_1(\hat{V}_2)|n\rangle}{(E_n-E_m)(E_n-E_l)} \tag{IV.4.19}$$

The first term in (IV.4.15) reads

$$ {}_{V_1+V_2}\langle n^{(1)}|O^{\mathrm{TB}}|n^{(1)}\rangle^{\times}_{V_1+V_2} = \sum_{m\neq n}\sum_{l\neq n}\left(\frac{\langle n|\hat{V}_1|m\rangle\langle m|O^{\mathrm{TB}}|l\rangle\langle l|\hat{V}_2|n\rangle}{(E_n-E_m)(E_n-E_l)}\right. $$
$$ \left.+\frac{\langle n|\hat{V}_2|m\rangle\langle m|O^{\mathrm{TB}}|l\rangle\langle l|\hat{V}_1|n\rangle}{(E_n-E_m)(E_n-E_l)}\right) \tag{IV.4.20}$$
$$ \tag{IV.4.21}$$

Similarly, one obtains for the second term in (IV.4.15)

$$ {}_{V_1+V_2}\langle n|O^{\mathrm{TB}}|n^{(2)}\rangle^{\times}_{V_1+V_2} \tag{IV.4.22}$$
$$ = G_{\mathrm{x}}G_{\mathrm{y}}\sum_{m\neq n}\sum_{l\neq n}\left(\frac{\langle n|O^{\mathrm{TB}}|m\rangle\langle m|\hat{V}_1|l\rangle\langle l|\hat{V}_2|n\rangle}{(E_n-E_m)(E_n-E_l)}+\frac{\langle n|O^{\mathrm{TB}}|m\rangle\langle m|\hat{V}_2|l\rangle\langle l|\hat{V}_1|n\rangle}{(E_n-E_m)(E_n-E_l)}\right) \tag{IV.4.23}$$
$$ - G_{\mathrm{x}}G_{\mathrm{y}}\sum_{m\neq n}\left(\frac{\langle n|\hat{O}|m\rangle\langle m|\hat{V}_1|n\rangle\langle n|\hat{V}_2|n\rangle}{(E_n-E_m)^2}+\frac{\langle n|O^{\mathrm{TB}}|m\rangle\langle m|\hat{V}_2|n\rangle\langle n|\hat{V}_1|n\rangle}{(E_n-E_m)^2}\right) \tag{IV.4.24}$$
$$ - \frac{1}{2}\langle n|O^{\mathrm{TB}}|n\rangle G_{\mathrm{x}}G_{\mathrm{y}}\sum_{m\neq n}\left(\frac{\langle m|\hat{V}_1|n\rangle\langle n|\hat{V}_2|m\rangle}{(E_n-E_m)^2}+\frac{\langle m|\hat{V}_2|n\rangle\langle n|\hat{V}_1|m\rangle}{(E_n-E_m)^2}\right) \tag{IV.4.25}$$
$$ \tag{IV.4.26}$$

In the following, the polarization is analyzed in z-direction and for the operator $\hat{O}$ the spin operator $\hat{\sigma}_{\mathrm{z}}$ is chosen. One can define

$$ t^{nmluv}_{1,V_1V_2}(\boldsymbol{k}) \equiv G_{\mathrm{x}}G_{\mathrm{y}}\frac{\langle n|\sigma^{\mathrm{TB}}_{\mathrm{x}}|u\rangle\langle u|\partial_{k_{\mathrm{y}}}\mathcal{H}|m\rangle\langle m|\sigma^{\mathrm{TB}}_{\mathrm{z}}|l\rangle\langle l|\sigma_{\mathrm{y}}|v\rangle\langle v\partial_{k_{\mathrm{x}}}\mathcal{H}|n\rangle}{(E_n-E_m)(E_n-E_l)(E_m-E_u)(E_n-E_v)} \tag{IV.4.27}$$
$$ t^{nmluv}_{1,V_2V_1}(\boldsymbol{k}) \equiv G_{\mathrm{x}}G_{\mathrm{y}}\frac{\langle n|\sigma^{\mathrm{TB}}_{\mathrm{y}}|u\rangle\langle u|\partial_{k_{\mathrm{x}}}\mathcal{H}|m\rangle\langle m|\sigma^{\mathrm{TB}}_{\mathrm{z}}|l\rangle\langle l|\sigma^{\mathrm{TB}}_{\mathrm{x}}|v\rangle\langle v|\partial_{k_{\mathrm{y}}}\mathcal{H}|n\rangle}{(E_n-E_m)(E_n-E_l)(E_m-E_u)(E_n-E_v)} \tag{IV.4.28}$$

$$ t^{nmluv}_{2,V_1V_2}(\boldsymbol{k}) \equiv 2\mathrm{Re}\left(G_{\mathrm{x}}G_{\mathrm{y}}\frac{\langle n|\sigma^{\mathrm{TB}}_{\mathrm{z}}|m\rangle\langle m|\sigma^{\mathrm{TB}}_{x}|u\rangle\langle u|\partial_{k_{\mathrm{y}}}\mathcal{H}|l\rangle\langle l|\sigma^{\mathrm{TB}}_{y}|v\rangle\langle v|\partial_{k_{\mathrm{x}}}\mathcal{H}|n\rangle}{(E_n-E_m)(E_n-E_l)(E_n-E_v)(E_l-E_u)}\right) \tag{IV.4.29}$$
$$ t^{nmluv}_{2,V_2V_1}(\boldsymbol{k}) \equiv 2\mathrm{Re}\left(G_{\mathrm{x}}G_{\mathrm{y}}\frac{\langle n|\sigma^{\mathrm{TB}}_{\mathrm{z}}|m\rangle\langle m|\sigma^{\mathrm{TB}}_{y}|u\rangle\langle u|\partial_{k_{\mathrm{x}}}\mathcal{H}|l\rangle\langle l|\sigma^{\mathrm{TB}}_{x}|v\rangle\langle v|\partial_{k_{\mathrm{y}}}\mathcal{H}|n\rangle}{(E_n-E_m)(E_n-E_l)(E_n-E_v)(E_l-E_u)}\right) \tag{IV.4.30}$$

$$t^{nmuv}_{3,V_1V_2}(\boldsymbol{k}) \equiv 2\mathrm{Re}\left(G_\mathrm{x}G_\mathrm{y}\frac{\langle n|\sigma^{\mathrm{TB}}_\mathrm{z}|m\rangle\langle m|\sigma^{\mathrm{TB}}_x|u\rangle\langle u|\partial_{k_\mathrm{y}}\mathcal{H}|n\rangle\langle n|\sigma^{\mathrm{TB}}_y|v\rangle\langle v|\partial_{k_\mathrm{x}}\mathcal{H}|n\rangle}{(E_n-E_m)^2(E_n-E_u)(E_n-E_v)}\right) \tag{IV.4.31}$$

$$t^{nmuv}_{3,V_2V_1}(\boldsymbol{k}) \equiv -2\mathrm{Re}\left(G_\mathrm{x}G_\mathrm{y}\frac{\langle n|\sigma^{\mathrm{TB}}_\mathrm{z}|m\rangle\langle m|\sigma^{\mathrm{TB}}_y|u\rangle\langle u|\partial_{k_\mathrm{x}}\mathcal{H}|n\rangle\langle n|\sigma^{\mathrm{TB}}_x|v\rangle\langle v|\partial_{k_\mathrm{y}}\mathcal{H}|n\rangle}{(E_n-E_m)^2(E_n-E_u)(E_n-E_v)}\right) \tag{IV.4.32}$$

$$t^{nmuv}_{4,V_1V_2}(\boldsymbol{k}) \equiv -2\mathrm{Re}\left(G_\mathrm{x}G_\mathrm{y}\frac{1}{2}\langle n|\sigma^{\mathrm{TB}}_\mathrm{z}|n\rangle\frac{\langle m|\sigma^{\mathrm{TB}}_\mathrm{x}|u\rangle\langle u|\partial_{k_\mathrm{y}}\mathcal{H}|n\rangle\langle n|\sigma^{\mathrm{TB}}_\mathrm{y}|v\rangle\langle v|\partial_{k_\mathrm{x}}\mathcal{H}|m\rangle}{(E_n-E_m)^2(E_n-E_u)(E_m-E_v)}\right) \tag{IV.4.33}$$

$$t^{nmuv}_{4,V_2V_1}(\boldsymbol{k}) \equiv -2\mathrm{Re}\left(G_\mathrm{x}G_\mathrm{y}\frac{1}{2}\langle n|\sigma^{\mathrm{TB}}_\mathrm{z}|n\rangle\frac{\langle m|\sigma^{\mathrm{TB}}_\mathrm{y}|u\rangle\langle u|\partial_{k_\mathrm{x}}\mathcal{H}|n\rangle\langle n|\sigma^{\mathrm{TB}}_\mathrm{x}|v\rangle\langle v|\partial_{k_\mathrm{y}}\mathcal{H}|m\rangle}{(E_n-E_m)^2(E_n-E_u)(E_m-E_v)}\right) \tag{IV.4.34}$$

as an abbreviated notation for the cross terms and

$$t^{nmu}_{0,V_{1(2)}}(\boldsymbol{k}) \equiv 2\mathrm{Re}\left(G_\mathrm{y}(G_\mathrm{x})\langle n|\sigma^{\mathrm{TB}}_\mathrm{z}|m\rangle\frac{\langle m|\,(\pm)\,\sigma^{\mathrm{TB}}_{x(y)}|u\rangle\langle u|\partial_{k_\mathrm{y}(k_\mathrm{x})}\mathcal{H}|n\rangle}{(E_n-E_m)(E_n-E_u)}\right) \tag{IV.4.35}$$

$$t^{nmluv}_{1,V_{1(2)}V_{1(2)}}(\boldsymbol{k}) \equiv G^2_\mathrm{y}(G^2_\mathrm{x})\frac{\langle n|\,(\pm)\,\sigma^{\mathrm{TB}}_{\mathrm{x(y)}}|u\rangle\langle u|\partial_{k_\mathrm{y}(k_\mathrm{x})}\mathcal{H}|m\rangle\langle m|\sigma^{\mathrm{TB}}_\mathrm{z}|l\rangle\langle l|\,(\pm)\,\sigma_{\mathrm{x(y)}}|v\rangle\langle v\partial_{k_\mathrm{y}(k_\mathrm{x})}\mathcal{H}|n\rangle}{(E_n-E_m)(E_n-E_l)(E_m-E_u)(E_n-E_v)} \tag{IV.4.36}$$

$$\begin{aligned} t^{nmluv}_{2,V_{1(2)}V_{1(2)}}(\boldsymbol{k}) \equiv 2\mathrm{Re}\Big(&G^2_\mathrm{y}(G^2_\mathrm{x}) \\ &\times\frac{\langle n|\sigma^{\mathrm{TB}}_\mathrm{z}|m\rangle\langle m|\,(\pm)\,\sigma^{\mathrm{TB}}_{\mathrm{x(y)}}|u\rangle\langle u|\partial_{k_\mathrm{y}(k_\mathrm{x})}\mathcal{H}|l\rangle\langle l|\,(\pm)\,\sigma^{\mathrm{TB}}_{\mathrm{x(y)}}|v\rangle\langle v|\partial_{k_\mathrm{y}(k_\mathrm{x})}\mathcal{H}|n\rangle}{(E_n-E_m)(E_n-E_l)(E_n-E_v)(E_l-E_u)}\Bigg) \end{aligned} \tag{IV.4.37}$$

$$\begin{aligned} t^{nmuv}_{3,V_{1(2)}V_{1(2)}}(\boldsymbol{k}) \equiv 2\mathrm{Re}\Big(&G^2_\mathrm{y}(G^2_\mathrm{x}) \\ &\times\frac{\langle n|\sigma^{\mathrm{TB}}_\mathrm{z}|m\rangle\langle m|\,(\pm)\,\sigma^{\mathrm{TB}}_{\mathrm{x(y)}}|u\rangle\langle u|\partial_{k_\mathrm{y}(k_\mathrm{x})}\mathcal{H}|n\rangle\langle n|\,(\pm)\,\sigma^{\mathrm{TB}}_{\mathrm{x(y)}}|v\rangle\langle v|\partial_{k_\mathrm{y}(k_\mathrm{x})}\mathcal{H}|n\rangle}{(E_n-E_m)^2(E_n-E_u)(E_n-E_v)}\Bigg) \end{aligned} \tag{IV.4.38}$$

$$\begin{aligned} t^{nmuv}_{4,V_{1(2)}V_{1(2)}}(\boldsymbol{k}) \equiv -2\mathrm{Re}\Big(&G^2_\mathrm{y}(G^2_\mathrm{x}) \\ &\times\frac{1}{2}\langle n|\sigma^{\mathrm{TB}}_\mathrm{z}|n\rangle\frac{\langle m|\,(\pm)\,\sigma^{\mathrm{TB}}_{\mathrm{x(y)}}|u\rangle\langle u|\partial_{k_\mathrm{y}(k_\mathrm{x})}\mathcal{H}|n\rangle\langle n|\,(\pm)\,\sigma^{\mathrm{TB}}_{\mathrm{x(y)}}|v\rangle\langle v|\partial_{k_\mathrm{y}(k_\mathrm{x})}\mathcal{H}|m\rangle}{(E_n-E_m)^2(E_n-E_u)(E_m-E_v)}\Bigg) \end{aligned} \tag{IV.4.39}$$

for the other terms. By use of the abbreviated notation, the change in the spin polarization in z-direction up to second order becomes

$$\delta s_{\mathrm{xy,z}}(\boldsymbol{k}) \equiv \sum_{n(\mathrm{occ})} \left({}_{V_1+V_2}\widetilde{\langle n|}\sigma_{\mathrm{z}}^{\mathrm{TB}}\widetilde{|n\rangle}_{V_1+V_2} - \langle n|\sigma_{\mathrm{z}}^{\mathrm{TB}}|n\rangle\rangle \right)$$
$$= \sum_{j=1}^{2} \sum_{n_{\mathrm{occ}}} \sum_{\substack{m\neq n \\ u\neq n}} \left(t_{0,V_j}^{nmu}(\boldsymbol{k}) + \sum_{i=2}^{4} \sum_{p=1}^{2} \left(\sum_{\substack{l\neq n \\ v\neq l}} t_{i,V_jV_p}^{nmluv}(\boldsymbol{k}) + \sum_{v\neq n} t_{i,V_jV_p}^{nmuv}(\boldsymbol{k}) \right)\right). \qquad \text{(IV.4.40)}$$

The cross terms of the spin polarization response in second order perturbation theory are

$$\delta s_{\mathrm{xy,z}}^{\times}(\boldsymbol{k}) = \sum_{j=1}^{2} \sum_{n(\mathrm{occ})} \sum_{\substack{m\neq n \\ u\neq n}} \sum_{i=2}^{4} \sum_{p\neq j\in\{1,2\}} \left(\sum_{\substack{l\neq n \\ v\neq l}} t_{i,V_jV_p}^{nmluv}(\boldsymbol{k}) + \sum_{v\neq n} t_{i,V_jV_p}^{nmuv}(\boldsymbol{k}) \right) \qquad \text{(IV.4.41)}$$

containing only products of V_1 and V_2. The magnetization is simply the summation of all spin polarizations over momentum space denoted as

$$\delta m_{\mathrm{xy,z}} = \sum_{\boldsymbol{k}} \delta s_{\mathrm{xy,z}}(\boldsymbol{k}) \qquad \text{(IV.4.42)}$$
$$\delta m_{\mathrm{xy,z}}^{\times} = \sum_{\boldsymbol{k}} \delta s_{\mathrm{xy,z}}^{\times}(\boldsymbol{k}). \qquad \text{(IV.4.43)}$$

In the following, the changes in the magnetization $\delta m_{\mathrm{xy,z}}$ given in (IV.4.41) are analyzed for the Chern insulator and the topological s-wave superconductor. In the case of the Chern insulator, the pseudo-spin is supposed to couple to a pseudo-magnetic field and the operator being measured is the pseudo-spin polarization in the z-direction of the pseudo-spin. In the case of the topological s-wave superconductor, the magnetization in z-direction is analyzed and the system is perturbed in x- and y-direction with magnetic fields linearly dependent on r_{x} and r_{y}, respectively.

IV.5. Higher orders and finite temperature

The Schrödinger equation (A.6.1) can be solved yielding higher orders in $\hat{V}$ given in (IV.4.11). For this purpose, the perturbing term in the Hamiltonian can be represented in the eigenbasis (the Bloch basis) of the lattice periodic Hamiltonian $\hat{\mathcal{H}}$. The position operator given in $\hat{V}$ is unbounded and therefore problematic, since $\hat{V}$ diverges as the size of the systems goes to infinity. However, as investigated in Section III, the spin polarization in the systems analyzed are in good approximation translation invariant. Thus, the contributions of $\hat{V}$ to the analyzed polarization can be regularized. It is then concluded that the lattice periodic part of the position operator which is given by the first term in (IV.3.7) is the important part. The consequence is that the matrix elements of the Hamiltonian in the Bloch basis can be written down more explicit using the representation of the position operator in the Bloch basis given in (A.4.40) yielding

$$\begin{aligned}V^{\mathrm{TB}} &= \sum_{n,n'} V^{\mathrm{TB}}_{\boldsymbol{k},nn'} |n\rangle\langle n'| \\ &= \sum_{n}\sum_{n'}\sum_{n''} \Big(-G_{\mathrm{y}} \Big(\langle n|\hat{\sigma}_{\mathrm{x}}|n''\rangle\langle n''|\mathrm{i}\left(\nabla_{k_{\mathrm{y}}}|n'\rangle\right) + \langle n|\mathrm{i}\left(\nabla_{k_{\mathrm{x}}}|n''\rangle\right)\langle n''|\hat{\sigma}_{\mathrm{x}}|n'\rangle\Big) \\ &\left(G_{\mathrm{x}}\langle n|\hat{\sigma}_{\mathrm{y}}|n''\rangle\langle n''|\nabla_{k_{\mathrm{x}}}|n'\rangle + G_{\mathrm{x}}\langle n|\mathrm{i}\left(\nabla_{k_{\mathrm{x}}}|n''\rangle\right)\langle n''|\hat{\sigma}_{\mathrm{y}}|n'\rangle\right)\Big) |n\rangle\langle n'|. \end{aligned} \tag{IV.5.1}$$

The assumption that $\hat{V}$ defined in (IV.4.11) can be well approximated by (IV.5.1) is confirmed by the obtained numerical results shown below. The total Hamiltonian $\hat{H}$ of the perturbed system reads

$$\hat{H} = \hat{\mathcal{H}} + \hat{V}. \tag{IV.5.2}$$

while the matrix elements of $\hat{\mathcal{H}}$ in the Bloch basis is simply given by

$$\tilde{\mathcal{H}} = \sum_{n} |n\rangle\langle n|\hat{\mathcal{H}}|n'\rangle\langle n'| = \sum_{n} E_n |n\rangle\langle n| \tag{IV.5.3}$$

Now, the total Hamiltonian can be diagonalized and the eigenvectors $|n\rangle_{\mathrm{H}}$ and eigenvalues $E_{n,\mathrm{H}}(\boldsymbol{k})$ can be obtained. With these, the expectation value for the polarization in z-direction can be calculated. In general, the matrix-elements of $H(\boldsymbol{k})$ are changed in the eigenbasis of $\mathcal{H}(\boldsymbol{k})$ due to the gradient field.

$$\sigma^{\mathrm{TB}}_{\mathrm{z,H}} = \frac{\partial H(\boldsymbol{k})}{\partial h_{\mathrm{z}}}. \tag{IV.5.4}$$

The magnetization is in general determined through Equation (A.7.51). The magnetization can thus be calculated for the perturbed system $H(\boldsymbol{k})$ to all orders with

$$M_{\mathrm{z}} = -\frac{1}{N}\frac{\partial\Omega}{\partial h_{\mathrm{z}}} = \frac{1}{2N}\sum_{\boldsymbol{k}} \langle n|\sigma^{\mathrm{TB}}_{\mathrm{z,H}}|n\rangle_{\mathrm{H}} \tanh\left(\frac{\beta\lambda_{n,H}}{2}\right). \tag{IV.5.5}$$

where $\lambda_{n,H}$ denotes the eigenvalues of the total Hamiltonian H. On the other hand, the Hamiltonian can directly be expressed in real space, which avoids the description of the position operator in the Bloch-state basis. There are thus in principle two different approaches to describe the Hamiltonian containing the magnetic field gradients. It can be described in momentum space using the Bloch-state representation of the position operator or alternatively in real space. The real space description has the advantage, that open boundaries can analyzed and the subtlety of the divergent parts of the position operator in a periodic system in momentum space can be avoided.

IV.6. Response in the spin polarization to external magnetic field gradients

Numerical results for the spin-polarization response in the z-direction to an in-plane applied magnetic field gradient are discussed in this section. There, the response is analyzed in the Bloch state basis and alternatively in real space with either periodic or open boundary conditions.

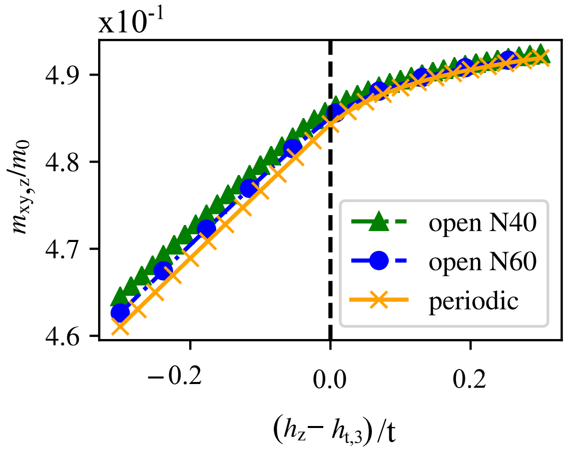

Figure IV.4.: The total ground state magnetization in z-direction $m_{xy,z}$ with respect to the saturation magnetization m_0 in the presence of the magnetic field gradients in x- and y-direction, obtained from the real space description for open boundary conditions and for periodic boundary conditions from real and momentum space (in the Bloch state basis) calculations. $h_{t,3}$ is indicated by the black dashed line. Further, $\alpha_R = 0.25t$ was used. N counts the number of lattice points of a square lattice in one direction $N = N_x = N_y$. The open boundary calculations have been performed for two different values of N. The results from real space calculations and from the Bloch state description coincide and are labeled as "periodic".

Periodic boundary conditions signify in that case that the Hamiltonian without the gradient field contributions is periodic. Obviously, the inclusion of the gradient breaks translation invariance.

First, the total magnetization and the total response to the gradient field is analyzed. Subsequently, the linear and quadratic response terms are discussed. The calculations are performed in real and in momentum space. The results agree well with each other, which confirms the validity of the results. Moreover, the real space calculations have the advantage that edge state contributions can be taken into account as well. On the other hand, the representation in Bloch-state basis for systems with periodic boundary conditions — as described above — allow to calculate the first and second order perturbations in the states explicitly.

Response in the magnetization at open and periodic boundary conditions

The results of the total magnetization per lattice point normalized with the saturation magnetization m_0 in z-direction are analyzed. The numerical data is displayed in Figure IV.4. The calculation of the real space Hamiltonian is performed for system sizes of $N \equiv N_x = N_y = 40$ and $N = 60$. The results for open boundary conditions are clearly dependent on the system size. The results obtained from the calculation at open boundary conditions converge towards the results for periodic boundary conditions as one would expect. The influence of the edge on large systems is seen to be very small.

From the perturbation theory in the Bloch-state representation, described in Sections IV.4, the first and second order perturbations can be calculated explicitly. On the other hand, these

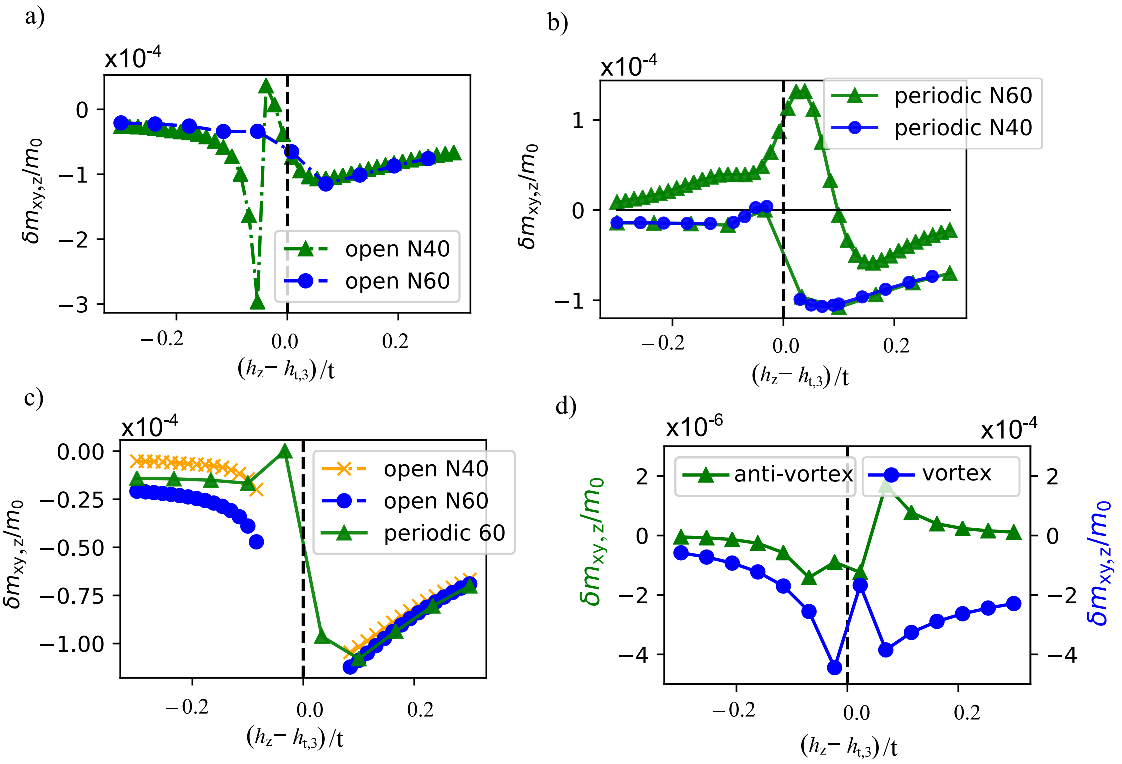

Figure IV.5.: Evaluation of the response $\delta m_{\mathrm{xy,z}}$ with a) open boundary conditions b) periodic boundary conditions. c) Comparison of the results with open and periodic boundary conditions. d) Comparison of the signature for a spin-texture transition around the momentum $\boldsymbol{k}_{\mathrm{t},3}$ with either a vortex or an antivortex texture. The magnetic fields are $h_{\mathrm{x}}(0, y) = -0.0228t$, $h_{\mathrm{x}}(L, y) = 0.0228t$, $h_{\mathrm{x}}(x, 0) = -0.0228t$ and $h_{\mathrm{x}}(x, L) = 0.0228t$ and $\alpha_{\mathrm{R}} = 0.25t$.

calculations in real space provide the results to all orders.

The results for the thermodynamic response to an in-plane magnetic field gradient denoted with $\delta m_{\mathrm{xy,z}}$ is discussed for open boundary conditions for systems with $N = 40 \times 40$ or $N = 60 \times 60$ lattice points. The results are displayed in Figure IV.5 a). The change of the magnetization is given as a function of the homogeneous magnetic field in z-direction h_{z} while additional magnetic field gradients are applied in both x- and y-direction simultaneously. In the smaller system, a pronounced jump in $\delta m_{\mathrm{xy,z}}$ is visible around the phase transition. This vast change in $\delta m_{\mathrm{xy,z}}$ turns into a smooth curve which is steepest around the phase transitions in the larger system. The discontinuous transition in the smaller system is suggested to originate from the influence of edge modes which becomes less important in the larger system. This assumption is reinforced by the observation that the most pronounced signatures are present in the topologically non-trivial state at which the edge states are identified.

The results of the real space calculations with periodic boundary conditions are shown in

Subfigure IV.5 b). As expected, the results are independent of the system size. Like for open boundary conditions, a steep change in $\delta m_{\mathrm{xy,z}}$ is obtained close to the topological transition field h_{t}. The comparison of the results for open and periodic boundary conditions are given in Subfigure IV.5 c). The difference between the results are small in the trivial phase at which edge states are absent and the open boundary conditions are converging towards the results for periodic boundary conditions. In the non-trivial phase displayed on the left hand side of the subfigure, this difference is much more pronounced. For both calculated system sizes, the contributions of the edge modes to the signatures in the magnetization are significant. The results, however, indicate that the differences between the open and periodic boundary conditions converge for larger systems. This is consistent with the expectation that a thermodynamic signature should depend on the bulk in the thermodynamic limit.

The topology of a spin-texture does not depend on whether the spin-texture is of a vortex or antivortex type. Therefore, the change in the magnetization across a topological phase transition is shown in Figure IV.5 d) for both vortex and antivortex spin textures around the gap closing point $\boldsymbol{k}_{\mathrm{t},3}$. The results obtained for $\delta m_{\mathrm{xy,z}}$ are strongly different for vortices and antivortices. The signatures obtained for the antivortex spin-texture is two orders of magnitude smaller than the results obtained for the vortex type texture. This is the result of additive or subtractive regions in momentum space dependent on the directions of the applied magnetic field gradient as shown in Figure A.3 in Appendix A.2. A topologically trivial spin-texture transition of a vortex in combination with an antivortex does therefore not yield vanishing results in $\delta m_{\mathrm{xy,z}}$ underpinning that the incorporation of the total change in the magnetization does not yield sufficient information about the topological character of a spin-texture transition even though clear signatures can be identified.

However, the signature in $\delta m_{\mathrm{xy,z}}$ clearly indicates a structural change in the spin-texture. In order to encounter the question whether the total change in the magnetization is a sufficient indication for a topological phase transition, the analysis of total change in the magnetization in the in-plane magnetic field gradient setup is split into the linear contributions and the quadratic perturbations.

Linear perturbation theory

Fist, the linear response in the magnetization to an in-plane magnetic field gradient is discussed. The question is examined whether thermodynamic response signatures — linear in the magnetic field gradient — indicate a topological phase transition and if the observation of those are sufficient to conclude that a non-trivial phase transitions is seen.

The numerical results are given in Figure IV.6. The results confirm that the linear response in the in-plane magnetic field gradient can yield perceptible signatures at topological phase transitions. These signatures from first order Rayleight-Schrödinger perturbation theory are, however, not limited to non-trivial spin-texture transitions.

There are important requirements for a signature to be in accordance with non-trivial spin-texture transitions. These involve an exclusive dependence of the signature on the vorticity. On the other hand, it must not matter whether the spins (for example a Bloch-type vortex) wind clockwise or counterclockwise around a vortex center. Therefore, a class of Hamiltonians was introduced in Section IV.6 III.4 to test whether the thermodynamic signatures described below unambiguously indicate topological spin-texture transitions. This model allows for vorticities $\mathcal{V} \neq 1$ and thus for higher vorticities and also for trivial spin-textures where, however, the bulk gap closes and reopens as a function of the parameter h_z, which is also a prerequisite for the existence of topological phase transitions.

In Subfigure IV.6 a), the linear response in the magnetization $\delta m_{x,z}$ across a topological spin-texture transition is displayed for three distinct cases. These include the spin-texture transition at $\boldsymbol{k}_t = (0, 0)$ for $h_{t,3}$ introduced in Section II.3 for three different vorticities $\mathcal{V}(\boldsymbol{k}_t) = 0, 1, 2$ around the momentum $\boldsymbol{k}_t = (0, 0)$ in the QWZ-model. First, the case $\mathcal{V}(\boldsymbol{k}_t) = 1$, which is given by the blue curve, is discussed. The topological trivial phase is identified at $h_{t,3} - h_z < 0$ and the non-trivial phase is given in the range of $h_{t,3} - h_z > 0$. The linear response is negative and its absolute value is increasing towards $h_z = h_{t,3}$ in the trivial phase.

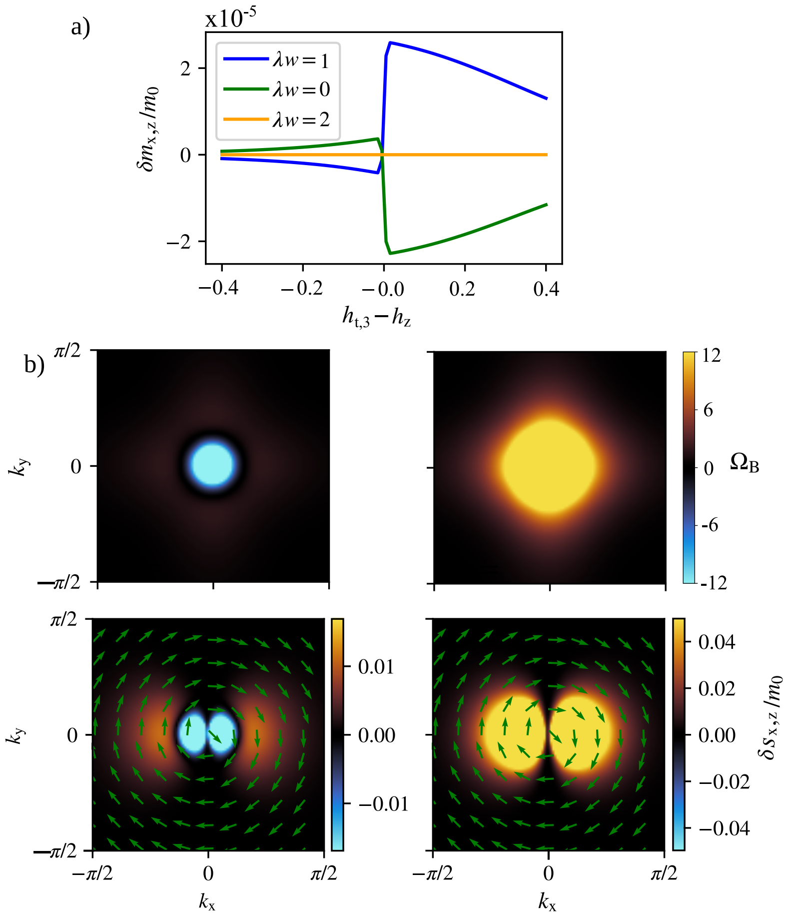

Figure IV.6.: Linear response terms $\delta m_{x,z}$ in the vicinity of a topological phase transition. Subfigure a) shows $\delta m_{x,z}/m_0$ for different parameters λ and w. Subfigures b) display Ω_B (figures above) and $\delta s_{x,z}(\boldsymbol{k})/m_0$ (figures below) for $\mathcal{V} = \lambda w = 1$. The figures in the left correspond to the trivial phase and the figures on the right correspond to the non-trivial phase. The green arrows represent the in-plane spin vector normalized to unit length.

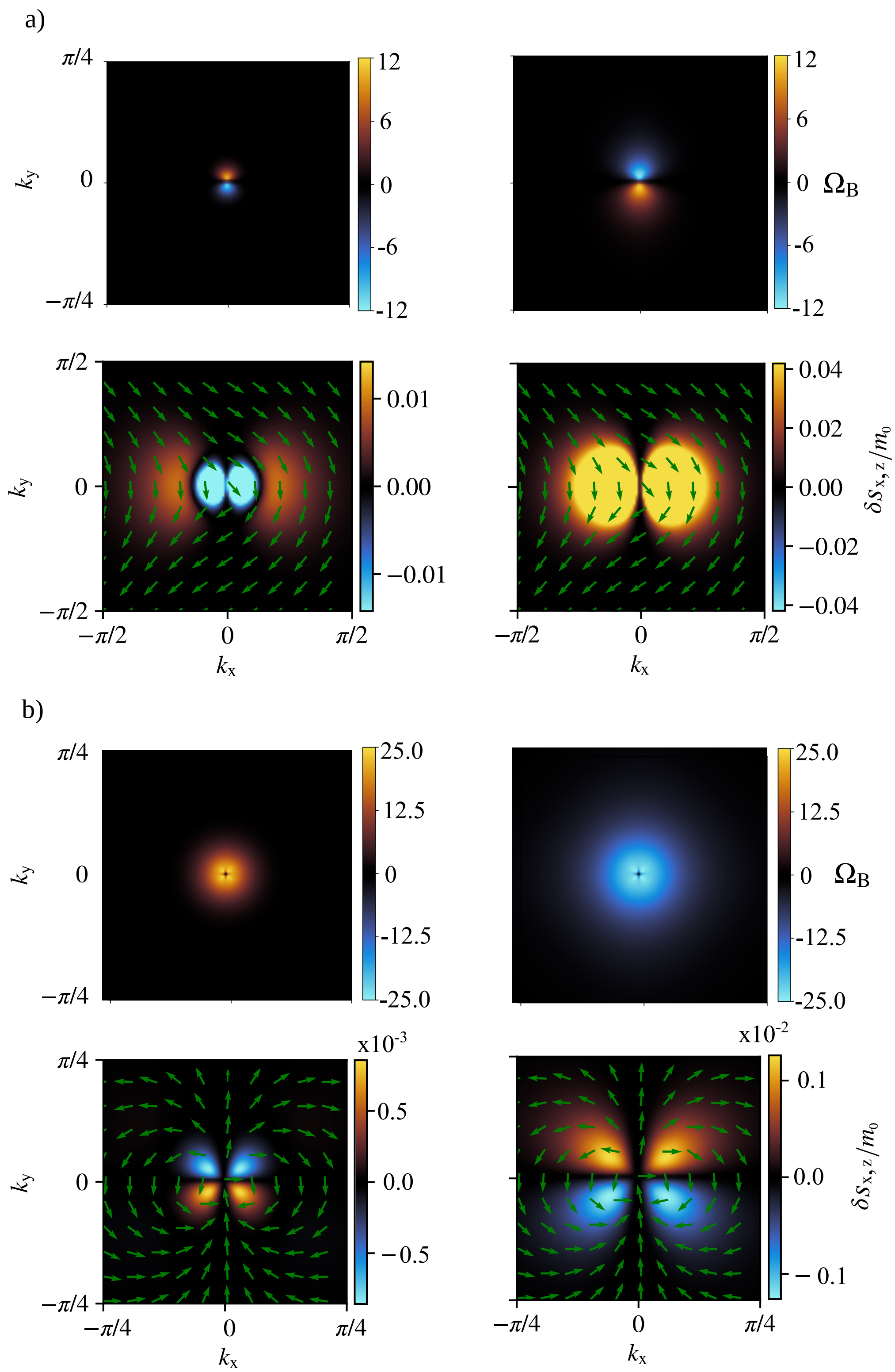

Figure IV.7.: $\Omega_B(\boldsymbol{k})$ (figures above) and $\delta s_{x,z}(\boldsymbol{k})/m_0$ (figures below) for the trivial state (left) and the topological state (right) for a) $\mathcal{V} = 0$ and b) $\mathcal{V} = 2$.

At the phase transition, the response term is increasing rapidly to a much larger absolute value with opposite sign. In the non-trivial phase, the magnetization response is decreasing with increasing h_z. The increase of the signal towards $h_{t,3}$ is attributed to a reduction of the band gap such that perturbations are amplified. The results show that signatures are smaller in the trivial phase than in the non-trivial phase which can be understood by the analysis of the momentum-resolved signals. In such a momentum-resolved presentation, the liner response signatures show mutually canceling regions in the trivial phase which are absent in the non-trivial phase shown in Subfigure IV.6 b). Interestingly, the occurrence of canceling regions in the signature is correlated with the occurrence of such regions in the Berry curvature as depicted in the Subfigure fig:LinearResponseTerms b). In contrast to the Berry curvature, the linear response term depends on whether the in-plane component of the spins winds around the vortex center point clockwise or anticlockwise. The sign change in the linear perturbation signature across the topological phase transition stems from the fact that the s_z-expectation value changes its sign around the momentum $\boldsymbol{k}_t$ at which the essential topological spin-texture transition occurs. The linear response for an anti-clockwise winding of these Bloch-type spin texture is equal but with an inverted sign as depicted in Figure A.3 a) and b) in Appendix A.2. This dependence on the direction of the spin-texture winding around the momentum $\boldsymbol{k}_t$ testifies the importance of the in-plane spin texture evolution in reciprocal space to the response signature.

These results suggest the existence of clear linear response signatures at topological phase transitions. However, the linear response terms can be vanishing even at non-trivial phase transitions which is the case, for example, for spin textures with vorticity $\mathcal{V} = 2$ which is given by the orange curve in Subfigure IV.6 a). The corresponding momentum space response is depicted in Figure IV.7 a) showing the cancellation in the Brillouin zone. The linear response term is thus not sufficient to draw conclusions about topological phase transitions.

This observation is corroborated by the results on the trivial spin-texture transition with $\mathcal{V} = 0$ which is realized by setting $f(\varphi) = \sin(\varphi)$ in Equations (III.4.1) to (III.4.3). The response signature is given by the green curve in Figure IV.6 a) which is not vanishing. The corresponding signature in momentum space for trivial and topological phase are shown in Figure IV.6 b) clearly showing the non-canceling contributions. The Berry curvature, on the other hand, is not vanishing. This example of a trivial spin-texture transition proves that the linear response terms are not indicative of non-trivial texture transitions in all cases.

These examples suggest that distinct signatures in the linear response terms of the spin magnetization are possible. These, however, imply not necessarily a topological phase transition. The question arises whether non-zero signatures restricted to non-trivial topological spin-texture transitions exist. As shown in the following, the second order cross terms defined in (IV.4.27) to (IV.4.34) included in $\delta s^{\times}_{xy,z}(\boldsymbol{k})$ indeed satisfy this condition.

Second order perturbation

Using the expression obtained from perturbation theory, $\delta s^{\times}_{xy,z}(\boldsymbol{k})$ can be calculated and analyzed directly. In the real space calculations $\delta s^{\times}_{xy,z}(\boldsymbol{k})$ contains the second order terms plus higher perturbations, these higher order terms are, however, small as long as the perturbation is weak compared to the energy gap. The results are shown in Figure IV.8 a) and IV.8 b) for open and periodic boundary conditions, respectively. The results for open boundary conditions show distinct differences between a small and a larger system size.

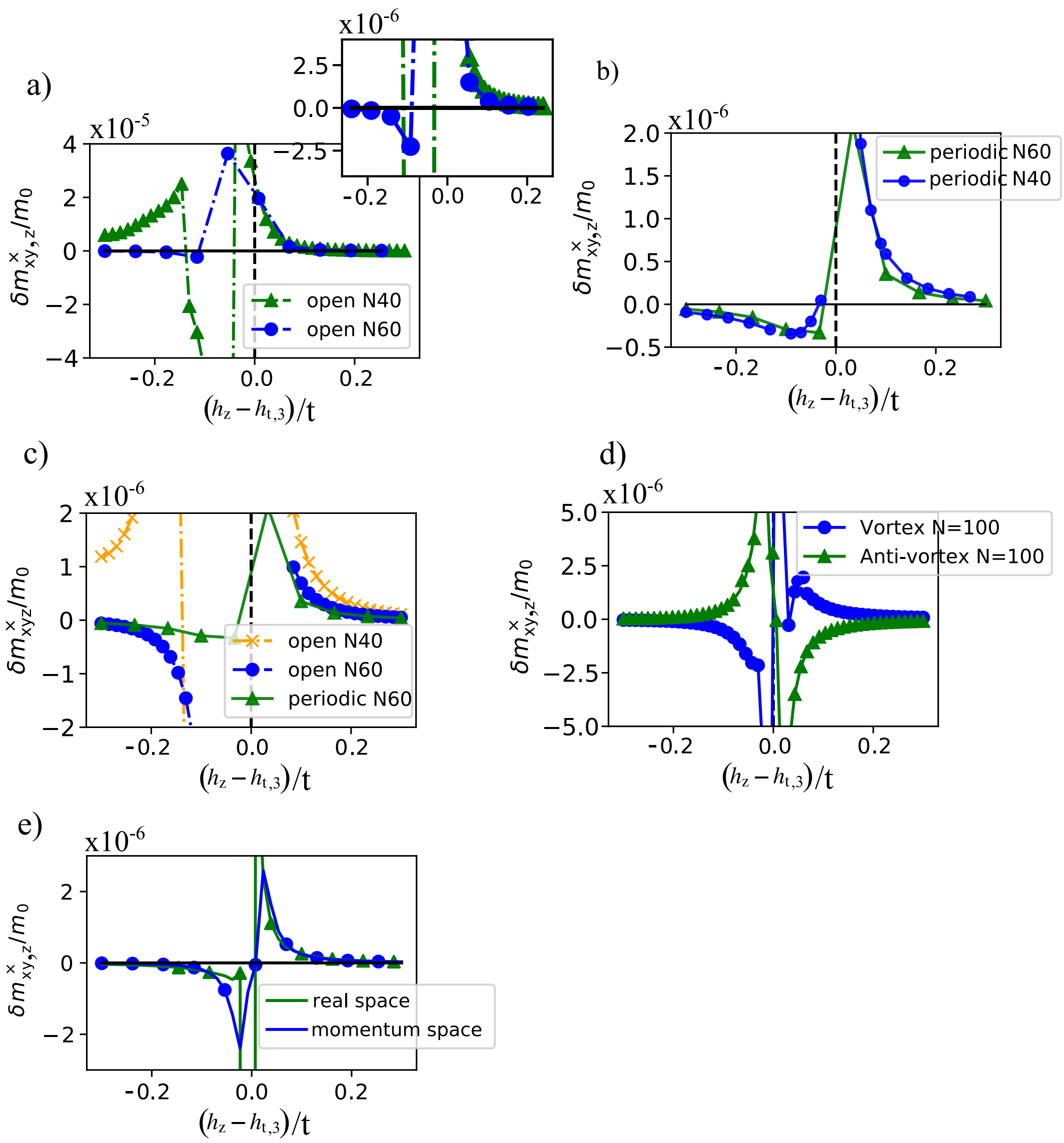

Figure IV.8.: Evaluation of the response $\delta m^{\times}_{\text{xy,z}}$ across a topological spin-texture transition for open and periodic boundary conditions in a magnetic gradient field setup with $h_x(0, y) = -0.0228t$, $h_x(L, y) = 0.0228t$, $h_x(x, 0) = -0.0228t$ and $h_x(x, L) = 0.0228t$. The figures show in a) and b) $\delta m_{\text{xy,z}}/m_0$ and $\delta m^{\times}_{\text{xy,z}}(h_z)/m_0$ for open and periodic boundary conditions, respectively. Figure c) shows the direct comparison of the results obtained from open and periodic boundary conditions. The results for vortex and anti-vortex spin-textures are analyzed in d). In figure e), the comparison of the results obtained from real and momentum space is depicted.

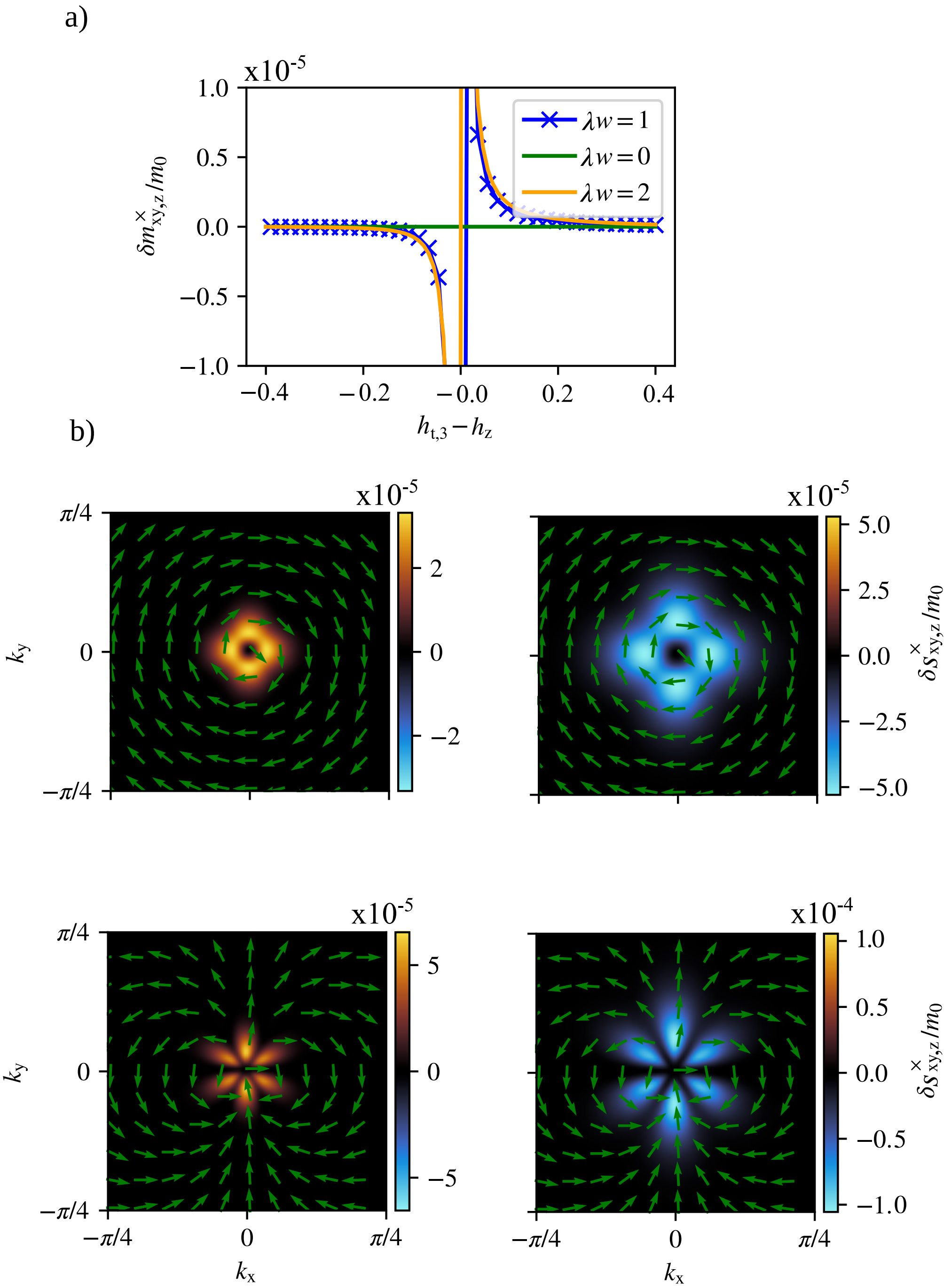

Figure IV.9.: a) Quadratic response of the spin magnetization showing signatures at the topological phase transition for distinct $\mathcal{V} = \lambda w$. The figures in b) show $\delta s^{\times}_{\mathrm{xy,z}}(\boldsymbol{k})$ for $h_{\mathrm{z}} = h_{\mathrm{t}} - 0.1t$ (left side) and $h_{\mathrm{z}} = h_{\mathrm{t}} - 0.1t$ (right side) for $\mathcal{V} = \lambda w = 1$ (figures above) and $\mathcal{V} = \lambda w = 2$ (figures below).

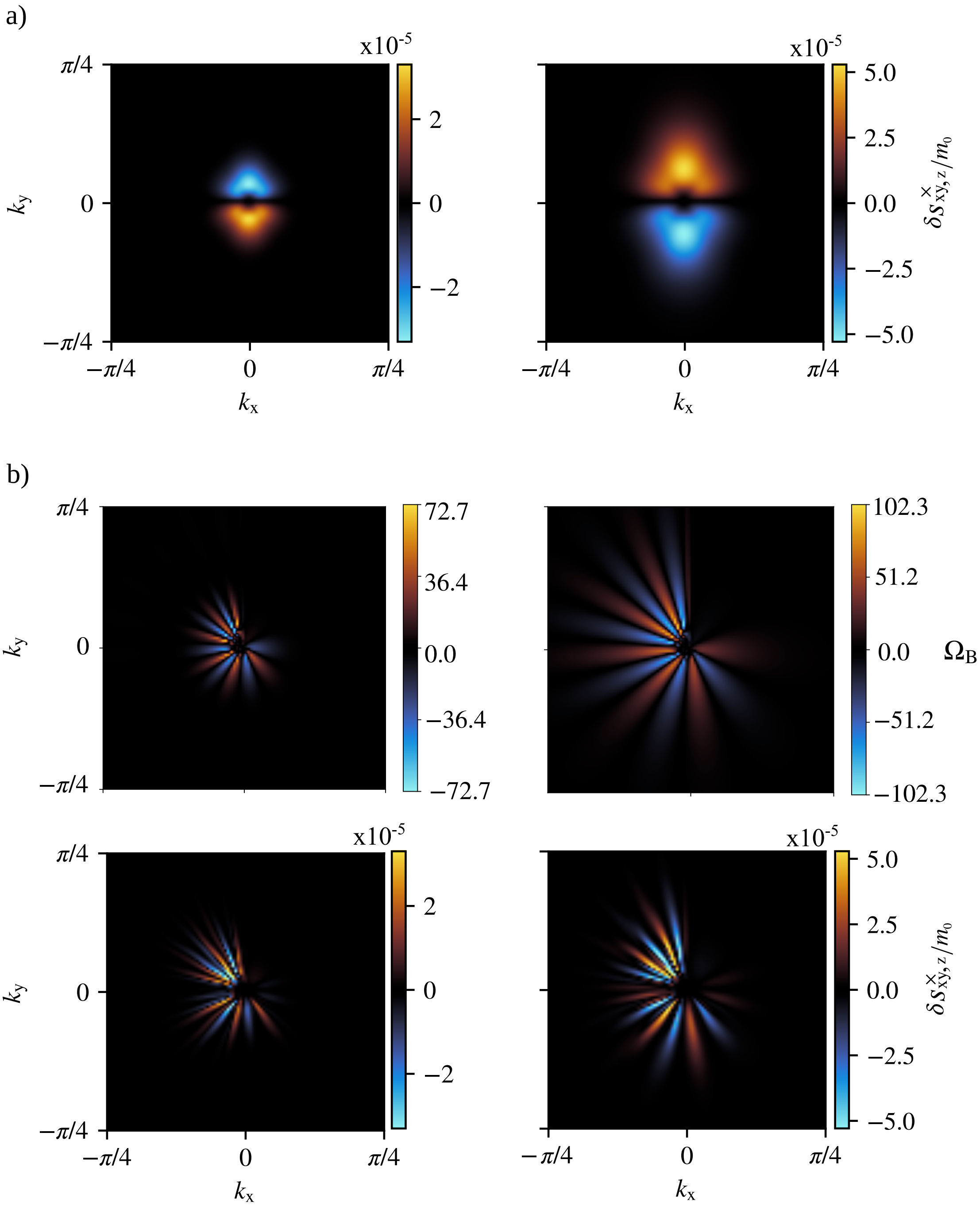

Figure IV.10.: a) $\delta s^{\times}_{\mathrm{xy,z}}(\boldsymbol{k})$ for $\mathcal{V} = 0$ with $f(\varphi) = \sin(\varphi)$. b) $\Omega_{\mathrm{B}}(\boldsymbol{k})$ (figures above) and $\delta s^{\times}_{\mathrm{xy,z}}(\boldsymbol{k})$ (figures below) for $\mathcal{V} = 0$ realized with $f(\varphi) = \sin(\varphi^2 - 2\pi\varphi)$. The angle is given by $\varphi = \arctan 2(k_y/k_x)$. In the figures on the left side $h_z = h_{t,3} - 0.1t$ was used and in the figures on the right side $h_z = h_{t,3} + 0.1t$ was chosen.

However, as the figures indicate, the system approaches the results obtained from the periodic boundary conditions as the system size in increased as one would expect since magnetizations are non-zero in the bulk which should be dominating in large systems displayed in Figure IV.8 c) where the results obtained from open and periodic boundary conditions are compared directly. Changing the vorticity of the spin-texture from $\mathcal{V} = 1$ to $\mathcal{V} = -1$ yields the same absolute values of $\delta m^{\times}_{\mathrm{xy,z}}$ but opposite signs. On the other hand, changing the winding of the spin-textures from clockwise to anticlockwise and vice versa does not have any effect on the signature as depicted in Figure A.4 in Appendix A.2. These are very important observations since the topology does exclusively depend on the vorticity and is not dependent on whether the spins point in a clockwise or anticlockwise direction around the vortices. Thus, the simultaneous change of the spin-polarization at a vortex type and an antivortex type spin texture — which corresponds to a topologically trivial spin-texture transition — cancels resulting in a vanishing signal in $\delta m^{\times}_{\mathrm{xy,z}}$.

In order to analyze the dependence of the signatures in $\delta m^{\times}_{\mathrm{xy,z}}$ on non-trivial spin-texture transitions, similar to the analysis of the linear order terms, the signatures are investigated for four distinct cases. These include the vorticities $\mathcal{V} = 0, 1, 2$ while two different realizations of $\mathcal{V} = 0$ are analyzed which are described in more detail below. The dependence of $\delta m^{\times}_{\mathrm{xy,z}}$ on the magnetic field h_{z} is depicted in Figure IV.9 a) for all of these cases. The blue curve corresponds to the situation with $\mathcal{V} = 1$ at the topological spin-texture transition around $\boldsymbol{k}_{\mathrm{t}}$ at which the essential spin-texture transition occurs. For this situation, a clear signature is obtained in $\delta m^{\times}_{\mathrm{xy,z}}$. The other non-trivial spin-texture transition realized with $\mathcal{V} = 2$ is given by the orange curve which also shows distinct signatures at the topological spin-texture transition. There are also two distinct situations with trivial spin-texture transitions. Both include a spin-texture with $\mathcal{V} = 0$ but the function $f(\varphi)$ defined in Equation (III.4.1) is different in both cases.

The green curve is realized by $f_1(\varphi) = \sin(\varphi)$. The signature is absent for this spin-texture transition. To exclude the possibility that the contributions only cancel each other out by chance a second realization of $\mathcal{V} = 0$ is analyzed with $f_2(\varphi) = \sin(\varphi^2 - 2\pi\varphi)$ which fulfills the requirement $f(0) = f(2\pi)$. Also in this second realization of a trivial spin-texture transition, the signature in $\delta m^{\times}_{\mathrm{xy,z}}$ vanishes yielding the green curve in Figure IV.9 a). Figure (IV.9) b) displays the momentum-resolved change in the spin-polarization $\delta s^{\times}_{\mathrm{xy,z}}(\boldsymbol{k})$ for the non-trivial phase transition with $\mathcal{V} = 1$ (figure above) and $\mathcal{V} = 2$ (figures below) for values of $h_{\mathrm{z}} > h_{\mathrm{t}}$ (right panel) and $h_{\mathrm{z}} < h_{\mathrm{t}}$ (left panel). The corresponding Berry curvatures are given in Figure IV.6 b). Similarly $\delta s^{\times}_{\mathrm{xy,z}}(\boldsymbol{k})$ is shown in Figures IV.10 a) and b) for $\mathcal{V} = 0$ realized by $f_1(\varphi)$ and $f_2(\varphi)$, respectively. The corresponding Berry curvatures for the latter are given in Figure IV.6 b) in the above panels. All these examples indicate a distinct correlation between the Berry curvature and $\delta s^{\times}_{\mathrm{xy,z}}(\boldsymbol{k})$. The momentum-resolved results of $\delta s^{\times}_{\mathrm{xy,z}}(\boldsymbol{k})$ are confirmed by the real space calculations for the example of $\mathcal{V} = -1$ shown in Figure IV.11.

These results demonstrates that the response of the polarization is of topological quality, since they indeed provide information about the spin vorticity and the spin polarization in the z-direction. The numerical observations therefore strongly suggest that the signatures are a clear indication of non-trivial spin-texture transitions and moreover imply that a momentum-resolved measurement of the spin polarization obtained from photoelectron spectroscopy [116] of the spin polarization could be used to visualize phase information about the Berry curvature.

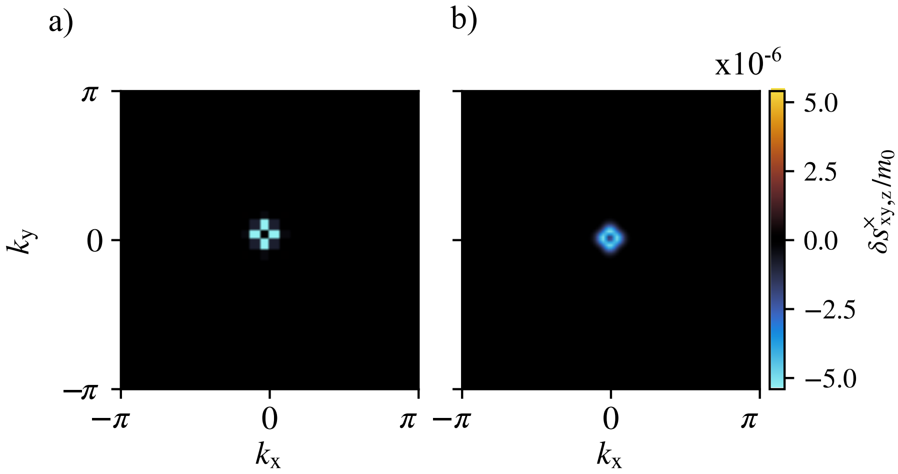

Figure IV.11.: Comparison of $\delta s^{\times}_{xy,z}(\boldsymbol{k})$ for a) N=20 with open boundary conditions with b) the results from second order perturbation theory using the representation of the position operator in the Bloch state basis. The values $h_x(0, y) = -0.0228t$, $h_x(L, y) = 0.0228t$, $h_x(x, 0) = -0.0228t$ and $h_x(x, L) = 0.0228t$, $\alpha = 0.25t$ and $h_z = h_{t,3} - 0.1t$ and $\mathcal{V}(\boldsymbol{k}_t) = -1$ have been used.

The dependence of $\delta m_{xy,z}$ on the direction of the magnetic field gradients is investigated. This dependence is displayed in Figure IV.12 a) and shows that the ratio of the system response depends on the direction of the magnetic field gradients. There, $\delta m_{xy,z}(\phi)$ and $\delta m^{\times}_{xy,z}(\phi)$ are plotted as a function of ϕ which is the angle between the directions of both applied magnetic field gradients. Of course, $\delta m^{\times}_{xy,z}(0) = \delta m^{\times}_{xy,z}(\pi) = 0$ since "cross" terms do not exist when both field gradients are parallel and these cross terms are largest for fully perpendicular field gradients. The dependence of $\delta m_{xy,z}$ on the angle ϕ is similar as in $\delta m^{\times}_{xy,z}(\phi)$ but at $\phi = 0$ the total change in the magnetization $\delta m_{xy,z} \neq 0$. Its change is minimal at $\phi = \pi/2$ where the contributions from the gradient in y-direction and the gradient in x-direction are partially canceling and maximal at $\phi = 3\pi/4$ where both gradient directions are constructively adding.

These results strongly suggest that the signature in $\delta s^{\times}_{xy,z}(\boldsymbol{k})$ is related to the Berry curvature and sufficient to conclude non-trivial spin-texture transitions. Furthermore, these results imply that analyzing $\delta m^{\times}_{xy,z}$ allows one to conclude whether the skyrmion number has increased or decreased since trivial combinations of spin-texture transitions at distinct vortices seem to lift away and the transitions for a vortex-texture and an antivortex texture differs by a sign.

Topological s-wave superconductor

To confirm the applicability of the above analysis of magnetization in a second-order perturbation theory, the topological s-wave superconductor is studied analogously. However, the following solutions were not generated in self-consistent calculations which may lead to additional peculiarities in the results not considered in this thesis. At first, the results are analyzed in the immediate vicinity of the topological phase transition. The contributions to the linear response terms around the topological phase transition in the low filling regime are equivalent to those of the QWZ-model

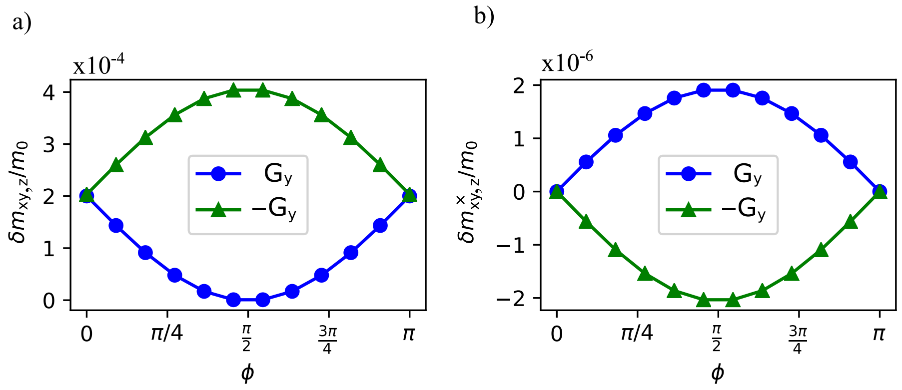

Figure IV.12.: Figures a) and b) show $\delta m_{\mathrm{xy,z}}(\phi)$ (left) and $\delta m^{\times}_{\mathrm{xy,z}}(\phi)$ right). The definition of ϕ is given in the main text. The magnetic field gradient is used such that $h_{\mathrm{x}}(0, y) = -0.0228t$, $h_{\mathrm{x}}(L, y) = 0.0228t$, $h_{\mathrm{x}}(x, 0) = -0.0228t$ and $h_{\mathrm{x}}(x, L) = 0.0228t$. Further, $h_{\mathrm{z}} = h_{\mathrm{t},3} - 0.1t$ was taken.

which can show distinct signatures at the phase transitions, but the existence of such signals are not dependent on topologically non-trivial spin-texture transitions.

As further confirmation, the solutions obtained from the real space calculations with open and periodic boundary conditions are shown in Figure IV.13 a) for $\delta m^{\times}_{\mathrm{xy,z}}$. The topological phase transition is clearly indicated in $\delta m^{\times}_{\mathrm{xy,z}}$. The blue and the green curve show the results applying open boundary conditions for a system with size $N = N_{\mathrm{x}} = N_{\mathrm{y}} = 40$ and $N = 60$, respectively. The orange curve corresponds to the calculations with periodic boundary conditions. As for the QWZ-model, the difference between the results for periodic boundary conditions and for open boundary conditions is larger in the topological non-trivial phase which could be attributed to the occurrence of topological edge modes. The analysis of the edge mode contributions are still under investigation. Nevertheless, the results allow to conclude that the solutions for the open boundary conditions converge to the solutions for the periodic boundary conditions as a function of the system size.

The linkage of the response in the spin polarization from second order perturbation theory with the Berry curvature is also confirmed for the topological s-wave superconductor. Figure IV.13 b) displays the Berry curvature $\Omega_{\mathrm{B}}(\boldsymbol{k})$ and $\delta m^{\times}_{\mathrm{xy,z}}(\boldsymbol{k})$ in momentum space. The agreement of the results compared with those of the two-band model is apparent. Just like the Berry curvature, $\delta m_{\mathrm{xy,z}}$ does not depend on the direction how the spins point around the vortex cores, but on the vorticity.

Thus, the results demonstrate that the signatures of the topological phase transition for the QWZ model also apply to the topological s-wave superconductor. After all, these topological systems are quite different. The QWZ model is a two-band model while the superconductor is effectively a four-band model. Also, both systems are significantly different in terms of their topological spin textures. The QWZ model possesses skyrmion type spin textures whereas the topological s-wave superconductor has a meron like spin texture. However, this example demonstrates the applicability of the study of $\delta m^{\times}_{\mathrm{xy,z}}$ to a system other than the QWZ model.

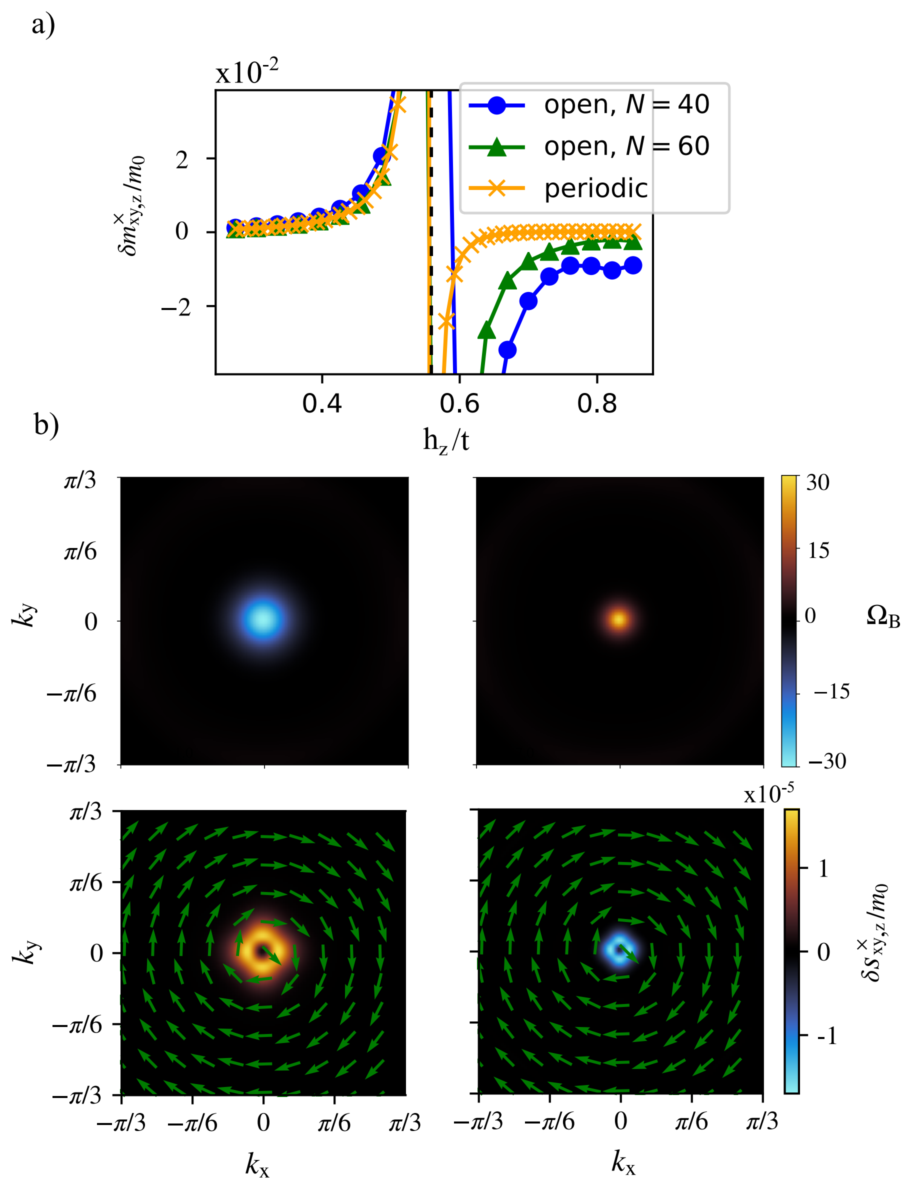

Figure IV.13.: a) $\delta m^{\times}_{xy,z}$ in the topological s-wave superconductor for different system sizes for open boundary conditions and for periodic boundary conditions. b) Ω_B (figures above) and $\delta s^{\times}_{xy,z}(\boldsymbol{k})$ (figures below) in the trivial phase (left) and the non-trivial phase (right).

IV.7. Scales and temperature dependence

In the analyses above, a magnetic field gradient is applied to a translation invariant system while the magnetic field is set to a specific value at the ends of a finite size system (in the two dimensional setup as sketched in Figure IV.3). Then, the size of the system is changed while keeping the magnetic field at the system edges constant. This way it is guaranteed that the magnetic fields do not become too large at the edges of the system. As shown in the results above, the thermodynamic signatures of the topological phase transition is increasing towards the topological phase transition. The signatures in the finite size systems or in periodic systems with the Bloch state representation are finite. The question arises, how large the signature can become and if they are measurable.

For this purpose, the linear perturbation theory term and $\delta m^{\times}_{\mathrm{xy,z}}$ are analyzed for large N for the QWZ-model and the topological s-wave superconductor. In the discussions above, the scale of the energy was in the range of the hopping energy t and units were used such that $k_{\mathrm{B}} = 1$ and $\hbar = 1$. In order to examine the size of the signatures, it is advantageous to specify the the quantities in common units. The magnetic induction is specified in Tesla (T) and the volume magnetization is given in the commonly used unit of emu/cm^3 while this converts into the SI units as 1 emu/cm^3= 10^3 A/m. In the following, the lattice spacing a=4Å is assumed and the tight binding hopping energy t=0.25 eV is set which corresponds roughly to the energy range of LAO/STO for such nearest neighbor tight binding hopping energies. The Rashba spin-orbit coupling $\alpha_{\mathrm{R}} = 25$ meV is chosen which is large but reasonable as the Rashba coupling in LAO/STO is within this range [43, 117].

Thus, in the equations used above, it is necessary to replace the magnetic field $\boldsymbol{h} \to \mu_{\mathrm{B}}\boldsymbol{B}$ in order to perform the calculations in SI units. The expectation values for the operator $\hat{\sigma_{\mathrm{z}}}$ are to be replaced such that $\langle n|\sigma^{\mathrm{TB}}_{\mathrm{z}}|m\rangle \to \mu_{\mathrm{B}}\langle n|\sigma^{\mathrm{TB}}_{\mathrm{z}}|m\rangle$. Further, the wave vector $\boldsymbol{k}$ has to be replaced by $\boldsymbol{k}\cdot a$ in the matrix elements of the tight-binding Hamiltonian. The changes in the spin polarization are thus given by

$$\delta s_{\mathrm{xy,z}}(\boldsymbol{k}) = \mu_{\mathrm{B}}^3 \sum_{j=1}^{2}\sum_{n_{\mathrm{occ}}}\sum_{\substack{m\neq n\\ u\neq n}}\left(\frac{t^{nmo}_{0,V_j}(\boldsymbol{k})}{\mu_{\mathrm{B}}} + \sum_{i=1}^{4}\sum_{p=1}^{2}\left(\sum_{\substack{l\neq n\\ v\neq l}} t^{nmluv}_{i,V_jV_p}(\boldsymbol{k})(\boldsymbol{k}) + \sum_{v\neq n} t^{nmuv}_{i,V_jV_p}(\boldsymbol{k})\right)\right)$$

$$\delta s^{\times}_{\mathrm{xy,z}}(\boldsymbol{k}) = \mu_{\mathrm{B}}^3 \sum_{j=1}^{2}\sum_{n_{\mathrm{occ}}}\sum_{\substack{m\neq n\\ u\neq n}}\sum_{i=1}^{4}\sum_{p=1}^{2}\left(\sum_{\substack{l\neq n\\ v\neq l}} t^{nmluv}_{i,V_jV_p}(\boldsymbol{k}) + \sum_{v\neq n} t^{nmuv}_{i,V_jV_p}(\boldsymbol{k})\right)$$

and one has

$$\mu_{\mathrm{B}} \approx 5.8\cdot 10^{-5}\frac{\mathrm{eV}}{\mathrm{T}}. \tag{IV.7.1}$$

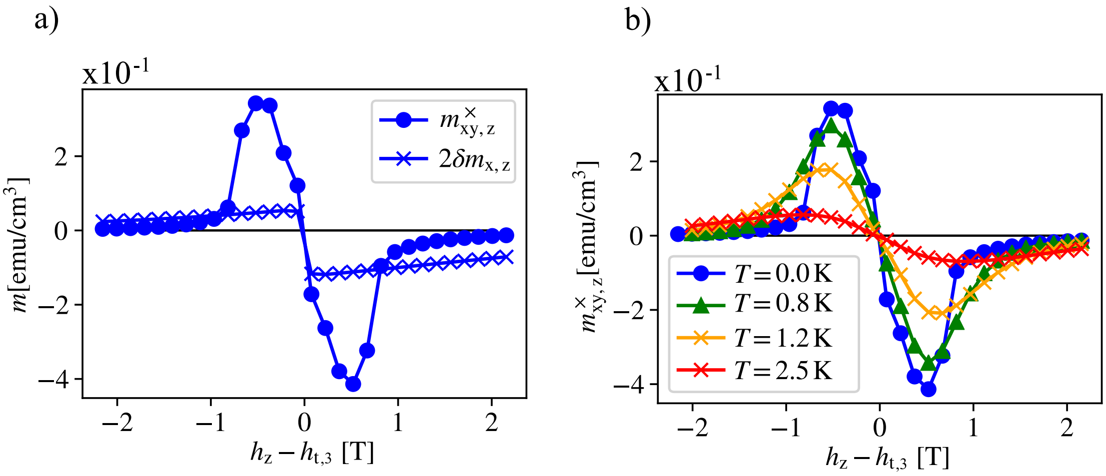

Figure IV.14.: a) Comparison of the linear perturbation terms $\delta m_{\mathrm{x,z}}$ with $\delta m^{\times}_{\mathrm{xy,z}}$; b) finite temperature calculations of $\delta m^{\times}_{\mathrm{xy,z}}$ using Equation (IV.5.5). The parameters used are $\alpha_{\mathrm{R}} = 0.2\,\mathrm{eV}$, $B_{\mathrm{x}}(0, y) = -0.1\,\mathrm{T}$, $B_{\mathrm{x}}(L, y) = 0.1\,\mathrm{T}$, $B_{\mathrm{y}}(x, 0) = -0.1\,\mathrm{T}$, $B_{\mathrm{y}}(x, L) = 0.1\,\mathrm{T}$.

In the following, the QWZ model is analyzed. There, a linear magnetic field gradient is applied such that $B_{\mathrm{x}}(0, y) = B_{\mathrm{y}}(x, 0) = -0.1\,\mathrm{T}$ and $B_{\mathrm{x}}(L, y) = B_{\mathrm{y}}(x, L) = 0.1\,\mathrm{T}$ while $L = L_{\mathrm{x}} = L_{\mathrm{y}}$. The (pseudo-) magnetic field $h_z - h_t$ is varied from $-2\,\mathrm{T}$ up to $2\,\mathrm{T}$. These values are reasonable for the usual magnetic fields and in pseudo-magnetic fields where the latter can even be several hundred Tesla in size [118]. Figure IV.14 a) depicts the comparison of the linear perturbations $\delta m_{\mathrm{x,z}}$ and the second order perturbation terms $\delta m^{\times}_{\mathrm{xy,z}}$ for the ground state. Close to the topological phase transition, the second order terms exceed the linear order terms until orders higher than the second order dominate where $\delta m^{\times}_{\mathrm{xy,z}}$ vanishes as $h_z - h_{t,3}$. The previous results have been calculated for the ground state $T = 0$. It is very important to determine how temperature affects the results. Therefore, $\delta m^{\times}_{\mathrm{xy,z}}$ is given as a function of $h_z - h_{t,3}$ at the distinct temperatures $T = 0, 0.8, 1.2, 2.5\,\mathrm{K}$. The results are within a common measuring range with a maximum of roughly $3 \cdot 10^{-1}\,\mathrm{emu/cm^3}$ in the ground state. Due to the finite temperatures, the signal is broadened. Further away from the phase transition, the signature is thus increased. In the vicinity of the phase transition, the signature is, on the other hand, decreased and the maximal amplitude of the signal is suppressed. This observation is in accordance with the expected usual broadening of thermodynamic signatures at finite temperatures. For the chosen parameter set, the maximal amplitude of the signature at 2.5 K is roughly eight times smaller than the maximum of ground state amplitude.

Such magnetizations may be measured using SQUID (Superconducting Quantum Interference Device) magnetometers [119, 120]. Common SQUID magnetometers can measure magnetization with very high sensitivity allowing to measure magnetic moments $\leq 10^{-8}$ emu [121] in external magnetic inductions up to several Tesla [122]. In the context of pseudo-spins, pseudo-magnetic fields have to be measured [57, 123]. Such investigation capabilities depend on the particular systems in question. A detailed discussion of possible implementations in specific pseudo-spin systems is extensive and is beyond the scope of this thesis.

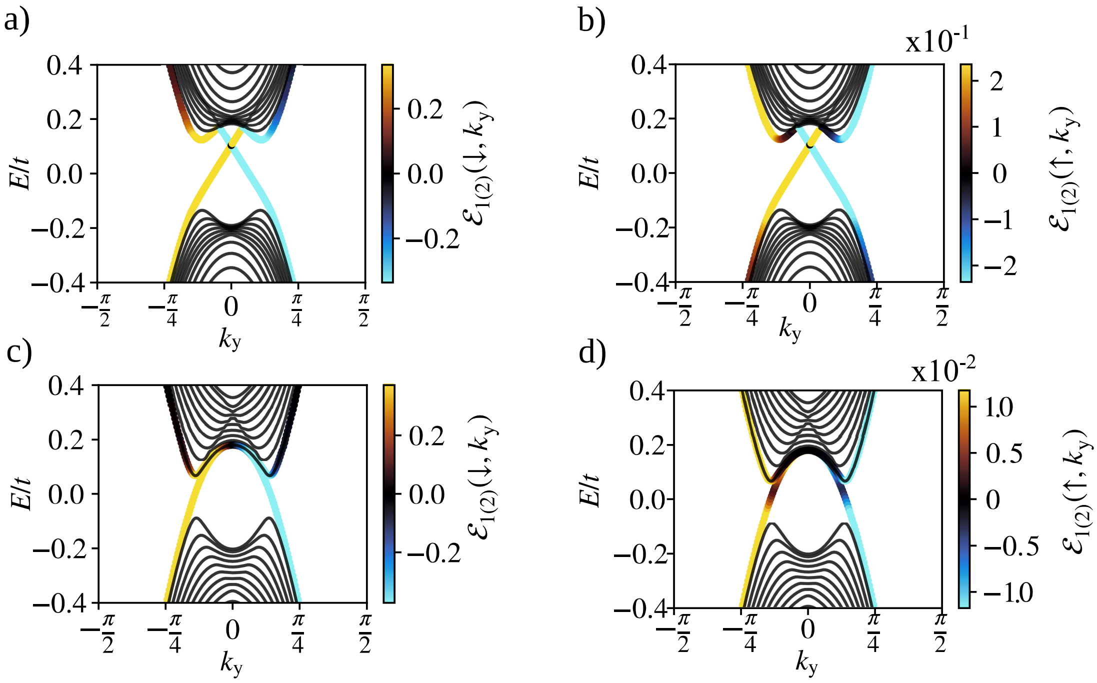

Figure IV.15.: Dispersion in the QWZ model for a gradient field with a) $h_x(0) = -0.1t$ and $h_x(L) = 0.1t$ and b) $h_x(0) = -0.3t$ and $h_x(L) = 0.3t$. Edge modes found at $r_x = 0$ are yellow and edge modes found at the $r_x = L$ are light blue. Further, $h_z = h_{t,3} - 0.2t$ and $\alpha_R = 0.25t$ was used.

IV.8. Influence of magnetic gradient fields on topological edge states

Topological states are most often characterized by topological edge states rather than by topological bulk properties. It is thus the question how the magnetic gradient terms affect the edge states and whether topological phase transitions can be driven by the gradient terms. This question is discussed exemplarily for the QWZ model and the topological s-wave superconductor. The findings described in Section III.3 show that the bulk boundary correspondence is fulfilled in the s-wave superconductor but chiral edge states exist even in the topological trivial phase in this system. The matrix elements of the current density operator is defined as [2]

$$\langle \boldsymbol{k}, n | \hat{\boldsymbol{J}} | \boldsymbol{k}, n \rangle = ne\hat{v} = ne\langle \boldsymbol{k}, n | \frac{\partial H}{\partial \boldsymbol{k}} | \boldsymbol{k}, n \rangle \tag{IV.8.1}$$

where n and e denote the density and the elementary charge, respectively. The edge currents for the QWZ model and the topological s-wave superconductor in the topological and trivial bulk phases are shown in Figures A.1 and A.2, respectively. In those figures, the expectation values have been calculated spin-resolved, distinguishing ↑-spins and ↓-spins through the calculation of the matrix elements

$$J_n(s, \boldsymbol{k}) = \langle \boldsymbol{k}, n | \hat{s}\hat{\boldsymbol{J}} | \boldsymbol{k}, n \rangle \tag{IV.8.2}$$

with $\hat{s} \in \{\hat{\uparrow}, \hat{\downarrow}\}$ where $\hat{\uparrow}$ and $\hat{\downarrow}$ denote the ↑-spin and ↓-spin operators, respectively. Boundary states and edge currents are absent in the topologically trivial phase in the QWZ model. It is therefore important to investigate how the magnetic field gradients affect the boundary states in both systems.

The topological edge states are displayed in Figure IV.15 a) to d) for the QWZ model at a nonzero magnetic field gradient. Subfigure IV.15 a) shows the dispersion in the non-trivial phase. The bulk states are black and the edge modes are colored analogously as introduced in Section III.3. For a vanishing magnetic field gradient, the band crossing is found at $E/t = 0$ as given in Figure III.12. However, for this non-vanishing field gradient, the band crossing is lifted in energy. The linear band crossing of the edge modes is, nevertheless, preserved. The comparison of Subfigure IV.15 a) and b) shows that the edge states remain within the bulk gap for ↑-spin and ↓-spin at the edges. For a large enough field gradient the band crossing is moved into the bulk bands. While the states in the bulk gap retain a ↓-spin expectation value at the edge, shown in Subfigure IV.15 c). The ↑-spin states are moved into the bulk as the colors indicate in Subfigure IV.15 d).

The effect of the magnetic field gradient on the states higher in energy is weaker then on the states smaller in energy. The effect on the bulk states is therefore weaker than on the edge states which is evident from the comparison of Figures IV.15 a and b) with c) and d). The edge modes are shifted by around $0.2t$ which corresponds to the energy scale of the applied magnetic field at the boundary. This observation is consistent with the expectation that the states localized at the edge are most strongly modified by the magnetic field gradient. As a result, the band crossing is shifted in energy into the energy range of the bulk states. This creates touching points of the bulk bands with the boundary bands which show a non-linear dispersion at the touching point.

The effects of the dispersion on the trivial phase is not shown. However, the gradient terms have not been identified to drive topological ground state phase transitions.

The topological superconductor, on the other hand, has edge states in the trivial and topological phases. Figures IV.17 shows the dispersion when a small (relative to the band gap) gradient field is used. As in the QWZ model, the boundary states are lifted in energy. The non-trivial phase is given in Subfigure IV.17 c) and d) for the corresponding expectation values. The dependence of the edge states on the gradient field is analogous to that in the QWZ-model. In the trivial phase, however, the states in the bulk gap close to the Γ-point are shifted towards the bulk states, The edge states in between $\pm\pi/2$ and $\pm\pi/4$ are lifted in energy. Figures IV.17 a) and b) show the dispersion for an applied magnetic gradient field in the trivial phase for a small applied magnetic field gradient. Like in the non-trivial phase, two band crossings emerge for even larger magnetic field gradients. Subfigures IV.17 c) and d) shows the bandcrossing to be shifted into the bulk states just as in the QWZ-model for a larger magnetic field gradient.

Similar results are shown in Figures IV.17 e) to h) for the dispersion in the topologically non-trivial phase. In small magnetic field gradients the bands of the edge modes are lifted in energy and a magnetic field gradient exists at which the edge modes are energetically shifted into the energy range of the bulk modes.

Edge states, which are energetically still in the band gap, are not significantly pushed from the edge into the bulk. Thus, edge states do not disappear by the application of gradient fields. A topological state can thus be described by the existence of edge states even in the presence of the gradient fields. However, topological band crossing points are energetically shifted.

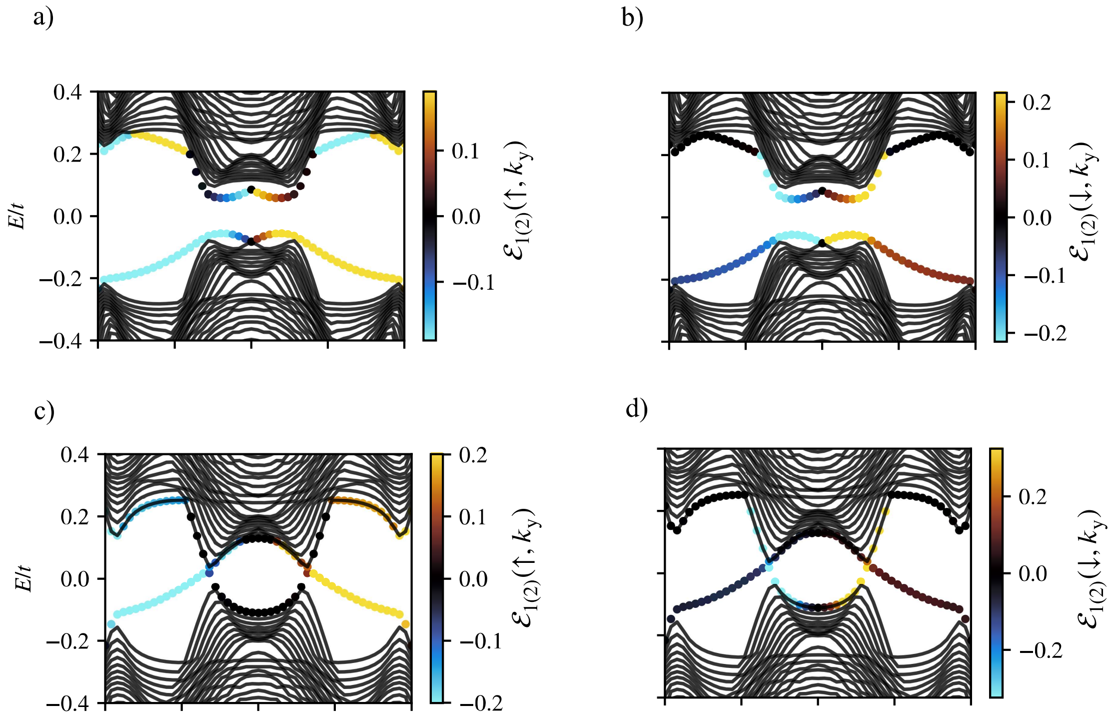

Figure IV.16.: Dispersion in the topological phase of the topological s-wave superconductor for $h_z = h_{t,3} - 0.2t$ for a gradient field with a) and b) $h_x(0) = -0.1t$ and $h_x(L) = 0.1t$, and c), d) $h_x(0) = -0.3t$ and $h_x(L) = 0.3t$. Edge modes found at $r_x = 0$ are yellow and edge modes found at the $r_x = L$ are light blue. Further, $\alpha_R = 0.25t$, $\mu = -3.2t$ and $\Delta = 0.5t$ was used.

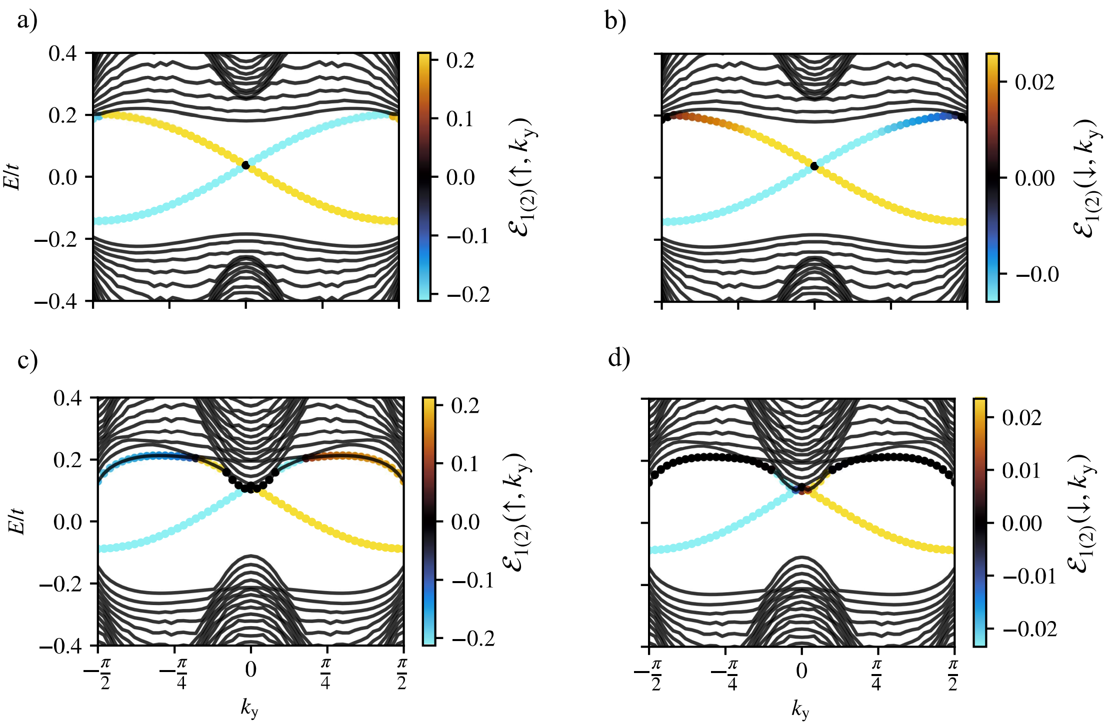

Figure IV.17.: Dispersion in the topological phase of the topological s-wave superconductor for $h_z = h_{t,3} - 0.2t$ for a gradient field with a) and b) $h_x(0) = -0.1t$ and $h_x(L) = 0.1t$, and c), d) $h_x(0) = -0.3t$ and $h_x(L) = 0.3t$. Edge modes found at $r_x = 0$ are yellow and edge modes found at the $r_x = L$ are light blue. Further, $\alpha_R = 0.25t$, $\mu = -3.2t$ and $\Delta = 0.5t$ was used.

V. Outlook

The thermodynamic response signals for in-plane magnetic field gradients are shown to be related to non-trivial spin-texture transitions. This relation has been verified for arbitrary vorticities and qualitative information about whether a skyrmion number is increased or decreased across a phase transition has been extracted from such signals. Furthermore, it is of great interest to quantitatively evaluate the response in the magnetization to possibly extract information about the value of the topological invariants in the respective phases. These investigations are still ongoing. If such quantitative information can be identified from a bulk measurement, it would be a significant finding and provide an alternative to measuring changes in topological invariants. Therefore, it is important to gain a deeper understanding of the relation between the Berry curvature and the signature in the magnetization due to the in-plane magnetic field gradients. The results presented here suggest that the signatures in the magnetization are directly associated with non-trivial spin-texture transitions. A rigorous analytical proof has not been accomplished yet and further studies may be necessary.

The experimental realization seems to be possible in general. However, further discussion is needed concerning the experimental implementation. The realization of the necessary gradient fields can, for example, be achieved by common gradient coils [124]. Another possibility could be magnetic surface engineering which allows for very large magnetic field gradients [125]. In Reference [126], for example, magnetic field gradients of up to $5 \cdot 10^5$ T/m have been reported. The measurability in pseudo-spin systems depends on the system in question. Highly strained graphene for example, where strain acts as a pseudo-magnetic field, fields up to 300 T have been attained [127]. Pseudo-spins have been measured [57] and therefore an investigation as presented in this work could be carried out in principle.

As a further step, especially in the superconducting systems, the orbital coupling effects of the magnetic field should be taken into account by the inclusion of the Peierls phase as discussed in Section II.2. Such orbital coupling is responsible for the formation of vortex states and thus largely determines the critical field at which superconductivity breaks down. The study of superconducting systems is special in many ways. The topological s-wave superconductor studied in this work was treated partially self-consistent. In particular, in the case of gradient fields, a self-consistent calculation of the order parameter was waived. Such self-consistency is very significant, but also requires a considerable effort that could not yet be accomplished within the scope of this work. It is suggested that the self-consistent investigation be addressed in further studies.

A particular difficulty of the topological s-wave superconductor is the realization of non-trivial topological states. Other topological superconductors may be better suited to realize topologically non-trivial states. It is therefore important to investigate whether the response of magnetization in the z-direction to in-plane magnetic gradient fields in other superconducting systems is suitable for an unambiguous identification of topological phase transitions.

Edge states and edge currents have been identified in the topologically trivial phase of the s-wave superconductor. A closer study of the influence of the edge states on the response of the magnetization to the magnetic field gradients is an interesting task that should be addressed in future investigations.

VI. Summary

Topological phases in two-dimensional electronic systems are usually described by a non-trivial Berry phase which is related in many cases to non-trivial topological pseudo-spin textures. Within this thesis, connections between topological spin-texture transitions and thermodynamic signatures are investigated. Thermal responses of topological spin textures in homogeneous external magnetic fields can show signatures at the topological phase transitions. These are, however, not limited to non-trivial topological phase transitions.

The results in this thesis strongly suggest the existence of unique signatures of topological phase transitions manifest in the quadratic response terms of the spin polarization to external magnetic field gradients. These signatures in the spin magnetization are generated by mutually perpendicular magnetic field gradients. The signatures are contained in cross terms defined by the difference between the total magnetization response to the magnetic field gradient in two mutually perpendicular directions within the plane and the sum of the individual magnetization responses to the respective gradient field directions. These signatures represent a new type of thermodynamic analysis appropriate to analyze topological phase transitions.

The signals show to be significantly enhanced towards the phase boundary with a sign change across the phase transition. The sign in the change of the magnetization yields information about changes in the skyrmion number characterizing the non-trivial spin textures. The quadratic response of the spin polarization does therewith also yield information about Chern number transitions because, if existent, non-trivial spin-textures are related to non-trivial Berry phases. While linear response of conductivity of topologically non-trivial systems in electric fields depends on boundary states, magnetization response in magnetic gradient fields is a bulk quantity. Besides the quadratic response signature, linear response terms in the magnetization to a magnetic field gradient can also show signatures at the phase transitions. It is shown that the linear response is, however, not sufficient to describe non-trivial spin-texture transitions.

Both, the response of the magnetization in homogeneous magnetic fields and in magnetic gradient fields are discussed exemplarily in the Qi-Wu-Zhang model, a non-trivial Chern insulating system, and in the topological s-wave superconductor with Rashba spin-orbit coupling. The dependence on the temperature and on finite size effects of thermodynamic signatures were also discussed in these systems. Finite temperatures are manifest in a broadening of the signatures, where the scale for which the cross terms in the magnetization response remain in the range of the ground state signature is set by the scale of the Zeeman splitting at the boundaries. The explicit calculation with usual energy scales shows that the described cross terms provide signals in the measurable range. The finite size calculations show distinct dependencies on the boundary conditions in small systems which however vanish as the system increases.

Because non-trivial spin phases are only defined in the continuum description, topological phases cannot be described in finite size systems. Here a topological spin-texture character is introduced which is equivalent to the topological phase invariant in the continuum limit but which can be defined in finite size lattice models by the identification of vortex textures. It is shown that the topological character of the spin textures depends on the size of the system and transitions between topological character phases can be caused by a change of the systems size. Therefore, the character of the spin texture is a function of the parameters of the Hamiltonian and the size of the system. In contrast to the QWZ-model, the topological spin-texture character is found to be trivial at any finite size in the topological s-wave superconductor. A similar conclusion can be drawn from finite temperature calculations. The topological phases in the QWZ-model are stable against finite temperature, whereas the topological character in the topological s-wave superconductor is destroyed. The spin-texture of the topological s-wave superconductor is therefore highly fragile due to a meron-like spin texture.

Furthermore, a connection between the Chern number and the skyrmion number in terms of topological spin textures is shown to be still present in mixed parity superconductors with s-wave and $p_\mathrm{x} + \mathrm{i} p_\mathrm{y}$ triplet admixture. At topological phase transitions, vortex-antivortex pairs can emerge or disappear showing that the type of vorticity and the total number of vorticities can vary at different topological phases.

As pointed out, another possibility to describe non-trivial topological bulk states is the identification of chiral and gapless edge states showing linear crossing points of the edge modes within the bulk gap (in finite size systems) which is referred to as the bulk-boundary correspondence. In both analyzed systems, the bulk boundary correspondence is fulfilled. However, the analysis in this thesis shows that significant differences in the QWZ-model and the topological s-wave superconductor regarding the edge states exist. While edge states are only present in topological non-trivial phases in the QWZ-model, chiral but gapped edge modes have been identified in the topological s-wave superconductor also in the trivial phase. Moreover, chiral edge currents can be obtained in the topological s-wave superconductor in both, the trivial and the topological phase. These observations suggest that a topological characterization of the topological s-wave superconductor through edge modes may be fraught with difficulties. A bulk thermodynamic description of topological phase transitions can therefore be essential in particular in topological superconductors.

Appendix

Additional information and derivations of equations from main text are given below. The appendix consists on the one hand of detailed summaries of known results from the literature, on the other hand detailed calculations of the results of this thesis are presented.

A.1. Derivative of eigenvalues and eigenvectors

The first derivative of an eigenvector can be found with the normalization condition together with the eigenvalue equation. The following derivation of the derivative of an eigenvector or an eigenvalue can be found in the literature [128–130]. The eigenequation and the normalization condition reads

$$(\boldsymbol{M} - \lambda_i)v_i = 0; \quad v_i^\dagger v_i = 1 \tag{A.1.1}$$

where $\boldsymbol{M}$ denotes some hermitian matrix with eigenvalues λ and eigenvectors v. The derivative of the eigenvalue equation is taken, yielding

$$(\boldsymbol{M} - \lambda_i)\dot{v}_i + (\dot{\boldsymbol{M}} - \dot{\lambda}_i)v_i = 0; \tag{A.1.2}$$

Multiplying with $v_i^\dagger$ on the left hand side of (A.1.2) yields $\dot{\lambda}$

$$\begin{aligned} v_i^\dagger(\boldsymbol{M} - \lambda_i)\dot{v}_i + v_i^\dagger(\dot{\boldsymbol{M}} - \dot{\lambda}_i)v_i &= 0 \\ \Leftrightarrow (\lambda_i - \lambda_i)\dot{v}_i + v_i^\dagger(\dot{\boldsymbol{M}} - \dot{\lambda}_i)v_i &= 0 \\ \Leftrightarrow v_i^\dagger \dot{\boldsymbol{M}} v_i &= \dot{\lambda}_i. \end{aligned} \tag{A.1.3}$$

The derivative of the eigenvector can be obtained by multiplying (A.1.2) with $v_j^\dagger$ while $j \neq i$, yielding

$$v_j^\dagger \boldsymbol{M} \dot{v}_i - \lambda_i v_j^\dagger \dot{v}_i + v_j^\dagger \dot{\boldsymbol{M}} v_i - \dot{\lambda} v_j^\dagger v_i = 0 \tag{A.1.4}$$

from $v_j^\dagger v_i = 0$ one has $\dot{v}_j^\dagger v_i + v_j^\dagger \dot{v}_i = 0$. We have

$$\begin{aligned} v_j^\dagger \boldsymbol{M} \dot{v}_i - \lambda_i v_j^\dagger \dot{v}_i + v_j^\dagger \dot{\boldsymbol{M}} v_i &= 0 \\ \Leftarrow v_j^\dagger \dot{v}_i &= \frac{v_j^\dagger \dot{\boldsymbol{M}} v_i}{\lambda_i - \lambda_j} \end{aligned} \tag{A.1.5}$$

and thus, the derivative of an eigenvector can be determined by

$$\dot{v}_i = \sum_{j \neq i} \frac{v_j^\dagger \dot{\boldsymbol{M}} v_i}{\lambda_i - \lambda_j} v_j. \tag{A.1.6}$$

A.2. Supplemental figures on the magnetization response and on edge state calculations

Below, additional figures are provided to supplement the results of the main text where the references to these figures are given.

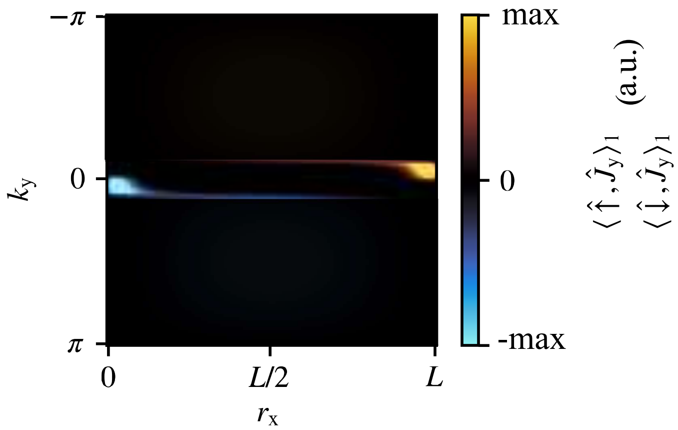

Figure A.1.: Edge currents in the QWZ model. a) Edge currents with ↑-spin or similarly ↑-spin expectation values for $h_z = h_{t,3} - 0.2t$ and $\alpha_R = 0.25\,t$.

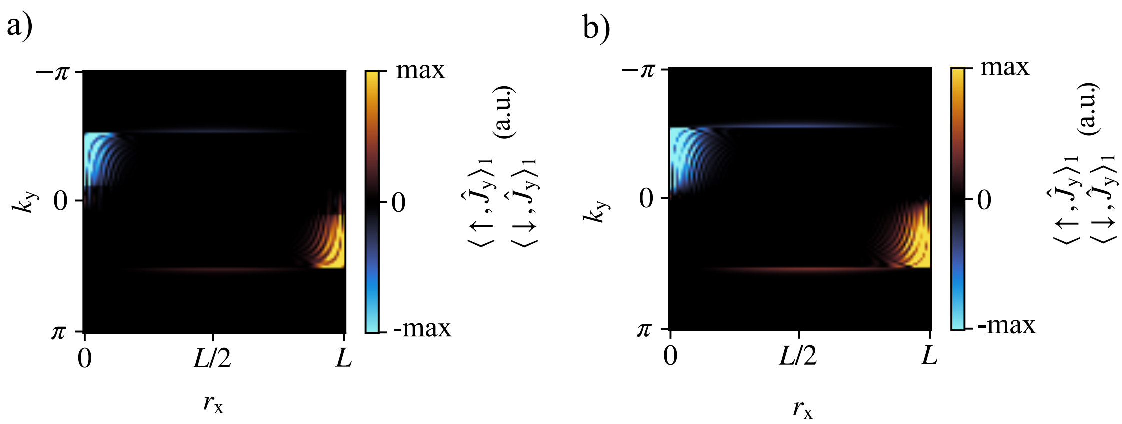

Figure A.2.: Edge currents in the topological s-wave superconductor in a) the trivial and b) the non-trivial phase. The results are clearly similar. Parameters used are $h_z = h_{t,1} \pm 0.1t$, $\alpha_R = 0.25t$, $\Delta = 0.5t$ and $\mu = -3.2t$. The results are not obtained from self consistent calculations.

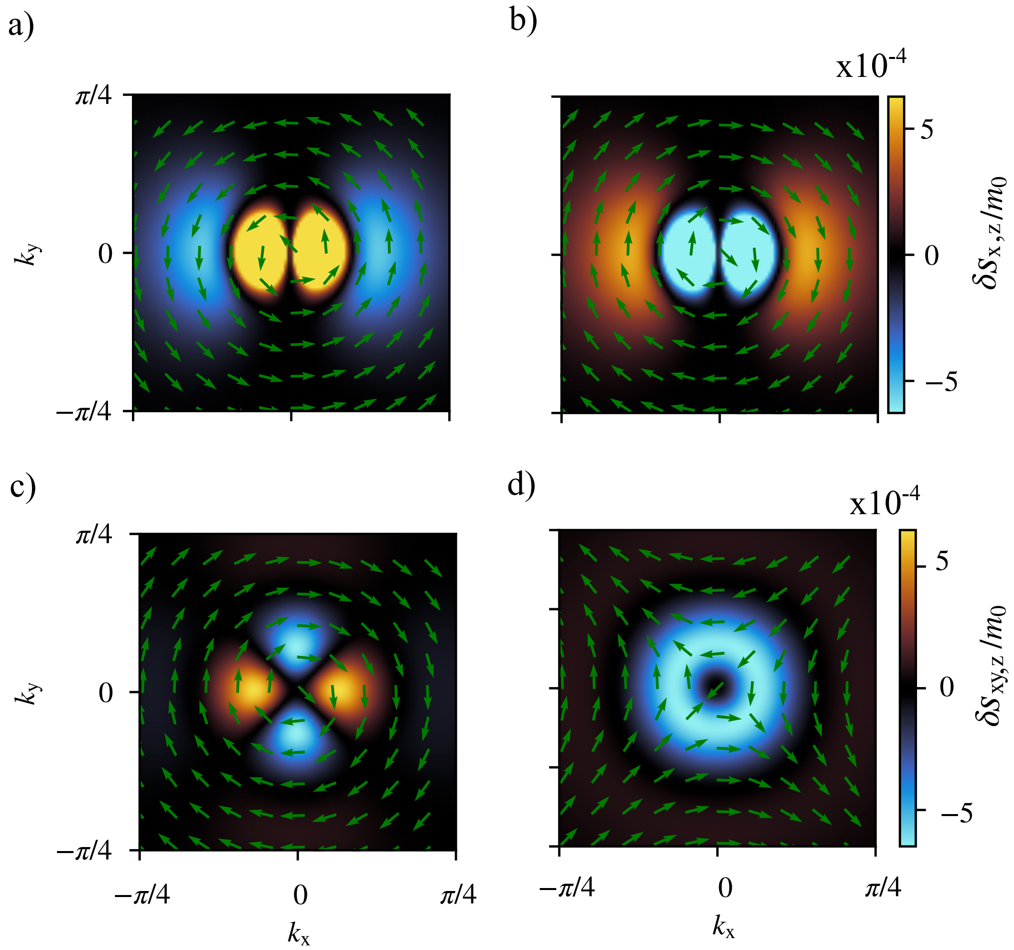

Figure A.3.: Linear response in the polarization to an in-plane magnetic field gradient. $\delta s_{x,z}/m_0$ is shown for a) $\mathcal{V} = 1$ and for b) $\mathcal{V} = -1$ in the QWZ model. In addition, the total change in the magnetization $\delta s_{xy,z}$ for $\mathcal{V} = 1$ in c) an anticlockwise spin alignment and d) an clockwise spin alignment around a vortex center are depicted. The magnetic fields are $h_x(0, y) = -0.0228t$, $h_x(L, y) = 0.0228t$, $h_x(x, 0) = -0.0228t$ and $h_x(x, L) = 0.0228t$ and $\alpha_R = 0.25t$.

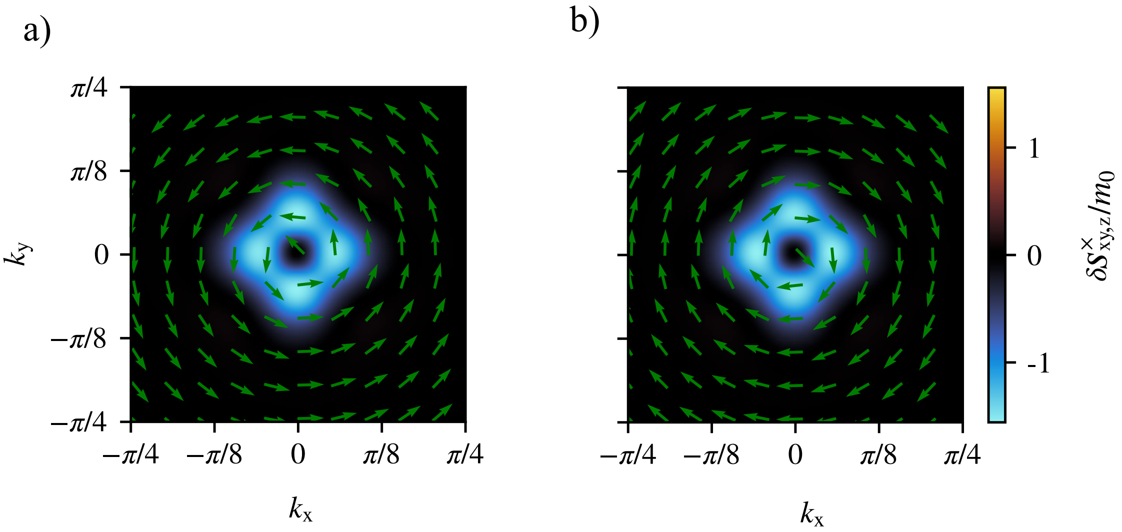

Figure A.4.: The figure shows the cross terms $\delta s^{\times}_{\mathrm{xy,z}}$ for $\mathcal{V} = 1$ in a) an anticlockwise spin alignment and b) a clockwise spin alignment around a vortex center. The magnetic fields are $h_\mathrm{x}(0, y) = -0.0228t$, $h_\mathrm{x}(L, y) = 0.0228t$, $h_\mathrm{x}(x, 0) = -0.0228t$ and $h_\mathrm{x}(x, L) = 0.0228t$. Further, $\alpha_\mathrm{R} = 0.25t$.

A.3. Thermodynamic potential of the topological s-wave superconductor

By use of the Grassmann algebra of which the basics are given in Appendix A.7, the partition function and therefore the grand canonical potential for the topological s-wave superconductor can be obtained. These results are well known and found for example in References [131]. However, for completeness, the calculation is presented in the following. The Hamiltonian for the topological s-wave superconductor is given in the introduction of the main text. Using Equation (A.7.25) and (A.7.26), the partition function of the topological s-wave superconductor can be obtained which reads

$$\begin{aligned}\mathcal{Z} = \int \mathcal{D}\phi^* \mathcal{D}\phi \, \exp \Bigg[N\beta\frac{\mu}{2} + \frac{1}{2}\int_0^{\hbar\beta} \mathrm{d}\tau \Big[-\frac{1}{\hbar}\sum_{\boldsymbol{k}} \boldsymbol{\phi}^*_{\boldsymbol{k}}(\tau)\big[\hbar\frac{\partial}{\partial\tau} + \epsilon(\boldsymbol{k}) + \epsilon_\mathrm{R}(\boldsymbol{k}) + \epsilon^\mathrm{Z}\big]\boldsymbol{\phi}_{\boldsymbol{k}}(\tau)\Big] \\ + \frac{V}{N\hbar}\sum_{\boldsymbol{k},\boldsymbol{k}'}\sum_{\boldsymbol{q}}\sum_{s,s}(\mathrm{i}\sigma_\mathrm{y})_{s,s'}\phi^*_{\boldsymbol{k},s}\phi^*_{-\boldsymbol{k}+\boldsymbol{q},s'}\phi_{-\boldsymbol{k}'+\boldsymbol{q},s'}\phi_{\boldsymbol{k}',s}\Bigg]. \end{aligned} \tag{A.3.1}$$

where $\epsilon(\boldsymbol{k})$ and $\epsilon_\mathrm{R}(\boldsymbol{k})$ are defined in the main text (Equation II.2.7 and II.2.11, respectively) and $\epsilon^\mathrm{Z} = \boldsymbol{B\sigma}$ denotes the Zeeman splitting while the vector notation $\boldsymbol{\phi}^*_{\boldsymbol{k}} = (\phi^*_{\boldsymbol{k},\uparrow}, \phi^*_{\boldsymbol{k},\downarrow})^\mathrm{T}$ is introduced. Combining two Grassmann fields such that [51]

$$B^\dagger(\boldsymbol{q}) = \sum_{\boldsymbol{k}}\sum_{\sigma_1,\sigma_2}(\mathrm{i}\sigma_y)_{\sigma_1,\sigma_2}\phi^*_{\boldsymbol{k},\sigma_1}\phi^*_{-\boldsymbol{k}+\boldsymbol{q},\sigma_2} \tag{A.3.2}$$

the partition function can be brought to the form

$$\mathcal{Z} = \int \mathcal{D}\phi^*\mathcal{D}\phi \,\exp\left[N\frac{\beta\mu}{2}\int_0^{\hbar\beta}\mathrm{d}\tau\Big[-\frac{1}{\hbar}\sum_{\boldsymbol{k}}\boldsymbol{\phi}^*_{\boldsymbol{k}}(\tau)\big[\hbar\frac{\partial}{\partial\tau}+\epsilon(\boldsymbol{k})+\epsilon_{\mathrm{R}}(\boldsymbol{k})+\epsilon^{\mathrm{Z}}\big]\boldsymbol{\phi}_{\boldsymbol{k}}(\tau)\Big] + \frac{V}{\hbar}\sum_{\boldsymbol{q}}B^\dagger(\boldsymbol{q})B(\boldsymbol{q})\right]. \quad \text{(A.3.3)}$$

The two particle interaction term contains the product of four Grassmann fields included in the product of the two $B(\boldsymbol{q})$. It is well known how to solve the one-particle partition functions with the use of the Gaussian integrals. Therefore, it is highly advantageous to rewrite the two-particle interaction term in a form of one particle terms by use of the Hubbard-Stratonovich transformation [132, 133] which introduces an auxiliary scalar complex field Δ. Let $a, b \in \mathbb{C}$ and $\Delta = u + iv$ with $u, v \in \mathbb{R}$, then the Hubbard-Stratonovich transformation reads [134]

$$\mathrm{e}^{ab} = \frac{1}{\pi}\int \mathcal{D}\Delta^*\mathcal{D}\Delta\, \mathrm{e}^{a\Delta+b\Delta^*-|\Delta|^2}. \quad \text{(A.3.4)}$$

By use of (A.3.4) the interaction term in the partition function (A.3.3) becomes

$$\exp\left[\frac{V}{2\hbar}\int_0^{\hbar\beta}\mathrm{d}\tau\sum_{\boldsymbol{q}}B^\dagger(\boldsymbol{q})B(\boldsymbol{q})\right] = \int \mathcal{D}\Delta\mathcal{D}\Delta^*\exp\left[\frac{1}{\hbar}\int_0^{\hbar\beta}\mathrm{d}\tau\sum_{\boldsymbol{q}}\left(B^\dagger(\boldsymbol{q})\Delta(\boldsymbol{q})+B(\boldsymbol{q})\Delta^*(\boldsymbol{q})-\frac{|\Delta(\boldsymbol{q})|^2}{V}\right)\right]. \quad \text{(A.3.5)}$$

Inserting (A.3.5) leads to a form of the partition function (A.3.3) that is only dependent on one particle terms — which means that only products of two Grassmann fields occur and the integration of the fermionic degree of freedom is hence possible in with a Gaussian integration. It has to be emphasized that the partition function given in (A.3.5) is exact — approximations are however necessary for the following analysis and are discussed in the following.

Defining the order parameter

$$\Delta_{\sigma_1,\sigma_2}(\boldsymbol{q},\boldsymbol{k},\tau) = \Delta(\boldsymbol{q},\tau)\mathrm{i}\sigma_{\mathrm{y}_{\sigma_1,\sigma_2}} \quad \text{(A.3.6)}$$

in the Nambu spin basis

$$\tilde{\phi}^\dagger = (\phi^*_{\boldsymbol{k},\uparrow}, \phi^*_{\boldsymbol{k},\downarrow}, \phi_{-\boldsymbol{k}+\boldsymbol{q}_1,\uparrow}, \phi_{-\boldsymbol{k}+\boldsymbol{q}_1,\downarrow}, \phi_{-\boldsymbol{k}+\boldsymbol{q}_2,\uparrow}, \phi_{-\boldsymbol{k}+\boldsymbol{q}_2,\downarrow}, \dots)^{\mathrm{T}}, \quad \text{(A.3.7)}$$

the partition function can be integrated out with the use of (A.7.31) yielding the grand canonical potential

$$\Omega = -\frac{1}{\beta}\ln\left(\int \mathcal{D}\Delta\mathcal{D}\Delta^*\exp\left[N\beta\frac{\mu}{2}-\frac{1}{\hbar}\int_0^{\hbar\beta}\mathrm{d}\tau\left(-\frac{1}{2}\sum_{\boldsymbol{k}}\sum_{\boldsymbol{q}}\mathrm{Tr}\left(\ln\left[\mathcal{G}^{-1}(\tau,\boldsymbol{k},\boldsymbol{q})\right]\right) + \sum_{\boldsymbol{q}}\frac{|\Delta(\boldsymbol{q})|^2}{V}\right)\right]\right), \quad \text{(A.3.8)}$$

where $\mathcal{G}^{-1}$ is the inverse Matsubara Green's function. In general, Equation (A.3.8) allows for many distinct $\boldsymbol{q}$ vectors. Most often, the simple situation where the magnetic field points in z-direction is discussed. In the general scheme, the inverse Green's function is given by Equation (II.2.20) In order to make further progress, an approximation is used. The simplest possible is the saddle point approximation which is commonly used to describe superconductors [51–54] yielding

$$\Omega \approx -\frac{1}{\beta} \ln\left(\exp\left(-S_{\mathrm{eff}}(\Delta_0)\right)\right) \tag{A.3.9}$$

with the effective action S_{eff} given by

$$S_{\mathrm{eff}}(\Delta) = N\beta\frac{\mu}{2} - \frac{1}{\hbar}\int_0^{\hbar\beta} \mathrm{d}\tau \left(-\frac{1}{2}\mathrm{Tr}\,(\ln)\left[\mathcal{G}^{-1}(\tau)\right]_{\Delta(\boldsymbol{q})=\Delta(\boldsymbol{q})} + \sum_{\boldsymbol{q}} \frac{|\Delta(\boldsymbol{q})|^2}{V}\right). \tag{A.3.10}$$

which is the effective action (II.2.17) used in the main text.

A.4. Electron spin in a magnetic field gradient

In this thesis, the effects of magnetic gradient fields on electron spins on lattice models with periodic boundary conditions are studied. In the following a detailed derivation of Equation (A.4.42) is presented. For this reason it is necessary to begin with some properties of electrons in periodic potentials. The Hamiltonian H describing the energy of electrons in a periodic potential

$$V(\boldsymbol{r}) = V(\boldsymbol{r} + \boldsymbol{R}) \tag{A.4.1}$$

with $\boldsymbol{R}$ being a lattice vector is given in the most simple case by

$$H = \frac{\boldsymbol{p}^2}{2m} + V(\boldsymbol{r}) \tag{A.4.2}$$

while $\boldsymbol{p}$ is the momentum of an electron with mass m. It is well known, that the eigenstates of periodic lattice Hamiltonians are the Bloch states [135] $|\psi_{nk}\rangle$ which are expressed in position space as

$$\psi_{n,\boldsymbol{k}}(\boldsymbol{r}) = \langle \boldsymbol{r}|\psi_{n,\boldsymbol{k}}\rangle = \mathrm{e}^{\mathrm{i}\boldsymbol{k}\boldsymbol{r}} u_{nk}(\boldsymbol{r}) \tag{A.4.3}$$

where $\mathrm{e}^{\mathrm{i}\boldsymbol{k}\boldsymbol{r}}$ is a plane wave-part and $u_{nk}(\boldsymbol{r})$ is a lattice-periodic function

$$u_{nk}(\boldsymbol{r} + \boldsymbol{R}) = u_{nk}(\boldsymbol{r}). \tag{A.4.4}$$

The Bloch-state on the other hand fulfills twisted periodic boundary conditions with respect to a unit cell.

$$\psi_{n,\boldsymbol{k}}(\boldsymbol{r} + \boldsymbol{R}) = \mathrm{e}^{\mathrm{i}\boldsymbol{k}\boldsymbol{R}} \psi_{nk}(\boldsymbol{r}). \tag{A.4.5}$$

However, $\psi_{n,\boldsymbol{k}}(\boldsymbol{r})$ is periodic in the Brillouin zone

$$\psi_{n,\boldsymbol{k}+\boldsymbol{G}}(\boldsymbol{r}) = \psi_{n,\boldsymbol{k}}(\boldsymbol{r}) \tag{A.4.6}$$

while $\boldsymbol{G}$ denotes a lattice vector in reciprocal space. Without the use of a specific representation basis, the Bloch state can be defined as

$$|\psi_{n,\boldsymbol{k}}\rangle = \mathrm{e}^{\mathrm{i}\boldsymbol{k}\hat{\boldsymbol{r}}} |u_{n,\boldsymbol{k}}\rangle \mathrm{e}^{i\phi_n(\boldsymbol{k})} \tag{A.4.7}$$

where $\hat{\boldsymbol{r}}$ is introduced as the position operator. The phase $\phi_n(\boldsymbol{k})$ is arbitrary and set to zero since it has no influence on the signatures discussed below. It can be verified that (A.4.7) yields (A.4.3) in position space representation

$$\langle \boldsymbol{r}|\psi_{n,\boldsymbol{k}}\rangle = \langle \boldsymbol{r}|\mathrm{e}^{\mathrm{i}\boldsymbol{k}\hat{\boldsymbol{r}}}|u_{n,\boldsymbol{k}}\rangle = \mathrm{e}^{\mathrm{i}\boldsymbol{k}\boldsymbol{r}} \langle \boldsymbol{r}|u_{n,\boldsymbol{k}}\rangle = \mathrm{e}^{\mathrm{i}\boldsymbol{k}\boldsymbol{r}} u_{n,\boldsymbol{k}}(\boldsymbol{r}). \tag{A.4.8}$$

The eigenequation of a lattice periodic Hamiltonian reads

$$H|\psi_{n,\boldsymbol{k}}\rangle = E_{n\boldsymbol{k}}|\psi_{n,\boldsymbol{k}}\rangle. \tag{A.4.9}$$

This eigenequation can be written in terms of $|u_{n,\boldsymbol{k}}\rangle$ which yields

$$H_{\boldsymbol{k}}|u_{n,\boldsymbol{k}}\rangle = E_{n,\boldsymbol{k}}|u_{n,\boldsymbol{k}}\rangle \tag{A.4.10}$$

where $H_{\boldsymbol{k}} := \mathrm{e}^{-\mathrm{i}\boldsymbol{k}\hat{\boldsymbol{r}}} H \mathrm{e}^{\mathrm{i}\boldsymbol{k}\hat{\boldsymbol{r}}}$ [111] is introduced. The Bloch states are orthonormalized

$$\langle \psi_{n',\boldsymbol{k}'} | \psi_{n,\boldsymbol{k}} \rangle = \delta_{n,n'} \delta_{\boldsymbol{k},\boldsymbol{k}'} = \langle u_{n',\boldsymbol{k}'} | \mathrm{e}^{\mathrm{i}\hat{\boldsymbol{r}}(\boldsymbol{k}-\boldsymbol{k}')} | u_{n,\boldsymbol{k}} \rangle \tag{A.4.11}$$

and hence one has

$$\langle u_{n',\boldsymbol{k}} | u_{n,\boldsymbol{k}} \rangle = \delta_{n,n'}. \tag{A.4.12}$$

The translation operator T_{R} which shifts the argument of a function $f(\boldsymbol{r})$ by a lattice vector $\boldsymbol{R}$ can be written such that

$$T_{\mathrm{R}} f(\boldsymbol{r}) = f(\boldsymbol{r} - \boldsymbol{R}) \tag{A.4.13}$$

and likewise the inverse translation operator $T_{\boldsymbol{R}}^{-1}$ is defined through

$$T_{\mathrm{R}}^{-1} T_{\mathrm{R}} = \hat{1} \tag{A.4.14}$$

where $\mathbb{1}$ is the identity operator. The inverse translation operator can equivalently be defined through

$$T_{\mathrm{R}}^{-1} f(\boldsymbol{r}) = f(\boldsymbol{r} + \boldsymbol{R}). \tag{A.4.15}$$

The translation operator T_{R} commutes with any Hamiltonian who's eigenstates are Bloch-states since

$$H = \sum_n \sum_{\boldsymbol{k}} |\psi_{n,\boldsymbol{k}}\rangle E_{n,\boldsymbol{k}} \langle \psi_{n,\boldsymbol{k}}| = \int \mathrm{d}\boldsymbol{r} \int \mathrm{d}\boldsymbol{r}' \sum_n \sum_{\boldsymbol{k}} |\boldsymbol{r}'\rangle E_{n,\boldsymbol{k}} \psi_{n,\boldsymbol{k}}(\boldsymbol{r}') \psi^*_{n,\boldsymbol{k}}(\boldsymbol{r}) \langle \boldsymbol{r}| \tag{A.4.16}$$

and hence

$$\begin{aligned} T_{\mathrm{R}} H T_{\mathrm{R}}^{-1} &= \int \mathrm{d}\boldsymbol{r} \oint \mathrm{d}\boldsymbol{r}' \sum_n \sum_{\boldsymbol{k}} |\boldsymbol{r}' + \boldsymbol{R}\rangle E_{n,\boldsymbol{k}} \psi_{n,\boldsymbol{k}}(\boldsymbol{r}') \psi^*_{n,\boldsymbol{k}}(\boldsymbol{r}) \langle \boldsymbol{r} + \boldsymbol{R}| \\ &= \int \mathrm{d}\boldsymbol{r} \int \mathrm{d}\boldsymbol{r}' \sum_n \sum_{\boldsymbol{k}} |\boldsymbol{r}' + \boldsymbol{R}\rangle E_{n,\boldsymbol{k}} \mathrm{e}^{-\mathrm{i}\boldsymbol{k}\boldsymbol{R}} \psi_{n,\boldsymbol{k}}(\boldsymbol{r}' + \boldsymbol{R}) \psi^*_{n,\boldsymbol{k}}(\boldsymbol{r} + \boldsymbol{R}) \mathrm{e}^{\mathrm{i}\boldsymbol{k}\boldsymbol{R}} \langle \boldsymbol{r} + \boldsymbol{R}| \end{aligned} \tag{A.4.17}$$

$$= \int \mathrm{d}\boldsymbol{r} \int \mathrm{d}\boldsymbol{r}' \sum_n \sum_{\boldsymbol{k}} |\boldsymbol{r}'\rangle E_{n,\boldsymbol{k}} \psi_{n,\boldsymbol{k}}(\boldsymbol{r}') \psi^*_{n,\boldsymbol{k}}(\boldsymbol{r}) \langle \boldsymbol{r}| = H. \tag{A.4.18}$$

Therefore, for the commutator the identity

$$\left[T_{\mathrm{R}}, H\right] = 0 \tag{A.4.19}$$

holds. More general, operators that are translationally invariant commute with T_{R}. In the main text, the thermodynamic response to magnetic field gradients are analyzed. Therefore it is necessary to describe the position operator $\hat{\boldsymbol{r}}$ as the magnetic field is proportional to $\hat{\boldsymbol{r}}$. Such a description is straightforward in finite size systems in real-space representation. In order to obtain an expression for the position operator for periodic systems, it is natural to represent the position operator in the Bloch-state basis. The position operator is of course not translation invariant, specifically it transforms as

$$T_{\mathrm{R}}\hat{\boldsymbol{r}}T_{\mathrm{R}}^{-1} = \sum_{\boldsymbol{r}} T_{\mathrm{R}}|\boldsymbol{r}\rangle\boldsymbol{r}\langle\boldsymbol{r}|T_{\mathrm{R}}^{-1} = \sum_{\boldsymbol{r}} |\boldsymbol{r}+\boldsymbol{R}\rangle\boldsymbol{r}\langle\boldsymbol{r}+\boldsymbol{R}| = \sum_{\boldsymbol{r}} |\boldsymbol{r}+\boldsymbol{R}\rangle\,(\boldsymbol{r}+\boldsymbol{R}-\boldsymbol{R})\,\langle\boldsymbol{r}+\boldsymbol{R}| \tag{A.4.20}$$

$$= \sum_{\boldsymbol{r}} |\boldsymbol{r}+\boldsymbol{R}\rangle\,(\boldsymbol{r}+\boldsymbol{R})\,\langle\boldsymbol{r}+\boldsymbol{R}| - \sum_{\boldsymbol{r}} |\boldsymbol{r}+\boldsymbol{R}\rangle\boldsymbol{R}\langle\boldsymbol{r}+\boldsymbol{R}| = \hat{\boldsymbol{r}} - \boldsymbol{R}. \tag{A.4.21}$$

The commutator of T_{R} and $\hat{\boldsymbol{r}}$ is thus given by

$$\left[T_{\mathrm{R}}, \hat{\boldsymbol{r}}\right] = -\boldsymbol{R}T_{\mathrm{R}}. \tag{A.4.22}$$

The representation of the velocity operator in the Bloch basis is in general defined as

$$\boldsymbol{v} = \frac{-\mathrm{i}}{\hbar}\left[\hat{\boldsymbol{r}}, \boldsymbol{H}\right] \tag{A.4.23}$$

and furthermore, the matrix elements of the position operator in Bloch Basis can be written in terms of the velocity operator as [113]

$$\langle\psi_{n',\boldsymbol{k}'}|\hat{\boldsymbol{r}}|\psi_{n,\boldsymbol{k}}\rangle = \frac{\langle\psi_{n',\boldsymbol{k}'}|\left[\hat{\boldsymbol{r}}, H\right]|\psi_{n,\boldsymbol{k}}\rangle}{\left(E_{n',\boldsymbol{k}'} - E_{n,\boldsymbol{k}}\right)} = \frac{\langle\psi_{n',\boldsymbol{k}'}|\hat{\boldsymbol{v}}|\psi_{n,\boldsymbol{k}}\rangle}{\left(E_{n',\boldsymbol{k}'} - E_{n,\boldsymbol{k}}\right)} \quad \text{for } E_{n,\boldsymbol{k}} \neq E_{n',\boldsymbol{k}'}. \tag{A.4.24}$$

The velocity operator commutes with the translation operator T_{R} since

$$\left[T_{\mathrm{R}}, \left[\hat{\boldsymbol{r}}, H\right]\right] = -\left[H, \left[T_{\mathrm{R}}, \hat{\boldsymbol{r}}\right]\right] - \left[\hat{\boldsymbol{r}}, \left[H, T_{\mathrm{R}}\right]\right] = -R\left[H, T_{\mathrm{R}}\right] = 0 \tag{A.4.25}$$

where it is used that $[H, T_{\mathrm{R}}] = 0$ and $[\hat{r}, T_{\mathrm{R}}] = \boldsymbol{R}T_{\mathrm{R}}$. It is thus found that

$$\langle\psi_{n',\boldsymbol{k}'}|\hat{\boldsymbol{v}}|\psi_{n,\boldsymbol{k}}\rangle = \langle\psi_{n',\boldsymbol{k}'}|T_{\mathrm{R}}^{-1}T_{\mathrm{R}}\hat{\boldsymbol{v}}T_{\mathrm{R}}^{-1}T_{\mathrm{R}}|\psi_{n,\boldsymbol{k}}\rangle = \langle\psi_{n',\boldsymbol{k}'}|\hat{\boldsymbol{v}}|\psi_{n,\boldsymbol{k}}\rangle\mathrm{e}^{-\mathrm{i}(\boldsymbol{k}-\boldsymbol{k}')\boldsymbol{R}}. \tag{A.4.26}$$

So, the off-diagonal elements in (A.4.24) with respect to $\boldsymbol{k}$ and $\boldsymbol{k}'$ vanish because $\mathrm{e}^{\mathrm{i}(\boldsymbol{k}-\boldsymbol{k}')\boldsymbol{R}} \neq 1$ in general. So, $\boldsymbol{v}$ is block-diagonal in the quantum numbers $\boldsymbol{k}$ and $\boldsymbol{k}'$ labeling the eigenvalues of T_R yielding

$$\langle\psi_{n',\boldsymbol{k}'}|\hat{\boldsymbol{r}}|\psi_{n,\boldsymbol{k}}\rangle = \frac{\langle\psi_{n',\boldsymbol{k}}|\hat{\boldsymbol{v}}|\psi_{n,\boldsymbol{k}}\rangle}{\left(E_{n',\boldsymbol{k}} - E_{n,\boldsymbol{k}}\right)}\delta_{\boldsymbol{k},\boldsymbol{k}'}. \tag{A.4.27}$$

The velocity operator for a Hamiltonian of the form (A.4.2) is given by

$$\hat{\boldsymbol{v}} = \frac{\hat{\boldsymbol{p}}}{m}. \tag{A.4.28}$$

In this simple case one can find [113]

$$\langle\psi_{n',\boldsymbol{k}}|\boldsymbol{v}|\psi_{n,\boldsymbol{k}}\rangle = \langle\psi_{n',\boldsymbol{k}}|\frac{\hat{\boldsymbol{p}}}{m}|\psi_{n,\boldsymbol{k}}\rangle = \langle u_{n',\boldsymbol{k}}|\frac{\hat{\boldsymbol{p}}+\hbar\boldsymbol{k}}{m}|u_{n,\boldsymbol{k}}\rangle = \frac{1}{\hbar}\langle u_{n',\boldsymbol{k}}|\frac{\partial H_{\boldsymbol{k}}}{\partial\boldsymbol{k}}|u_{n,\boldsymbol{k}}\rangle. \tag{A.4.29}$$

In a different approach, the position operator can also be expressed in terms of derivatives with respect to $\boldsymbol{k}$ as shown in the following.

In the following, the position operator is expressed in the Bloch-state basis where the matrix elements are given by [111]

$$\langle\psi_{n',k'}|\hat{\boldsymbol{r}}|\psi_{n,k}\rangle = \langle\psi_{n'k'}|(-\mathrm{i}\nabla_{\boldsymbol{k}})|\psi_{n,k}\rangle + \langle\psi_{n',k'}|\mathrm{e}^{\mathrm{i}\boldsymbol{k}\hat{\boldsymbol{r}}}\mathrm{i}\nabla_{\boldsymbol{k}}\mathrm{e}^{-\mathrm{i}\boldsymbol{k}\hat{\boldsymbol{r}}}|\psi_{n,k}\rangle \tag{A.4.30}$$

$$= -\mathrm{i}\nabla_{\boldsymbol{k}}\delta_{\boldsymbol{k},\boldsymbol{k}'}\delta_{n,n'} + \langle\psi_{n',k'}|\mathrm{e}^{\mathrm{i}\boldsymbol{k}\hat{\boldsymbol{r}}}\mathrm{i}\nabla_{\boldsymbol{k}}\mathrm{e}^{-\mathrm{i}\boldsymbol{k}\hat{\boldsymbol{r}}}|\psi_{n,k}\rangle \tag{A.4.31}$$

$$= -\mathrm{i}\nabla_{\boldsymbol{k}}\delta_{\boldsymbol{k},\boldsymbol{k}'}\delta_{n,n'} + \langle u_{n',k'}|\mathrm{i}\nabla_{\boldsymbol{k}}|u_{n,k}\rangle. \tag{A.4.32}$$

The second term in (A.4.32) is translation invariant since

$$\langle\psi_{n',k'}|\mathrm{e}^{\mathrm{i}\boldsymbol{k}\hat{\boldsymbol{r}}}\mathrm{i}\nabla_{\boldsymbol{k}}\mathrm{e}^{-\mathrm{i}\boldsymbol{k}\hat{\boldsymbol{r}}}|\psi_{n,k}\rangle = \langle\psi_{n',k'}|T_{\mathrm{R}}^{-1}T_{\mathrm{R}}\mathrm{e}^{\mathrm{i}\boldsymbol{k}\hat{\boldsymbol{r}}}\mathrm{i}\nabla_{\boldsymbol{k}}\mathrm{e}^{-\mathrm{i}\boldsymbol{k}\hat{\boldsymbol{r}}}T_{\mathrm{R}}^{-1}T_{\mathrm{R}}|\psi_{n,k}\rangle \tag{A.4.33}$$

$$= \langle\psi_{n',k'}|\mathrm{e}^{\mathrm{i}\boldsymbol{k}'\boldsymbol{R}}\mathrm{e}^{\mathrm{i}\boldsymbol{k}\hat{\boldsymbol{r}}}\mathrm{e}^{-\mathrm{i}\boldsymbol{k}\boldsymbol{R}}T_{\mathrm{R}}\mathrm{i}\nabla_{\boldsymbol{k}}T_{\mathrm{R}}^{-1}\mathrm{e}^{-\mathrm{i}\boldsymbol{k}\hat{\boldsymbol{r}}}\mathrm{e}^{\mathrm{i}\boldsymbol{k}\boldsymbol{R}}\mathrm{e}^{-\mathrm{i}\boldsymbol{k}\boldsymbol{R}}|\psi_{n,k}\rangle \tag{A.4.34}$$

$$= \langle\psi_{n',k'}|\mathrm{e}^{\mathrm{i}(\boldsymbol{k}'-\boldsymbol{k})\boldsymbol{R}}\mathrm{e}^{\mathrm{i}\boldsymbol{k}\hat{\boldsymbol{r}}}T_{\mathrm{R}}T_{\mathrm{R}}^{-1}\mathrm{i}\nabla_{\boldsymbol{k}}\mathrm{e}^{-\mathrm{i}\boldsymbol{k}\hat{\boldsymbol{r}}}|\psi_{n,k}\rangle \tag{A.4.35}$$

$$= \mathrm{e}^{\mathrm{i}(\boldsymbol{k}'-\boldsymbol{k})\boldsymbol{R}}\langle\psi_{n',k'}|\mathrm{e}^{\mathrm{i}\boldsymbol{k}\hat{\boldsymbol{r}}}\mathrm{i}\nabla_{\boldsymbol{k}}\mathrm{e}^{-\mathrm{i}\boldsymbol{k}\hat{\boldsymbol{r}}}|\psi_{n,k}\rangle \tag{A.4.36}$$

$$= \delta_{\boldsymbol{k},\boldsymbol{k}'}\langle\psi_{n'k}|\mathrm{e}^{\mathrm{i}\boldsymbol{k}\hat{\boldsymbol{r}}}\mathrm{i}\nabla_{\boldsymbol{k}}\mathrm{e}^{-\mathrm{i}\boldsymbol{k}\hat{\boldsymbol{r}}}|\psi_{n,k}\rangle. \tag{A.4.37}$$

The matrix elements of the second part of the position operator in Bloch-space given in (A.4.31) are thus diagonal with respect to $\boldsymbol{k}$ and one obtains the result Equation(IV.3.7) given in the main text

$$\langle\psi_{n',k'}|\hat{\boldsymbol{r}}|\psi_{n,k}\rangle = -\mathrm{i}\nabla_{\boldsymbol{k}}\delta_{\boldsymbol{k},\boldsymbol{k}'}\delta_{n,n'} + \delta_{\boldsymbol{k},\boldsymbol{k}'}\langle\psi_{n',k}|\mathrm{e}^{\mathrm{i}\boldsymbol{k}\hat{\boldsymbol{r}}}\mathrm{i}\nabla_{\boldsymbol{k}}\mathrm{e}^{-\mathrm{i}\boldsymbol{k}\hat{\boldsymbol{r}}}|\psi_{n,k}\rangle. \tag{A.4.38}$$

$$= -\mathrm{i}\nabla_{\boldsymbol{k}}\delta_{\boldsymbol{k},\boldsymbol{k}'}\delta_{n,n'} + \delta_{\boldsymbol{k},\boldsymbol{k}'}\langle u_{n',k}|\mathrm{i}\nabla_{\boldsymbol{k}}|u_{n,k}\rangle. \tag{A.4.39}$$

A spin operator $\hat{\boldsymbol{\sigma}}$ which acts only on the spin states commutes with the translation operator T_{R}. In spin-orbit coupled Hamiltonians, the spin is not independent of the momentum. However, as discussed in section III, the in-plane spin-components of the spin-expectation value are even for open boundary conditions translation invariant within the system boundaries. The z-component is dependent in the position in space. However, s_z is almost homogeneous in position space especially for larger systems. Therefore, the approximation that sigma in the Bloch basis is diagonal in momentum space is justified. Thus, it is assumed in the following that the spin-operator $\hat{\boldsymbol{\sigma}}$ is diagonal with respect to $\boldsymbol{k}$. In order to analyze the effect of the magnetic field gradients in the Bloch state representation, it is necessary to find the representation of the product of the spin-operator $\hat{\boldsymbol{\sigma}}$ and the position operator $\hat{\boldsymbol{r}}$ and so the matrix elements of the operator $\hat{\boldsymbol{\sigma}}\hat{\boldsymbol{r}}$ are given by

$$\langle\psi_{n',k'}|\hat{\boldsymbol{\sigma}}\hat{\boldsymbol{r}}|\psi_{n,k}\rangle = \sum_{n''}\langle\psi_{n',k'}|\hat{\boldsymbol{\sigma}}|\psi_{n'',k'}\rangle\langle\psi_{n'',k'}|\hat{\boldsymbol{r}}|\psi_{n,k}\rangle$$

$$= \sum_{n''}\langle u_{n',k'}|\hat{\boldsymbol{\sigma}}|u_{n'',k'}\rangle\left(-\mathrm{i}\nabla_{\boldsymbol{k}}\delta_{\boldsymbol{k},\boldsymbol{k}'}\delta_{n'',n} + \delta_{\boldsymbol{k}',\boldsymbol{k}}\langle u_{n'',k'}|\mathrm{i}\nabla_{\boldsymbol{k}}|u_{n,k}\rangle\right) \tag{A.4.40}$$

in the Bloch basis where the second term is diagonal in $\boldsymbol{k}$. Hence, quantities like

$$\begin{aligned}
&\sum_{n}\sum_{n'}\sum_{\boldsymbol{k}}\sum_{\boldsymbol{k}'}\langle\psi_{n',\boldsymbol{k}'}|\hat{\boldsymbol{\sigma}}\hat{\boldsymbol{r}}|\psi_{n,\boldsymbol{k}}\rangle f_n(\boldsymbol{k})\\
&\quad=\sum_{n}\sum_{n'}\sum_{\boldsymbol{k}}\sum_{\boldsymbol{k}'}\sum_{n''}\langle u_{n',\boldsymbol{k}'}|\hat{\boldsymbol{\sigma}}|u_{n'',\boldsymbol{k}'}\rangle\left(-\mathrm{i}\left(\nabla_{\boldsymbol{k}}\delta_{\boldsymbol{k},\boldsymbol{k}'}\right)\delta_{n,n''}+\delta_{\boldsymbol{k},\boldsymbol{k}'}\mathrm{i}\langle u_{n'',\boldsymbol{k}'}|\left(\nabla_{\boldsymbol{k}}|u_{n,\boldsymbol{k}}\rangle\right)\right)f_n(\boldsymbol{k})\\
&\quad\approx-\sum_{n}\sum_{n'}\frac{V}{4\pi}(-\mathrm{i})\langle u_{n',\boldsymbol{k}}|\hat{\boldsymbol{\sigma}}|u_{n,\boldsymbol{k}}\rangle\delta_{n,n}f_n(\boldsymbol{k})\Big|_{k_x=0}^{k_x=\pi}\\
&\quad+\sum_{n}\sum_{n'}\frac{V}{4\pi}\left((-\mathrm{i})\langle u_{n',\boldsymbol{k}}|\hat{\boldsymbol{\sigma}}|u_{n,\boldsymbol{k}}\rangle\delta_{n,n}f_n(\boldsymbol{k})\right)\Big|_{k_x=0}^{k_x=\pi}\\
&\quad+\sum_{n}\sum_{n'}\frac{V^2}{16\pi^2}\int\mathrm{d}\boldsymbol{k}\int\mathrm{d}\boldsymbol{k}'\langle u_{n',\boldsymbol{k}'}|\hat{\boldsymbol{\sigma}}|u_{n,\boldsymbol{k}'}\rangle\delta(\boldsymbol{k}-\boldsymbol{k}')\langle u_{n,\boldsymbol{k}'}|\mathrm{i}\left(\nabla_{\boldsymbol{k}}|u_{n,\boldsymbol{k}}\rangle\right)f_n(\boldsymbol{k})\\
&\quad=\sum_{n}\sum_{n'}\frac{V}{4\pi^2}\int\mathrm{d}^2k\langle u_{n',\boldsymbol{k}}|\hat{\boldsymbol{\sigma}}|u_{n,\boldsymbol{k}}\rangle\langle u_{n,\boldsymbol{k}}|\mathrm{i}\left(\nabla_{\boldsymbol{k}}|u_{n,\boldsymbol{k}}\rangle\right)f_n(\boldsymbol{k})
\end{aligned}\tag{A.4.41}$$

can be evaluated showing that the contributions from the first term in (A.4.40) which are related to momentum space surface contributions vanish. The first term in (IV.3.7) yields therefore surface contributions which vanish as long as $f_n(\boldsymbol{k})$ is a periodic function which has no discontinuities. Even if one allows for isolated point-like discontinuities in $f_n(\boldsymbol{k})$, they would not affect the result as long as $f_n(\boldsymbol{k})$ is not divergent at those points. The matrix elements of the product of the spin and the position operator are thus determined by

$$\sum_{\boldsymbol{k}}\sum_{\boldsymbol{k}'}\langle\psi_{n',\boldsymbol{k}'}|\hat{\boldsymbol{\sigma}}\hat{\boldsymbol{r}}|\psi_{n,\boldsymbol{k}}\rangle f_n(\boldsymbol{k})\approx\frac{V}{4\pi^2}\int\mathrm{d}^2k\sum_{n''}\langle u_{n',\boldsymbol{k}}|\hat{\boldsymbol{\sigma}}|u_{n'',\boldsymbol{k}}\rangle\langle u_{n'',\boldsymbol{k}}|\mathrm{i}\left(\nabla_{\boldsymbol{k}}|u_{n,\boldsymbol{k}}\rangle\right)f_n(\boldsymbol{k}).\tag{A.4.42}$$

A.5. Electron spin in a magnetic field gradient in the tight binding formalism

In the main text, the matrix elements of a tight binding Hamiltonian are expressed in terms of the Fourier transformed atomic basis functions where only the diagonal elements are considered

$$\mathcal{H}_{i,j,\mu,\nu}(\boldsymbol{k}):=\langle\chi_{\boldsymbol{k},i,\mu}|H|\chi_{\boldsymbol{k},j,\nu}\rangle\tag{A.5.1}$$

(See Equation (IV.4.6)). It is straightforward to confirm that the non-diagonal matrix elements of H with respect to $\boldsymbol{k}$ vanish since

$$\begin{aligned}
\mathcal{H}_{i,j,\mu,\nu}:=\langle\chi_{\boldsymbol{k}',i,\mu}|H|\chi_{\boldsymbol{k},j,\nu}\rangle&=\frac{1}{N}\sum_{\boldsymbol{R}'}\sum_{\boldsymbol{R}''}\mathrm{e}^{-\mathrm{i}\boldsymbol{k}'\boldsymbol{R}'}\langle\phi_{\boldsymbol{R}',i,\mu}|H|\phi_{\tilde{\boldsymbol{R}},j,\nu}\rangle\mathrm{e}^{\mathrm{i}\boldsymbol{k}\boldsymbol{R}''}\\
&=\frac{1}{N}\sum_{\boldsymbol{R}'}\sum_{\tilde{\boldsymbol{R}}}\mathrm{e}^{-\mathrm{i}\boldsymbol{k}'(\boldsymbol{R}')}\langle\phi_{\boldsymbol{R}',i,\mu}|H|\phi_{\boldsymbol{R}'+\tilde{\boldsymbol{R}},j,\nu}\rangle\mathrm{e}^{\mathrm{i}\boldsymbol{k}(\boldsymbol{R}'+\tilde{\boldsymbol{R}})}\\
&=\sum_{\tilde{\boldsymbol{R}}}H(\tilde{\boldsymbol{R}})\mathrm{e}^{\mathrm{i}\boldsymbol{k}\tilde{\boldsymbol{R}}}\delta_{\boldsymbol{k},\boldsymbol{k}'}.
\end{aligned}\tag{A.5.2}$$

The part of the position operator in the Bloch-state basis $\langle\psi_{n',\boldsymbol{k}}|\mathrm{e}^{\mathrm{i}\boldsymbol{k}\hat{\boldsymbol{r}}}\mathrm{i}\nabla_{\boldsymbol{k}}\mathrm{e}^{-\mathrm{i}\boldsymbol{k}\hat{\boldsymbol{r}}}|\psi_{n,\boldsymbol{k}}\rangle$ contained in (IV.3.7) can be expressed in terms of the tight-binding expansion coefficients. There, the expansion of the Bloch-states given in Equation (IV.4.7) yields

$$\begin{aligned}
&\langle\psi_{n',\boldsymbol{k}}|\mathrm{e}^{\mathrm{i}\boldsymbol{k}\hat{\boldsymbol{r}}}\mathrm{i}\nabla_{\boldsymbol{k}}\mathrm{e}^{-\mathrm{i}\boldsymbol{k}\hat{\boldsymbol{r}}}|\psi_{n,\boldsymbol{k}}\rangle \\
&= \frac{1}{N}\sum_i\sum_j\sum_\mu\sum_\nu C^*_{n',\boldsymbol{k},j,\mu}\sum_{\boldsymbol{R}'}\sum_{\boldsymbol{R}}\mathrm{e}^{-\mathrm{i}\boldsymbol{k}\boldsymbol{R}'}\langle\phi_{\boldsymbol{R}',j,\mu}|\mathrm{e}^{\mathrm{i}\boldsymbol{k}\hat{\boldsymbol{r}}}\mathrm{i}\nabla_{\boldsymbol{k}}\mathrm{e}^{-\mathrm{i}\boldsymbol{k}\hat{\boldsymbol{r}}}|\phi_{\boldsymbol{R},i,\nu}\rangle C_{n,\boldsymbol{k},i,\nu}\mathrm{e}^{\mathrm{i}\boldsymbol{k}\boldsymbol{R}} \\
&= \sum_i\sum_j\sum_\mu\sum_\nu C^*_{n',\boldsymbol{k},j,\mu}\mathrm{i}\nabla_{\boldsymbol{k}}C_{n,\boldsymbol{k},i,\nu} \\
&= \boldsymbol{C}^\dagger_{n',\boldsymbol{k}}\mathrm{i}\nabla_{\boldsymbol{k}}\boldsymbol{C}_{n,\boldsymbol{k}}.
\end{aligned} \tag{A.5.3}$$

In the discrete tight-binding formalism, the $u_{n,\boldsymbol{k}}$ are replaced by the vector $\boldsymbol{C}_{n,\boldsymbol{k}}$ where the elements of the vector are given by $C_{n,\boldsymbol{k},i,\mu}$. Likewise for the matrix elements $\langle\psi_{n',\boldsymbol{k}}|\hat{\boldsymbol{\sigma}}|\psi_{n,\boldsymbol{k}}\rangle$ one obtains

$$\begin{aligned}
\langle\psi_{n',\boldsymbol{k}}|\hat{\boldsymbol{\sigma}}|\psi_{n,\boldsymbol{k}}\rangle &= \sum_i\sum_j\sum_\mu\sum_\nu C^*_{n',\boldsymbol{k},j,\mu}\underbrace{\langle\chi_{\boldsymbol{k},j,\mu}|\hat{\boldsymbol{\sigma}}|\chi_{\boldsymbol{k},i,\nu}\rangle}_{:=\sigma^{\mathrm{TB}}_{\boldsymbol{k},ji,\mu\nu}}C_{n,\boldsymbol{k},i,\nu} \\
&= \boldsymbol{C}^\dagger_{n',\boldsymbol{k}}\boldsymbol{\sigma}^{\mathrm{TB}}\boldsymbol{C}_{n,\boldsymbol{k}}
\end{aligned} \tag{A.5.4}$$

where $\sigma^{\mathrm{TB}}_{\boldsymbol{k},ji,\mu\nu}$ are the matrix elements of $\boldsymbol{\sigma}^{\mathrm{TB}}$ in the basis of the tight-binding states.

A.6. Rayleigh Schrödinger perturbation theory for Bloch states

In order to describe the modifications to a Hamiltonian due to some small perturbations, the Rayleigh Schrödinger perturbation theory, where the perturbed eigenstates are expressed in terms of the unperturbed states, is used. The expectation value of a hermitian operator $\hat{O}$ can be written in standard Rayleigh-Schrödinger perturbation theory [136] assuming some state $|n\rangle$ is perturbed due to an (external) perturbation. The explicit terms of the perturbation theory are usually given in the literature only up to the first order in the states but, in this thesis, perturbations up to the second order in the states are important. The Schrödinger equation reads

$$\hat{H}\widetilde{|n\rangle} = \widetilde{E}_n\widetilde{|n\rangle} \tag{A.6.1}$$

with

$$\hat{H} = \hat{H}_0 + \lambda\hat{V}. \tag{A.6.2}$$

Here, $\widetilde{|n\rangle}$ denotes the exact form of an (unknown) eigenstate of some Hamiltonian $\hat{H}$ consisting of $\hat{H}_0$ for which the eigenstates are known and $\lambda\hat{V}$ which is a perturbation to $\hat{H}_0$. If the perturbation $\lambda\hat{V}$ is assumed to be small, the eigenstates and the eigenvalue of the Schrödinger equation can be expanded in terms of a series in λ. Such expansions are, however, only useful when the expansions are truncated at some finite order. In the following, the expansions are considered up to second order, assuming that the truncation in second order yields a sufficient description of the states. The corrections of the states in first and second order are well known. These are given through [136]

$$|n^{(1)}\rangle = \sum_{k\neq n}|k\rangle\frac{\langle k|\hat{V}|n\rangle}{E_n - E_k} \tag{A.6.3}$$

$$|n^{(2)}\rangle = \sum_{m\neq n}\sum_{l\neq n}|m\rangle\frac{\langle m|\hat{V}|l\rangle\langle l|\hat{V}|n\rangle}{(E_n - E_m)(E_n - E_l)} - \sum_{m\neq n}|m\rangle\frac{\langle m|\hat{V}|n\rangle\langle n|\hat{V}|n\rangle}{(E_n - E_m)^2} - \frac{1}{2}\sum_{m\neq n}|n\rangle\frac{|\langle m|\hat{V}|n\rangle|^2}{(E_n - E_m)^2}. \tag{A.6.4}$$

The perturbed eigenstates are thus given through

$$\widetilde{|n\rangle} = |n\rangle + |n^{(1)}\rangle + |n^{(2)}\rangle \tag{A.6.5}$$

where the first and second order corrections to the eigenstates are denoted as $|n^{(1)}\rangle$ and $|n^{(2)}\rangle$, respectively. The unperturbed eigenstate is denoted as $|n\rangle$ and $\widetilde{|n\rangle}$ is the perturbed eigenstate consisting of the first and second order corrections. The expectation value of an operator can thus be written as

$$\widetilde{\langle n|}\hat{O}\widetilde{|n\rangle} \approx \langle n|\hat{O}|n\rangle + (\langle n^{(1)}|\hat{O}|n\rangle + \langle n|\hat{O}|n^{(1)}\rangle) + \left(\langle n^{(1)}|\hat{O}|n^{(1)}\rangle + \langle n^{(2)}|\hat{O}|n\rangle + \langle n|\hat{O}|n^{(2)}\rangle\right) \tag{A.6.6}$$

$$= \langle n|\hat{O}|n\rangle + 2\mathrm{Re}(\langle n|\hat{O}|n^{(1)}\rangle) + \left(\langle n^{(1)}|\hat{O}|n^{(1)}\rangle + 2\mathrm{Re}\left(\langle n|\hat{O}|n^{(2)}\rangle\right)\right) \tag{A.6.7}$$

up to second order. The first order corrections are linear with a perturbation parameter λ, whereas the second order terms are proportional to λ^2.

Now (A.6.3), (A.6.4) and (A.4.27) are used to find the first and second order corrections of a Bloch-state which is perturbed by the operator

$$\hat{V}_{\mathrm{x}} = \frac{1}{2} G_{\mathrm{x}} \left(\hat{\sigma}_{\mathrm{x}} \hat{r}_{\mathrm{x}} + \hat{r}_{\mathrm{x}} \hat{\sigma}_{\mathrm{x}} \right) \tag{A.6.8}$$

with

$$G_{\mathrm{x}} = \text{ constant} \tag{A.6.9}$$

and $\hat{\sigma}_{\mathrm{x}}$ being the x-component of the spin-operator in x-direction while $\hat{r}_{\mathrm{x}}$ denotes the position operator in x-direction. The operator $\hat{V}$ corresponds to a magnetic field in x-direction which is linearly dependent on $\hat{r}_{\mathrm{x}}$ with the magnetic field gradient given by G_{x}. The first and second order corrections of a Bloch state are thus

$$|\psi^{(1)}_{n,\boldsymbol{k}}\rangle = \sum_{\boldsymbol{k}',m\neq \boldsymbol{k},n} |\psi_{m,\boldsymbol{k}'}\rangle \frac{\langle \psi_{m,\boldsymbol{k}'}|\hat{V}_{\mathrm{x}}|\psi_{n,\boldsymbol{k}}\rangle}{E_{m,\boldsymbol{k}'} - E_{n,\boldsymbol{k}}} \tag{A.6.10}$$

$$\begin{aligned} |\psi^{(2)}_{n,\boldsymbol{k}}\rangle = & \sum_{\boldsymbol{k}',m\neq \boldsymbol{k},n} \sum_{\boldsymbol{k}'',l\neq \boldsymbol{k},n} |\psi_{m,\boldsymbol{k}'}\rangle \frac{\langle \psi_{m,\boldsymbol{k}'}|\hat{V}_{\mathrm{x}}|\psi_{l,\boldsymbol{k}''}\rangle\langle \psi_{l,\boldsymbol{k}''}|\hat{V}_{\mathrm{x}}|\psi_{n,\boldsymbol{k}}\rangle}{(E_{n,\boldsymbol{k}} - E_{m,\boldsymbol{k}'})(E_{n,\boldsymbol{k}} - E_{l,\boldsymbol{k}''})} \\ & - \sum_{\boldsymbol{k}',m\neq \boldsymbol{k},n} |\psi_{m,\boldsymbol{k}'}\rangle \frac{\langle \psi_{m,\boldsymbol{k}'}|\hat{V}_{\mathrm{x}}|\psi_{n,\boldsymbol{k}}\rangle\langle \psi_{n,\boldsymbol{k}}|\hat{V}_{\mathrm{x}}|\psi_{n,\boldsymbol{k}}\rangle}{(E_{n,\boldsymbol{k}} - E_{m,\boldsymbol{k}'})^2} \\ & - \frac{1}{2} \sum_{\boldsymbol{k}',m\neq \boldsymbol{k},n} |\psi_{n,\boldsymbol{k}}\rangle \frac{|\langle \psi_{m,\boldsymbol{k}'}|\hat{V}_{\mathrm{x}}|\psi_{n,\boldsymbol{k}}\rangle|^2}{(E_{n,\boldsymbol{k}} - E_{m,\boldsymbol{k}'})^2}. \end{aligned} \tag{A.6.11}$$

The position operator can either be represented in terms of the velocity operator or it can be directly expressed in the Bloch basis. The first requires inserting (A.4.27) into (A.6.10) and (A.6.11) while using (A.4.23). The latter option is to directly insert the matrix elements of the presentation of the position operator in Bloch-space yielding

$$\langle \psi_{n',\boldsymbol{k}'}|\hat{V}_{\mathrm{x}}|\psi_{n,\boldsymbol{k}}\rangle = \sum_{n''} \langle u_{n',\boldsymbol{k}'}|\hat{\sigma}_{\mathrm{x}}|u_{n'',\boldsymbol{k}'}\rangle \left(-\mathrm{i}\nabla_{k_{\mathrm{x}}} \delta_{\boldsymbol{k},\boldsymbol{k}'} \delta_{n'',n} + \delta_{\boldsymbol{k}',\boldsymbol{k}} \langle u_{n'',\boldsymbol{k}'}|\mathrm{i}\nabla_{k_{\mathrm{x}}}|u_{n,\boldsymbol{k}}\rangle \right) \tag{A.6.12}$$

(see (IV.3.7)). The corrections of the Bloch states to first and second order become

$$\begin{aligned} |\psi^{(1)}_{n,\boldsymbol{k}}\rangle = G_{\mathrm{x}} \sum_{n'} \sum_{m\neq n} \Bigg(& |\psi_{m,\boldsymbol{k}}\rangle \frac{\langle u_{m,\boldsymbol{k}}|\hat{\boldsymbol{\sigma}}|u_{n',\boldsymbol{k}}\rangle\langle u_{n',\boldsymbol{k}}|\mathrm{i}\left(\nabla_{\boldsymbol{k}}|u_{n,\boldsymbol{k}}\rangle\right)}{E_{m,\boldsymbol{k}} - E_{n,\boldsymbol{k}}} \\ & + |\psi_{m,\boldsymbol{k}}\rangle \frac{\langle u_{m,\boldsymbol{k}}|\mathrm{i}\left(\nabla_{\boldsymbol{k}}|u_{n',\boldsymbol{k}}\rangle\right)\langle u_{n',\boldsymbol{k}}|\hat{\boldsymbol{\sigma}}|u_{n,\boldsymbol{k}}\rangle}{E_{m,\boldsymbol{k}} - E_{n,\boldsymbol{k}}} \Bigg) \end{aligned} \tag{A.6.13}$$

$$
\begin{aligned}
|\psi^{(2)}_{n,\boldsymbol{k}}\rangle = G_{\mathrm{x}}^2 \sum_{n''}\sum_{n'}\sum_{m\neq n}\sum_{l\neq n} |\psi_{m,\boldsymbol{k}}\rangle & \left(\frac{\langle u_{m,\boldsymbol{k}}|\hat{\sigma}_{\mathrm{x}}|u_{n',\boldsymbol{k}}\rangle\langle u_{n',\boldsymbol{k}}|\mathrm{i}\left(\nabla_{\boldsymbol{k}_{\mathrm{x}}}|u_{l,\boldsymbol{k}}\rangle\right)}{(E_{n,\boldsymbol{k}}-E_{m,\boldsymbol{k}})(E_{n,\boldsymbol{k}}-E_{l,\boldsymbol{k}})} \right. \\
& \left. + \frac{\langle u_{m,\boldsymbol{k}}|\mathrm{i}\left(\nabla_{k_{\mathrm{x}}}|u_{n',\boldsymbol{k}}\rangle\right)\langle u_{n',\boldsymbol{k}}|\hat{\sigma_{k_{\mathrm{x}}}}|u_{l,\boldsymbol{k}}\rangle}{(E_{n,\boldsymbol{k}}-E_{m,\boldsymbol{k}})(E_{n,\boldsymbol{k}}-E_{l,\boldsymbol{k}})} \right) \\
\times \left(\frac{\langle u_{l,\boldsymbol{k}}|\hat{\sigma}_{\mathrm{x}}|u_{n'',\boldsymbol{k}}\rangle\langle u_{n'',\boldsymbol{k}}|\mathrm{i}\left(\nabla_{\boldsymbol{k}_{\mathrm{x}}}|u_{n,\boldsymbol{k}}\rangle\right)}{(E_{n,\boldsymbol{k}}-E_{m,\boldsymbol{k}})(E_{n,\boldsymbol{k}}-E_{l,\boldsymbol{k}})} \right. & \left. + \frac{\langle u_{l,\boldsymbol{k}}|\mathrm{i}\left(\nabla_{k_{\mathrm{x}}}|u_{n'',\boldsymbol{k}}\rangle\right)\langle u_{n'',\boldsymbol{k}}|\hat{\sigma}_{\mathrm{x}}|u_{n,\boldsymbol{k}}\rangle}{(E_{n,\boldsymbol{k}}-E_{m,\boldsymbol{k}})(E_{n,\boldsymbol{k}}-E_{l,\boldsymbol{k}})} \right) \\
- G_{\mathrm{x}}^2 \sum_{n''}\sum_{n'}\sum_{m\neq n}\sum_{l\neq n} |\psi_{m,\boldsymbol{k}}\rangle & \left(\frac{\langle u_{m,\boldsymbol{k}}|\hat{\sigma}_{\mathrm{x}}|u_{n',\boldsymbol{k}}\rangle\langle u_{n',\boldsymbol{k}}|\mathrm{i}\nabla_{k_{\mathrm{x}}}|u_{n,\boldsymbol{k}}\rangle}{(E_{n,\boldsymbol{k}}-E_{m,\boldsymbol{k}})^2} \right. \\
& \left. + \frac{\langle u_{m,\boldsymbol{k}}|\mathrm{i}\left(\nabla_{k_{\mathrm{x}}}|u_{n',\boldsymbol{k}}\rangle\right)\langle u_{n',\boldsymbol{k}}|\hat{\sigma_{\mathrm{x}}}|u_{n,\boldsymbol{k}}\rangle}{(E_{n,\boldsymbol{k}}-E_{m,\boldsymbol{k}})^2} \right) \\
\times \left(\frac{\langle u_{n,\boldsymbol{k}}|\hat{\sigma}_{\mathrm{x}}|u_{n'',\boldsymbol{k}}\rangle\langle u_{n'',\boldsymbol{k}}|\mathrm{i}\nabla_{k_{\mathrm{x}}}|u_{n,\boldsymbol{k}}\rangle}{(E_{n,\boldsymbol{k}}-E_{m,\boldsymbol{k}})^2} \right. & \left. + \frac{\langle u_{n,\boldsymbol{k}}|\mathrm{i}\left(\nabla_{k_{\mathrm{x}}}|u_{n'',\boldsymbol{k}}\rangle\right)\langle u_{n'',\boldsymbol{k}}|\hat{\sigma_{\mathrm{x}}}|u_{n,\boldsymbol{k}}\rangle}{(E_{n,\boldsymbol{k}}-E_{m,\boldsymbol{k}})^2} \right) \\
- \frac{1}{2}G_{\mathrm{x}}^2 \sum_{n'}\sum_{m\neq n} |\psi_{n,\boldsymbol{k}}\rangle & \left(\frac{|\langle u_{m,\boldsymbol{k}}|\hat{\sigma}_{\mathrm{x}}|u_{n',\boldsymbol{k}}\rangle\langle u_{n',\boldsymbol{k}}|\mathrm{i}\nabla_{k_{\mathrm{x}}}|u_{n,\boldsymbol{k}}\rangle|^2}{(E_{n,\boldsymbol{k}}-E_{m,\boldsymbol{k}})^2} \right. \\
& \left. + \frac{|\langle u_{m,\boldsymbol{k}}|\mathrm{i}\left(\nabla_{k_{\mathrm{x}}}|u_{n',\boldsymbol{k}}\rangle\right)\langle u_{n',\boldsymbol{k}}|\hat{\sigma_{\mathrm{x}}}|u_{n,\boldsymbol{k}}\rangle|^2}{(E_{n,\boldsymbol{k}}-E_{m,\boldsymbol{k}})^2} \right). \qquad \text{(A.6.14)}
\end{aligned}
$$

Instead of (A.6.13) and (A.6.14) the change in $|u_{n,\boldsymbol{k}}\rangle$ can be expressed as

$$
|u^{(1)}_{n,\boldsymbol{k}}\rangle = G_{\mathrm{x}} \sum_{n'}\sum_{m\neq n} |u_{m,\boldsymbol{k}}\rangle \frac{\langle u_{m,\boldsymbol{k}}|\hat{\sigma}|u_{n',\boldsymbol{k}}\rangle\langle u_{n',\boldsymbol{k}}|\mathrm{i}\nabla_{\boldsymbol{k}}|u_{n,\boldsymbol{k}}\rangle}{E_{m,\boldsymbol{k}}-E_{n,\boldsymbol{k}}} + \frac{\langle u_{m,\boldsymbol{k}}|\mathrm{i}\left(\nabla_{k_{\mathrm{x}}}|u_{n',\boldsymbol{k}}\rangle\right)\langle u_{n',\boldsymbol{k}}|\hat{\sigma}_{\mathrm{x}}|u_{n,\boldsymbol{k}}\rangle}{E_{m,\boldsymbol{k}}-E_{n,\boldsymbol{k}}} \qquad \text{(A.6.15)}
$$

$$
\begin{aligned}
|u^{(2)}_{n,\boldsymbol{k}}\rangle = G_{\mathrm{x}}^2 \sum_{n''}\sum_{n'}\sum_{m\neq n}\sum_{l\neq n} |u_{m,\boldsymbol{k}}\rangle & \left(\frac{\langle u_{m,\boldsymbol{k}}|\hat{\sigma}|u_{n',\boldsymbol{k}}\rangle\langle u_{n',\boldsymbol{k}}|\mathrm{i}\nabla_{\boldsymbol{k}}|u_{l,\boldsymbol{k}}\rangle}{(E_{n,\boldsymbol{k}}-E_{m,\boldsymbol{k}})(E_{n,\boldsymbol{k}}-E_{l,\boldsymbol{k}})} \right. \\
& \left. + \frac{\langle u_{m,\boldsymbol{k}}|\mathrm{i}\left(\nabla_{k_{\mathrm{x}}}|u_{n',\boldsymbol{k}}\rangle\right)\langle u_{n',\boldsymbol{k}}|\hat{\sigma}_{\mathrm{x}}|u_{l,\boldsymbol{k}}\rangle}{(E_{n,\boldsymbol{k}}-E_{m,\boldsymbol{k}})(E_{n,\boldsymbol{k}}-E_{l,\boldsymbol{k}})} \right) \\
\times \left(\frac{\langle u_{l,\boldsymbol{k}}|\hat{\sigma}|u_{n'',\boldsymbol{k}}\rangle\langle u_{n'',\boldsymbol{k}}|\mathrm{i}\left(\nabla_{\boldsymbol{k}}|u_{n,\boldsymbol{k}}\rangle\right)}{(E_{n,\boldsymbol{k}}-E_{m,\boldsymbol{k}})(E_{n,\boldsymbol{k}}-E_{l,\boldsymbol{k}})} \right. & \left. + \frac{\langle u_{l,\boldsymbol{k}}|\mathrm{i}\left(\nabla_{k_{\mathrm{x}}}|u_{n'',\boldsymbol{k}}\rangle\right)\langle u_{n'',\boldsymbol{k}}|\hat{\sigma}_{\mathrm{x}}|u_{n,\boldsymbol{k}}\rangle}{(E_{n,\boldsymbol{k}}-E_{m,\boldsymbol{k}})(E_{n,\boldsymbol{k}}-E_{l,\boldsymbol{k}})} \right) \\
- G_{\mathrm{x}}^2 \sum_{n''}\sum_{n'}\sum_{m\neq n}\sum_{l\neq n} |u_{m,\boldsymbol{k}}\rangle & \left(\frac{\langle u_{m,\boldsymbol{k}}|\hat{\sigma}_{\mathrm{x}}|u_{n',\boldsymbol{k}}\rangle\langle u_{n',\boldsymbol{k}}|\mathrm{i}\nabla_{k_{\mathrm{x}}}|u_{n,\boldsymbol{k}}\rangle}{(E_{n,\boldsymbol{k}}-E_{m,\boldsymbol{k}})^2} \right. \\
& \left. + \frac{\langle u_{m,\boldsymbol{k}}|\mathrm{i}\left(\nabla_{k_{\mathrm{x}}}|u_{n',\boldsymbol{k}}\rangle\right)\langle u_{n',\boldsymbol{k}}|\hat{\sigma}_{\mathrm{x}}|u_{n,\boldsymbol{k}}\rangle}{(E_{n,\boldsymbol{k}}-E_{m,\boldsymbol{k}})^2} \right)
\end{aligned} \qquad \text{(A.6.16)}
$$

$$\times \left(\frac{\langle u_{n,\boldsymbol{k}}|\hat{\sigma}_{\mathrm{x}}|u_{n'',\boldsymbol{k}}\rangle\langle u_{n'',\boldsymbol{k}}|\mathrm{i}\nabla_{k_{\mathrm{x}}}|u_{n,\boldsymbol{k}}\rangle}{(E_{n,\boldsymbol{k}}-E_{m,\boldsymbol{k}})^2} + \frac{\langle u_{n,\boldsymbol{k}}|\mathrm{i}\left(\nabla_{k_{\mathrm{x}}}|u_{n'',\boldsymbol{k}}\rangle\right)\langle u_{n'',\boldsymbol{k}}|\hat{\sigma}_{\mathrm{x}}|u_{n,\boldsymbol{k}}\rangle}{(E_{n,\boldsymbol{k}}-E_{m,\boldsymbol{k}})^2} \right)$$
$$- \frac{1}{2}G_{\mathrm{x}}^2 \sum_{n'}\sum_{m\neq n} |u_{n,\boldsymbol{k}}\rangle \left(\frac{|\langle u_{m,\boldsymbol{k}}|\hat{\sigma}_{\mathrm{x}}|u_{n',\boldsymbol{k}}\rangle\langle u_{n',\boldsymbol{k}}|\mathrm{i}\nabla_{k_{\mathrm{x}}}|u_{n,\boldsymbol{k}}\rangle|^2}{(E_{n,\boldsymbol{k}}-E_{m,\boldsymbol{k}})^2} + \frac{|\langle u_{m,\boldsymbol{k}}|\mathrm{i}\left(\nabla_{k_{\mathrm{x}}}|u_{n',\boldsymbol{k}}\rangle\right)\langle u_{n',\boldsymbol{k}}|\hat{\sigma}_{\mathrm{x}}|u_{n,\boldsymbol{k}}\rangle|^2}{(E_{n,\boldsymbol{k}}-E_{m,\boldsymbol{k}})^2} \right). \tag{A.6.17}$$

In the tight-binding formalism, the states $|u_{n,\boldsymbol{k}}\rangle$ in (A.6.13) and (A.6.14) are to be replaced by $\boldsymbol{C}_{n,\boldsymbol{k}}$ which is the vector with elements $C_{n,\boldsymbol{k},j,\mu}$ defined in (IV.4.7) while the operators need to be expressed in the $|\chi\rangle$-basis (see Section A.5) yielding

$$\boldsymbol{C}_{n,\boldsymbol{k}}^{(1)} = G_{\mathrm{x}} \sum_{n'}\sum_{m\neq n} \boldsymbol{C}_{m,\boldsymbol{k}} \left(\frac{\boldsymbol{C}_{m,\boldsymbol{k}}^{\dagger}\sigma_{\mathrm{x}}^{\mathrm{TB}}\boldsymbol{C}_{n',\boldsymbol{k}}\boldsymbol{C}_{n',\boldsymbol{k}}^{\dagger}\mathrm{i}\left(\nabla_{k_{\mathrm{x}}}\boldsymbol{C}_{n,\boldsymbol{k}}\right)}{E_{m,\boldsymbol{k}}-E_{n,\boldsymbol{k}}} + \frac{\boldsymbol{C}_{m,\boldsymbol{k}}^{\dagger}\mathrm{i}\left(\nabla_{k_{\mathrm{x}}}\boldsymbol{C}_{n',\boldsymbol{k}}\right)\boldsymbol{C}_{n',\boldsymbol{k}}^{\dagger}\sigma_{\mathrm{x}}^{\mathrm{TB}}\boldsymbol{C}_{n,\boldsymbol{k}}}{E_{m,\boldsymbol{k}}-E_{n,\boldsymbol{k}}} \right) \tag{A.6.18}$$

$$\begin{aligned}
\boldsymbol{C}_{n,\boldsymbol{k}}^{(2)} = {} & G_{\mathrm{x}}^2 \sum_{n''}\sum_{n'}\sum_{m\neq n}\sum_{l\neq n} \boldsymbol{C}_{m,\boldsymbol{k}} \left(\frac{\boldsymbol{C}_{m,\boldsymbol{k}}^{\dagger}\sigma_{\mathrm{x}}^{\mathrm{TB}}\boldsymbol{C}_{n',\boldsymbol{k}}\boldsymbol{C}_{n',\boldsymbol{k}}^{\dagger}\mathrm{i}\left(\nabla_{\boldsymbol{k}}\boldsymbol{C}_{l,\boldsymbol{k}}\right)}{(E_{n,\boldsymbol{k}}-E_{m,\boldsymbol{k}})(E_{n,\boldsymbol{k}}-E_{l,\boldsymbol{k}})} + \frac{\boldsymbol{C}_{m,\boldsymbol{k}}^{\dagger}\mathrm{i}\left(\nabla_{k_{\mathrm{x}}}\boldsymbol{C}_{n',\boldsymbol{k}}\right)\boldsymbol{C}_{n',\boldsymbol{k}}^{\dagger}\sigma_{\mathrm{x}}^{\mathrm{TB}}\boldsymbol{C}_{l,\boldsymbol{k}}}{(E_{n,\boldsymbol{k}}-E_{m,\boldsymbol{k}})(E_{n,\boldsymbol{k}}-E_{l,\boldsymbol{k}})} \right) \\
& \times \left(\frac{\boldsymbol{C}_{l,\boldsymbol{k}}^{\dagger}\sigma_{\mathrm{x}}^{\mathrm{TB}}\boldsymbol{C}_{n'',\boldsymbol{k}}\boldsymbol{C}_{n'',\boldsymbol{k}}^{\dagger}\mathrm{i}\left(\nabla_{\boldsymbol{k}}\boldsymbol{C}_{n,\boldsymbol{k}}\right)}{(E_{n,\boldsymbol{k}}-E_{m,\boldsymbol{k}})(E_{n,\boldsymbol{k}}-E_{l,\boldsymbol{k}})} + \frac{\boldsymbol{C}_{l,\boldsymbol{k}}^{\dagger}\mathrm{i}\left(\nabla_{k_{\mathrm{x}}}\boldsymbol{C}_{n'',\boldsymbol{k}}\right)\boldsymbol{C}_{n'',\boldsymbol{k}}^{\dagger}\sigma_{\mathrm{x}}^{\mathrm{TB}}\boldsymbol{C}_{n,\boldsymbol{k}}}{(E_{n,\boldsymbol{k}}-E_{m,\boldsymbol{k}})(E_{n,\boldsymbol{k}}-E_{l,\boldsymbol{k}})} \right) \\
& - G_{\mathrm{x}}^2 \sum_{n''}\sum_{n'}\sum_{m\neq n}\sum_{l\neq n} \boldsymbol{C}_{m,\boldsymbol{k}} \left(\frac{\boldsymbol{C}_{m,\boldsymbol{k}}^{\dagger}\sigma_{\mathrm{x}}^{\mathrm{TB}}\boldsymbol{C}_{n',\boldsymbol{k}}\boldsymbol{C}_{n',\boldsymbol{k}}^{\dagger}\mathrm{i}\nabla_{k_{\mathrm{x}}}\boldsymbol{C}_{n,\boldsymbol{k}}}{(E_{n,\boldsymbol{k}}-E_{m,\boldsymbol{k}})^2} + \frac{\boldsymbol{C}_{m,\boldsymbol{k}}^{\dagger}\mathrm{i}\left(\nabla_{k_{\mathrm{x}}}\boldsymbol{C}_{n',\boldsymbol{k}}\right)\boldsymbol{C}_{n',\boldsymbol{k}}^{\dagger}\sigma_{\mathrm{x}}^{\mathrm{TB}}\boldsymbol{C}_{n,\boldsymbol{k}}}{(E_{n,\boldsymbol{k}}-E_{m,\boldsymbol{k}})^2} \right) \\
& \times \left(\frac{\boldsymbol{C}_{n,\boldsymbol{k}}^{\dagger}\sigma_{\mathrm{x}}^{\mathrm{TB}}\boldsymbol{C}_{n'',\boldsymbol{k}}\boldsymbol{C}_{n'',\boldsymbol{k}}^{\dagger}\mathrm{i}\nabla_{k_{\mathrm{x}}}\boldsymbol{C}_{n,\boldsymbol{k}}}{(E_{n,\boldsymbol{k}}-E_{m,\boldsymbol{k}})^2} + \frac{\boldsymbol{C}_{n,\boldsymbol{k}}^{\dagger}\mathrm{i}\left(\nabla_{k_{\mathrm{x}}}\boldsymbol{C}_{n'',\boldsymbol{k}}\right)\boldsymbol{C}_{n'',\boldsymbol{k}}^{\dagger}\sigma_{\mathrm{x}}^{\mathrm{TB}}\boldsymbol{C}_{n,\boldsymbol{k}}}{(E_{n,\boldsymbol{k}}-E_{m,\boldsymbol{k}})^2} \right) \\
& - \frac{1}{2}G_{\mathrm{x}}^2 \sum_{n'}\sum_{m\neq n} \boldsymbol{C}_{n,\boldsymbol{k}} \left(\frac{\left|\boldsymbol{C}_{m,\boldsymbol{k}}^{\dagger}\sigma_{\mathrm{x}}^{\mathrm{TB}}\boldsymbol{C}_{n',\boldsymbol{k}}\boldsymbol{C}_{n',\boldsymbol{k}}^{\dagger}\mathrm{i}\nabla_{k_{\mathrm{x}}}\boldsymbol{C}_{n,\boldsymbol{k}}\right|^2}{(E_{n,\boldsymbol{k}}-E_{m,\boldsymbol{k}})^2} + \frac{\left|\boldsymbol{C}_{m,\boldsymbol{k}}^{\dagger}\mathrm{i}\left(\nabla_{k_{\mathrm{x}}}\boldsymbol{C}_{n',\boldsymbol{k}}\right)\boldsymbol{C}_{n',\boldsymbol{k}}^{\dagger}\sigma_{\mathrm{x}}^{\mathrm{TB}}\boldsymbol{C}_{n,\boldsymbol{k}}\right|^2}{(E_{n,\boldsymbol{k}}-E_{m,\boldsymbol{k}})^2} \right)
\end{aligned} \tag{A.6.19}$$

These expressions for the change in the Bloch states in the tight binding formalism are used to find the expression for the different terms contained in Equation (IV.4.41) discussed in Section IV.4

Kubo formula

In the main text, it is mentioned that the transverse Hall conductivity σ_{xy} is proportional to the Chern number. The transverse Hall conductivity can be derived from the perturbation theory as this has been done in the References [19, 137] yielding the well known Kubo formula [138]. Instead of a magnetic field gradient, an electric potential gradient is used as a perturbative term given by $E_{\mathrm{x}} r_{\mathrm{x}}$ and instead of the spin operator, the current-density operator is analyzed. Thus, using Equation (IV.4.16) and $\hat{V} = E_{\mathrm{x}} \hat{r}_{\mathrm{x}}$ while considering the expectation value of the current density operator $\hat{j} = ne\hat{v}_{\mathrm{x}}$ leads directly to the Kubo formula [2]

$$\delta\langle\hat{j}\rangle = 2\mathrm{Re}\left(\langle n|ne\hat{v}|n^{(1)}\rangle\right) = 2\mathrm{Re}\left(E_{\mathrm{x}} n\mathrm{e} \sum_{n_{\mathrm{occ}}} \sum_{m\neq n} \frac{\langle n|\hat{v}_{\mathrm{x}}|m\rangle\langle m|\mathrm{i}\left(\nabla_{k_{\mathrm{y}}}|n\rangle\right)}{\lambda_n - \lambda_m}\right) \tag{A.6.20}$$

$$= 2\mathrm{Im}\left(E_{\mathrm{x}} ne \sum_{n_{\mathrm{occ}}} \sum_{j\neq n} \frac{\langle n|\nabla_{k_{\mathrm{x}}} \mathcal{H}(\boldsymbol{k})|m\rangle\langle m|\nabla_{k_{\mathrm{y}}} \mathcal{H}(\boldsymbol{k})|n\rangle}{(\lambda_n - \lambda_m)^2}\right) \tag{A.6.21}$$

where n is the electron density and e is the elementary charge.

A.7. Basics from field theory

In this work, thermodynamic signatures for the QWZ model and for a topological s-wave superconductor are discussed. Decisive for the thermodynamics are the thermodynamic potentials. In the following, the basics from the field theory are discussed, which have been used to calculate the grand canonical potentials used in the main text.

Grassmann algebra

The Grassmann algebra was introduced in the context of exterior algebras which is a part of differential geometry [139]. The Grassmann algebra is often applied in physics, especially in quantum field theory due to their useful mathematical properties [55]. Most important in partition functions of fermionic systems, the Grassmann algebra is used to integrate out the fermionic degrees of freedom.

In the following, the major aspects of the Grassmann algebra which is of direct relevance within this work is revisited. The following content can be found for example in the References [55, 140]. There, complex valued Grassmann fields ϕ_i are defined such that they obey a number of properties which are:

1. The Grassmann fields anticommute with each other such as the fermionic creation and annihilation operators
$$[\phi_1, \phi_2]_+ = 0. \tag{A.7.1}$$
2. Additionally, one defines the Grassmann fields such that they anticommute with the fermionic annihilation and creation operators.
$$[\phi, \hat{\psi}]_+ = 0; \qquad [\phi, \hat{\psi}^\dagger]_+ = 0. \tag{A.7.2}$$

3. The Grassmann fields obey special integration and differentiation rules. There are three distinct integrations over Grassmann fields possible, these are

$$\int \mathrm{d}\phi = 0 \tag{A.7.3}$$

$$\int \mathrm{d}\phi\phi = 1 \tag{A.7.4}$$

$$\int \mathrm{d}\phi\phi^*\phi = -\phi^*. \tag{A.7.5}$$

Due to the property

$$\phi^2 = 0 \tag{A.7.6}$$

resulting from the anticommutativity of the Grassmann fields all higher integrals over Grassmann fields are zero.

4. The derivatives of Grassmann fields are defined such that

$$\frac{\partial}{\partial\phi}c = 0; \quad \text{with } c \text{ being a constant} \tag{A.7.7}$$

$$\frac{\partial}{\partial\phi}\phi = 1 \tag{A.7.8}$$

$$\frac{\partial}{\partial\phi}\phi^*\phi = -\frac{\partial}{\partial\phi}\phi\phi^* = -\phi^*. \tag{A.7.9}$$

Therefore, as a very special property, the integration of Grassmann fields behaves effectively like the derivative with respect to the Grassmann field which is apparent from (A.7.3) to (A.7.9). The benefit of the Grassmann fields is explained below.

One of the most important benefits is that it is possible to define coherent fermionic states which are eigenstates of the fermionic annihilation operator with by use of these Grassmann fields. These coherent fermionic states can be defined through

$$|\phi\rangle = \mathrm{e}^{-\sum_\alpha \phi_\alpha \hat{\psi}_\alpha}|0\rangle. \tag{A.7.10}$$

It is not obvious that this state fulfills the desired properties, however, the property of this state being an eigenstate of the fermionic annihilation operator can of course easily be verified directly by applying the annihilation operator to that state yielding

$$\hat{\psi}_\gamma|\phi\rangle = \hat{\psi}_\gamma \prod_\alpha \left(1 - \phi_\alpha \hat{\psi}_\alpha^\dagger\right)|0\rangle = \prod_{\beta\neq\gamma}(1 - \phi_\beta\hat{\psi}_\beta^\dagger)\hat{\psi}_\gamma(1 - \phi_\gamma\hat{\psi}_\gamma^\dagger)|0\rangle. \tag{A.7.11}$$

$$= \prod_{\beta\neq\gamma}(1 - \phi_\beta\hat{\psi}_\beta^\dagger)\phi_\gamma|0\rangle = \phi_\gamma \prod_{\beta\neq\gamma}(1 - \phi_\beta\hat{\psi}_\beta^\dagger)(1 - \phi_\gamma\hat{\psi}_\gamma^\dagger)|0\rangle \tag{A.7.12}$$

$$= \phi_\gamma \prod_\alpha (1 - \phi_\alpha\hat{\psi}_\alpha^\dagger)|0\rangle = \phi_\gamma|\phi\rangle. \tag{A.7.13}$$

Thus, the state (A.7.10) is indeed the eigenstate of $\hat{\psi}_\gamma$ with eigenvalue ϕ_γ. By use of these coherent fermionic states, the identity operator can be expressed in terms of these states and is given by

$$\int \mathcal{D}\phi^* \int \mathcal{D}\phi \mathrm{e}^{-\sum_\alpha \phi^*_\alpha \phi_\alpha} |\phi\rangle\langle\phi| = \prod_\alpha \prod_\beta \prod_\gamma \int \mathrm{d}\phi^* \alpha \mathrm{d}\phi_\alpha \mathrm{e}^{-\phi^*_\alpha \phi_\alpha} \mathrm{e}^{-\phi_\beta \hat{\psi}^\dagger_\beta} |0\rangle\langle 0| \mathrm{e}^{-\phi^*_\gamma \hat{\psi}_\gamma} \quad \text{(A.7.14)}$$

$$= \prod_\alpha \prod_\beta \prod_\delta \int \mathrm{d}\phi^*_\alpha \mathrm{d}\phi_\alpha (1 - \phi^*_\alpha \phi_\alpha)(1 - \phi_\beta \hat{\psi}^\dagger_\beta)|0\rangle\langle 0|(1 - \phi^*_\gamma \hat{\psi}_\gamma) = |0\rangle\langle 0| + \sum_\alpha |\alpha\rangle\langle\alpha| = \mathbb{1}. \quad \text{(A.7.15)}$$

Using the representation of the identity operator given in (A.7.15) the trace of an operator at which fermionic creation and annihilation operators occurs in even products as

$$\int \mathcal{D}\phi^* \mathcal{D}\phi \exp\left(-\sum_\alpha \phi^*_\alpha \phi_\alpha\right) \langle -\phi|\hat{O}|\phi\rangle = \prod_\alpha \prod_\beta \prod_\gamma \int \mathrm{d}\phi^*_\alpha \mathrm{d}\phi_\alpha \mathrm{e}^{\phi^*_\alpha \phi_\alpha} \langle 0| \mathrm{e}^{-\phi^*_\beta \hat{\psi}_\beta} \hat{O} \mathrm{e}^{-\phi_\gamma \hat{\psi}^\dagger_\gamma} |0\rangle \quad \text{(A.7.16)}$$

$$= \prod_\alpha \prod_\beta \prod_\gamma \int \mathrm{d}\phi^*_\alpha \mathrm{d}\phi_\alpha (1 - \phi^*_\alpha \phi_\alpha)\langle 0|(1 + \phi^*_\beta \hat{\psi}_\beta)\hat{O}(1 - \phi_\gamma \hat{\psi}^\dagger_\gamma)|0\rangle \quad \text{(A.7.17)}$$

$$= \langle 0|\hat{O}|0\rangle + \sum_\alpha \langle\alpha|\hat{O}|\alpha\rangle = \mathrm{Tr}(\hat{O}). \quad \text{(A.7.18)}$$

Here, the integration rules of the Grassmann algebra and the anticommutation property of the Grassmann fields is used. This notation of the trace of a fermionic operator is useful to calculate fermionic partition functions due to the simple integration and differentiation rules of the Grassmann fields.

Partition function

From statistical physics, it is well known that the grand canonical partition function is defined as

$$Z_\mathrm{G} = \mathrm{Tr}\left[\mathrm{e}^{-\beta(\hat{H} - \mu\hat{N})}\right]. \quad \text{(A.7.19)}$$

By use of the expression of a trace of an operator in terms of an integral over Grassmann fields given in (A.7.18), the grand canonical partition function can be written as

$$Z_\mathrm{G} = \int \mathcal{D}\phi^* \mathcal{D}\phi \exp\left(-\sum_\alpha \phi^*_\alpha \phi_\alpha\right) \langle -\phi| \mathrm{e}^{-\beta(\hat{H} - \mu\hat{N})} |\phi\rangle; \quad \int \mathcal{D}\phi := \prod_i \int \mathrm{d}\phi_i. \quad \text{(A.7.20)}$$

In order to make further progress the time $\tau = \hbar\beta$ is introduced and split into N_α parts such that $\tau_\alpha = \alpha\hbar\beta/N_\alpha = \alpha\Delta\tau$ with $\alpha \in \left\{1, 2, \dots, N_\alpha\right\}$ and $N_\alpha \to \infty$. Therefore one obtains

$$\mathrm{e}^{-\tau(\hat{H} - \mu\hat{N})/\hbar} = \prod_{\alpha=1}^{N_\alpha} \mathrm{e}^{-\Delta\tau(\hat{H} - \mu\hat{N})/\hbar}. \quad \text{(A.7.21)}$$

The final fermionic state is now denoted as $\langle\phi_\mathrm{f}|$ and the initial fermionic coherent state is denoted by $|\phi_\mathrm{i}\rangle$. Inserting the identity operator (A.7.15) between each element of the product in (A.7.21) yields

$$\mathcal{Z} = \int \mathcal{D}\phi^*\mathcal{D}\phi \prod_{\beta=1}^{N_\alpha} \exp\left(-\sum_\alpha \phi^*_{\alpha,\beta}\phi_{\alpha,\beta}\right)\langle\phi_\beta|\phi_{\beta-1}\rangle$$
$$\times \exp\left(-\frac{\Delta\tau}{\hbar}(H[\phi^*_{\alpha,\beta},\phi_{\alpha,\beta-1}] - \mu N[\phi^*_{\alpha,\beta},\phi_{\alpha,\beta-1}])\right). \qquad \text{(A.7.22)}$$

Here, it is used that the coherent state is the eigenstate of the creation operator such that the fermionic creation and annihilation operators in the Hamiltonian are replaced by the eigenstates of the fermionic coherent states, the Grassmann fields. This is possible if the Hamiltonian is in normal order since the coherent state is the eigenstate of the fermionic annihilation operator as shown in (A.7.13). The partition function can then be further brought to the form

$$\mathcal{Z} = \int \mathcal{D}\phi^*\mathcal{D}\phi \prod_{\beta=1}^{N_\alpha} \exp\left(-\hbar\frac{\Delta\tau}{\hbar}\sum_\alpha \phi^*_{\alpha,\beta}\left(\frac{\phi_{\alpha,\beta}-\phi_{\alpha,\beta-1}}{\Delta\tau}\right)\right) \qquad \text{(A.7.23)}$$
$$\times \exp\left(-\frac{\Delta\tau}{\hbar}\sum_\alpha\left(H[\phi^*_{\alpha,\beta},\phi_{\alpha,\beta-1}] - \mu N[\phi^*_{\alpha,\beta},\phi_{\alpha,\beta-1}]\right)\right). \qquad \text{(A.7.24)}$$

Taking the limit $N_\alpha \to \infty$ and so $\Delta\tau \to 0$ yields

$$\mathcal{Z} = \int_{\langle\phi(\hbar\beta)|=-\langle\phi(0)|} \mathcal{D}\phi^*\mathcal{D}\phi\, \exp\left(-\frac{1}{\hbar}S[\phi^*,\phi]\right) \qquad \text{(A.7.25)}$$

with

$$S = \int_0^{\hbar\beta} \mathrm{d}\tau \sum_\alpha \hbar\phi^*_\alpha(\tau)\left(\frac{\partial\phi_\alpha(\tau)}{\partial\tau}\right) + \left(H[\phi^*_\alpha(\tau),\phi_\alpha(\tau)] - \mu N[\phi^*_\alpha(\tau),\phi_\alpha(\tau)]\right). \qquad \text{(A.7.26)}$$

In general, the Hamiltonian H can be expanded to Nambu space, doubling the number of bands and the commutator relations for creation and annihilation operators have to be taken into account which reads

$$\{\hat{\psi}^\dagger_a, \hat{\psi}_b\} = \delta_{ab} \qquad \text{(A.7.27)}$$

and a factor of 1/2 has to be included where $\{\ldots,\ldots\}$ is the anticommutator, yielding

$$S = \frac{1}{2}\int_0^{\hbar\beta} \mathrm{d}\tau \sum_\alpha \left[\hbar\phi^*_\alpha(\tau)\left(\frac{\partial\phi_\alpha(\tau)}{\partial\tau}\right) + \left(H[\phi^*_\alpha(\tau),\phi_\alpha(\tau)] - \mu N[\phi^*_\alpha(\tau),\phi_\alpha(\tau)]\right)\right] \qquad \text{(A.7.28)}$$
$$+\frac{\beta}{2}K - \frac{1}{2}\int_0^{\hbar\beta} \mathrm{d}\tau \sum_\alpha \left[-\hbar\phi_\alpha(\tau)\left(\frac{\partial\phi^*_\alpha(\tau)}{\partial\tau}\right) + \left(H[\phi_\alpha(\tau),\phi^*_\alpha(\tau)] - \mu N[\phi_\alpha(\tau),\phi^*_\alpha(\tau)]\right)\right]$$
$$\text{(A.7.29)}$$

in particle-hole space with K denoting a constant that has to be included due to the commutator relations of the Fermion operators. The fermionic degree of freedom in the partition function can be integrated out. It has to be emphasized at this point that $\phi^*\partial_\tau\phi = -\partial_\tau\phi\phi^* = \phi\partial_\tau\phi^*$ because of the definition of the derivative of a Grassmann field and the use of the anticommutativity of the Grassmann fields. Therefore the second term containing ∂_τ possesses the minus sign. In general, one finds

$$\int \prod_i \mathrm{d}\phi_i^* \mathrm{d}\phi_i \exp\left(-\sum_{\alpha,\beta} \phi_\alpha^* O_{\alpha\beta} \phi_\beta\right) = \int \mathcal{D}\phi_i^* \mathcal{D}\phi_i \prod_i \prod_j (1 - \phi_i^* O_{ij} \phi_j) \tag{A.7.30}$$

$$= \det O = \exp(\ln(\det(O))). \tag{A.7.31}$$

Using (A.7.31), the partition function given in (A.7.25) can be expressed as

$$\mathcal{Z} = \mathrm{e}^{-\frac{\beta}{2}K} \left(\det\left(\mathcal{G}^{-1}\right)\right)^{1/2} \tag{A.7.32}$$

where $\mathcal{G}^{-1}$ is the inverse Matsubara Green's function given through

$$\mathcal{G}^{-1} = \hbar \frac{\partial}{\partial \tau} + \mathcal{H} \tag{A.7.33}$$

where $\mathcal{H}$ denotes the matrix elements of the Hamiltonian. As mentioned above, by integrating the partition function, one has to obey the antiperiodicity in the imaginary Matsubara time. This antiperiodicity needs to be considered when transforming the Green's function Matsubara time into the fermionic Matsubara frequency space. There one defines the fermionic Matsubara frequency

$$\omega_n = \frac{(2n+1)\pi}{\hbar\beta} \quad \text{with } n \in \{0, \pm 1, \pm 2, \pm 3, \dots\} \tag{A.7.34}$$

and the fermionic Grassmann fields transform into the fermionic Matsubara frequency space as

$$\phi_\alpha(\hbar\omega) = \int_0^{\hbar\beta} \mathrm{d}\tau \phi_\alpha(\tau) \exp\left(\mathrm{i}\omega_n \tau\right) \tag{A.7.35}$$

$$\phi_\alpha(\tau) = \sum_{-\infty}^{\infty} \phi_\alpha(\hbar\omega_n) \exp\left(-\mathrm{i}\omega_n \tau\right). \tag{A.7.36}$$

Sums over Matsubara frequencies and thermodynamics

The grand canonical potential Ω can, with the use of (A.7.32), be written as

$$\Omega = -\frac{1}{\beta} \ln \mathcal{Z} = \frac{K}{2} - \frac{1}{\beta} \sum_{\omega_n} \ln\left(\left(\det\left[\hbar\mathcal{G}^{-1}(\omega_n)\right]\right)^{1/2}\right). \tag{A.7.37}$$

Assuming that the inverse Green's function is diagonal in momentum space, Equation (A.7.37) becomes

$$\Omega = \frac{K}{2} - \frac{1}{2\beta} \sum_{\omega_n} \sum_{\boldsymbol{k}} \ln\left(\det\left[\mathcal{G}^{-1}(\omega_n, \boldsymbol{k})\right]\right). \tag{A.7.38}$$

$$= \frac{K}{2} - \frac{1}{2\beta} \sum_{\omega_n} \sum_{\boldsymbol{k}} \ln\left[\prod_i \left(\lambda_i(\boldsymbol{k}) - \mathrm{i}\hbar\omega_n\right)\left(-\lambda_i(\boldsymbol{k}) - \mathrm{i}\hbar\omega_n\right)\right]. \tag{A.7.39}$$

where λ_i are the different eigenvalues of the Hamiltonian $\mathcal{H}$. The subsequent calculations of the Matsubara sums follow the presentation in Reference [141]. Further information about Matsubara frequency sum evaluations can be found in Reference [142]. In order to carry out the summation over the Matsubara frequencies ω_n is written as

$$\omega_n = \frac{2\pi(n+1/2)}{\beta} = \frac{2\pi n}{\hbar\beta} + \frac{\pi}{\hbar\beta} \equiv \omega_0 n + \kappa. \tag{A.7.40}$$

The derivative of Ω with respect to λ_i yields

$$-\frac{\partial\Omega}{\partial\lambda_i} = \frac{1}{2}\sum_{n=-\infty}^{\infty} \frac{2\lambda_i}{(-(\mathrm{i}(\omega_0 n+\kappa))^2+\lambda_i^2} = \frac{1}{2\omega_0}\sum_{n=-\infty}^{\infty}\left[\frac{1}{\frac{\lambda_i}{\omega_0}-\mathrm{i}n-\mathrm{i}\frac{\kappa}{\omega_0}} + \frac{1}{\frac{\lambda_i}{\omega_0}+\mathrm{i}n+\mathrm{i}\frac{\kappa}{\omega_0}}\right]. \tag{A.7.41}$$

In the last step the numerator and denominator was multiplied by $1/\omega_0$. Further, using the known sum

$$\sum_{n=-\infty}^{\infty}\frac{1}{y\pm\mathrm{i}n} = \pi\coth(\pi y) \tag{A.7.42}$$

the term in (A.7.41) can be rewritten as

$$\frac{1}{2\omega_0}\sum_{n=-\infty}^{\infty}\left[\frac{1}{\frac{\lambda_i}{\omega_0}-\mathrm{i}n-\mathrm{i}\frac{\kappa}{\omega_0}} + \frac{1}{\frac{\lambda_i}{\omega_0}+\mathrm{i}n+\mathrm{i}\frac{\kappa}{\omega_0}}\right] \tag{A.7.43}$$

$$= \frac{\beta}{2}\left[\coth\left(\frac{\beta}{2}\left(\lambda_i+\mathrm{i}\frac{\pi}{\beta}\right)\right) + \coth\left(\frac{\beta}{2}\left(\lambda_i-\mathrm{i}\frac{\pi}{\beta}\right)\right)\right] \tag{A.7.44}$$

And therefore,

$$\frac{\partial\Omega}{\partial\lambda_i} = -\sum_{\boldsymbol{k}}\frac{\beta}{2}\left[\coth\left(\frac{\beta}{2}\left(\lambda_i+\mathrm{i}\frac{\pi}{\beta}\right)\right) + \coth\left(\frac{\beta}{2}\left(\lambda_i-\mathrm{i}\frac{\pi}{\beta}\right)\right)\right]. \tag{A.7.45}$$

One can then integrate with respect to λ_i obtaining

$$\int \mathrm{d}\lambda_i \coth\left(\frac{\beta}{2}\left(\lambda_i-\mathrm{i}\frac{\pi}{\beta}\right)\right) = C + \frac{2\ln\left(\cosh\left(\frac{\beta\lambda_i}{2}\right)\right)}{\beta}. \tag{A.7.46}$$

Hence, the grand canonical potential Ω is given by

$$\Omega = K - \sum_i \frac{1}{\beta}\ln\left(2\cosh\left(\frac{\beta\lambda_i}{2}\right)\right). \tag{A.7.47}$$

The factor 2 in front of cosh is necessary to obtain the correct entropy as will be more obvious below and stems from the determination of the integration constant C in (A.7.46).

From the grand canonical potential (A.7.47), all thermodynamic quantities can be determined. The total differential of the grand canonical potential reads

$$\mathrm{d}\Omega = -S\mathrm{d}T - P\mathrm{d}\mathcal{V} - N\mathrm{d}\mu - M\mathrm{d}H \tag{A.7.48}$$

identifying the natural variables of Ω being the temperature T, the volume $\mathcal{V}$, the chemical potential μ and the magnetic field H. From (A.7.48), three important thermodynamic quantities, analyzed within this thesis are obtained; these are

$$S = -\left.\frac{\partial\Omega}{\partial T}\right|_{\mathcal{V},\mu,H} \tag{A.7.49}$$

$$N = -\left.\frac{\partial\Omega}{\partial \mu}\right|_{\mathcal{V},H,T} \tag{A.7.50}$$

$$M = -\frac{1}{V}\left.\frac{\partial\Omega}{\partial H}\right|_{\mathcal{V},\mu,T} \tag{A.7.51}$$

with S, N and M denoting the entropy, particle number and magnetization, respectively. The entropy can be written down explicitly in terms of the eigenvalues of a given system using (A.7.49) and (A.7.47) yielding

$$S = -k_\mathrm{B}\left.\frac{\partial\Omega}{\partial T}\right|_{h,\mu,V} = k_\mathrm{B}\sum_{\boldsymbol{k}}\sum_i\left(\ln\left(2\cosh\left(\frac{\beta}{2}\lambda_i\right)\right) - \frac{1}{2}\frac{\lambda_i}{k_\mathrm{B}T}\tanh\left(\frac{\beta}{2}\lambda_i\right)\right) : \tag{A.7.52}$$

Using the identities

$$\frac{1}{2}\tanh\left(\frac{x}{2}\right) = -n_\mathrm{F}(x) \tag{A.7.53}$$

and

$$\cosh\left(\frac{x}{2}\right) = \frac{1}{2}\exp\left(-\frac{x}{2}\right)n_\mathrm{F}^{-1}(x) \tag{A.7.54}$$

with the Fermi distribution

$$n_\mathrm{F}(x) = \frac{1}{\exp(x)+1} \tag{A.7.55}$$

yields the well known result for the entropy of a fermionic system which is given by

$$S = -k_\mathrm{B}\sum_{\boldsymbol{k}}\sum_i\left[(1-n_\mathrm{F}(\boldsymbol{k},i))\ln(1-n_\mathrm{F}(\boldsymbol{k},i)) + n_\mathrm{F}\ln(n_\mathrm{F}(\boldsymbol{k},i))\right]. \tag{A.7.56}$$

The particle number and the magnetization are hence

$$n = -\frac{1}{2}\frac{\partial\Omega}{\partial\mu} = \frac{1}{2}\sum_{\boldsymbol{k}}\sum_i\left(\frac{\partial K}{\partial\mu} + \frac{1}{2}\tanh\left(\frac{\beta}{2}\lambda_i\right)\frac{\partial\lambda_i}{\partial\mu}\right) \tag{A.7.57}$$

$$\boldsymbol{m} = \frac{1}{2}\sum_{\boldsymbol{k}}\sum_i\tanh\left(\frac{\beta}{2}\lambda_i\right)\frac{\partial\lambda_i}{\partial\boldsymbol{h}}. \tag{A.7.58}$$

These thermodynamic quantities are used in the main text to determine and analyze topological phase transitions.

Bibliography

[1] F. Duncan and M. Haldane, *Nobel lecture. NobelPrize.org*, 2016.

[2] D. J. Thouless, M. Kohmoto, M. P. Nightingale, et al., “Quantized Hall Conductance in a Two-Dimensional Periodic Potential”, Phys. Rev. Lett. **49**, 405 (1982).

[3] K. v. Klitzing, G. Dorda, and M. Pepper, “New Method for High-Accuracy Determination of the Fine-Structure Constant Based on Quantized Hall Resistance”, Phys. Rev. Lett. **45**, 494 (1980).

[4] F. D. M. Haldane, *Nobel lecture. NobelPrize.org*, 1985.

[5] K. v. Klitzing, “The quantized Hall effect”, Rev. Mod. Phys. **58**, 519 (1986).

[6] B. J. Wieder, B. Bradlyn, J. Cano, et al., “Topological materials discovery from crystal symmetry”, Nat. Rev. Mater. **7**, 196 (2022).

[7] M. Sato and Y. Ando, “Topological superconductors: a review”, Rep. Prog. Phys. **80**, 076501 (2017).

[8] M. Z. Hasan and C. L. Kane, “*Colloquium*: topological insulators”, Rev. Mod. Phys. **82**, 3045 (2010).

[9] B. Yan and C. Felser, “Topological Materials: Weyl Semimetals”, Annu. Rev. Condens. Matter Phys. **8**, 337–354 (2017).

[10] B. A. Bernevig, T. L. Hughes, and S.-C. Zhang, “Quantum Spin Hall Effect and Topological Phase Transition in HgTe Quantum Wells”, Science **314**, 1757 (2006).

[11] S. B. Zhang, H. Z. Lu, and S. Q. Shen, “Edge states and integer quantum Hall effect in topological insulator thin films”, Sci. Rep. **5**, 13277 (2015).

[12] N. Romming, C. Hanneken, M. Menzel, et al., “Writing and deleting single magnetic skyrmions”, Science **341**, 636 (2013).

[13] L. Peng, K. Karbube, Y. Taguchi, et al., “Dynamic transition of current-driven single-skyrmion motion in a room-temperature chiral-lattice magnet”, Nat. Commun. **12**, 6797 (2021).

[14] A. Fert, N. Reyren, and C. V, “Magnetic skyrmions: advances in physics and potential applications”, Nat Rev Mater **2**, 17031 (2017).

[15] X. L. Qi, Y. S. Wu, and S. C. Zhang, “Topological quantization of the spin Hall effect in two-dimensional paramagnetic semiconductors”, Phys. Rev. B **74**, 085308 (2006).

[16] N. Mohanta, A. P. Kampf, and T. Kopp, “Emergent Momentum-Space Skyrmion Texture on the Surface of Topological Insulators”, Sci. Rep. **7**, 45664 (2017).

[17] I. M. Lifshitz, “Anomalies of Electron Characteristics of a Metal in the High Pressure Region”, Sov. Phys. JETP **11**, [Fiz. Nizk. Temp. **43**, 57 (2017)], 1130 (1960).

[18] G. E. Volovik, “Topological Lifshitz transitions”, Low Temp. Phys. **43**, 47 (2017).

[19] S. Zhuo Bin, M. B. A. Jalil, and S. G. Tan, “Hamiltonian term for a uniform dc electric field under the adiabatic approximation”, Phys. Rev. A **97**, 022101 (2018).

[20] B. A. Bernevig, *Topological Insulators and Topological Superconductors* (Princeton University Press, Princeton, 2013).

[21] L. Euler, “Elementa doctrine solidorum”, Novi Comment. Acad. Sci. Imp. Petropol. **4**, 109 (1752).

[22] M. Nakahara, *Geometry, topology and physics*, Graduate student series in physics (Hilger, Bristol, 1990).

[23] S. Lhuilier, “Mémoire sur la polyédrométrie, contenant une démonstration du théorème d’Euler sur les polyèdres, et un examen de diverses exceptions auxquelles ce théorème est assujetti”, Gergonne Ann. Math. **3**, 169 (1812).

[24] A. M. Legendre, *Élements de géométrie* (Firmin-Didot(Paris), 1794).

[25] D. S. Richeson, *Euler’s Gem: The Polyhedron Formula and the Birth of Topology* (Princeton University Press, 2008).

[26] H. Poincare, “Sur l’Analysis situs, note de Henri Poincare”, C. R. Acad. Sci. **115**, 633 (1892).

[27] C. F. Gauß, “Theorema egregium”, in *Werke Band 4* (1873), p. 219.

[28] A. Pressley, *The First Fundamental Form* (Springer Undergraduate Mathematics Series. Springer, 2001).

[29] P. O. Bonnet, “Mémoire sur la théorie générale des surfaces”, J. Ec. Polytech. - Math. **32** (1848).

[30] G. E. Bredon, *Topology and geometry* (Springer, 1993).

[31] L. Brouwer, “Über Abbildung von Mannigfaltigkeiten”, Math. Ann. **71**, 97 (1911).

[32] M. Nagumo, “A theory of degree of mappings based upon infinitesimal analysis”, Amer. J. Math. **73**, 485 (1951).

[33] T. Surazhsky, E. Magid, O. Soldea, et al., “A comparison of Gaussian and mean curvatures estimation methods on triangular meshes”, IEEE Int. Conf. Robot. Autom. **1**, 1021 (2003).

[34] M. V. Berry, “The Quantum Phase, Five Years”, in *Geometric Phases in Physics* (1989), p. 7.

[35] M.-C. Chang, “Berry phase in solid state physics”, http://phy.ntnu.edu.tw/ changmc/Paper /Berry_IFF_FF_4.pdf, Accessed: 2022-09-22.

[36] M. V. Berry, “Quantal phase factors accompanying adiabatic changes”, Proc. R. Soc. Lond. **392**, 45 (1984).

[37] F. Loder, A. P. Kampf, T. Kopp, et al., “Momentum-space spin texture in a topological superconductor”, Phys. Rev. B **96**, 024508 (2017).

[38] J. D. Sau, R. M. Lutchyn, S. Tewari, et al., "Generic New Platform for Topological Quantum Computation Using Semiconductor Heterostructures", Phys. Rev. Lett. **104**, 040502 (2010).

[39] M. Sato, Y. Takahashi, and S. Fujimoto, "Non-Abelian Topological Order in s-Wave Superfluids of Ultracold Fermionic Atoms", Phys. Rev. Lett. **103**, 020401 (2009).

[40] M. Sato, Y. Takahashi, and S. Fujimoto, "Non-Abelian topological orders and Majorana fermions in spin-singlet superconductors", Phys. Rev. B **82**, 134521 (2010).

[41] F. Loder, A. P. Kampf, and T. Kopp, "Route to Topological Superconductivity via Magnetic Field Rotation", Sci. Rep. **5**, 15302 (2015).

[42] C. R. Ast and I. Gierz, "*sp*-band tight-binding model for the Bychkov-Rashba effect in a two-dimensional electron system including nearest-neighbor contributions from an electric field", Phys. Rev. B **86**, 085105 (2012).

[43] A. D. Caviglia, M. Gabay, S. Gariglio, et al., "Tunable Rashba Spin-Orbit Interaction at Oxide Interfaces", Phys. Rev. Lett. **104**, 126803 (2010).

[44] M. Ben Shalom, M. Sachs, D. Rakhmilevitch, et al., "Tuning Spin-Orbit Coupling and Superconductivity at the $SrTiO_3/LaAlO_3$ Interface: A Magnetotransport Study", Phys. Rev. Lett. **104**, 126802 (2010).

[45] Z. Zhong, A. Tóth, and K. Held, "Theory of spin-orbit coupling at $LaAlO_3/SrTiO_3$ interfaces and $SrTiO_3$ surfaces", Phys. Rev. B **87**, 161102 (2013).

[46] V. P. Mineev, K. Samokhin, and A. V. Malyavkin, *Introduction to unconventional superconductivity* (CRC Press, 1999).

[47] W. Zhang and W. Yi, "Topological Fulde–Ferrell–Larkin–Ovchinnikov states in spin–orbit-coupled Fermi gases", Nat Commun **4**, 2711 (2013).

[48] F. Loder, A. P. Kampf, and T. Kopp, "Superconductivity with Rashba spin-orbit coupling and magnetic field", J. Phys. Condens. Matter **25**, 362201 (2013).

[49] P. Fulde and R. A. Ferrell, "Superconductivity in a Strong Spin-Exchange Field", Phys. Rev. **135**, A550–A563 (1964).

[50] A. I. Larkin and Y. N. Ovchinnikov, "Nonuniform state of superconductors", Zh. Eksp. Teor. Fiz. **47**, 1136–1146 (1964).

[51] K. V. Samokhin, "Magnetic properties of superconductors with strong spin-orbit coupling", Phys. Rev. B **70**, 104521 (2004).

[52] J. Tempere, N. Klimin, and J. T. Devreese, "Effect of population imbalance on the Berezinskii-Kosterlitz-Thouless phase transition in a superfluid Fermi gas", Phys. Rev. A **79**, 053637 (2009).

[53] J. P. A. Devreese, J. Tempere, and C. A. R. Sa de Melo, "Effect of population imbalance on the Berezinskii-Kosterlitz-Thouless phase transition in a superfluid Fermi gas", Phys. Rev. A **92**, 043618 (2015).

[54] Y. Xu and C. Zhang, "Berezinskii-Kosterlitz-Thouless Phase Transition in 2D Spin-Orbit-Coupled Fulde-Ferrell Superfluids", Phys. Rev. Lett. **114**, 110401 (2015).

[55] J. W. Negele and H. Orland, *Quantum Many-particle Systems* (Westview Press, 1998).

[56] K. Shakouri and F. M. Peeters, “Spin- and pseudospin-polarized quantum Hall liquids in HgTe quantum wells”, Phys. Rev. B **92**, 045416 (2015).

[57] A. Georgi, P. Nemes-Incze, R. Carrillo-Bastos, et al., “Tuning the Pseudospin Polarization of Graphene by a Pseudomagnetic Field”, Nano Lett. **17**, 2240 (2017).

[58] O. Viyuela, A. Rivas, and M. A. Martin-Delgado, “Uhlmann Phase as a Topological Measure for One-Dimensional Fermion Systems”, Phys. Rev. Lett. **112**, 130401 (2014).

[59] S. Woo, “Elusive spin textures discovered”, Nature **564**, 43 (2018).

[60] P. M. Chaikin and T. C. Lubensky, *Principles of Condensed Matter Physics* (Cambridge University Press, Cambridge, 1995).

[61] D. J. Thouless, *Topological Quantum Numbers in Nonrelativistic Physics* (World Scientific, Singapore, 1998).

[62] X. L. Qi and S. C. Zhang, “Topological insulators and superconductors”, Rev. Mod. Phys **83**, 1057 (2011).

[63] J. E. Moore, “The birth of topological insulators”, Nature **464**, 194 (2010).

[64] J. E. Haldane, “Model for a Quantum Hall Effect without Landau Levels: Condensed-Matter Realization of the “Parity Anomaly“”, Phys. Rev. Lett. **61**, 2015 (1988).

[65] H. Sumiyoshi and S. Fujimoto, “Quantum Thermal Hall Effect in a Time-Reversal-Symmetry-Broken Topological Superconductor in Two Dimensions: Approach from Bulk Calculations”, Journal of the Physical Society of Japan **82**, 023602 (2013).

[66] Y. Imai, K. Wakabayashi, and M. Sigrist, “Thermal Hall conductivity and topological transition in a chiral *p*-wave superconductor for Sr_2RuO_4”, Phys. Rev. B **93**, 024510 (2016).

[67] R. S. K. Mong and V. Shivamoggi, “Edge states and the bulk-boundary correspondence in Dirac Hamiltonians”, Phys. Rev. B **83**, 125109 (2011).

[68] T. Senthil, J. B. Marston, and M. P. A. Fisher, “Spin quantum Hall effect in unconventional superconductors”, Phys. Rev. B **60**, 4245 (1999).

[69] F. Loder, A. P. Kampf, T. Kopp, et al., “Momentum-space spin texture in a topological superconductor”, Phys. Rev. B **96**, 024508 (2017).

[70] K. Björnson and A. M. Black-Schaffer, “Skyrmion spin texture in ferromagnetic semiconductor–superconductor heterostructures”, Phys. Rev. B **89**, 134518 (2014).

[71] U. Rößler, A. Bogdanov, and C. Pfleiderer, “Spontaneous skyrmion ground states in magnetic metals”, Nature **442**, 797 (2006).

[72] X. Yu, W. Koshibae, Y. Tokunaga, et al., “Transformation between meron and skyrmion topological spin textures in a chiral magnet”, Nature **564**, 95 (2018).

[73] Andriy Nych and Jun-ichi Fukuda and Uliana Ognysta and Slobodan Žumer and Igor Muševič, “Spontaneous formation and dynamics of half-skyrmions in a chiral liquid-crystal film”, Nature Phys. **13**, 1215 (2017).

[74] S. R. Gorol, F. Loder, D. Braak, et al., "Signatures of Topological Phase Transitions in the S-Wave Superconductor at Finite Temperature", Phys. Status Solidi B **259**, 2100156 (2022).

[75] S. Tewari1, T. D. Stanescu, J. D. Sau, et al., "Topologically non-trivial superconductivity in spin–orbit-coupled systems: bulk phases and quantum phase transitions", New J. Phys. **13**, 065004 (2011).

[76] R. A. Klemm, A. Luther, and M. R. Beasley, "Theory of the upper critical field in layered superconductors", Phys. Rev. B **12**, 877 (1975).

[77] S. Rachel, E. Mascot, S. Cocklin, et al., "Quantized charge transport in chiral Majorana edge modes", Phys. Rev. B **96**, 205131 (2017).

[78] M. Sato, Y. Takahashi, and S. Fujimoto, "Non-Abelian Topological Order in s-Wave Superfluids of Ultracold Fermionic Atoms", Phys. Rev. Lett. **103**, 020401 (2009).

[79] R. P. Kaur, D. F. Agterberg, and M. Sigrist, "Helical Vortex Phase in the Noncentrosymmetric $CePt_3Si$", Phys. Rev. Lett. **94**, 137002 (2005).

[80] V. Barzykin and L. P. Gor'kov, "Inhomogeneous Stripe Phase Revisited for Surface Superconductivity", Phys. Rev. Lett. **89**, 227002 (2002).

[81] K. Michaeli, A. C. Potter, and P. A. Lee, "Superconducting and Ferromagnetic Phases in $SrTiO_3/LaAlO_3$ Oxide Interface Structures: Possibility of Finite Momentum Pairing", Phys. Rev. Lett. **108**, 117003 (2012).

[82] P. Fulde and R. A. Ferrell, "Superconductivity in a Strong Spin-Exchange Field", Phys. Rev. **135**, A550 (1964).

[83] A. I. Larkin and Y. N. Ovchinnikov, "Nonuniform state of superconductors", Sov. Phys. JETP **20**, [Zh. Eksp. Teor. Fiz. **47**, 1136 (1964)], 762 (1965).

[84] B. Zhou, H.-Z. Lu, R.-L. Chu, et al., "Finite Size Effects on Helical Edge States in a Quantum Spin-Hall System", Phys. Rev. Lett. **101**, 246807 (2008).

[85] S. Oh, "The Complete Quantum Hall Trio", Science **340**, 153–154 (2013).

[86] H. G. Ahmad, M. Minutillo, R. Capecelatro, et al., "Coexistence and tuning of spin-singlet and triplet transport in spin-filter Josephson junctions", Commun. Phys. **5**, 2 (2022).

[87] L. P. Gor'kov and E. I. Rashba, "Superconducting 2D System with Lifted Spin Degeneracy: Mixed Singlet-Triplet State", Phys. Rev. Lett. **87**, 037004 (2001).

[88] L. Fu and C. L. Kane, "Superconducting Proximity Effect and Majorana Fermions at the Surface of a Topological Insulator", Phys. Rev. Lett. **100**, 096407 (2008).

[89] S. Nakosai, Y. Tanaka, and N. Nagaosa, "Two-dimensional p-wave superconducting states with magnetic moments on a conventional s-wave superconductor", Phys. Rev. B **88**, 180503 (2013).

[90] Y. Maeno, M. T. Rice, and M. Sigrist, "The Intriguing Superconductivity of Strontium Ruthenate", Phys. Today **54**, 42 (2001).

[91] R. Gonczarek, L. Jacak, M. Krzyzosiak, et al., “Competition mechanism between singlet and triplet superconductivity in the tight-binding model with anisotropic attractive potential”, Eur. Phys. J. B **49**, 171 (2006).

[92] M. Mashkoori, A. G. Moghaddam, M. H. Hajibabaee, et al., “Impact of topology on the impurity effects in extended s-wave superconductors with spin-orbit coupling”, Phys. Rev. B **99**, 014508 (2019).

[93] A. Quelle, E. Cobanera, and C. Morais Smith, “Thermodynamic signatures of edge states in topological insulators”, Phys. Rev. B **94**, 075133 (2016).

[94] S. N. Kempkes, A. Quelle, and C. Morais Smith, “Universalities of thermodynamic signatures in topological phases”, Sci. Rep. **6**, 38530 (2016).

[95] L. He and X.-G. Huang, “Superfluidity and collective modes in Rashba spin–orbit coupled Fermi gases”, Ann. Phys. **337**, 163 (2013).

[96] Y. Dong, L. Dong, M. Gong, et al., “Dynamical phases in quenched spin–orbit-coupled degenerate Fermi gas”, Nat. Commun. **6**, 6103 (2015).

[97] A. A. Varlamov and A. V. Pantsulaya, Zh. Eksp. Teor. Fiz. **89**, [ZhETF **89**, 2188 (1985)], 2188 (1985).

[98] K. Seo, C. Zhang, and S. Tewari, “Thermodynamic signatures for topological phase transitions to Majorana and Weyl superfluids in ultracold Fermi gases”, Phys. Rev. A **87**, 063618 (2013).

[99] Z. Zheng, H. Pu, X. Zou, et al., “Thermodynamic properties of Rashba spin-orbit-coupled Fermi gas”, Phys. Rev. A **90**, 063623 (2014).

[100] A. Uhlmann, “Parallel transport and “quantum holonomy” along density operators”, Reports Math. Phys. **24**, 229 (1986).

[101] S. N. Kempkes, A. Quelle, and C. Morais Smith, “Universalities of thermodynamic signatures in topological phases”, Sci. Rep. **6**, 38530 (2016).

[102] J. C. Budich and S. Diehl, “Topology of density matrices”, Phy. Rev. B **91**, 165140 (2015).

[103] L. Leonforte, D. Valenti, B. Spagnolo, et al., “Uhlmann number in translational invariant systems”, Sci. Rep. **9**, 9106 (2019).

[104] H. Chi, C. Zhang, G. Gu, et al., “Lifshitz transition mediated electronic transport anomaly in bulk $ZrTe_5$”, New J. Phys. **19**, 015005 (2017).

[105] R. D. Duncan and C. A. R. Sá de Melo, “Thermodynamic properties in the evolution from BCS to Bose-Einstein condensation for a d-wave superconductor at low temperatures”, Phys. Rev. B **62**, 9675 (2000).

[106] S. S. Botelho and C. A. R. Sá de Melo, “Lifshitz transition in d-wave superconductors”, Phys. Rev. B **71**, 134507 (2005).

[107] J. P. A. Devreese, J. Tempere, and C. A. R. Sá de Melo, “Quantum phase transitions and Berezinskii-Kosterlitz-Thouless temperature in a two-dimensional spin-orbit-coupled Fermi gas”, Phys. Rev. A **92**, 043618 (2015).

[108] W. Tang, X. C. Xie, L. Wang, et al., "Quantized thermal Hall conductance from edge current calculations in lattice models", Phys. Rev. B **100**, 155112 (2019).

[109] Z. B. Siu, Y. Wang1, H. Yang, et al., "Spin accumulation in topological insulator thin films—influence of bulk and topological surface states", J. Phys. D: Appl. Phys. **51**, 425301 (2018).

[110] R. Cheng and Q. Niu, "Microscopic derivation of spin-transfer torque in ferromagnets", Phys. Rev. B **88**, 024422 (2013).

[111] E. Blount, *Formalisms of Band Theory*, edited by F. Seitz and D. Turnbull, Vol. 13, Solid State Physics (Academic Press, 1962), pp. 305–373.

[112] D. Vanderbilt, *Berry Phases in Electronic Structure Theory: Electric Polarization, Orbital Magnetization and Topological Insulators* (Cambridge University Press, 2018).

[113] S. M. Girvin and K. Yang, *Modern Condensed Matter Physics* (Cambridge University Press, 2019).

[114] B. A. Foreman, "Consequences of local gauge symmetry in empirical tight-binding theory", Phys. Rev. B **66**, 165212 (2002).

[115] T. B. Boykin, M. Luisier, M. Salmani-Jelodar, et al., "Strain-induced, off-diagonal, same-atom parameters in empirical tight-binding theory suitable for [110] uniaxial strain applied to a silicon parametrization", Phys. Rev. B **81**, 125202 (2010).

[116] M.-M. Liu, Y. Shao, M. Han, et al., "Energy- and Momentum-Resolved Photoelectron Spin Polarization in Multiphoton Ionization of Xe by Circularly Polarized Fields", Phys. Rev. Lett. **120**, 043201 (2018).

[117] Z. Zhong, A. Toth, and K. Held, "Theory of spin-orbit coupling at $LaAlO_3/SrTiO_3$ interfaces and $SrTiO_3$ surfaces", Phys. Rev. B **87**, 161102(R) (2012).

[118] N. Levys, A. B. K. L. Makerm, M. Panlasiguia, et al., "Strain-Induced Pseudo–Magnetic Fields Greater Than 300 Tesla in Graphene Nanobubbles", Science **329**, 544 (2010).

[119] J. A. Bert, B. Kalisky, C. Bell, et al., "Direct imaging of the coexistence of ferromagnetism and superconductivity at the $LaAlO_3/SrTiO_3$ interface", Nature Phys **7**, 767 (2011).

[120] L. Li, C. Richter, and J. Mannhart, "Coexistence of magnetic order and two-dimensional superconductivity at $LaAlO_3/SrTiO_3$ interfaces", Nature Phys **7**, 762 (2011).

[121] *MPMS3 The next generation of advanced SQUID magnetometry*, `https://www.optixs.cz/data/ke-stazeni/mpms3_en-d794.pdf`, Accessed: 2012-11-08.

[122] M. Buchner, K. Höfler, B. Henne, et al., "Tutorial: Basic principles, limits of detection, and pitfalls of highly sensitive SQUID magnetometry for nanomagnetism and spintronics", Journal of Applied Physics **124**, 161101 (2018).

[123] T. Shen, V. Ostwal, K. Y. Camsari, et al., "Demonstration of a pseudo-magnetization based simultaneous write and read operation in a $Co_{60}Fe_{20}B_{20}/Pb(Mg_{1/3}Nb_{2/3})_{0.7}Ti_{0.3}O_3$ heterostructure", Sci. Rep. **10**, 10791 (2020).

[124] S. Hidalgo-Tobon, "Theory of gradient coil design methods for magnetic resonance imaging", Concepts Magn. Reson. A: Bridg. Educ. Res. **36A**, 223–242 (2010).

[125] V. Zablotskii, T. Polyakova, O. Lunov, et al., “How a High-Gradient Magnetic Field Could Affect Cell Life”, Sci Rep **6**, 37407 (2016).

[126] N. M. Dempsey, D. Le Roy, M.-H. Mathevon, et al., “Micro-magnetic imprinting of high field gradient magnetic flux sources”, Appl. Phys. Lett. **104**, 262401 (2014).

[127] N. Levy, S. A. Burke, K. L. Meaker, et al., “Strain-Induced Pseudo–Magnetic Fields Greater Than 300 Tesla in Graphene Nanobubbles”, Science **329**, 544–547 (2010).

[128] R. L. Fox and M. P. Kapoor, “Rates of change of eigenvalues and eigenvectors”, AIAA J. **6**, 2426–2429 (1968).

[129] L. C. Rogers, “Derivatives of eigenvalues and eigenvectors”, AIAA J. **8**, 943–944 (1970).

[130] D. V. Murthy and R. T. Haftka, “Derivatives of eigenvalues and eigenvectors of a general complex matrix”, Int. J. Numer. Methods Eng. **26**, 293–311 (1988).

[131] J. P. A. Devreese, J. Tempere, and C. A. R. Sá de Melo, “Effects of Spin-Orbit Coupling on the Berezinskii-Kosterlitz-Thouless Transition and the Vortex-Antivortex Structure in Two-Dimensional Fermi Gases”, Phys. Rev. Lett. **113**, 165304 (2014).

[132] J. Hubbard, “Calculation of Partition Functions”, Phys. Rev. Lett. **3**, 77–78 (1959).

[133] R. L. Stratonovich, “Statistical Derivation of the Fundamental Scalar Field”, Dokl. Phys. **2**, 416 (1957).

[134] D. Lehmann, *Mathematical Methods of Many-Body Quantum Field Theory* (Chapman & Hall/CRC, 2004).

[135] N. W. Ashcroft and N. D. Mermin, *Solid State Physics* (Holt-Saunders, 1976).

[136] L. D.Landau and E. M. Lifshitz, in *Quantum Mechanics*, Vol. 3, Course of Theroretical Physics (Pergamon Press, 1965).

[137] Z. B. Siu, M. B. A. Jalil, and S. G. Tan, *Gauge field in systems with spin orbit interactions and additional discrete degrees of freedom to real spin*, 2016.

[138] D. J. Thouless, M. Kohmoto, M. P. Nightingale, et al., “Quantized Hall Conductance in a Two-Dimensional Periodic Potential”, Phys. Rev. Lett. **49**, 405–408 (1982).

[139] H. Grassmann, *Die Lineale Ausdehnungslehre ein neuer Zweig der Mathematik: Dargestellt und durch Anwendungen auf die übrigen Zweige der Mathematik, wie auch auf die Statik, Mechanik, die Lehre vom Magnetismus und die Krystallonomie erläutert*, Cambridge Library Collection - Mathematics (Cambridge University Press, 2012).

[140] H. Kleinert, *Collective Classical and Quantum Fields* (World Scientific, 2018).

[141] A. Kumar, “Matsubara Frequency Sums”, arXiv:1002.4692 [physics.gen-ph] (2010).

[142] A. Nieto, “Evaluating sums over the Matsubara frequencies”, Computer Physics Communications **92**, 54 (1995).